DATE DUE	DATE DUE	DATE DUE

AGES AND CHEMICAL EVOLUTION OF TEPHRA SEQUENCES IN SOUTHWESTERN NEVADA

By

Kristin T. Huysken

A DISSERTATION

Submitted to
Michigan State University
in partial fulfillment of the requirements
for the degree of

DOCTOR OF PHILOSOPHY

Department of Geological Sciences

1996

ABSTRACT

AGES AND CHEMICAL EVOLUTION OF TEPHRA SEQUENCES IN SOUTHWESTERN NEVADA

By

Kristin T. Huysken

Compositional and $^{40}Ar/^{39}Ar$ ages in three tephra sequences from the southwestern Nevada record the chemical history and timing of eruption from the parent magmas producing these volcanoclastic sequences. Compositional changes within two of the tephra sequences, the Post-Grouse Canyon and the Pre-Rainier Mesa tephra sequences, correspond with changes in $^{40}Ar/^{39}Ar$ ages.

The Post-Grouse Canyon tephra sequence is divided into three main corresponding age and compositional groups. The compositional groups are not easily related by crystal fractionation or magma mixing and are interpreted to represent distinct magma batches derived from separate sources. A highly compositionally variable layer occurring within the middle age group, is interpreted to reflect the eruption of an additional distinct magma type. This pattern of emplacement and eruption of unrelated magmas recorded in the Post-Grouse Canyon tephra sequence mimics the inferred processes operating in large-volume magmatic systems in this region.

The Pre-Rainier Mesa tephra sequence is divided into two discrete age and compositional groups. The upper sequence is the age and chemical equivalent of the high-silica, low Th/Nb portion of the overlying Rainier Mesa Tuff (11.6 Ma). The sequence is the age equivalent of the underlying Tiva Canyon Tuff (12.7 Ma), however is compositionally unlike the Tiva Canyon Tuff. The lower Pre-Rainier Mesa tephra sequence is consistent with at least two magma mixing combinations. Both combinations involve mixing of magma compositionally similar to the low Th/Nb, high silica group from the Rainier Mesa Tuff. The inferred presence of Rainier Mesa-like magma at 12.7 Ma suggests that more than one magma pulse was emplaced from the source rocks that produced the Rainier Mesa magma. The emplacement of multiple magma pulses is in contrast to the inferred single pulse emplacement style for the large-volume magmatic systems in the region.

The third tephra sequence, the Pre-Ammonia Tanks tephra sequence, does not exhibit a compositional change with respect to stratigraphic position. In general, the entire compositional range (70-78% SiO_2) is present throughout the sequence. This compositional variation is consistent with the overlying Ammonia Tanks ash-flow sheet. Ages for the Pre-Ammonia Tanks tephra sequence are not well constrained and may be partially reset.

For Erik

ACKNOWLEDGMENTS

Above all, I thank my advisor, Tom Vogel, for guidance, support, and friendship that has surpassed all of my expectations. I am fortunate to have worked closely with someone so devoted to his students and so committed to geology. I thank Tom with my deepest respect and appreciation.

My committee, Bill Cambray, Dave Matty, and Kaz Fujita, are thanked for their review of this dissertation and guidance throughout the course of this study. Additional thanks to Bill Cambray for facilitating many insightful discussions during this study.

I would like to thank Tim Flood for his help, sound advice, and "professional" discussions in the field.

Fellow students, Ben Saltoun, and Rich Stern deserve special thanks for the many occasions when they shared their ideas and philosophy related to geology, graduate school, and life.

I thank John Brannen for his detailed sample collection, field notes, and related discussions; Jason Price for his help, knowledge, and camaraderie in the field; Ed Masters and Paul DeKonig for the wonderful job they did preparing samples of the Pre-ammonia Tanks tephra sequence; and Rick Warren of Los Alamos National Laboratory and Bill McKinnis of

Lawrence Livermore National Laboratory for their help locating outcrops of the Pre-ammonia Tanks tephra sequence.

This research was aided by a Grant-in-Aid of Research from Sigma Xi, The Scientific Research Society, and the Lipman Research Award for 1994 (Grant No. 5372-94) from the Geological Society of America. In addition, Michigan State University provided fellowship funds that undoubtedly hastened the completion of this dissertation.

Finally, I thank my family for emotional support, especially my mother, who has diligently plugged through everything I have written (sorry this one is so long). As always, many thanks to Maureen Walton, Alex Guimaraes, and Matt Casselton for love and support, but mostly for friendship.

TABLE OF CONTENTS

LIST OF TABLES

LIST OF FIGURES

Chapter 1

INTRODUCTION

Purpose of Study

Chemically and mineralogically zoned ash-flow sheets provide good evidence that the source magmas were also zoned (Lipman et al., 1966; Smith 1979; Hildreth 1981; Mahood 1981; and Baker 1985). Because of this, zoned ash-flow sheets have been studied extensively to evaluate the origin and evolution of zoned magma bodies. In almost all of these studies, the inferred trends towards the top of the magma bodies are increasing silica and H_2O, and decreasing temperature and phenocrysts.

Tephra sequences often associated with zoned ash-flow sheets receive less attention than the associated ash-flow sheets. Typically, these deposits are considered to be merely pre-eruptive "burps" from the uppermost portion of the magma body, and are often neglected in studies of large-volume magmatic systems. However, smaller volume tephra sequences may be far more useful in interpreting the petrologic history of an area than is generally recognized. For example, a recent $^{40}Ar/^{39}Ar$ age study on sanidine phenocrysts from the Laacher See Tephra by van den Bogaard (1995) records

a complex history of emplacement, crystallization, and eruption of a smaller volume (< 5 km^3) tephra deposits.

In the Southwest Nevada Volcanic Field, major caldera forming eruptions led to the formation of large-volume, chemically zoned, ash-flow sheets with smaller volume tephras intercollated between the large ash-flow deposits. These small units may provide valuable information central to our understanding of the origin and evolution of these voluminous magmatic systems. This study focuses on these smaller volume tephra sequences, and their relationship to the large-volume ash-flow sheets.

These small-volume tephra sequences may be used to determine the processes that modified magmatic systems and ultimately led to the eruption of the large volume ash-flow sheets. Furthermore, they may provide information related to the time scales over which these processes occurred (that is, the rates of magmatic evolution).

The central hypotheses of this study are: To investigate the chemical and age variations of individual tephra sequences in order to determine the processes and rates of these processes that formed the larger magmatic systems.

The Southwest Nevada Volcanic Field contains four very large volume, chemically zoned ash-flow sheets (>900 km^3) and at least eight other ash-flow sheets larger than 100 km^3. Although closely related in time and place, many of these very large eruptive deposits have distinct chemical

compositions. Associated with many of these ash-flows, are sequences of smaller volume tephra deposits that record numerous, small-volume, eruptive events. These tephra sequences consist of pumice and ash-fall deposits, and small volume ash-flow layers. Some of the tephra sequences have significant chemical variation, indicating that they represent more than merely the uppermost portion of a large fractionating magma body (Huysken et al., 1994). Instead, these tephra sequences record magmatic changes that took place in the system between eruption of the major ash-flow sheets. They provide a unique glimpse into a large, dynamic magmatic system.

Compositional changes, related to changing stratigraphic position, occur in the tephra sequences. Because the tephra sequences represent a time sequence, it is inferred that these chemical changes reflect magmatic changes occurring as these tephras were erupted. Relating chemical changes in these sequences to magmatic processes (e.g., crystal fractionation, magma mixing), provide insight into the magmatic development of the associated large-volume ash-flow sheets. Chemical changes along with changes in radiometric ages throughout these tephra sequences, provide information concerning the rates of the petrologic processes that chemically modified these systems.

Crystal fractionation, magma mixing and assimilation, or partial melting of a single source are models that can be tested by the variation in a tephra sequence. If these major petrologic processes (or combinations of

them) cannot account for the observed variation from layer to layer, the null hypothesis (that these layers are unrelated and therefore must represent melts from a different sources) must be concluded. Understanding the processes that control chemical variation of these sequences is just one step in understanding the dynamics of magmatic systems. Equally significant, are the rates at which magmatic processes occur.

Theoretical and experimental work establishing rates of magmatic processes (Spera and Crisp, 1981; Crisp, 1984; Trial and Spera, 1990; Wolff et al., 1990; Christiansen and DePaolo, 1993; de Silva and Wolff, 1994; and others) provide only first order estimates on the timing of these processes. Variables used in theoretical and experimental models such as heat capacities, diffusion coefficients, amount of undercooling, temperature, pressure, volume, and chamber shape, may be poorly constrained. In natural systems, more direct means for measuring rates of change must be employed. $^{40}Ar/^{39}Ar$ radiometric age dating, provides a method of direct measurement for the timing of chemical changes taking place in these systems.

In this study, stratigraphically detailed chemical and age measurements were obtained for three tephra sequences. They are, the Post-Grouse Canyon tephra sequence, the Pre-Rainier Mesa tephra sequence, and the Pre-Ammonia Tanks tephra sequence. These data were used to test whether these tephra sequences could be used to decipher magmatic changes

that took place between large eruptive events; and, to determine the rates of these magmatic processes.

General Geology

The Southwest Nevada Volcanic Field (Figure 1) was most active from approximately 15.25 Ma to 6.3 Ma and was related to igneous activity that occurred throughout the Basin and Range Province from approximately 37 to 5 Ma ago (Eaton, 1984). Six major volcanic centers produced more than thirty major ash-flow sheets and lava flows (Byers, 1976). An extensional tectonic regime has operated in this region throughout the Cenozoic and, in a general way, volcanism increased from 15.25 Ma to 11.45 Ma, and then waned to 6.3 Ma (Sawyer et al., 1994). Volumetrically, ash flows are the major eruptive product of this volcanic activity. Many of the ash-flow sheets are chemically zoned and some are very large in volume (>900 km^3). The composition of major eruptive units also changes with time, and with erupted volume.

Earlier ash-flow deposits were dominated by peralkaline compositions. The eruption of the Grouse Canyon Tuff at 13.7 Ma and Deadhorse Flat Tuff at 13.5 Ma, mark the end of this stage of peralkaline volcanism. Eruption of the large-volume, metaluminous ash-flow sheets of the Paintbrush and Timber Mountain Groups followed. Together, these units total more than 4000 km^3 in volume, marking the most intense eruptive activity in this area.

This stage of eruption ended after the eruption of the Ammonia Tanks Tuff (1000 km^3) at 11.45 Ma. Later, peralkaline ash flows were again the

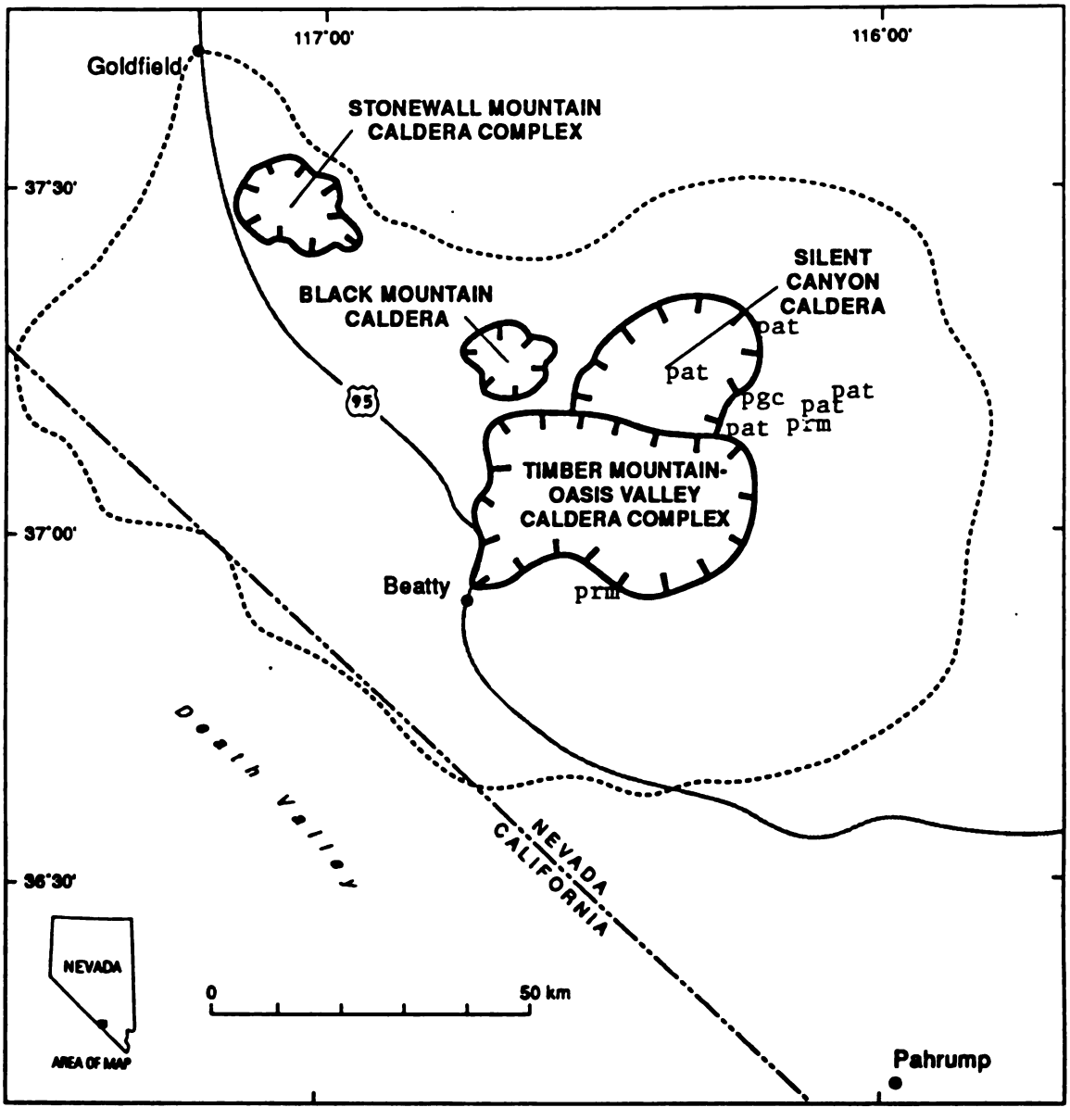

Figure 1. Map of the Southwest Nevada Volcanic Field indicating calderas. Sampled locations are labeled 'pgc' (Post-Grouse Canyon tephra sequence), 'prm' (Pre-Rainier Mesa tephra sequence) and 'pat' (Pre-Ammonia Tanks tephra sequence)

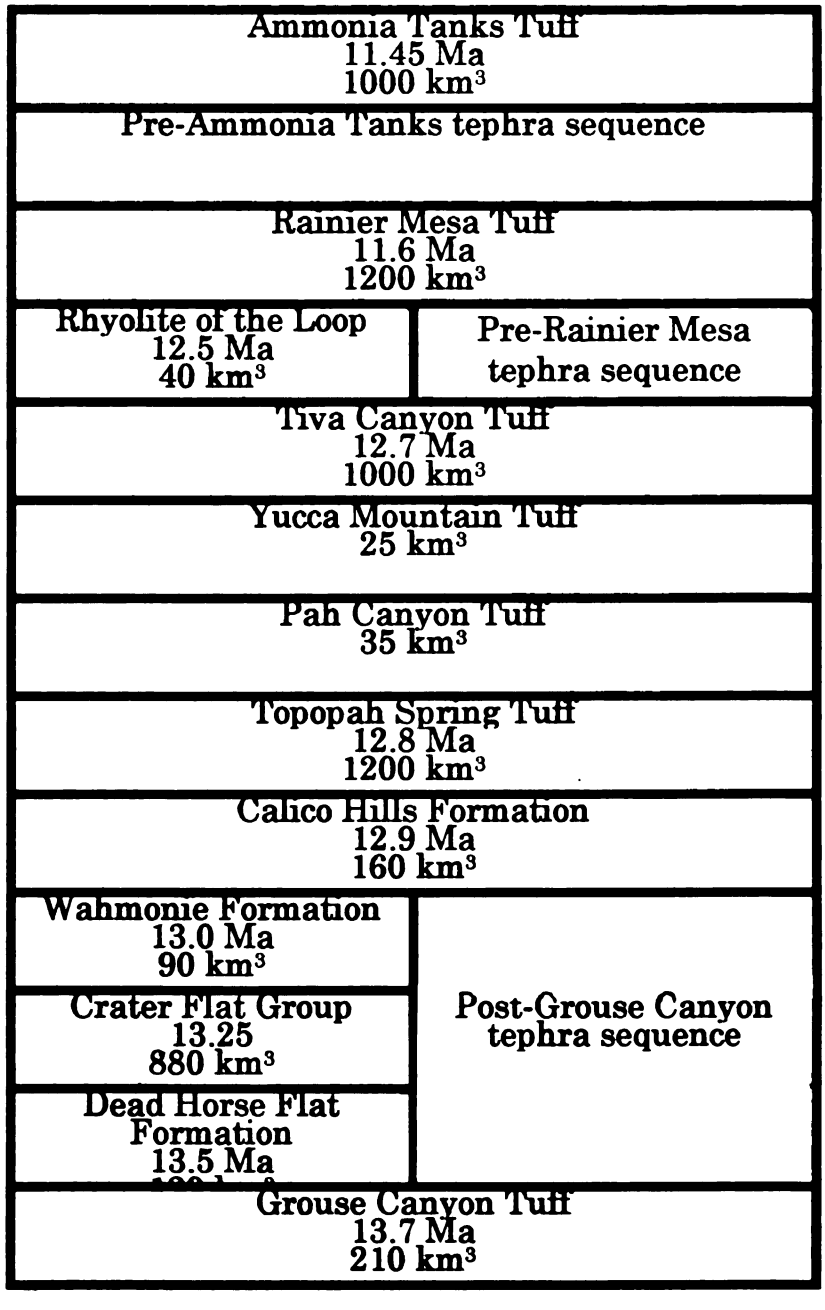

Figure 2. Generalized stratigraphy of volcanic units from the Southwest Nevada Volcanic Field, erupted from 13.7 to 11.45 Ma. Ages, volumes, and unit names are for all units except the tephra sequences are from Sawyer et al. (1994).

dominant ash-flow type. A generalized regionally stratigraphy (after Sawyer et al., 1994) is used here to correlate units regionally, based on $^{40}Ar/^{39}Ar$ ages of sanidines and chemical composition of individual units (Figure 2).

The present study focuses on tephra sequences associated with large-volume ash-flow sheets erupted during the period of metaluminous volcanism. The three tephra sequences used for this study lie respectively above the Grouse Canyon Tuff, beneath the Rainier Mesa Tuff, and beneath the Ammonia Tanks Tuff. The following is a summary of work done to date for the tephra sequences and associated ash-flow sheets used in this study. All ages from previous work (and from this study) are reported with a 2σ error.

The Grouse Canyon Tuff

The Grouse Canyon Tuff is one of the last peralkaline units to erupt prior to the onset voluminous metaluminous volcanism in this area. It was erupted from the Silent Canyon Caldera (Noble et al., 1968), and is smaller (210 km^3) than the following metaluminous eruptions from the Claim Canyon Caldera and Timber Mountain-Oaisis Valley Caldera Complex (Figure 1). $^{40}Ar/^{39}Ar$ ages on sanidines from the Grouse Canyon Tuff yield an age of 13.7 $\pm$ 0.08 (Sawyer et al., 1994).

The Post-Grouse Canyon Tephra Sequence

Above the Grouse Canyon ash-flow sheet lies a thick sequence of tephra fall and interbedded small ash-flow layers. It is very well exposed on Pahute Mesa, where it is approximately 175 meters thick, and is truncated above by the surge deposit of the Rainier Mesa ash-flow sheet. At this location, the sequence consists of bedded pumice- and ash-fall deposits interbedded with small ash-flow layers (Figure 3a). The pumice falls consist of moderately to very well sorted, light gray and brown pumice fragments. Individual pumice fragments range in size from sand to cobbles. These layers are commonly well stratified, exhibit normal or reverse grading, and commonly contain minor amounts of lithic and light gray obsidian fragments up to 0.5 centimeters in diameter. The ash layers are light to medium gray and brown and range in thickness from less than 0.25 centimeters to several meters.

Interbedded with the tephra-fall layers are numerous small ash-flow layers. These layers are very poorly sorted, nonstratified to poorly stratified mixtures of pumice, lithics, and ash (Figure 3b). They are often discontinuous within an individual exposure, and contain basal zones (2-5 centimeters) of reworked material. Many small ash-flow layers exhibit a color change from white or very light gray at the base of the layer, to brown at the top. Most of the color change occurs in the ashy matrix and in the smaller pumice fragments, while the larger pumice fragments are consistently light gray throughout the layer. Some tephra-fall and small ash-

Figure 3. (a) Bedded tephra deposits from the Post-Grouse Canyon tephra sequence. (b) small ash-flow layer contained within the tephra sequence.

flow layers contain organic remains (probably plant roots) in the upper few centimeters of the layer. In addition, at least two 1 centimeters thick layers of very dark brown and black organic rich layers are present within the sequence.

Two very localized channel deposits are present within the sequence. One is a 'V' shaped deposit, approximately 1 meters wide and 1.5 meters high, consisting of coarse gravel and pebbles. The deposit is two to three meters across and less than a meter in height. In this case, the channel fill consists of ash-flow material.

The Post-grouse Canyon tephra sequence contains a 50 meters thick mass flow unit within it. Unlike the smaller ash-flow layers in the sequence, this unit exhibits no color change. There is a 0.3 meters thick surge deposit of white ash at the base, overlain by a white ash-flow containing boulder-sized lithic and pumice fragments. Though thick, this unit is extremely localized and probably fills a small paleochannel or depression.

The Dead Horse Flat Formation, Crater Flat Group, Wahmonie Formation, and Calico Hills Formation

Regional stratigraphic units overlying the Grouse Canyon Tuff include the Dead Horse Flat Formation (13.5 ± 0.04 Ma), the Crater Flat Group which includes the Bullfrog Tuff (13.25 ± 0.04), the Wahmonie Formation (13.0 ± 0.18 Ma), and the Calico Hills Formation (12.9 ± 0.04 Ma). $^{40}Ar/^{39}Ar$

ages for these units were determined by Sawyer et al. (1994). In the revised stratigraphic framework proposed by Sawyer et al. (1994), The Dead Horse Flat Tuff is the youngest formation in the Belted Range Tuff and is the last major peralkaline unit to have erupted prior to the voluminous metaluminous deposits making up the Paintbrush and Timber Mountain Groups. Three formations make up the Crater Flat Group. The Bullfrog Tuff consists of two metaluminous ash-flow sheets and is the most voluminous formation of the Crater Flat Group. The Wahamonie Formation consists of andesitic and dacitic lavas and tephras that are generally widespread but are not present in the area where the Post-grouse Canyon tephra sequence outcrops.

The Topopah Springs Tuff

Eruption of the Topopah Springs Tuff followed the eruption of the Post-Grouse Canyon tephra sequence. The Topopah Springs Tuff is a 1200 km^3 (Byers, 1976; Scott et al., 1984) compound cooling unit (Lipman et al., 1966), erupted at 12.8 ± .04 Ma (Sawyer et al., 1994). It is compositionally zoned with high silica rhyolite overlain by a crystal-rich quartz latite; and, inferred to be the result of eruption from a layered magma body with a sharp compositional interface between the high silica rhyolite and quartz latite magmas (Schuraytz et al., 1989).

Yucca Mountain and Pah Canyon Tuffs

Two smaller eruptions followed the eruption of the Topopah Springs Tuff. The Pah Canyon Tuff (35 km^3) and the Yucca Mountain Tuff (25 km^3) make up two metaluminous formations of the Paintbrush Group. Major and trace element composition of the Pah Canyon Tuff is consistent with mixing of the lower and upper portions of the Topopah Spring Tuff (Flood et al., 1989). The Yucca Mountain Tuff likely represents initial eruption of the Tiva Canyon magma chamber (Flood et al., 1989).

The Tiva Canyon Tuff

Underlying the Timber Mountain Group is the Tiva Canyon Tuff (Figure 2). The Tiva Canyon Tuff is the youngest formation in the Paintbrush Group, and was erupted from the Oasis Valley-Timber Mountain Caldera complex (Figure 1). Radiometric $^{40}Ar/^{39}Ar$ ages on sanidines from the Timber Mountain Tuff gives an age of 12.7 ± 0.06 Ma (Sawyer et al., 1994). The Tiva Canyon Tuff has an erupted volume of 1000 km^3 and together with the other members of the Paintbrush Group have an erupted volume of 2200 km^3. Like many of the large-volume southwestern Nevada ash-flow sheets, the Tiva Canyon Tuff is chemically zoned. The highest silica portion is interpreted to represent a hybrid mixture of magmas, combined with crystal fractionation, of the underlying Pah Canyon Formation and quartz latite from the Tiva Canyon Tuff (Flood et al., 1989).

The Pre-Rainier Mesa Tephra Sequence

The Pre-Rainier Mesa Tephra Sequence lies stratigraphically between the Tiva Canyon and Rainier Mesa ash-flow sheets. It is well exposed at two locations on the Nevada Test Site and one location west of Yucca Mountain in the Crater Flats area (Figure 1). In all locations this sequence is truncated above by the Rainier Mesa ash-flow sheet. The section on Rainier Mesa conformably overlies the Tiva Canyon Tuff. At the other two locations, the base is fault bounded.

The Pre-Rainier Mesa tephra sequence ranges in thickness from about 30 meters to 60 m. Like the Post-grouse Canyon tephra sequence, the Pre-rainier Mesa tephra sequence consists of bedded pumice- and ash-fall deposits interbedded with small ash-flow layers. The pumice falls consist of moderately to very will sorted, light gray (almost white) to brown pumice fragments that range from approximately sand- to boulder-size. These layers are often well stratified and exhibit normal or reverse grading; they commonly contain minor amounts of lithic fragments. Ash-fall layers range in thickness from 0.25 centimeters to 4 meters in thickness. Their colors range from light to medium gray and brown.

Interbedded with the tephra-fall layers are numerous small ash-flow layers. These layers range in thickness from less than a meter thick to about 6 meters or more in thickness. Though no volume measurements have been

made, individual ash-flow layers generally are thicker towards the top of the sequence; this is interpreted to indicate a related increase in the erupted volume. The layers are very poorly sorted, nonstratified mixtures of pumice, lithics, and ash. They are often discontinuous, contain basal zones (2-5 centimeters) of reworked material, and have been interpreted to represent mass flow deposits by Warren and Valentine (1990). Many small ash-flow layers exhibits a color change from white or very light gray at the base of the layer, to brown at the top. Most of the color change occurs in the ashy matrix and smaller pumice fragments, while the larger pumice fragments remain light gray throughout the layer. A few tephra-fall layers and small ash-flow layers contain organic remains (probably plant roots) in the upper few centimeters of the layer.

The Rainier Mesa Tuff

The Timber Mountain Group is composed of two of the largest volume ash-flow sheets in the Southwest Nevada Volcanic Field. The Rainier Mesa Tuff (11.6 ± 0.06) is 1200 km^3 in volume and is the older of the two formations. Eruption of the Rainier Mesa Tuff led to the initial collapse of the Timber Mountain Caldera (Byers et al., 1976; Broxton et al., 1989; Farmer et al., 1991). The Rainier Mesa ash-flow sheet is chemically and mineralogically zoned (55 to 78% silica) and was produced by the eruption of a chemically stratified magma body (Mills, 1991). The ash-flow sheet

consists of low- and high-silica trends defined by a compositional gap at approximately 72% silica (Cambray et al., 1995). The high silica portion of the of the ash-flow sheet represents approximately ninety percent of the total erupted volume (Mills, 1991). The high-silica portion of the ash-flow sheet is, in turn, subdivided into two distinct high-silica groups based on differences in Th and Nb content; and, are interpreted to represent separate magmas that shared the same magma chamber and erupted simultaneously (Cambray et al., 1995; Saltoun, 1995). The low Th/Nb chemical group comprises the bulk of the high silica portion of the ash-flow sheet and is widespread. The high Th/Nb group is also widespread yet it represents only a minor volume of the high silica portion of the ash-flow sheet.

Prior to this study, the relationship of the Rainier Mesa Tuff to its associated tephra sequences (both the Pre-Rainier Mesa tephra sequence and the Pre-Ammonia Tanks tephra sequence [see below]) were largely unknown.

Pre-Ammonia Tanks Tephra Sequence

Situated between the Rainier Mesa and Ammonia Tanks Tuffs is the Pre-Ammonia Tanks Tephra Sequence. It is exposed in at least 5 locations on the Nevada Test Site, (Figure 1) and outcrops range from approximately 3.5 meters to 9 meters thick. The Pre-Ammonia Tanks Tephra Sequence is primarily composed of ash- and pumice-fall layers. At two locations, small ash-flow layers and possible paleosols are also present. The Pre-Ammonia

Tanks Tephra Sequence is the thinnest of the tephra sequences in this study and in many locations is not present between the two large ash-flow sheets. As noted for the Pre-Rainier Mesa Tephra Sequence, many of the small ash-flow layers within the Pre-Ammonia Tanks Tephra Sequence display a progressive color change from base to top.

Unlike the other sequences in this study, there is evidence of widespread hydrothermal alteration in the Pre-Ammonia Tanks tephra sequence. In many areas, this is shown by vividly colored pink, purple, and orange layers in the sequence.

The Ammonia Tanks Tuff

The youngest unit of the Timber Mountain Group is the Ammonia Tanks Tuff. This 1000 km^3 ash-flow sheet is composed of two cooling units (Byers et al., 1976) and, like the underlying Rainier Mesa Tuff, is accompanied in most locations by the associated tephra sequence discussed above. Eruption of the Ammonia Tanks ash-flow sheet resulted in the terminal collapse of the Timber Mountain Caldera (Byers et al., 1976; Christiansen et al., 1977; Broxton et al., 1989), approximately 11.45 million years ago. Like the Rainier Mesa Tuff, the Ammonia Tanks ash-flow sheet has a chemical range that spans from 57 to 78 wt.% SiO_2. The low and high silica compositions are separated by a compositional gap at about 72% SiO_2 (Rose, 1988; Mills, 1991; Cambray et al., 1995). The high-silica portion of the

Ammonia Tanks Tuff is consistent with crystal fractionation of the lower-silica portion combined with some mixing of the high silica portion of the Rainier Mesa Tuff (Rose, 1988). However, it has recently been suggested that the high-silica portion may be a product of mixing of the two high-silica groups from the Rainier Mesa Tuff (Cambray et al., 1995).

Chapter 2

METHODS

Sample Selection for chemical analyses

Site selection for this study was based on the quality of exposure and the completeness of the sequence at any one locality. For the tephra sequences associated with the Timber Mountain Group, attempts were made to collect samples from a variety of locations around the caldera. Limited exposures, however, restricted the number of sites sampled. For the Post-Grouse Canyon tephra sequence, one thick section was sampled. The location of this site is shown in Figure 1. Samples were collected from three locations of the Pre-Rainier Mesa tephra sequence, from locations northeast, north, and southwest of the caldera. The Pre-Ammonia Tanks tephra sequence was sampled at four locations. All of these locations were along the northern portion of the caldera (Figure 1).

Careful stratigraphic control and detailed sample collection were crucial to the success of this study. Once a sample site was selected, lithologic changes observed in the sequence and heterogeneity observed within a given layer determined the collection of samples.

Within an individual tephra layer, collection of individual pumice samples was based on size, color, and crystal content. Because glassy pumice fragment variations represent the variations in magmatic compositions at the time of eruption, an attempt was made to select as wide a variety of pumice fragments as possible from each layer.

Sample selection among layers throughout the tephra sequence was based on textural and color changes from layer to layer. Some lithologic changes in the tephra sequences take place on the millimeter scale. These probably do not reflect individual eruptions but rather small changes in wind direction, wind intensity, or settling velocities of different particle sizes after a single eruption. In such cases, samples were taken at regular intervals, provided that samples large enough for analyses could be found.

In addition to individual glassy pumice fragments, bulk tephra samples were collected from individual small ash-flow layers, and from thick ash-beds and laminated or thinly bedded ash beds where pumice fragments large enough for chemical analyses were not present. Glassy pumice analyses were used to facilitate comparisons between the tephra sequences and the associated large volume ash-flow sheets. The reasons for selecting bulk rock samples vs. individual glassy pumice fragments are discussed below.

Glassy pumice vs. bulk rock samples

Glassy pumice fragments most closely represent the geochemical and mineralogical compositions of the original magma (Wolff, 1985). This is because glassy pumice fragments are a direct sample of the crystal and liquid portions of the magma. It is for this reason that individual glassy pumice fragments are used in this study.

Unfortunately, individual glassy pumice fragments from small ash-flow layers within the tephra sequences used in this study, do not represent the entire chemical range of the ash-flow layer. Most of the chemical variation takes place in pumice fragments too small for analysis, and in the ashy matrix. In these cases, bulk samples were collected for analysis. Here, bulk samples have proved useful in comparing differences that take place within and among small ash-flow layers and among more fine grained deposits within a given tephra sequence.

Chemical analyses used for comparison from previous studies on the large ash-flow sheets (Schuraytz, 1988; Flood et al., 1989a, 1989b; Schuraytz et al., 1989; Mills and Rose, 1991; Cambray et al., 1995; Saltoun, 1996; Mills et al., *in review*) employ glassy pumice fragments exclusively. For this reason, only glassy pumice analyses from the tephra sequences are used when making comparisons between tephra sequences and ash-flow sheets. Because all the tephras from this study are secondarily hydrated, analyses

are normalized on a volatile free basis to facilitate comparisons among different units.

Sample selection and age calculation for $^{40}Ar/^{39}Ar$ analysis

$^{40}Ar/^{39}Ar$ radiometric ages were determined for samples collected from all seven sections in this study. The selection of samples for age dating was based on the freshness of tephra layers, stratigraphic position in the sequence, and known compositional variations within the sequence (based on a preliminary chemical study). In addition, samples were selected from above and below small unconformities with the expectation that the hiatus represented by unconformities might be distinguishable by $^{40}Ar/^{39}Ar$ methods.

Both the Post-Grouse Canyon and Pre-Rainier Mesa tephra sequences contained compositional changes from base to the top of the sequences. Consequently, layers throughout the sequence were dated. The Pre-Ammonia Tanks tephra sequence, though it contains a wide chemical variation, did not vary systematically, from base to top. Therefore, fewer layers were dated from the Pre-Ammonia Tanks tephra sequence. These dates are mainly from the uppermost and lowermost portions of the sequence. In all, 47 separate tephra layers were dated.

Laser ablation $^{40}Ar/^{39}Ar$ analyses were conducted on between five and eleven, hand picked sanidine grains were obtained for each tephra layer. In

selecting grains for analysis, care was taken to sample fresh parts of the outcrop and to select fresh grains, void of large inclusions for $^{40}Ar/^{39}Ar$ analysis. Many grains, however, did contain small glass inclusions. Residual glass was dissolved from grain surfaces using fluoboric acid, followed by a distilled water rinse.

Ideally, grains were analyzed individually, however, because the amount of argon released is proportional to the size of the crystal, two or more crystals were fused together when crystal size was very small (approximately less than 1mm in length).

Radiometric $^{40}Ar/^{39}Ar$ ages are calculated based on the equation:

$$t = 1/\lambda \ln\{J \cdot (^{40}Ar^*/^{39}Ar)+1\}$$

where $^{40}Ar^*$ is the amount of radiogenic ^{40}Ar present in the sample, λ is the decay constant for $^{40}K \rightarrow ^{40}Ar^*$, and J is a study specific, irradiation parameter based on the neutron flux during irradiation. All samples and standard Bern 4B were irradiated together at the McMaster nuclear reactor. The weighted average of J, based on the equation:

$$J = \frac{\left(e^{\lambda_{total} \cdot t_{standard}} - 1\right)}{\left(^{40}Ar^*/^{39}Ar\right)_{standard}},$$

is 0.000486 ±0.000008.

To minimize the contribution of ^{40}Ca, samples with large Ca/K ratios (>0.1), were eliminated from the database before ages for individual tephra layers were calculated. Samples containing very little $^{40}Ar^*$ (radiogenic

argon 40), were also eliminated. An acceptable range of $^{40}Ar^*$ was determined in the same manner as a recent study by Best et al. (1995). For each tephra sequence, there appeared to be a natural break in the data where the amount of $^{40}Ar^*$ in most samples was either above a certain level or far below it. For the Post-Grouse Canyon and Pre-Ammonia Tanks tephra sequences, this break occurred at 94% $^{40}Ar^*$. $^{40}Ar^*$ values for the Pre-Rainier Mesa tephra sequence were less tightly grouped as the other sequences. Radiogenic ^{40}Ar values as low as 75% were used for age calculations of this sequence.

The radiometric $^{40}Ar/^{39}Ar$ age of individual tephra layers are calculated as inverse variance weighted means, $\bar{t}$, and standard deviation, σ_t, based on the equation:

$$\bar{t} \pm \sigma_t = \frac{\sum_{i=1}^{n} t_i w_i}{\sum_{i=1}^{n} w_i} \pm \sqrt{\frac{1}{\sum_{i=1}^{n} w_i}},$$

where the weight $w_i = 1/\sigma_{ti}^2$, and t_i is an individual age measurement. Calculated ages from individual layers are then pooled to give an average age for that group. Uncertainties for pooled averages are calculated as the mean of the weighted deviates. $^{40}Ar/^{39}Ar$ analyses used for the calculation of the upper portion of the Pre-Rainier Mesa tephra sequence, are reported in Table 1.

Sample	% $^{40}Ar^*$	$^{40}Ar/^{39}Ar$	$^{37}Ca/^{39}K$	$^{40}Ar/^{39}Ar$ Age (Ma)	weighting factor
12R8-0-21	98.25	13.514	0.010	11.572 ± 0.054	342.936
12R8-0-23-1	79.20	16.624	0.026	11.465 ± 0.513	3.800
12R8-0-23-2	99.61	13.482	0.010	11.704 ± 0.057	307.787
12R8-0-24-1	92.03	14.278	0.013	11.454 ± 0.057	307.787
12R8-0-24-2	99.83	13.393	0.009	11.652 ± 0.067	222.767
12R8-0-25	98.19	13.507	0.009	11.559 ± 0.063	251.953
12R8-0-27-2	92.02	14.177	0.010	11.373 ± 0.593	2.844
Weighted mean age and uncertainty (Ma) 11.58 ± 0.03					
Sample	% $^{40}Ar^*$	$^{40}Ar/^{39}Ar$	$^{37}Ca/^{39}K$	$^{40}Ar/^{39}Ar$ Age (Ma)	weighting factor
12R8-3-12	81.30	16.334	0.005	11.578 ± 0.063	251.953
12R8-3-2	97.96	13.680	0.015	11.679 ± 0.058	297.275
12R8-3-5	96.13	13.946	0.008	11.684 ± 0.059	287.274
Weighted mean age and uncertainty (Ma) 11.65 ± 0.04					
Pooled weighted mean and uncertainty (Ma) 11.62 ± 0.04					

Table 1. Representative $^{40}Ar/^{39}Ar$ analyses and weighting factors for weighted mean age calculation.

Care should be taken when interpreting uncertainties from radiogenic age analyses. Three main sources of uncertainty exist. They are, 1) the precisional error of the instrumentation used in acquiring the analyses (in this case a laser mass spectrometer), 2) variation caused by sampling and

preparation techniques, and 3) variation caused by geological factors (e.g. Geyh and Schleicher, 1990).

Chapter 3

THE POST-GROUSE CANYON MAGMATIC SYSTEM

Previous Work

The 200 meters thick tephra sequence overlying the Grouse Canyon ash-flow sheet on Pahute Mesa, has not been previously studied. The Rainier Mesa ash-flow sheet truncates this sequence above. Chemically, the tephra sequence closely resembles the high silica portion of the metaluminous Rainier Mesa Tuff. This sequence is not chemically related to the peralkaline trend of the Grouse Canyon Tuff. In fact, the current designation, 'Post-Grouse Canyon' is based solely on new ages for the tephra sequence and not on its chemistry.

$^{40}Ar/^{39}Ar$ radiometric ages

Based on non-overlapping ages for individual tephra layers within the Post-grouse Canyon tephra sequence, $^{40}Ar/^{39}Ar$ radiometric ages on sanidines record at least three different age groups as shown in Figure 4. The pooled ages for the three groups are 13.52 ±0.04 for the base of the sequence, 13.33 ±0.06 for the middle portion of the tephra sequence, and 13.05 ±0.04 for the upper portion of the tephra sequence. The age break between the lower and

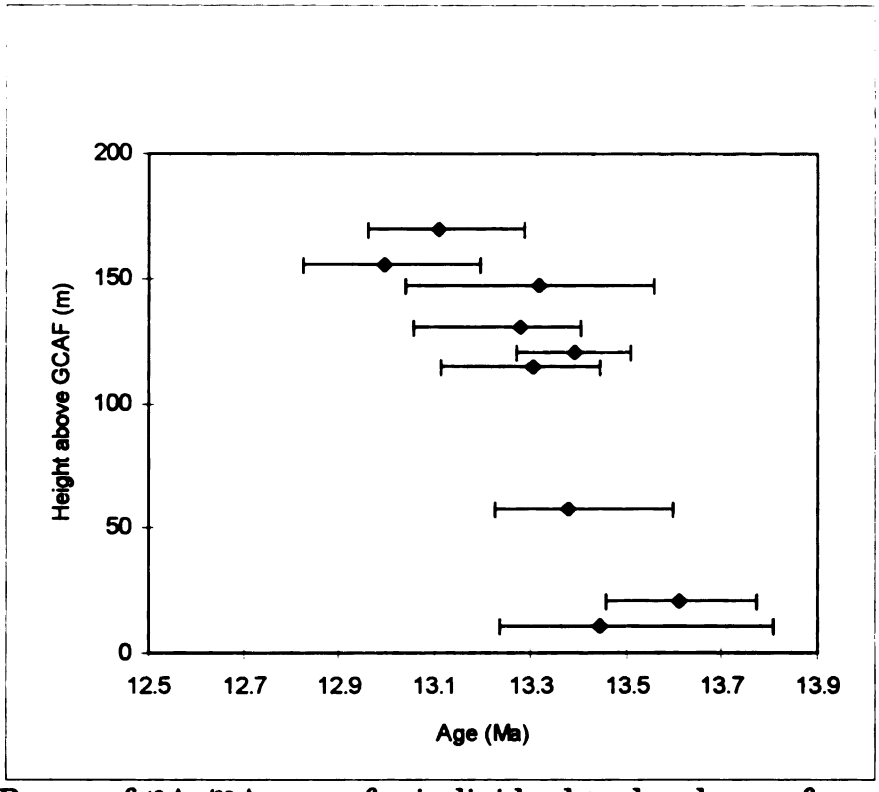

Figure 4. Range of $^{40}Ar/^{39}Ar$ ages for individual tephra layers from the Post-Grouse Canyon tephra sequence.

middle portions of the sequence is tightly constrained. However, the two layers underlying the break for the upper age group overlap the both middle and upper age groups. Because of geochemical considerations (see later) these layers are grouped with the middle portion of the sequence.

Geochemistry

The Post-Grouse Canyon tephra sequence has the largest chemical range of the three sequences in this study. SiO_2 ranges from 67 to 78%, and Zr, from 60 to 686 ppm (Figure 5). It is distinct from the underlying peralkaline Grouse Canyon ash-flow sheet based on both major and trace element chemistry of glassy pumice fragments collected for comparison.

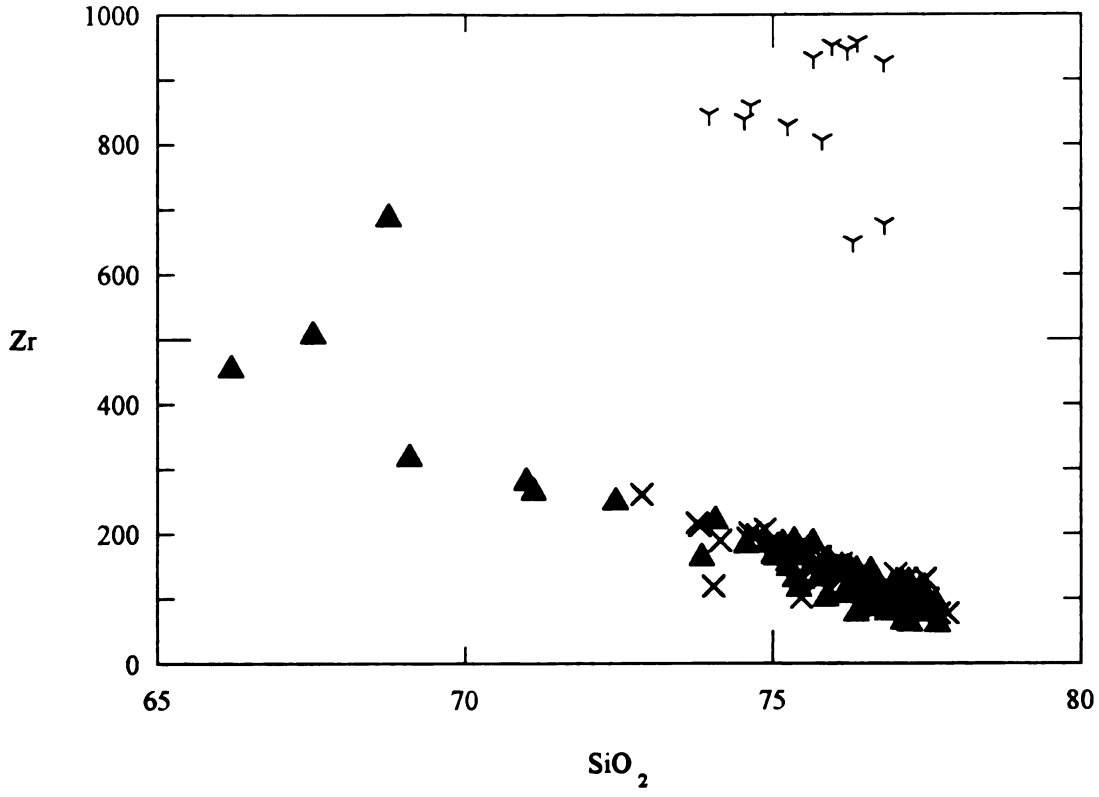

Figure 5. Zr vs. SiO_2 for the Post-Grouse Canyon tephra sequence and the Grouse Canyon Tuff.

CHEMICAL VARIATION WITH STRATIGRAPHIC POSITION

As discussed previously, bulk samples were collected mainly where individual pumice fragments large enough for chemical analysis, and representing the entire chemical variation of the tephra, were not available(small ash-flow layers, for example). Bulk tephra analyses from the middle portion of the tephra sequence, are chemically similar to analyses of individual glassy pumice fragments from corresponding portions of the

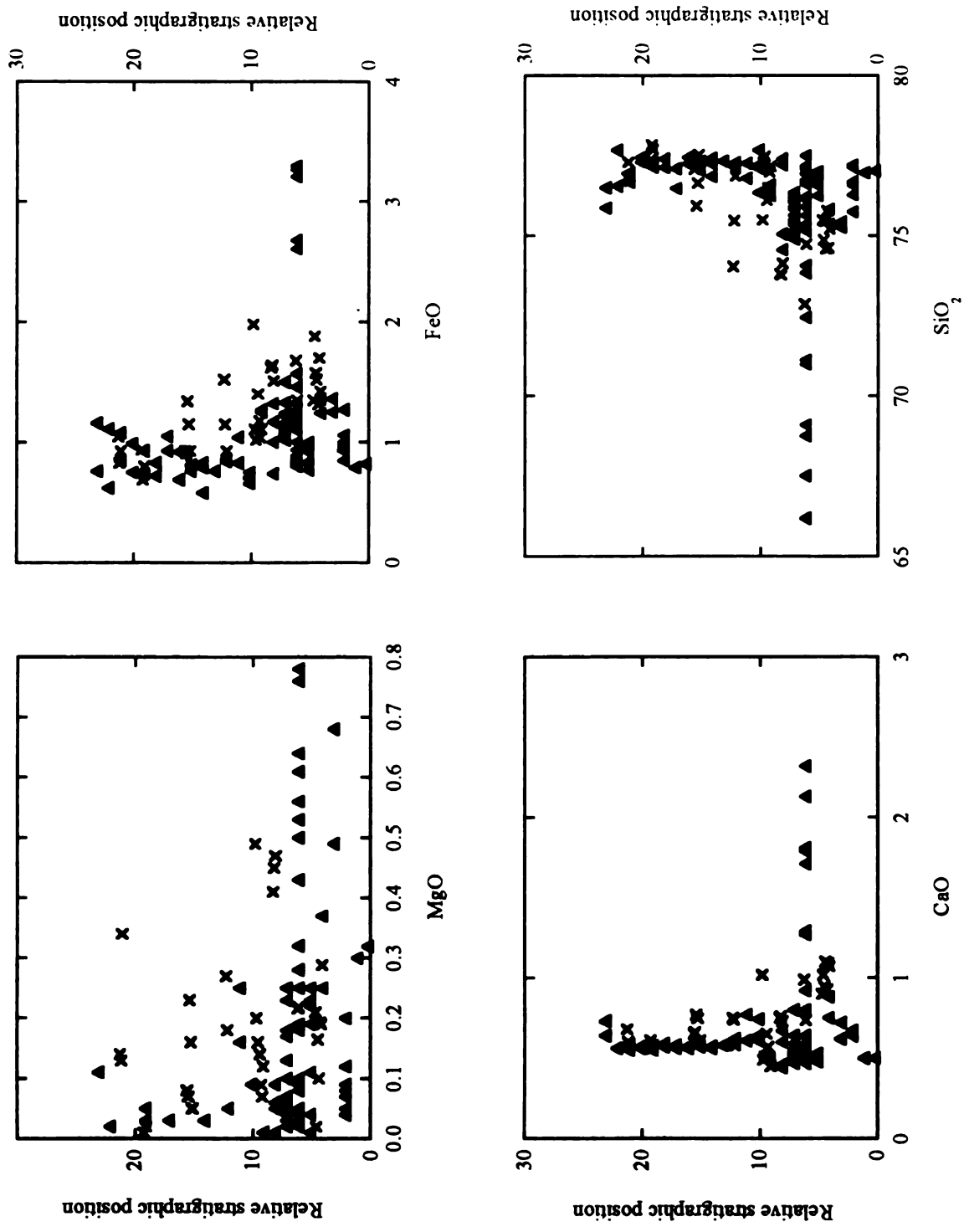

Figure 6. Variation of individual glassy pumice fragments and bulk tephra samples from the Post-Grouse Canyon tephra sequence (▲) = glassy pumice fragment; ✕ = bulk tephra sample).

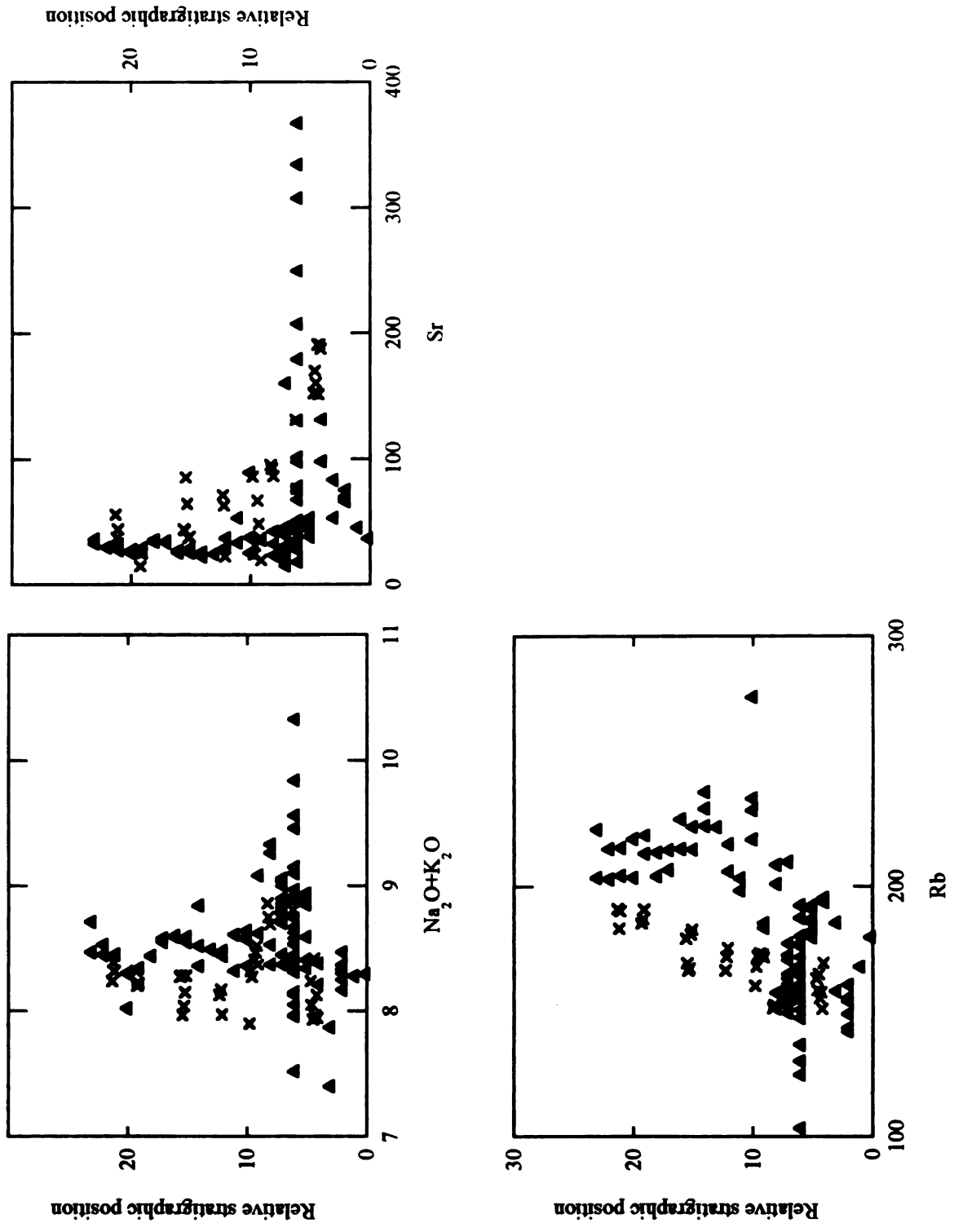

▲ = glassy pumice fragment; ✕ = bulk tephra sample.

Figure 6 (continued).

sequence. Two small ash-flow layers from the upper portion of the tephra sequence, however, are more variable than glassy pumice fragments from adjacent tephra layers (Figure 6). This is evident in plots of SiO_2, Sr, Na_2O+K_2O, FeO, and CaO. In addition, Rb and K_2O concentrations for most of the zoned ash-flow layers throughout the sequence are significantly lower than individual pumice fragments from nearby layers.

One explanation for the greater variability of the zoned ash-flow layers is that, lower silica magma may produce smaller fragments than the higher silica magma. As a result, pumice samples represent only one end of the chemical spectrum and contain smaller chemical ranges. Another possibility is that secondary weathering products and soil development in the bulk samples accounts for the observed chemical variation. Although some weathering of the tephra layers has certainly occurred, it probably does not account for the observed chemical variation.

First, glass shards to at least 250 μm, making up the ashy matrix of the ash-flow layers, are still vitreous. It is reasonable to assume that small glass fragments should be the first constituent to break down in a weathering ash-flow. It should be noted that some poorly developed soil horizons were observed, and avoided, during sampling of bulk tephra samples.

In addition, the CaO content of bulk tephra samples increases with increasing FeO (Figure 7). Prior to chemical analysis, samples were leached

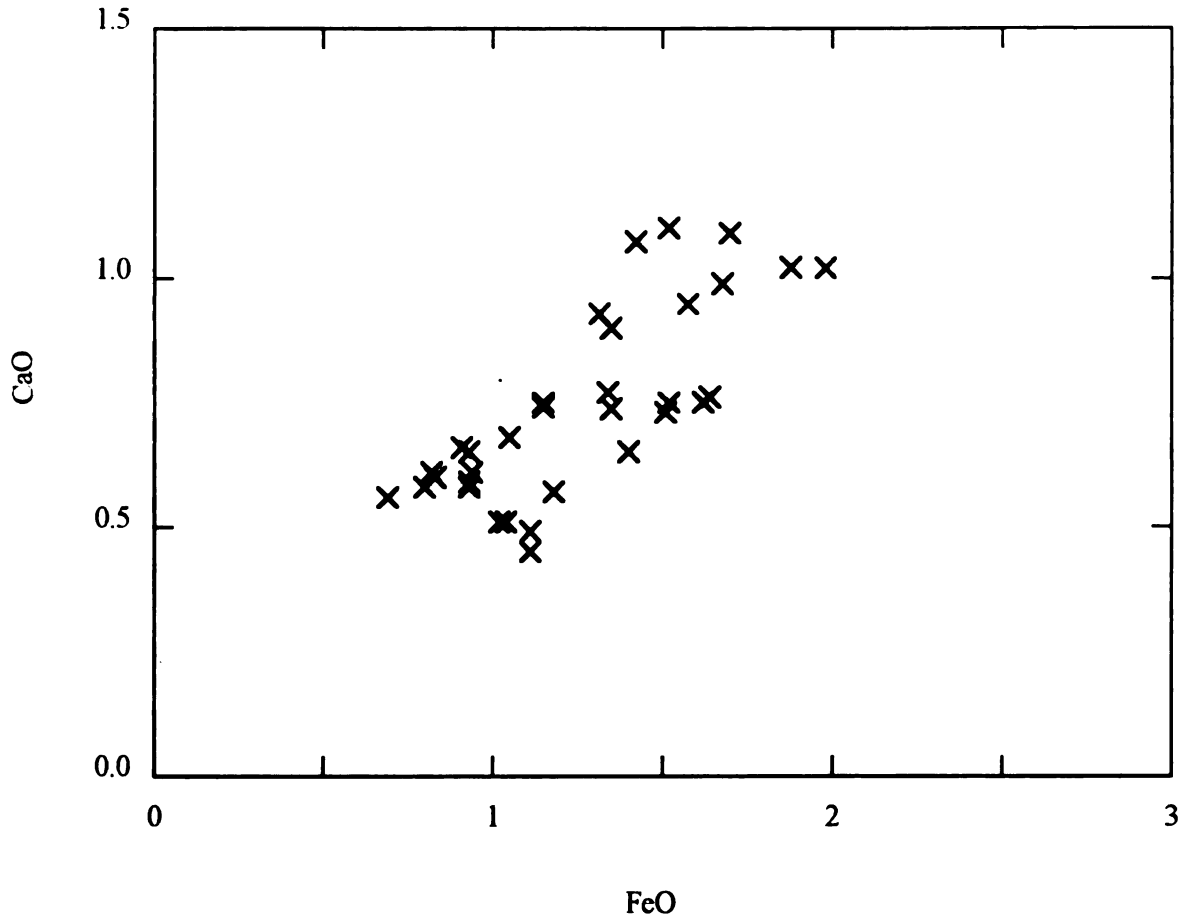

Figure 7. CaO vs. FeO for the bulk tephra samples from the Post-Grouse Canyon tephra sequence, where bulk samples were collected. This is evidence that the increase in CaO is primary, corresponding to more mafic magmatic compositions.

to remove any secondary carbonates. Therefore, if iron enrichment in these samples reflects secondary processes, the CaO enrichment should not increase correspondingly. The observed trend, however, is one of increasing CaO with increasing FeO for the middle and upper portions of the tephra.

A third possibility for the large chemical variation of the ash-flow layers, is that crystals are concentrated in these layers due to gravity and to wind effects during eruption and deposition. Field observations of the small

ash-flow layers, however, show no indication of crystal concentrations in the sampled zoned ash-flow layers.

Rb and ($Na_2O + K_2O$) values from bulk tephra samples are significantly lower than values for individual glassy pumice fragments (Figure 6). The high mobility of Rb and K_2O may have contributed to the difference in concentration between the two types of samples.

Because some elements display significant differences between bulk tephra samples, and because the cause of the variation between bulk tephra samples and glassy pumice fragments is not completely understood, individual glassy pumice fragments are used exclusively for further interpretations and comparisons of the Post-Grouse Canyon tephra sequence.

Because a stratigraphic sequence represents a time sequence, evaluation of magmatic changes as a function of time is best accomplished by comparing chemical variation with stratigraphic position (Figure 8). Two prominent chemical changes are present within the Post-Grouse Canyon tephra sequence. The first, and most distinct, is the dramatic increase in compositional variation in the tephra layer at 116 meters. Below the 116 meters layer, Sr (as an example) varies from only 45 to 131 ppm. In contrast, Sr values from the tephra layer at 116 m, varies from 18 to 367 ppm. Chemical ranges of Zr, Sr, Al_2O_3, and SiO_2, all exceed those from the underlying tephra layers.

The other distinct characteristic of this sequence, is the dramatic decrease in chemical variation in the upper portion of the tephra sequence

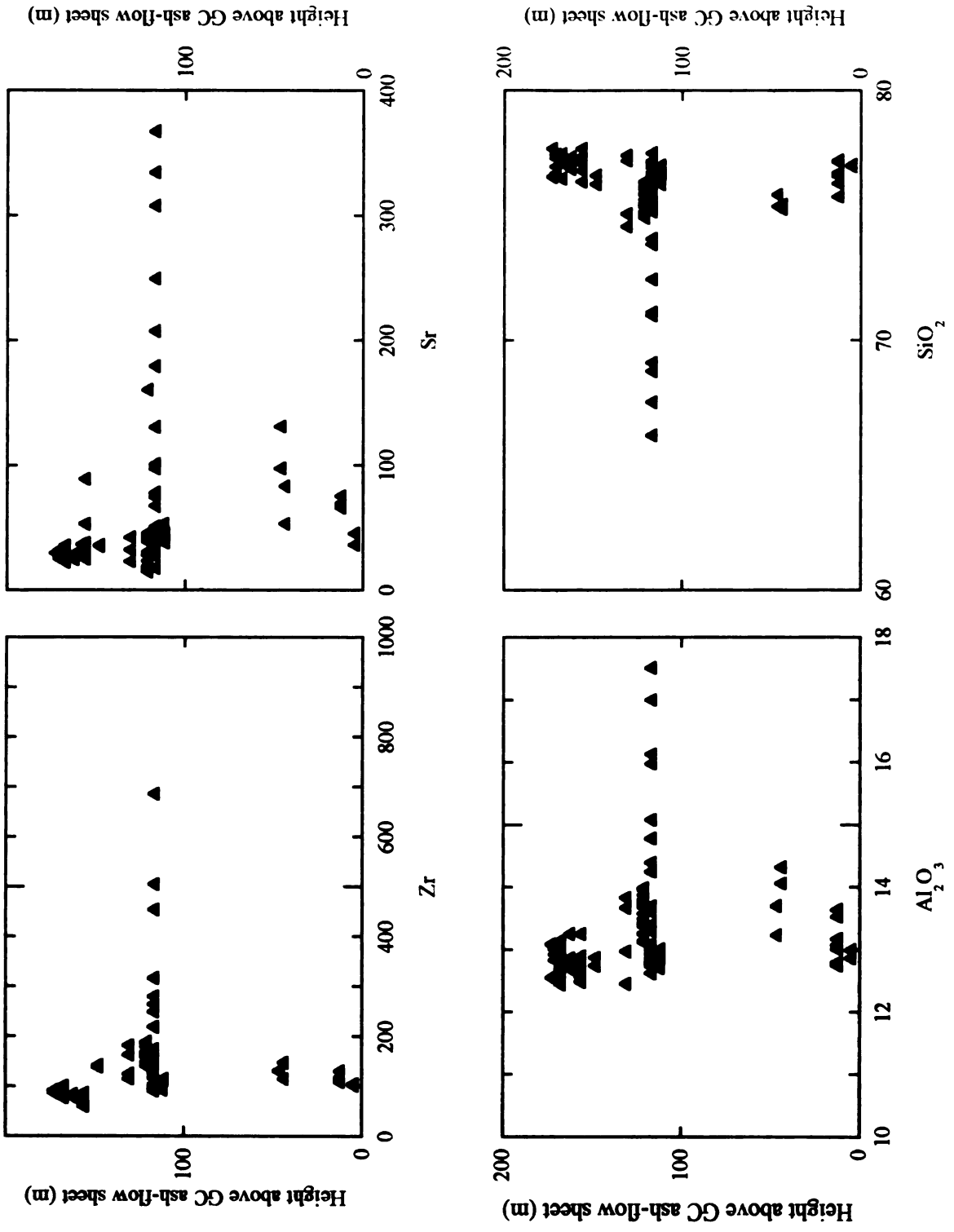

Figure 8. Variation of glassy pumice fragments with respect to stratigraphic position, from the Post-Grouse Canyon tephra sequence.

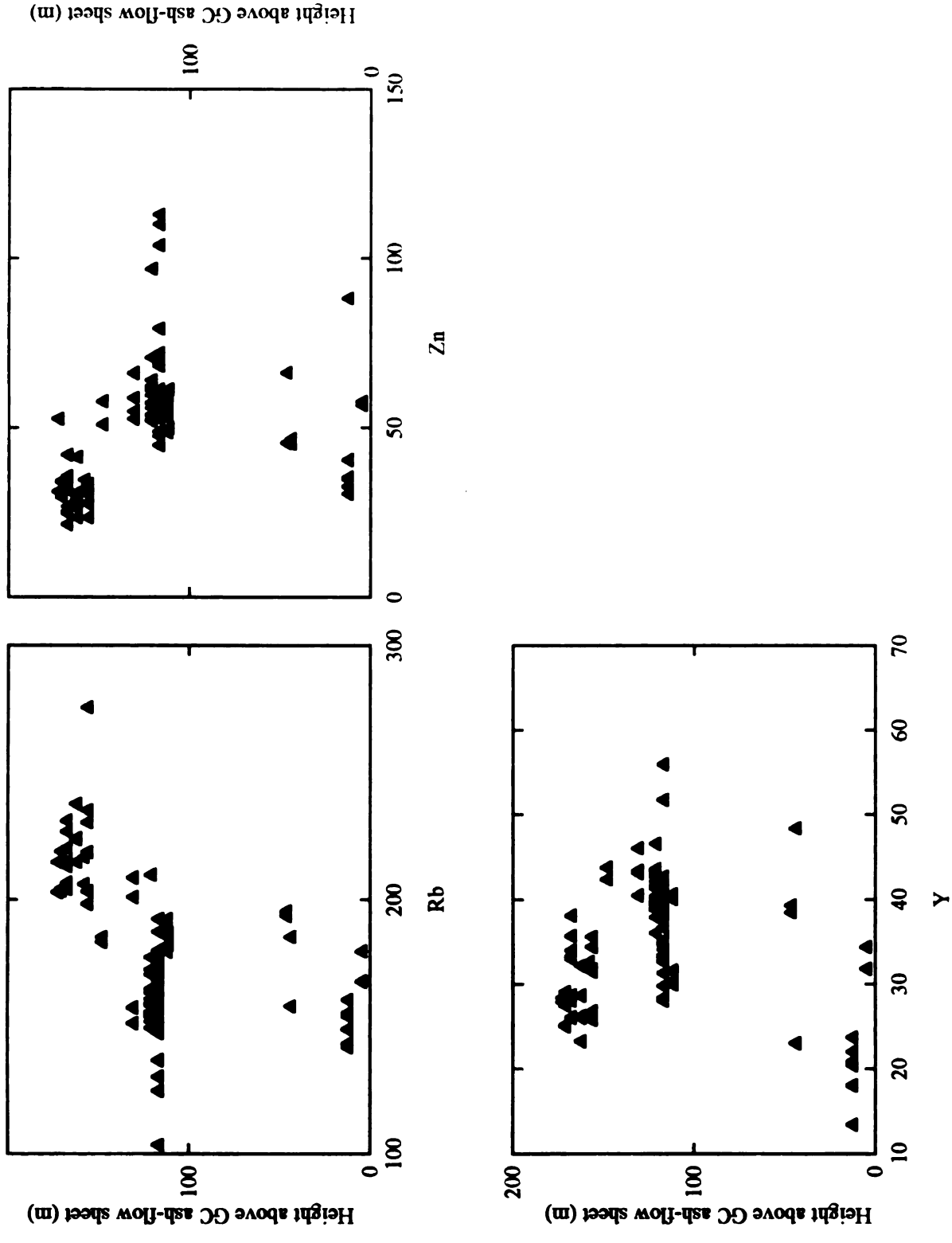

Figure 8 (continued).

with respect to trace element and major oxide concentrations. In addition, there are lower concentrations of Zn and Zr, and higher concentrations of Rb, than the underlying tephra layers. The abrupt change in chemistry, corresponds exactly to the change in radiometric ages from the 13.3 Ma age group to the 13.0 Ma age group.

Another change that occurs in the lower portion of the sequence, though less distinct, is the change in Y concentration at approximately 30 m. This tephra layer contains the lowest Y concentrations of any in the sequence (less than 14 ppm). Two samples from the layer directly overlying, have widely varying Y concentrations (22 and 49 ppm ± 6%). However, the remaining tephra layers, up to about 150 m, have Yttrium concentrations no lower than about 27 ppm. The layers with the lower Y concentrations fall in the oldest age group of the tephra sequence (13.5 Ma). Overlying layers, up to 150 m, correspond to the 13.3 Ma age group.

In summary, chemical changes in the Post-Grouse Canyon tephra sequence correspond to age and stratigraphic changes throughout the sequence. The exception, is the highly variable tephra layer at 116 m. The age of this layer falls in the 13.3 Ma age group. However, the chemical variation of this tephra layer is much larger than any other layer in the sequence.

The correlation of radiometric age dates to observed chemical changes in the sequence, marks this sequence as the best candidate for testing the

main hypothesis of the study. If the magmatic processes governing changes in the Post-Grouse Canyon tephra sequence can be distinguished, rates of these processes can be determined.

CHEMICAL GROUPS

Three groups can be defined based on the corresponding age, chemical, and stratigraphic changes that occur in the Post-Grouse Canyon tephra sequence. These three groups are referred to as the lower, middle, and upper portions of the Post-Grouse Canyon tephra sequence, respectively.

Contained within the middle age and stratigraphic group, is the highly variable tephra layer at 116 m. Because this layer has a much larger chemical range than the rest of the tephra layers in the middle portion of the tephra sequence, a separate plot symbol is assigned to this layer to facilitate comparisons. It is referred to as the highly variable tephra layer.

Almost all major and oxides and trace elements distinguish the upper and middle portions of the Post-Grouse Canyon tephra sequence (Figure 8). In a diagram of Zn vs. Zr (Figure 9), the middle portion of the tephra sequence has lower Zn concentrations (51 to 97 ppm), higher Zr concentrations (115 to 188 ppm), and does not overlap the upper portion of the tephra sequence (Zn = 21 to 53 ppm; Zr = 77 to 101 ppm). Additionally, the ratio of Rb/Sr vs. Zr defines two distinct trends for the middle and upper portions of the Post-Grouse Canyon tephra sequence.

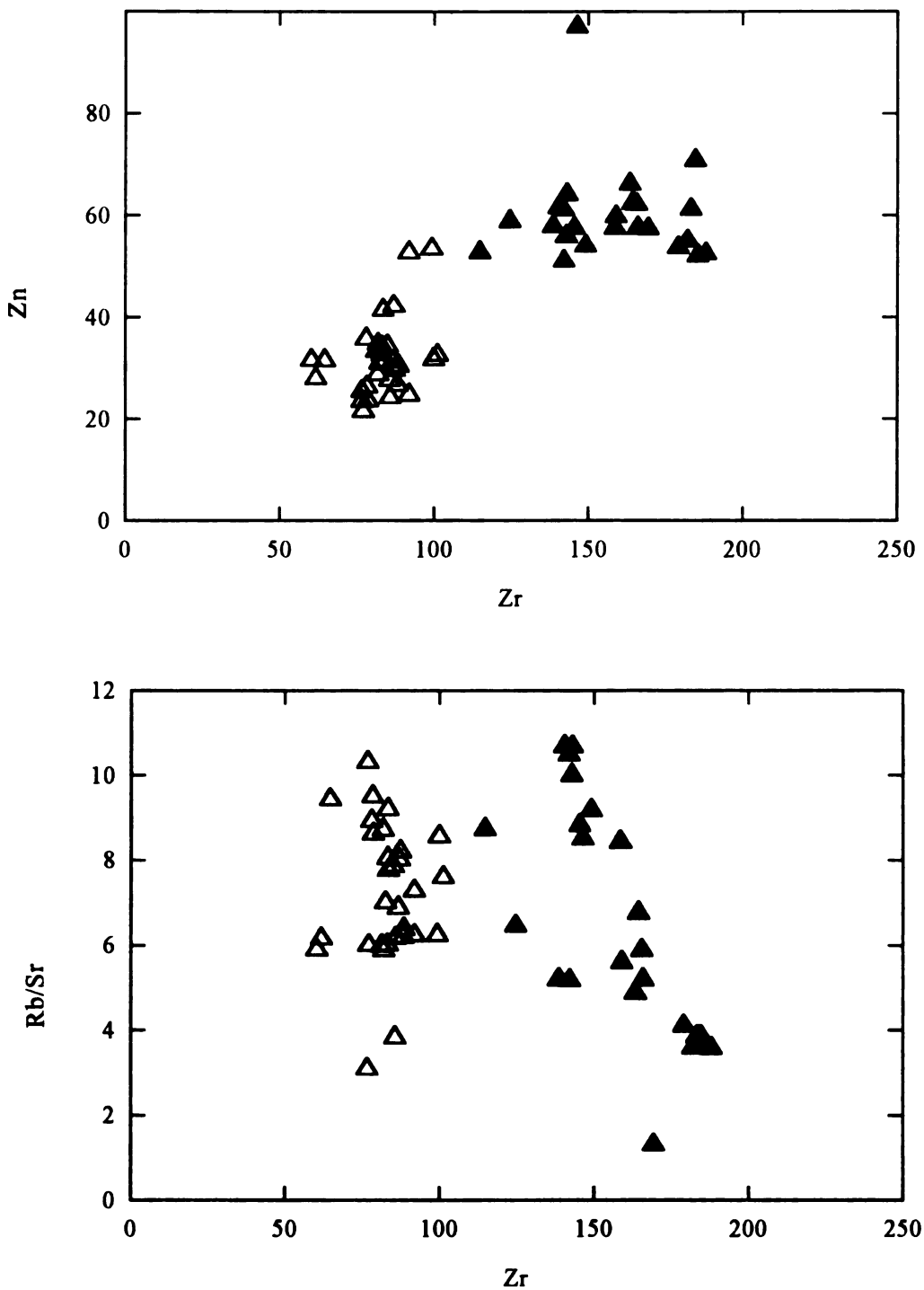

Figure 9. Zn vs. Zr, and Rb/Sr vs. Zr discrimination diagrams for the middle (▲) and upper (△) portions of the Post-Grouse Canyon tephra sequence.

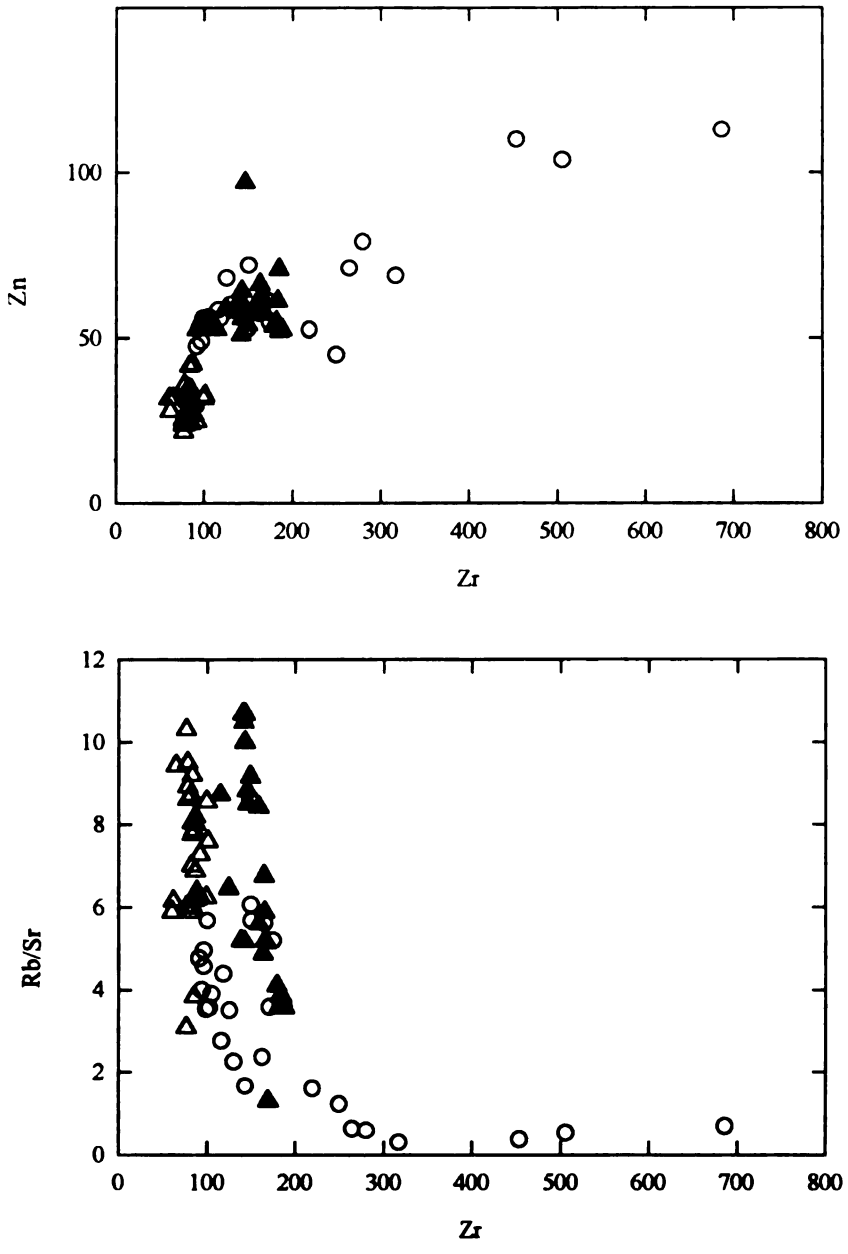

Figure 10. Trace element discrimination diagrams for the highly variable layer and the chemical groups from the upper and middle portions of the Post-Grouse Canyon tephra sequence (PGC).

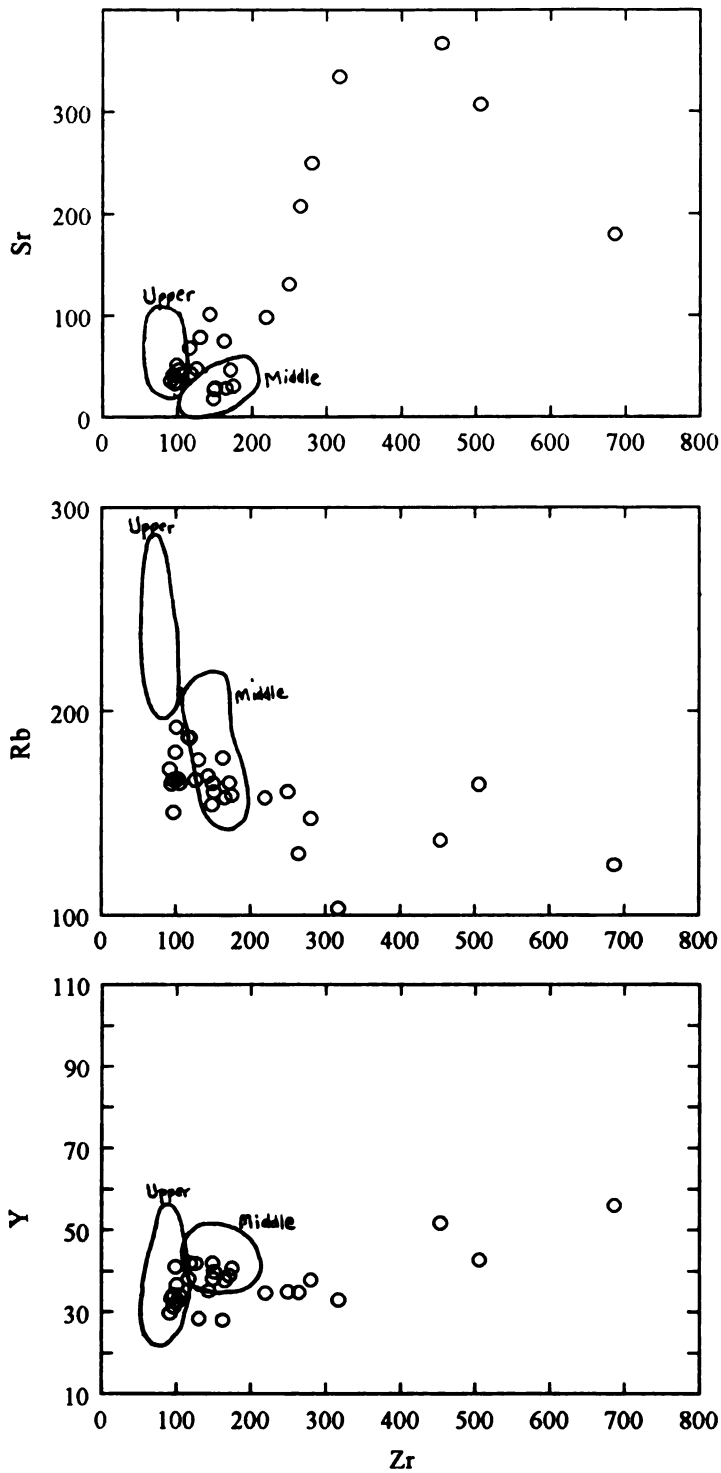

Figure 10 (continued).

Seven samples from the highly variable layer occur in the same chemical group as the middle portion of the Post-Grouse Canyon tephra sequence. In Figure 10, analyses from the highly variable layer are superimposed onto the diagrams of Zn vs. Zr, and Rb/Sr vs. Zr. The difference between the groups are best illustrated on the diagram of Rb/Sr vs. Zr, where chemical groups representing the middle and upper portions of the tephra sequence form distinct chemical trends, with five samples from the highly variable layer consistently plotting with the middle portion of the Post-Grouse Canyon tephra sequence.

Eight samples from the highly variable layer exhibit chemical behavior that is distinct from other chemical groups in the tephra sequence and from all other samples collected from the same tephra layer. Zn and Zr concentrations in these samples range from 60 to 115 ppm and 210 to 690 ppm, respectively (Figure 10). These samples account for most of the chemical variation within the highly variable layer. These eight samples will be referred to as the high Zr group from the highly variable layer. The remainder of the samples from the highly variable layer plot near the middle and upper portions of the tephra sequence but do not consistently plot with any other chemical group. These samples will be referred to as the low Zr group from the highly variable layer. Trace elements discriminating the highly variable layer from the middle and upper portions of the tephra sequence are also shown in diagrams of Sr, Rb, and Y vs. Zr (Figure 10).

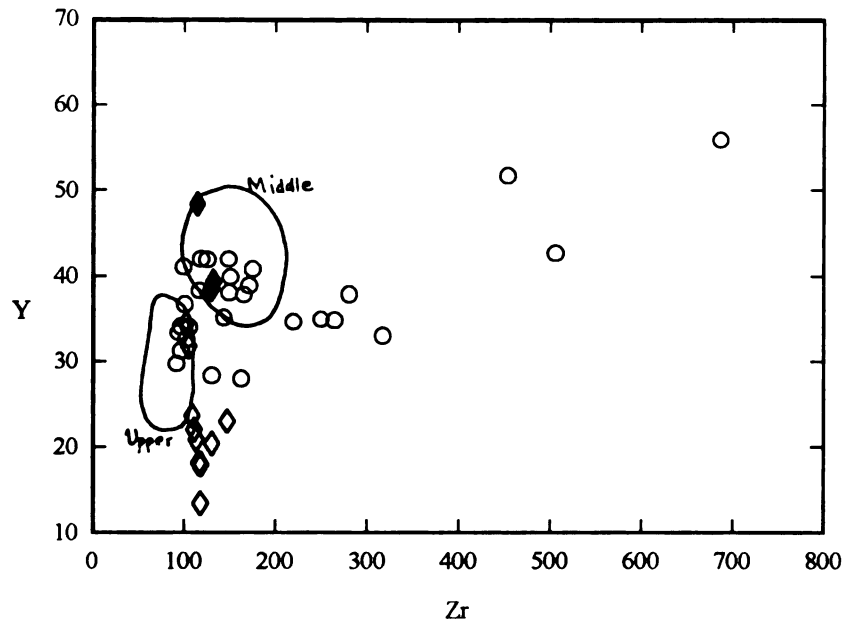

○ = low Zr samples from the highly variable layer

♦ = samples from tephra layers lying stratigraphically between the lower and middle portions of the tephra sequence.

◊ = lower portion of the Post-grouse Canyon tephra sequence

Figure 11. Y vs. Zr variation diagram discriminating the lower portion of the Post-Grouse Canyon tephra sequence from other chemical groups within the sequence.

The lower portion of the Post-Grouse Canyon tephra sequence is also chemically distinct from the middle and upper portions of the sequence, and from the highly variable layer. Chemical groups representing the middle and upper portions of the tephra sequence, as well as the highly variable layer, are compared with the lower portion of the tephra sequence (Figure 11). Most samples from the lower portion of the tephra sequence are characterized by lower Y concentrations (less than 14 to 25 ppm) than the other chemical groups and Zr concentrations that fall between the chemical

groups from the middle and upper portion of the tephra sequence. Three samples from the lower portion of the tephra sequence (filled diamonds) consistently plot with the middle portion of the tephra sequence. These samples were collected from layers situated between the lowermost dated layer from the middle portion of the tephra sequence, and the uppermost dated layer from the lower portion of the tephra sequence. Chemical correlation places these samples with the middle portion of the tephra sequence, though the age of these samples is unknown.

In summary, three distinct chemical groups within the Post-Grouse Canyon tephra sequence correspond to three distinct $^{40}Ar/^{39}Ar$ radiometric ages. The highly variable layer contains samples that belong to the middle portion of the tephra sequence, in addition to samples that are distinct from any of the age and stratigraphic groups from the tephra sequence.

Mineral chemistry

Mineral chemistry also distinguishes major chemical and age groups present in the Post-Grouse Canyon tephra sequence. Alkali feldspar compositions, especially BaO concentrations, reveal differences between the middle and upper portions of the tephra sequence (Figure 12). BaO concentrations are also distinct for the highly variable layer. For this layer, BaO wt.% concentrations in alkali feldspars range from 0.15 to 0.52. The remainder of the middle portion of the tephra sequence has BaO wt.% concentrations that range from 0.4 to greater than 0.6. BaO wt.% values in

Figure 12. Edge analyses of plagioclase (●) and alkali feldspar (O) from the Post-grouse Canyon tephra sequence showing K_2O, Na_2O, CaO, and BaO variation with stratigraphic depth.

the upper portion of the sequence range from nearly zero to just 0.4 wt. Na_2O ranges from 3.9 to 5.1 wt.% in alkali feldspars from the middle portion, and from 3.1 to 3.9 wt.% in the upper portion, with the exception of one alkali feldspar that has a higher Na_2O (4.6-4.9 wt.%). Likewise, there is a shift to greater concentrations of K_2O in the alkali feldspar from the upper portion of the tephra sequence. Na_2O and K_2O values do not distinguish alkali feldspars from the highly variable layer as well as BaO values. Plagioclase feldspars do not change from the middle to the upper portion of the sequence. Most feldspar grains are homogeneous or only slightly zoned. Two plagioclase grains from the middle portion of the tephra sequence display normal zoning, An_{15-22} and An_{18-32}, respectively. One zoned alkali grain was observed (Or_{30-59}).

Additional major phenocryst phases from the Post-Grouse Canyon tephra sequence include hornblende, biotite, pyroxene, magnetite, ilmenite, and quartz. Of these, very few phenocrysts display any compositional zoning. One exception, is a biotite phenocryst with a compositional range from 33 to 65% SiO_2 , 0.08 to 0.19 Cl and 2.5 to 8.2 wt.% F.

With the exception of the alkali feldspars discussed above, the highly variable layer does not exhibit highly variable or significantly different mineral chemistry when compared to other layers from the middle portion of the sequence, except for alkali feldspar concentrations discussed above. In

fact, the composition of individual minerals in this layer are slightly less variable than in other layers.

Correlation with Regional Volcanostratigraphic Units

Complex stratigraphic relationships among volcanic units make in depth correlation difficult. $^{40}Ar/^{39}Ar$ ages obtained in this study for the Post-Grouse Canyon tephra sequence closely correspond with revised ages obtained by Sawyer et al., (1994), for units in the Southwest Nevada Volcanic Field. In a revised volcanic stratigraphy by Sawyer et al. (1994), an $^{40}Ar/^{39}Ar$ age of 13.7 ±0.08 Ma was calculated for the Grouse Canyon Tuff of the Belted Range Group. This is followed by an age of 13.5 ±0.04 Ma for the Deadhorse Flat Formation (also part of the Belted Range Group) (Figure 2), and an age of 13.25 ±0.08 Ma for the Bullfrog Tuff of the Crater Flat Group. Above the Crater Flat Group, $^{40}Ar/^{39}Ar$ ages of 13.0 ±0.2 Ma and 12.9 ±0.08 Ma were obtained for the Wahmonie Formation and Calico Hills Formation, respectively.

Care must be taken when comparing radiometric ages from different laboratories. For all ages determined herein and all ages reported from previous work, 2σ error range is used.

Radiometric age ranges from the lower portion of the Post-Grouse Canyon tephra sequence overlap those of the Deadhorse Flat Formation [13.52 ±0.04 (2σ error) Ma] for the lower portion of the Post-Grouse Canyon

tephra sequence, compared with 13.5 ±0.04 (2σ error) Ma for the Deadhorse Flat Formation. However, the Deadhorse Flat Formation is part of the peralkaline volcanics of the Belted Range Group (Sawyer and Sargent, 1989; Sawyer et al., 1994), and cannot be chemically correlated with the metaluminous Post-Grouse Canyon tephras. Zr concentrations from the lower Post-Grouse Canyon tephra sequence are more closely related to the Crater Flat Group and the Calico Hills Formation (13.25 ±0.04 Ma and 12.9 ±0.04 Ma respectively (Sawyer et al., 1994)) than to the peralkaline Belted Range Group.

The middle portion of the Post-Grouse Canyon tephra sequence has a radiometric age of 13.33 ± 0.06 Ma. This corresponds to a 13.25 ± .04 Ma $^{40}Ar/^{39}Ar$ age determined for the Bullfrog Tuff of the Crater Flat Group by Sawyer et al., 1994. The middle portion of the Post-Grouse Canyon tephra sequence possess a significantly larger range of Zr variation than tephras from the Crater Flat Group, ranging from 100 to 750 ppm Zr, compared with a range of 100 to 250 ppm for the Crater Flat Group. Much of this variation, however, is caused by the highly variable layer that falls within this age group. The ratio of $\frac{MgO}{MgO + FeO}$ of biotite grains from the middle portion of the Post-Grouse Canyon tephra sequence are more variable than those for the Crater Flat Group (0.1 to 0.6 versus 0.35 to 0.6, respectively). This

variation takes place throughout the middle portion of the Post-Grouse Canyon tephra sequence and is not restricted to the highly variable layer.

The upper layers of the Post-Grouse Canyon tephra sequence, corresponding most closely in age with the Wahmonie Formation and the Calico Hills Tuff (13.0 and 12.9 Ma, respectively). The Wahmonie Formation consists of andesitic and dacitic lavas and tephras and are not present in the Post-Grouse Canyon sequence. Zirconium concentrations of the upper layers from the Post-Grouse Canyon, do correspond to those from the Calico Hills Tuff.

Summary

In summary, the Post-Grouse Canyon tephra sequence can be divided into three major groups based on age, compositional variation, and stratigraphic position. The lower tephra sequence has an $^{40}Ar/^{39}Ar$ age of 13.53 ± .04 Ma. It is characterized by lower Y concentrations than any other group and can be differentiated from the other groups based on the variation of Y vs. Zr (Figure 10). The middle tephra sequence has an $^{40}Ar/^{39}Ar$ age of 13.33 + .06 Ma and is distinguished from the lower tephra sequence by higher Y and lower Sr concentrations. It is distinguished from the upper tephra sequence by higher Zn concentrations, lower Rb concentrations, and significantly larger variation than any other group (Figure 8). Within the middle age and stratigraphic group of the tephra sequence, there is a highly

variable layer that can also be divided into distinct chemical groups. The highly variable layer contains samples that belong to the middle portion of the tephra sequence, in addition to samples that are distinct from any of the age and stratigraphic groups from the tephra sequence. The upper tephra sequence has an $^{40}Ar/^{39}Ar$ age of 13.05 ± .04 Ma. It has the highest Rb concentrations, the lowest Zn and Zr concentrations, and the least compositional variation of any group.

Chapter 4

THE PRE-RAINIER MESA MAGMATIC SYSTEM

Previous Work

Large chemical variations characterize the Pre-Rainier Mesa tephra sequence. For example, silica ranges from 66 to 78 wt.% (Huysken et al., 1994). This variation is greater than the chemical variation in the high silica portion of the overlying Rainier Mesa ash-flow sheet (73-78%) noted by Cambray et al., 1995. The high silica portion comprises about 90% of that unit, volumetrically.. Relatively large chemical variation also occurs in individual ash-flow layers within the tephra sequence (Huysken et al., 1994). These layers are normally zoned (Figure 13) with as much as 5 wt.% SiO_2 variation. Because the entire tephra sequence and the smaller ash-flow layers within are characterized by such large chemical variations, it is unlikely that they were erupted from the uppermost portion of a large (at least 1200 km^3), compositionally zoned, Rainier Mesa magma body.

In addition, layers from the lower portion of the tephra sequence are generally less silicic and less chemically evolved than those from the upper portion (Huysken et al., 1994) (Figure 13). Based on these observations, and the fact that the ash-flow layers are thicker towards the top of the sequence, Huysken et al. (1994) proposed that the Pre-Rainier Mesa tephra sequence

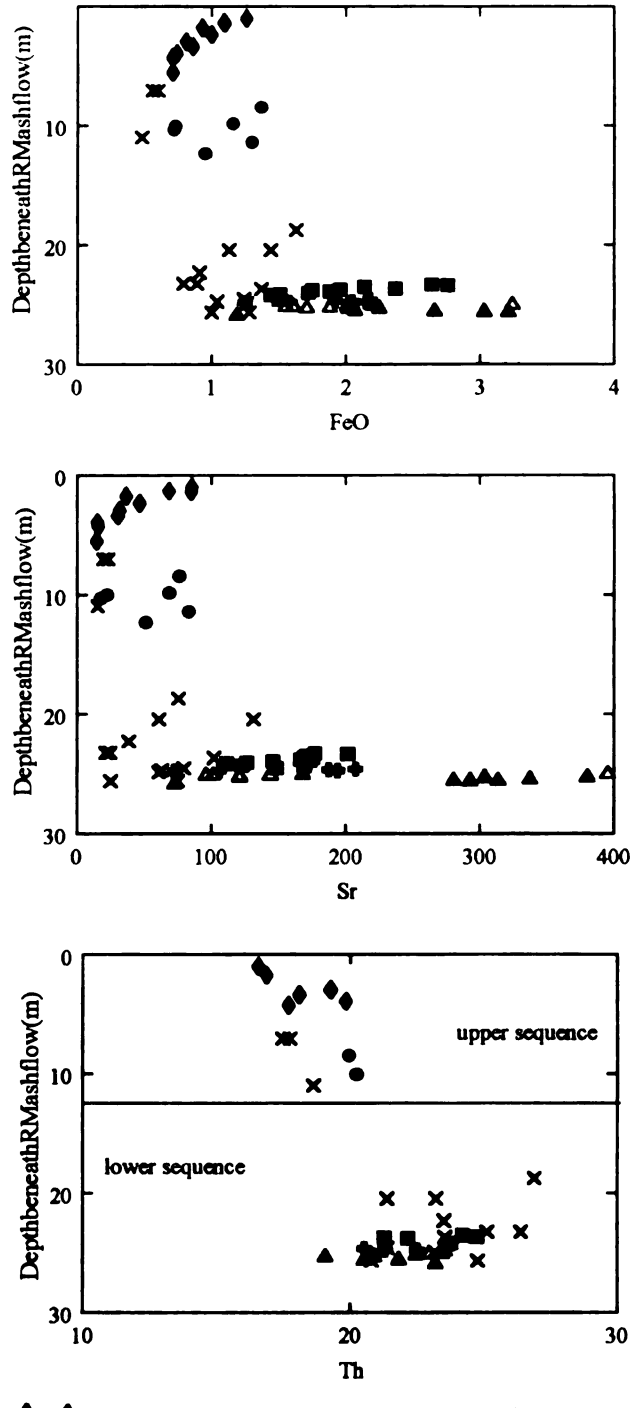

Figure 13. (a) Variation of FeO and Sr with Depth beneath the Rainier Mesa ash-flow sheet. (X) indicates individual glassy pumice fragments. All other plot symbols represent small ash-flow layers within the Pre-Rainier Mesa tephra sequence. (b) Variation of Th discriminating the lower (older) and upper (younger) Pre-Rainier Mesa tephra sequence.

was formed by periodic eruption of a continually evolving magma body that grew larger with time.

Preliminary $^{40}Ar/^{39}Ar$ ages from the lower- and uppermost layers of the sequence reveal a 1.31 ±.04 Ma radiometric age difference between the lower and upper portions of the Pre-Rainier Mesa tephra sequence (Huysken et al., 1994). These radiometric age dates, and the observation of changing compositions from the base to the top of the sequence, are the basis for the original proposal that rates of magmatic evolution of the Rainier Mesa magma body could be determined from the Pre-Rainier Mesa tephra sequence.

$^{40}Ar/^{39}Ar$ ages

The only complete section of the Pre-Rainier Mesa Tephra Sequence is located on Rainier Mesa and is characterized by a bimodal age distribution (Figure 14). At this location, the entire lower 13 meters of the Pre-Rainier Mesa Tephra Sequence has a radiometric $^{40}Ar/^{39}Ar$ age of 12.79 ±0.07 Ma. This age is consistent with ages obtained for the underlying Tiva Canyon ash-flow sheet (12.7 ± 0.06 Ma, Sawyer et al., 1994). The upper 12 meters of this section have a radiometric $^{40}Ar/^{39}Ar$ age of 11.62 ±0.04 Ma, which is consistent with the age obtained for the overlying Rainier Mesa ash-flow sheet [11.6 ±06 Ma (Sawyer et al., 1994)].

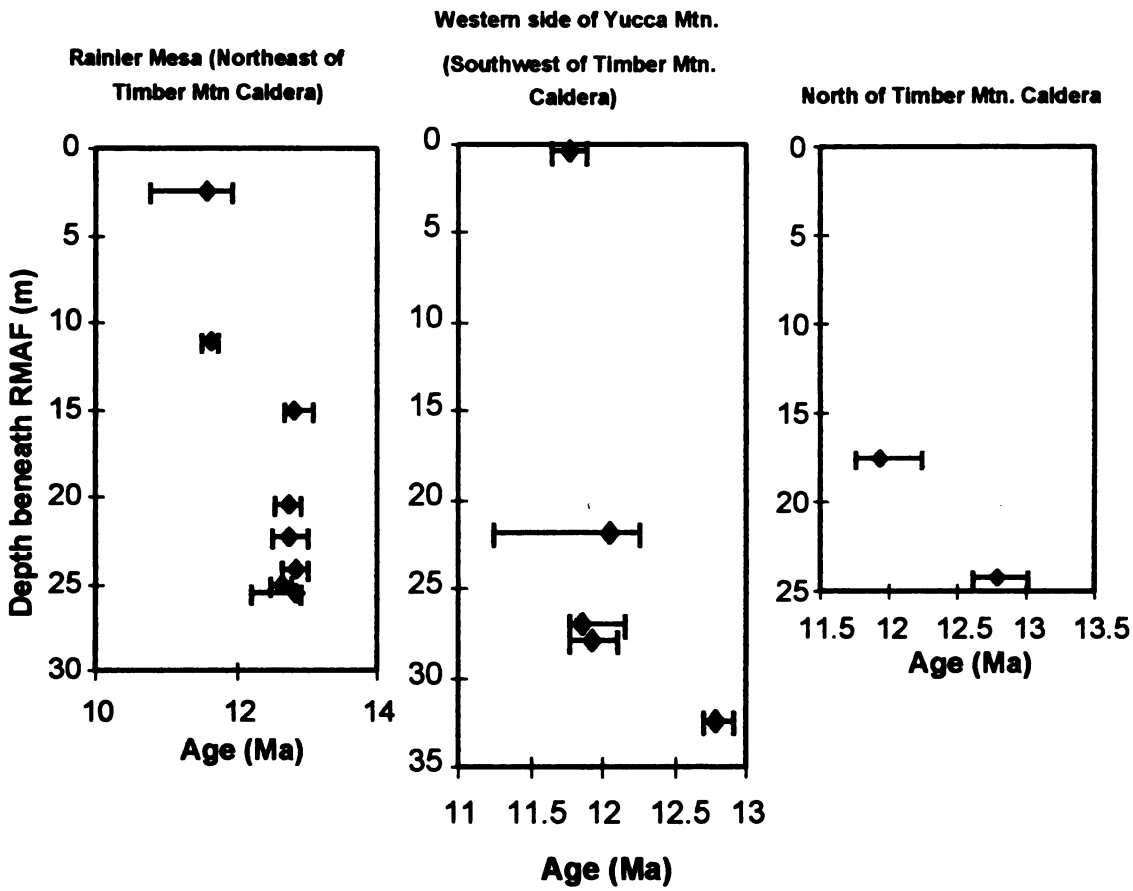

Figure 14. Range of $^{40}Ar/^{39}Ar$ ages for individual tephra layers from the Pre-Rainier Mesa tephra sequence.

In two other sections, located on the west side of Yucca Mountain, and on Buckboard Mesa Rd, $^{40}Ar/^{39}Ar$ ages also fall into two groups. The ages of the lower portion of these sections are consistent with those from the complete stratigraphic section on Rainier Mesa. Ages obtained for the upper layers in these sequences are 11.91 ±0.07 Ma and 11.94 ±0.04 Ma, respectively. Conceivably, ages from the sequence on Buckboard Mesa Road, may represent a portion of the sequence that is absent on Rainier Mesa. However, excellent stratigraphic correlation between the upper portion of the

sections on Rainier Mesa and the west side of Yucca Mountain, indicate that samples from these two locations come from the same portion of the tephra sequence. The most likely cause for the discrepancy in $^{40}Ar/^{39}Ar$ radiometric ages, is that geologic factors, such as partial resetting of $^{40}Ar/^{39}Ar$ ages by hydrothermal processes or heating from the overlying Rainier Mesa ash-flow sheet, have affected $^{40}Ar/^{39}Ar$ ratios.

Geochemistry

The determination of two distinct, non-overlapping, ages for the upper and lower portions of the Pre-Rainier Mesa tephra sequence, rather than a continuous age progression, was unexpected. Because of this, chemical variation as a function of stratigraphic position in the sequence has been examined in detail. The variation of Th, Sr, and FeO with stratigraphic position (Figure 13) best illustrate that the Pre-Rainier Mesa tephra sequence can be divided into a lower and upper portion that correspond with the age groups. The individual layers in the lower portion of the sequence are compositionally similar, even though each layer is characterized by large chemical variation. The upper portion of the sequence has smaller average Sr and FeO values (50 ppm Sr, and 1.0 wt.% FeO, compared with 150 ppm Sr, and 2.0 wt% FeO, for the lower portion of the sequence), and is much less chemically variable. This new grouping is in contrast to the previous interpretation (Huysken et al., 1994) that the tephra sequence becomes

progressively more chemically evolved from base to top. For a clear illustration of how bulk samples and individual glassy pumice fragments differ within the same unit, individual glassy pumice fragments represented as X's, and bulk tephra samples from small ash-flow layers are represented as a different symbol for each small ash-flow layer. Variation of the bulk rock samples is larger than that of individual glassy pumice fragments, and, as a group, individual glassy pumice fragments are more silicic.

The Pre-Rainier Mesa tephra sequence can be divided into two discrete, chemical groups that correspond exactly to the two age groups. They are, the lower (older) tephra sequence, and the upper (younger) tephra sequence. For the following comparisons, only individual glassy pumice fragments are included from the Pre-Rainier Mesa tephra sequence so that the lower (older), and upper (younger) portions of the tephra sequence are easily distinguished. Samples from the upper tephra sequence are plotted as open circles, and those from the lower sequence, are plotted as open squares.

Chemical variation of the upper Pre-Rainier Mesa tephra sequence is equivalent to the high silica portion of the overlying Rainier Mesa ash-flow sheet (Figure 15). Major and trace element variation of the tephra sequence compared to the overlying Rainier Mesa Tuff, indicates that the upper portion of the tephra sequence plots consistently with the high-silica, low Th/Nb group defined by Cambray et al. (1995), and Saltoun (1996). The same comparison for the lower portion of the Pre-Rainier Mesa tephra

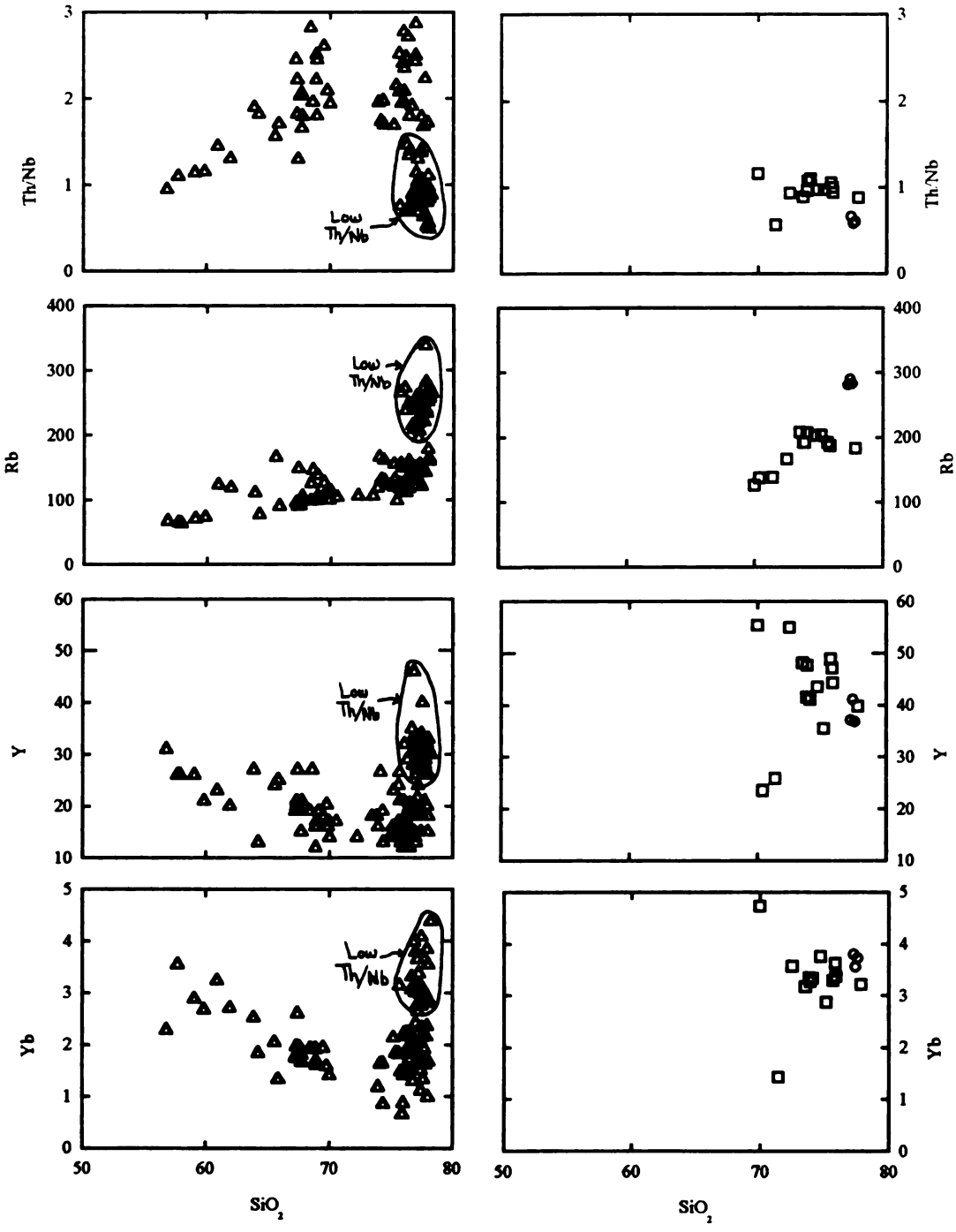

△ = Rainier Mesa ash-flow sheet
○ = upper Pre-rainier Mesa tephra sequence
□ = lower Pre-rainier Mesa tephra sequence

Figure 15. Trace element variation diagrams comparing individual glassy pumice fragments from the lower Pre-Rainier Mesa tephra sequence, the upper Pre-Rainier Mesa tephra sequence, and the Rainier Mesa Tuff.

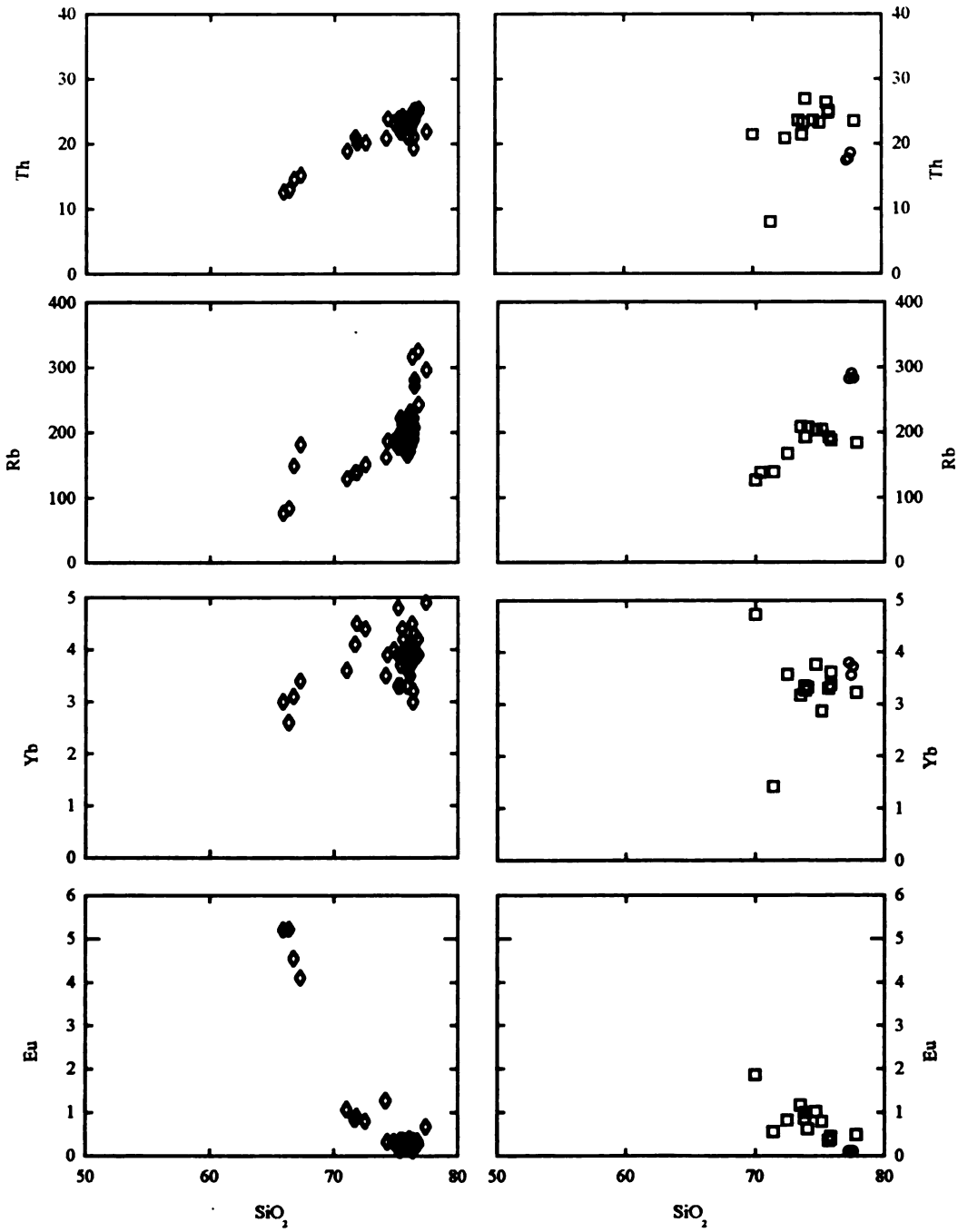

○ = upper Pre-rainier Mesa tephra sequence
□ = lower Pre-rainier Mesa tephra sequence
◆ = Tiva Canyon ash-flow sheet

Figure 16. Trace element variation diagrams comparing the Tiva Canyon ash-flow sheet, the lower Pre-Rainier Mesa tephra sequence, and the upper Pre-Rainier Mesa tephra sequence.

sequence reveals that this group is chemically distinct from the Rainier Mesa Tuff (Figure 15).

A chemical comparison of the lower portion of the Pre-Rainier Mesa tephra sequence (12.79 ± 0.07 Ma) to underlying Tiva Canyon ash-flow sheet (12.7 ± 0.03 Ma), (Figure 16) reveals that the lower portion of the tephra sequence is distinct from both the underlying Tiva Canyon ash-flow sheet (even though it is consistent in age with this ash-flow tuff), and the overlying Rainier Mesa ash-flow sheet.

In addition, differences in concentrations of Cs and Rb show that no reasonable crystal fractionation model can account for the chemical variation of the lower and upper portions of the Pre-Rainier Mesa tephra sequence (Figure 17). The lower tephra sequence is characterized by very little change in Cs (<5 ppm) over a large range in SiO_2. However, the upper Pre-Rainier Mesa Tephra Sequence is characterized by a higher Cs values (8-12 ppm) with very little increase in SiO_2. Rb variation is also characterized by little change in Rb with increasing SiO_2. However Rb values are significantly larger in the upper Pre-Rainier Mesa tephra sequence.

One sample from the lower Pre-Rainier Mesa tephra sequence has a silica content higher than any other individual glassy pumice fragment. This sample consistently plots with the upper Pre-Rainier Mesa tephra sequence with respect to silica but contains Cs and Rb values consistent with the lower tephra sequence. The reason for this difference in silica content is unknown,

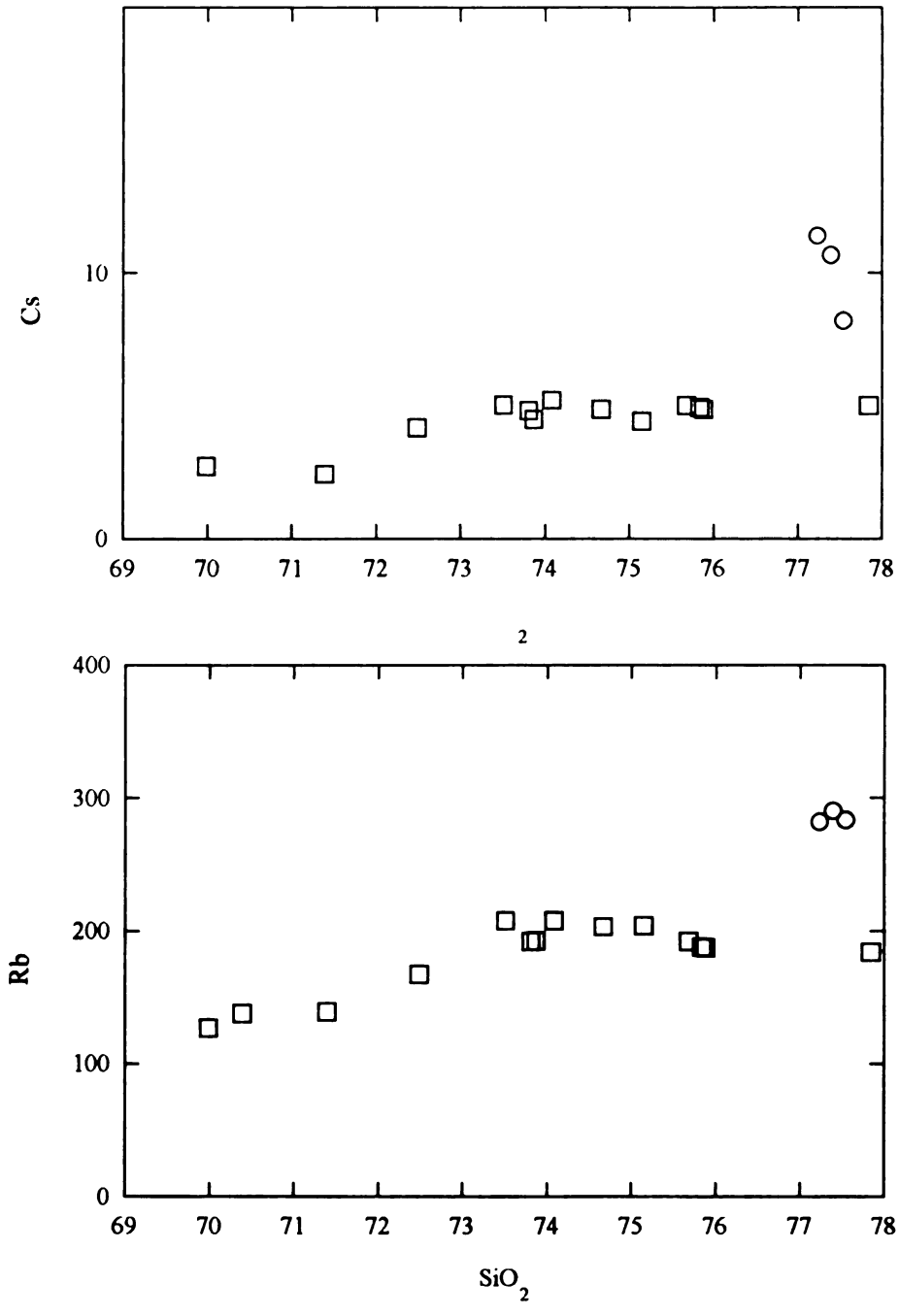

O = upper Pre-rainier Mesa tephra sequence
□ = lower Pre-rainier Mesa tephra sequence

Figure 17. Discrimination diagrams of Cs vs. SiO_2, and Rb vs. SiO_2, for the lower and upper Pre-Rainier Mesa tephra sequence.

however, this sample also consistently plots away from the lower tephra sequence in petrologic model comparisons (see below).

Mineralogy

Phenocryst phases present in the Pre-Rainier Mesa bulk tephra and pumice samples include plagioclase, orthoclase, biotite, hornblende, pyroxene, ilmenite, magnetite, and sphene. The main mineralogical contrasts between the upper and lower portions of the Pre-Rainier Mesa Tephra Sequence are, 1) compositional differences in phenocryst phases between the upper and lower portions of the sequence; and, 2) disequilibrium feldspars in the lower portion of the sequence.

The lower and upper portions of the Pre-Rainier Mesa Tephra sequence contain different feldspar compositions (Figure 18). The upper portion of the tephra sequence is characterized by an alkali feldspars range of Or_{57-71}, and a plagioclase compositions ranging from An_{16-17}. Most feldspars from the upper portion of the sequence are homogeneous, however, some orthoclase grains display normal zoning.

Feldspars from the lower portion of the Pre-Rainier Mesa Tephra Sequence have alkali feldspar ranges from Or_{40-69}, with the most intensely zoned feldspars ranging from Or_{45-69}. Plagioclase feldspars range from An_{15-45}. Most plagioclase grains are zoned, with some grains displaying reverse zoning. Three grains have plagioclase cores and orthoclase rims. These grains are likely in disequilibrium and may represent influx of a new magma into the system.

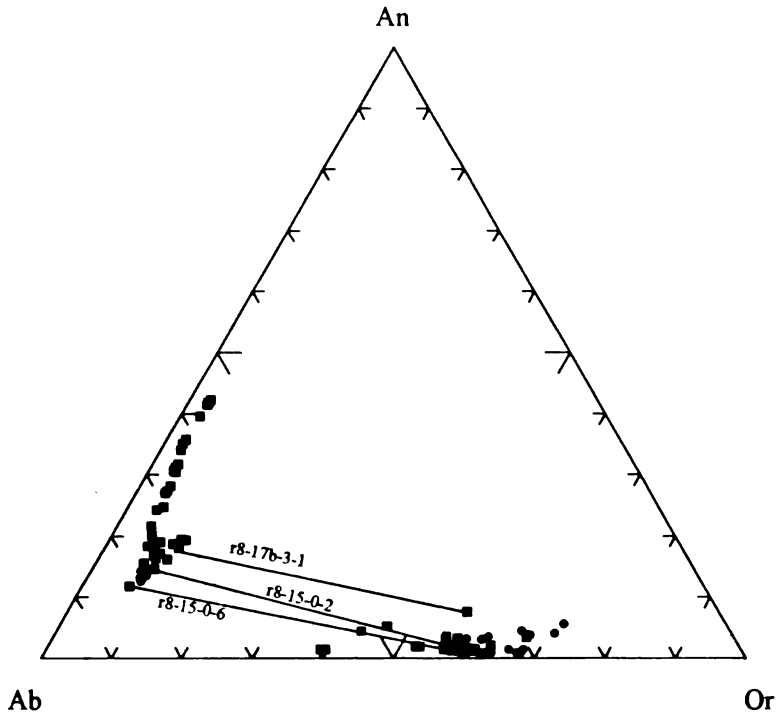

● = upper Pre-rainier Mesa tephra sequence
■ = lower Pre-rainier Mesa tephra sequence

Figure 18. Feldspar ternary diagram comparing feldspar compositions for the lower and upper Pre-Rainier Mesa tephra sequence.

Alkali feldspars from the upper portion of the Pre-Rainier Mesa tephra sequence are similar in composition to those of the overlying Rainier Mesa Tuff. Alkali feldspars from the lower portion of the Pre-Rainier Mesa Tephra Sequence display a large compositional range with most compositions falling between alkali feldspar compositions from the Rainier Mesa ash-flow sheet those from the Tiva Canyon ash-flow sheet.

Very few plagioclase grains were found in the upper portion of the Pre-Rainier Mesa Tephra Sequence. Three analyses from one of the small ash-

flow layers within the upper sequence shows a very narrow compositional range (An_{16-17}). This small range probably reflects of the small sample size since An compositions from the overlying high-silica portion of the Rainier Mesa ash-flow sheet have a larger compositional range.

Plagioclase grains from the lower portion of the tephra sequence have a considerably greater An compositional range than the upper portion of the tephra sequence. However, plagioclase compositions from the Tiva Canyon ash-flow sheet, Rainier Mesa ash-flow sheet, and Pre-Rainier Mesa Tephra Sequence all overlap.

Fe-Ti Oxide Temperatures

Temperatures were calculated for the Pre-Rainier Mesa Tephra Sequence in order to determine whether the upper and lower tephra sequence could be divided into thermometric groups corresponding to the chemical and radiometric age divisions already observed. In addition, thermometry provides an additional basis for comparison among the two subunits making up the Pre-Rainier Mesa tephra sequence to the much larger underlying and overlying ash-flow sheets.

Magmatic temperatures from the upper and lower portions of the Pre-Rainier Mesa Tephra Sequence were obtained using magnetite/ilmenite pairs. When possible, magnetite and ilmenite grains in contact were used to ensure equilibrium between the grains. However, some samples did not

provide grains in contact, so other means of testing equilibrium were employed.

One test for equilibrium is Mg/Mn partitioning between magnetite and ilmenite (Bacon and Hirschmann, 1988). The rationale for this test is that the exchange reaction

$$Mg_{il} + Mn_{mt} = Mn_{il} + Mg_{mt}$$

will produce a linear array of points (within analytical uncertainties) for equilibrium magnetite and ilmenite, on a plot of the $\log(Mg/Mn)_{mt}$ vs. $\log(Mg/Mn)_{il}$ (Bacon and Hirschmann, 1988). A positive result does not confirm equilibrium, however, a negative result does eliminate the possibility of equilibrium between a magnetite/ilmenite pair.

Magnetite and ilmenite grains in contact were considered as pairs and tested for equilibrium. Grains not in contact with an Fe-Ti oxide counterpart were paired with other separate grains from the same sample and tested for equilibrium. Magnetite/ilmenite pairs that fell outside of the analytical limits defined by Bacon and Hirschmann, were disregarded in subsequent temperature determinations.

Edge analyses give the best approximation of magnetite and ilmenite compositions being produced at the time of eruption. For this reason, only edge analyses of fresh grains were used for temperature determinations.

Temperatures were calculated using the "QUILF4.1" model developed by Andersen et al. (1993). Five temperature estimates from the lower Pre-

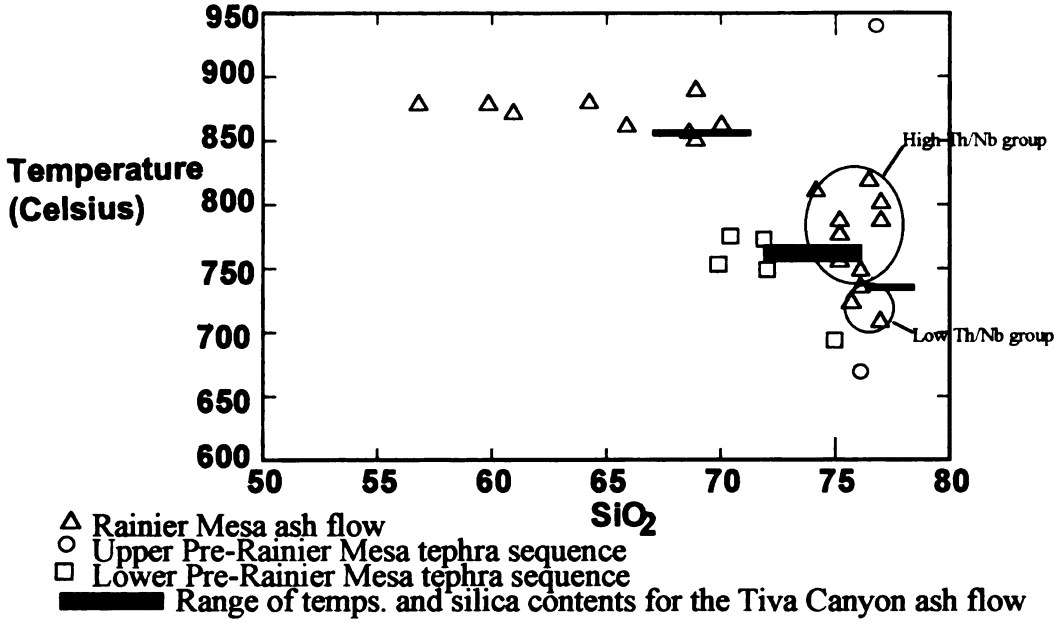

Figure 19. Comparison of Temperature vs. SiO_2 for Tiva Canyon ash-flow sheet, the Pre-Rainier Mesa tephra sequence, and the Rainier Mesa ash-flow sheet.

Rainier Mesa Tephra Sequence range from 694-775°C (Figure 19). Two temperatures were obtained from the upper Pre-Rainier Mesa Tephra Sequence. These were the lowest and the highest from the entire sequence (669°C and 958°C). The lower of these temperatures was obtained from a mt/il pair in contact. The higher of the two temperatures was obtained from two separate grains that passed the test for equilibrium. Absence of abundant Fe-Ti oxides in the upper portion of the sequence restricted efforts to obtain a more satisfying and statistically significant number of temperature analyses. From the temperatures obtained, it is not clear whether one, or both of the temperature measurements are incorrect.

A plot of temperature vs. SiO_2 (Figure 19), relates the four lower silica samples with temperatures ranging from 749-775 °C, and two of the three higher silica samples with temperatures ranging from 669-674 °C. The comparison of temperatures to silica content indicates a very general relationship between lower silica and higher temperatures. However, one high silica sample yields an extremely high temperature determination (958 °C). The overall relationship of decreasing temperature with increasing SiO_2 suggests that this temperature estimate is not correct. However, with only two temperature determinations from the upper portion of the sequence, any interpretations using temperature estimates should rely only on those from the lower tephra sequence.

Temperature determinations from the Rainier Mesa ash-flow sheet were initially conducted by Mills (1991). Temperatures were recalculated (Vogel, pers. comm., 1996), using the QUILF4.1 (Andersen and Lindsay, 1993). Additional temperature determinations were recently made by Saltoun (1995). These workers found that the three thermometric groups could be defined, coinciding with the three compositional groups of the Rainier Mesa Tuff (Cambray et al., 1995; Saltoun, 1995; Mills et al., in review). Compared with the Rainier Mesa Tuff, the Pre-Rainier Mesa tephra sequence possesses significantly lower temperatures for the same silica content. The same statement holds true when the tephra sequence is compared to the range of Fe-Ti Oxide temperatures and silica contents from

the Tiva Canyon ash flow sheet. Ranges of temperatures are given for the Tiva Canyon ash-flow because temperature estimates for the Tiva Canyon Tuff are uncertain due to the presence of sphene, rather than ilmenite, as the main Ti oxide phase (Flood, 1989). Temperatures from the Tiva are rough estimates only.

Summary

The Pre-rainier Mesa tephra sequence can be divided into two distinct groups based on $^{40}Ar/^{39}Ar$ ages and compositional differences between the lower and upper portions of the tephra sequence. The upper portion of the tephra sequence (11.62 ± .04) is equivalent in age and composition to the low Th/Nb, high silica group of the overlying Rainier Mesa ash-flow sheet (11.6 ± .06; Sawyer et al, 1994). The lower portion of the tephra sequence has the same $^{40}Ar/^{39}Ar$ age as the underlying Tiva Canyon ash-flow sheet [12.79 + .07 Ma for the lower Pre-rainier Mesa tephra sequence compared to 12.7 ± .06 Ma (Sawyer et al., 1994) for the underlying Tiva Canyon ash-flow sheet]. Compositionally, the lower portion of the tephra sequence is distinct from both the overlying Rainier Mesa ash-flow sheet and the underlying Tiva Canyon ash-flow sheet (Figure 15).

Chapter 5

THE PRE-AMMONIA TANKS MAGMATIC SYSTEM

Previous Work

Both the Rainier Mesa and Ammonia Tanks ash-flow sheets are chemically zoned with large variation (55-78 and 57-78 wt.% SiO_2 respectively) (Rose, 1988; Mills, 1991). In addition, both the Rainier Mesa and Ammonia Tanks ash-flow sheets erupted from the same caldera. The difference in eruption time between the two ash-flow sheets is only about 200,000 years, yet chemical differences between the Ammonia Tanks Tuff and underlying Rainier Mesa Tuff precludes their being related by differentiation of the same source magma body (Cambray et al., 1995). Based on these chemical differences, Cambray et al., (1995) proposed that the Rainier Mesa and Ammonia Tanks Tuffs represent separate lower crustal melts that have been emplaced along the same fracture system.

A compositional gap occurs between the low and high silica portions of the Ammonia Tanks Tuff (Mills, 1991; Cambray et al., 1995). In their recent study, Cambray et al., (1995) suggest that the high-silica portion of the Ammonia Tanks ash-flow sheet may represent a mixture of the two high-silica batches from the Rainier Mesa Tuff. This suggestion is based on the

fact that chemically, the high-silica portion of the Ammonia Tanks ash-flow sheet is intermediate between the two high-silica batches of the Rainier Mesa Tuff with respect to most trace elements. This contrasts with earlier studies (Rose, 1988) that indicate that the entire compositional range of the Ammonia Tanks can be produced by a combination of crystal fractionation and magma mixing. If Cambray et al. (1995) are correct, then magma mixing plays a far more important role in producing the higher silica portion of the Ammonia Tanks Tuff and crystal fractionation is relatively insignificant. It is important to note the difference in time scales for the two mechanisms. In the crystal fractionation/magma mixing model, the magma must be stored long enough for extensive fractionation to occur, however, the Cambray et al. (1995) model stresses brief residence time in the magma chamber before eruption.

$^{40}Ar/^{39}Ar$ age dates

$^{40}Ar/^{39}Ar$ radiometric ages for the Pre-Ammonia Tanks tephra range from 11.5 ± 0.04 to 11.9 ±.02 Ma. The Rainier Mesa Tuff has a radiometric $^{40}Ar/^{39}Ar$ age of 11.6 ±0.06 Ma (Sawyer et al., 1995). Since the Pre-Ammonia Tanks tephra sequence lies stratigraphically above the Rainier Mesa Tuff, one or both ages are in error. Coincidentally, the oldest ages from the Pre-Ammonia Tanks tephra sequence coincides with the youngest ages from the two incomplete sections of the Pre-Rainier Mesa tephra sequence that were

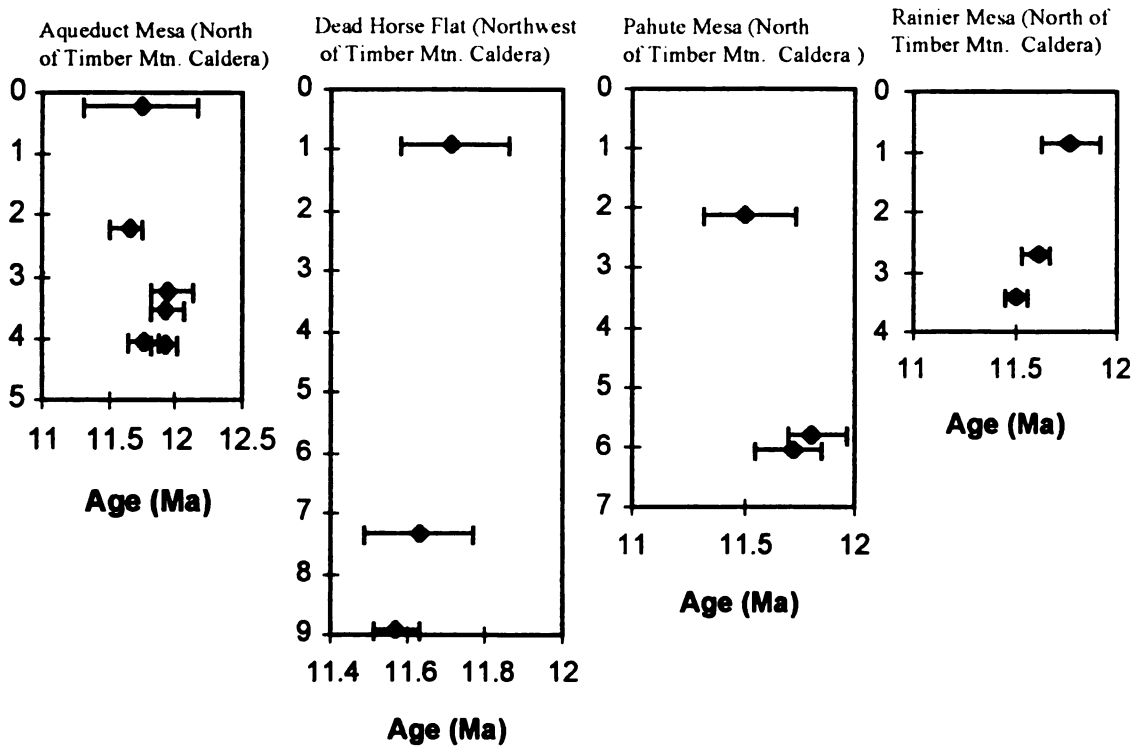

Figure 20. Range of $^{40}Ar/^{39}Ar$ ages for individual tephra layers from the Pre-Ammonia Tanks tephra sequence.

discussed previously; this includes the section at Yucca Mountain. It is possible that whatever processes affected the Pre-Rainier Mesa tephra sequence, also affected the Pre-Ammonia Tanks tephra sequence. One possible explanation for the discrepancy in ages is the apparent hydrothermal alteration that has taken place within the Pre-Ammonia Tanks tephra sequence.

Two of the four dated sections were useful in age interpretations of the Pre-Ammonia Tanks tephra sequence. Both of these sections have a 200,000 to 300,000 year average age difference between the base and the top of the sequence. In Figure 20, the age range for each layer is illustrated with

respect to stratigraphic position. Radiometric ages from the base and the top of a both sections overlap slightly, however still may give some indication that the upper portion of the sequence is younger than the lower portion.

Geochemistry

There is a large chemical variation in the Pre-Ammonia Tanks tephra sequence. The variation is illustrated by Zr vs. SiO_2 (Figure 21), and compared with the overlying Ammonia Tanks ash-flow sheet. Silica ranges from 69.1 to 77.5 wt.% and Zr ranges from 100 to 400 ppm.

For silica concentrations less than 70 wt.%, the Rainier Mesa and Ammonia Tanks ash-flow sheets are distinguishable by trace element variation (Figure 21). Only a few trace elements however, distinguish the higher silica portions of these ash-flow sheets. Of these, Rb, Y, and Nb provide a the greatest distinction between the two ash-flow sheets.

The chemical variation of individual glassy pumice fragments show that, with respect to Rb, the Pre-Ammonia Tanks tephra sequence is nearly identical to the overlying Ammonia Tanks Tuff. Four samples, collected from one location at various stratigraphic positions within the sequence, fall into the lower Rb, high-silica group of the underlying Rainier Mesa Tuff.

Contrasting this behavior, is the variation of Nb. Nb values from high silica samples from the Pre-Ammonia Tanks tephra sequence span the chemical ranges of both the underlying Rainier Mesa Tuff, and the overlying Ammonia Tanks Tuff. In addition, this plot shows that Nb values for the

●=A
+=P
○=P
△=P

Figu
sequ

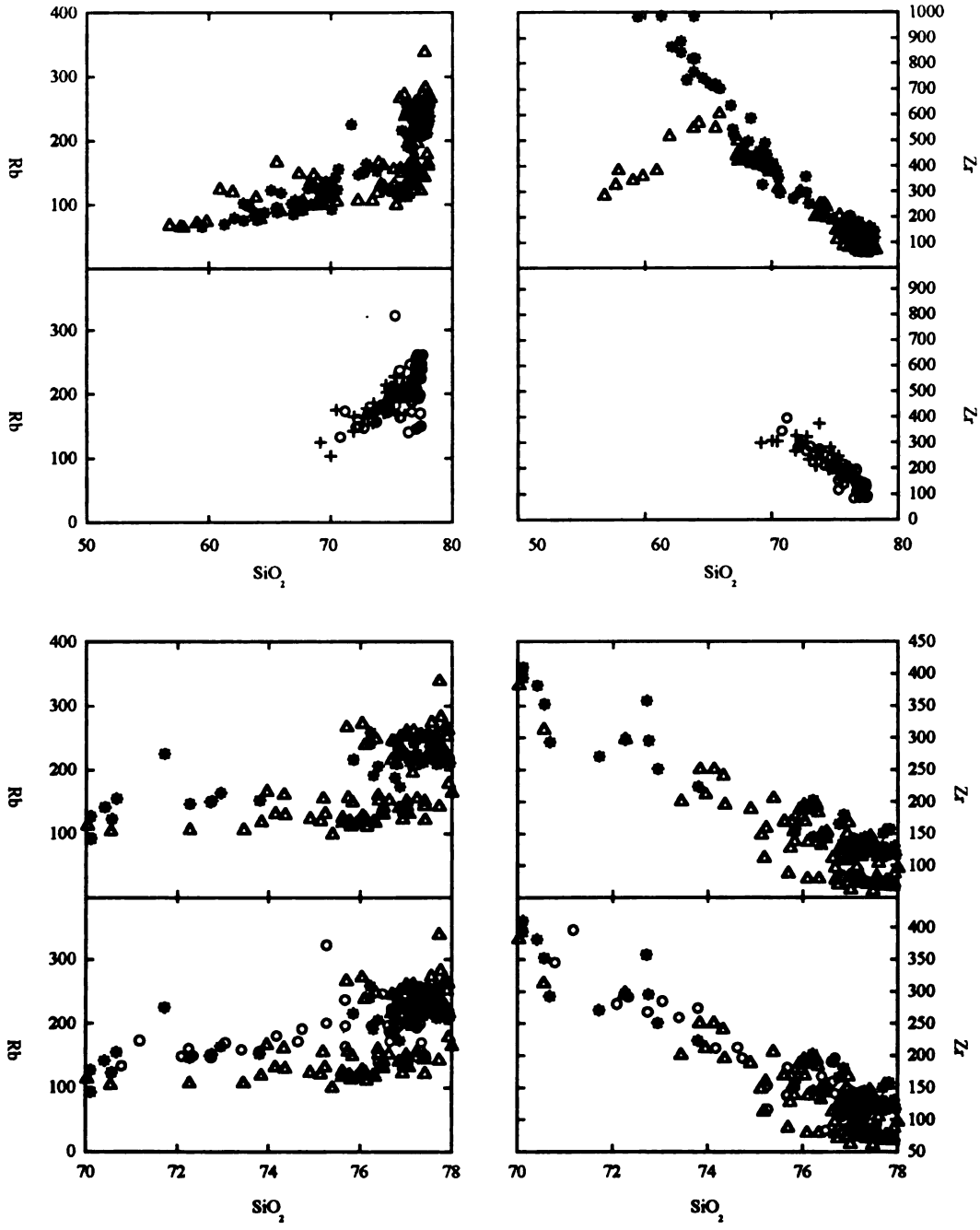

✱=Ammonia Tanks ash-flow sheet (individual glassy pumice fragments)
+=Pre-ammonia Tanks tephra sequence (bulk tephra)
O=Pre-ammonia Tanks tephra sequence(individual glassy pumice fragments)
Δ=Rainier Mesa ash-flow sheet (individual glassy pumice fragments)

Figure 21. Trace element discrimination of the Pre-Ammonia Tanks tephra sequence, the Rainier Mesa ash-flow sheet, and the Ammonia Tanks ash-flow sheet.

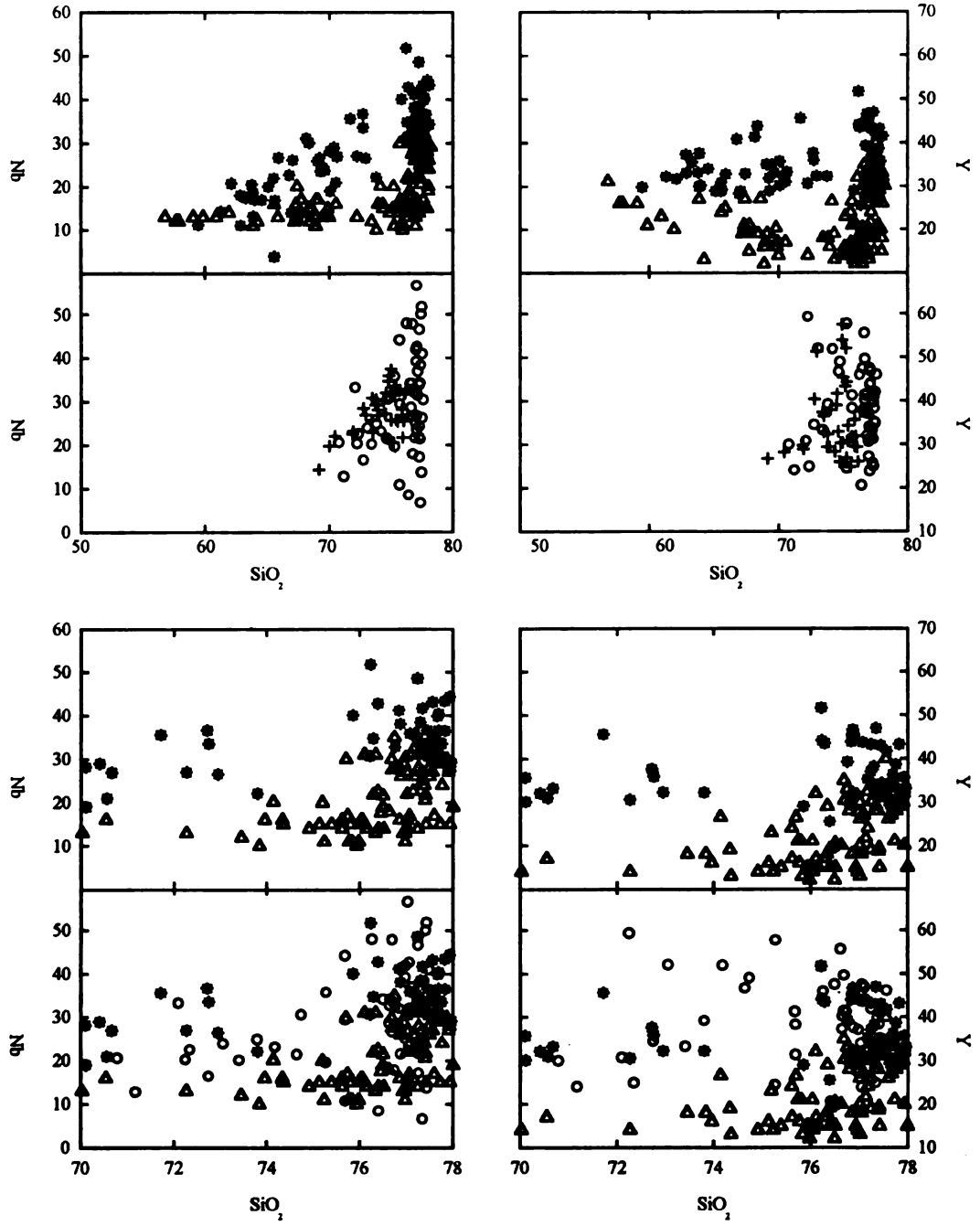

Figure 21 (continued).

high silica Ammonia Tanks Tuff do not fall between the two high-silica batches of the Rainier Mesa Tuff, suggesting that the high silica portion of the Ammonia Tanks Tuff is not a simple mixture of the high silica batches from the Rainier Mesa Tuff. Thus, the evolution mechanism suggested by Cambray et al. (1995) seems unlikely.

Most of the lower silica samples from the tephra sequence plot consistently with the low silica portion of the Ammonia Tanks Tuff (Figure 21). Three samples span a compositional gap that exists between the low and high silica portions of the Ammonia Tanks Tuff, and seem to be more closely related to the high silica group with respect to Y. Two samples from the lower silica portion of the Pre-Ammonia Tanks tephra sequence, that fall into the low silica Ammonia Tanks group, contain slightly higher Y concentrations than samples from the Ammonia Tanks Tuff. The different compositions of these samples is not caused by any amount of mixing of the Ammonia Tanks magma with Rainier Mesa magma. In a diagram of Zr vs. Y that includes chemical groups from the Rainier Mesa ash-flow sheet (Figure 22), inspection indicates that no mixing combination could produce the observed higher values of Y. One possible explanation is that wall rock assimilation produced this slight compositional difference.

Summary

The Pre-Ammonia Tanks tephra sequence is chemically similar to the overlying Ammonia Tanks Tuff. Nb concentrations from the high silica Pre-

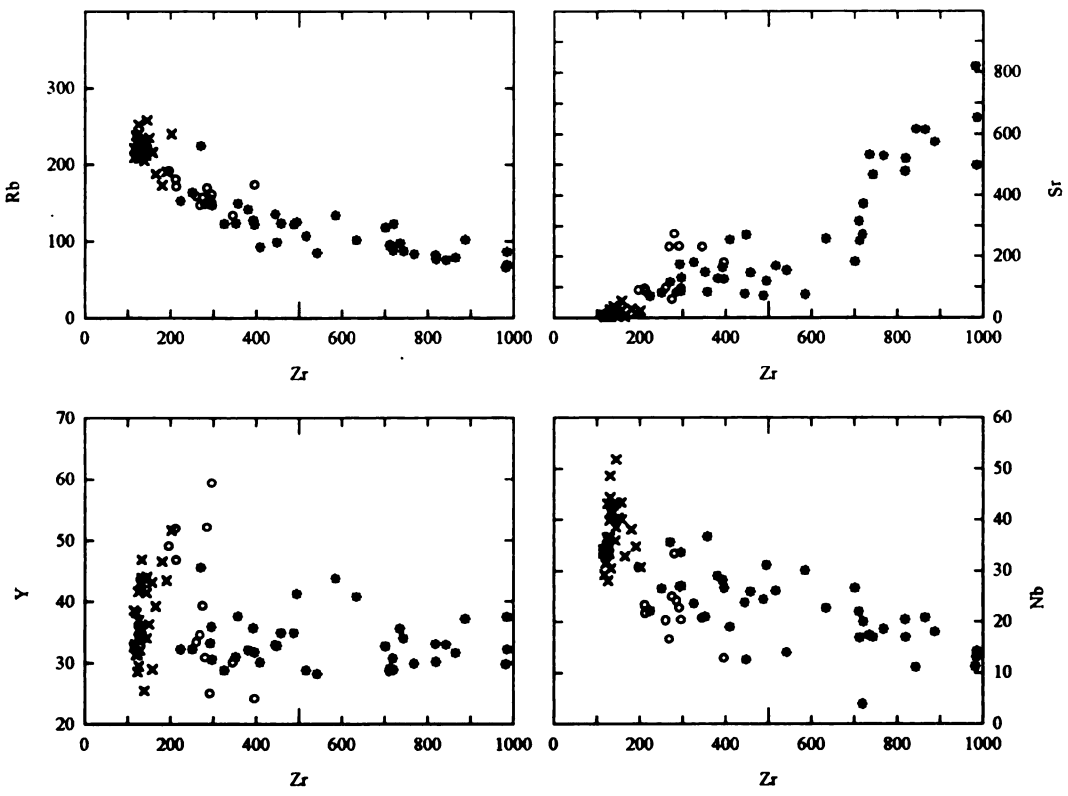

×=High SiO_2 Ammonia Tanks ash-flow sheet
✱=Low SiO_2 Ammonia Tanks ash-flow sheet
O=Low SiO_2 Pre-ammonia Tanks tephra sequence (glassy pumice)

Figure 22. Zr vs. Y comparing the Rainier Mesa ash-flow sheet, the Pre-ammonia Tanks tephra sequence, and the Ammonia Tanks ash-flow sheet.

Ammonia Tanks tephra sequence span the entire range of compositions of the high silica portion of the underlying Rainier Mesa ash-flow sheet and the overlying Ammonia Tanks ash-flow sheet. This behavior, and the high Nb concentrations of high silica samples from the Ammonia Tanks ash-flow sheet, strongly suggests that the high silica Ammonia Tanks pumice samples do not represent a mixture of the two Rainier Mesa high silica groups. Lower

silica samples from the tephra sequence fill the compositional gap between the low and high silica groups from the Ammonia Tanks ash-flow sheet.

Ages for the Pre-Ammonia Tanks tephra sequence are not well constrained, possibly due to hydrothermal alteration of the tephra sequence. However, there is a 250,000 radiometric age difference between the base and top of one section.

Chapter 6

DISCUSSION

The Post-grouse Canyon tephra sequence

The three main chemical, stratigraphic, and radiometric age groups in the Post-Grouse Canyon tephra sequence are, the lower, middle, and upper portions of the Post-Grouse Canyon tephra sequence. There is a fourth major compositional group, the highly variable layer, that falls into the same age group as the middle portion of the tephra sequence. This group has the largest variation in the sequence, and can also be divided into smaller chemical groups (see above). The large range of chemical variation in this tephra layer is evidence for the influx of new magma into the system prior to the eruption of this layer.

The focus of this section is, in part, to determine the petrologic relationships among the chemical groups of the Post-Grouse Canyon tephra sequence. However, permissible petrologic relationships among any of the chemical groups must also be consistent with age and stratigraphic constraints in the tephra sequence.

MAGMA MIXING

One powerful test of magma mixing is the comparison trace element ratios (e.g. Langmuir et al., 1977; Cox et al., 1979). If magma mixing is the only process relating a suite of rocks, the ratios of any four trace elements will plot on a hyperbola. Likewise, any of the initial ratios plotted against the ratio of the denominators will fall on a straight line. If both conditions are not satisfied, magma mixing as a dominant process must be rejected.

Magma mixing cannot relate the middle and upper portions of the Post-Grouse Canyon tephra sequence to each other, based on a diagram of the ratio Rb/Sr vs. Zr/Y (Figure 23). Trace element ratios for the two chemical groups produce trends that cannot plot on any mixing curve. Moreover, the accompanying plot, Rb/Sr vs. Y/Sr indicates that these groups do not fall on the same straight line.

Similarly, plots of Rb/Y vs. Zn/Sr and Rb/Y vs. Sr/Y reveal that magma mixing cannot relate the lower and upper portions of the Post-Grouse Canyon tephra sequence. Also, plots of Rb/Zr vs. Sr/Y and Rb/Zr vs. Y/Zr eliminate magma mixing as the main mechanism relating the lower and middle portions of the Post-Grouse Canyon tephra sequence.

As discussed above, the highly variable layer contains pumice fragments that consistently fit into the same chemical group as the rest of the middle portion of the tephra sequence. In Figure 24, these samples have been assigned the same as those from the middle portion of the tephra sequence. The highly variable layer also contains pumice fragments that are

(a)

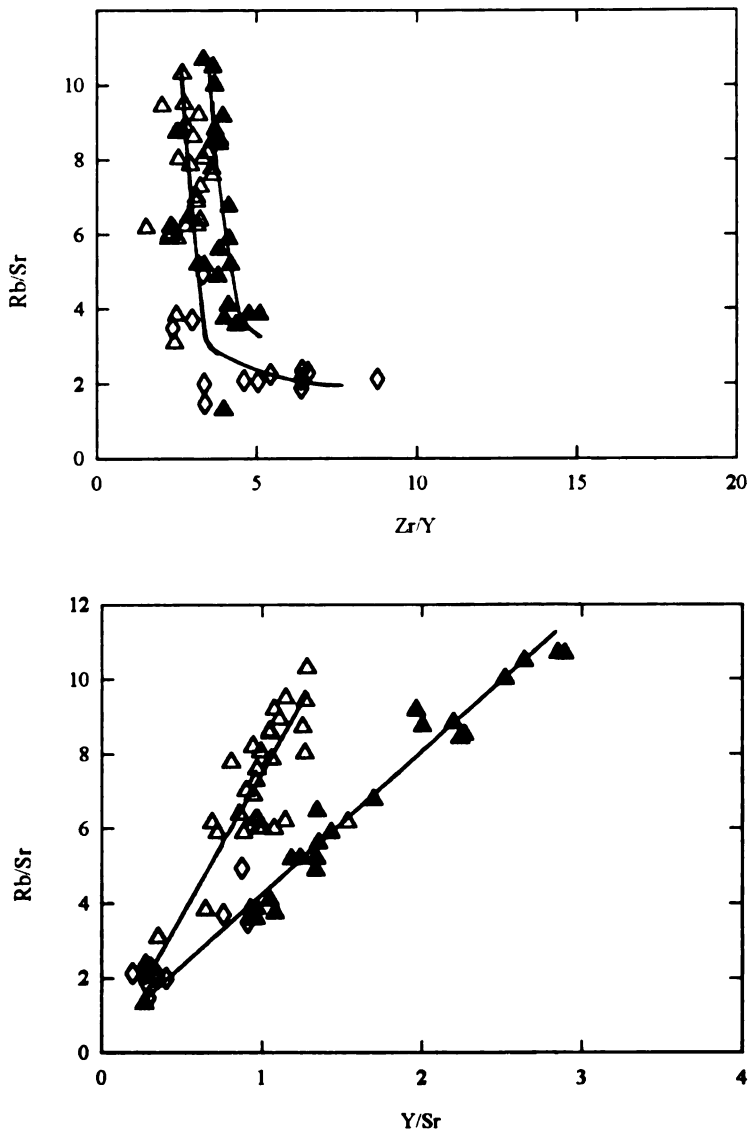

Figure 23. (a) Trace element ratio diagram of Rb/Sr vs. Zr/Y, and companion plot, illustrating that the middle and upper portions of the Post-Grouse Canyon tephra sequence are not related by magma mixing. (b) Trace element ratio diagram of Rb/Y and Zn/Sr, and companion plot, illustrating that the lower and upper portions of the Post-Grouse Canyon tephra sequence are not related by magma mixing.
(c) Trace element ratio diagram of Rb/Zr vs. Sr/Y, and companion plot, illustrating that the lower and middle portions of the Post-Grouse Canyon tephra sequence are related by magma mixing.

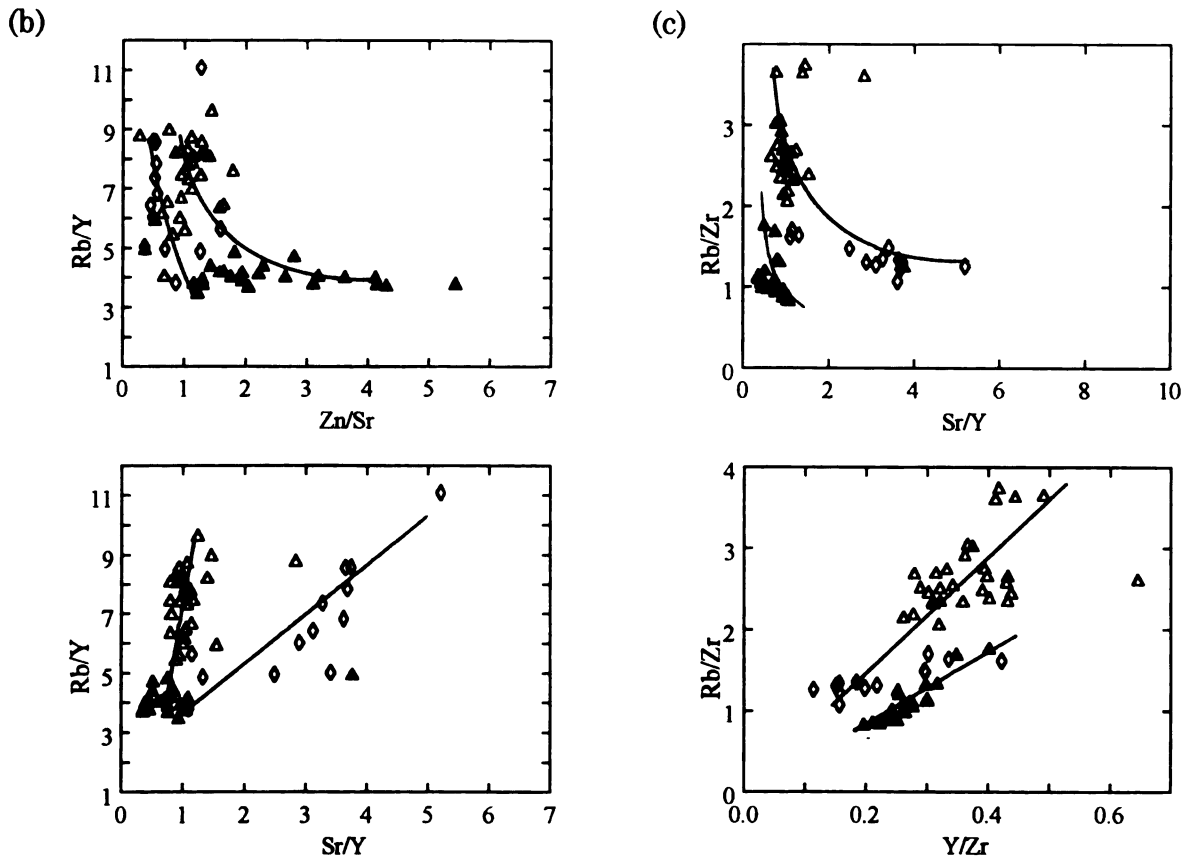

Figure 23. (continued)

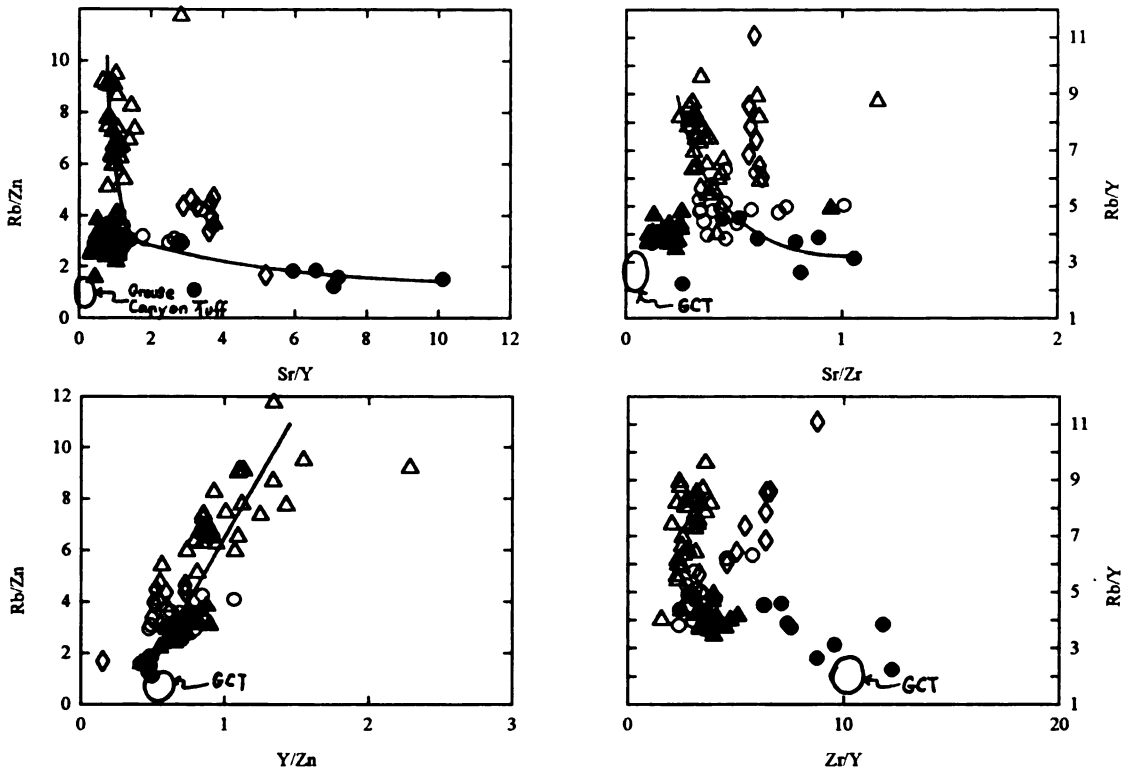

△ = upper Post-grouse Canyon tephra sequence
▲ = middle Post-grouse Canyon tephra sequence
○ = low Zr samples from the highly variable layer
● = high Zr samples from the highly variable layer
◊ = lower Post-grouse Canyon tephra sequence

Figure 24. (a) Trace element ratio diagram of Rb/Zn vs. Sr/Y and Rb/Y vs. Sr/Zr, and companion plots, illustrating that the middle portion of the Post-Grouse Canyon tephra sequence cannot be produced by mixing of the high Zr group from the highly variable layer with any other chemical group.

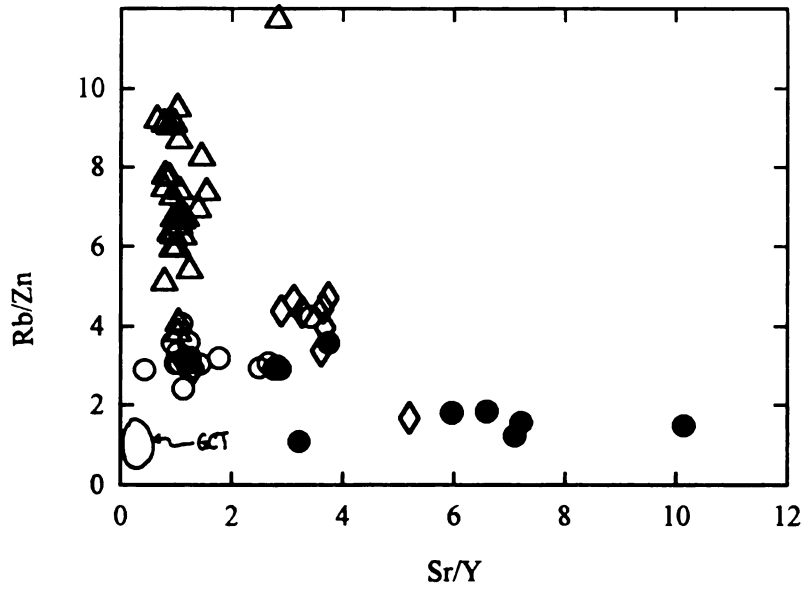

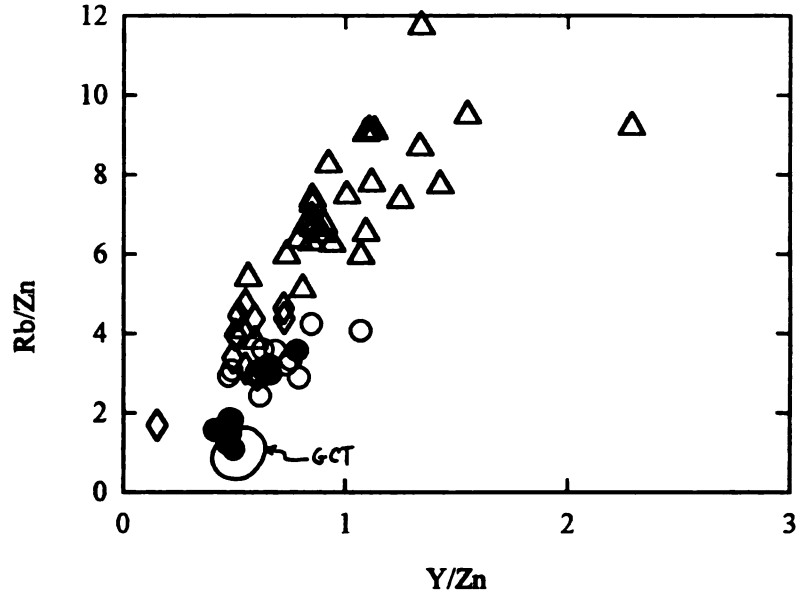

▲ = middle Post-grouse Canyon tephra sequence
○ = low Zr samples from the highly variable layer
● = high Zr samples from the highly variable layer
◊ = lower Post-grouse Canyon tephra sequence

Figure 24.(b) Trace element ratio diagram of Rb/Zn vs. Sr/Y, and associated companion plot, illustrating that the lower portion of the Post-Grouse Canyon tephra sequence is not produced by mixing of the high Zr group from the highly variable layer and any other chemical group from the tephra sequence.

distinct from all other chemical groups. These samples may also be divided into a high Zr and low Zr chemical groups (distinguished here as solid and open circles, respectively).

Plots of Rb/Zn vs. Sr/Y, and of Rb/Zn vs. Y/Zn best illustrate the relationship between the highly variable layer and the other chemical groups from the Post-Grouse Canyon tephra sequence (Figure 24a). Data for glassy pumice samples from the underlying Grouse Canyon Tuff (this study) are included to evaluate its potential as an end-member for mixing. The Grouse Canyon Tuff, however, can be eliminated as a potential end member upon inspection. Sr/Y ratios for the Grouse Canyon Tuff are lower than any samples from the overlying tephra sequence. Also, Rb/Zn concentrations are lower than all but a few samples from the highly variable layer. These low ratios eliminate the Grouse Canyon Tuff as an end-member for any mixing trends.

The middle portion of the tephra sequence could not have been produced by mixing any chemical group with the highly variable layer. In trace element ratio diagrams of Rb/Zn vs. Sr/Y, and Rb/Y vs. Sr/Zr, the average Sr/Y and Sr/Zr values for the middle tephra sequence are lower than any other chemical group (except the Grouse Canyon Tuff). Any mixing model for the middle portion of the tephra sequence, must produce Sr/Y and Rb/Y values intermediate between the end member concentrations.

It is also unlikely that magma mixing produced the lower portion of the tephra sequence. Figure 24b is the same as Figure 24a, with the symbols representing the middle portion of the tephra sequence removed. Rb/Zn values from the upper portion of the tephra sequence overlap nearly the entire range of Rb/Zn values from the lower portion of the tephra sequence, yet contain significantly lower Sr/Y values. Moreover, Sr/Y concentrations from the highly variable layer also overlap the Sr/Y range of the lower portion of the tephra sequence. There is no reasonable mixing process that can account for this variation.

The low Zr chemical group from the highly variable layer (open circles), also could not have formed by simple mixing of the upper portion of the tephra sequence and the high Zr chemical group from the highly variable layer (solid circles). The trends of the upper Post-Grouse Canyon tephra sequence and the high Zr group from the highly variable layer are nearly at right angles to one another. There is no simple mixing process or combination of mixing and crystal fraction that can account for the observed trend. It is interesting to note, that one sample from the low Zr group from the highly variable layer has a Sr/Y value lower than any sample from the upper portion of the tephra sequence. This would seem to indicate that the low Zr group could not have been produced by mixing of any chemical group with the upper portion of the tephra sequence.

The fact that the middle portion of the tephra sequence has a lower Sr/Y content than the upper portion of the sequence, and that the lower Zr group varies more widely than all of the other chemical groups combined (contains both higher and lower values) with respect to Sr/Y, is also good evidence that crystal fractionation combined with magma mixing could not have produced the middle or lower Post-Grouse Canyon chemical groups, or the high Zr group from the highly variable layer.

FRACTIONAL CRYSTALLIZATION

Fractional crystallization, as a mechanism for compositional modification, is tested below. As with magma mixing, certain fractionation schemes can be eliminated by inspection before numerical models are employed. In addition, an attempt is first made to relate the major compositional groups, then to evaluate the relationship of the highly variable layer to other compositional groups.

The variation of Zr best indicates that the lower, middle, and upper portions of the Post-Grouse Canyon tephra sequence are not related by crystal fractionation (Figure 25). In a diagram of Zr vs. SiO_2, the lower, middle, and upper portions of the tephra sequence are defined by three separate linear trends. Each is characterized by decreasing Zr with increasing SiO_2. The upper portion of the tephra sequence has the lowest Zr concentration (mean = 80 ppm), and the middle portion has the highest (mean = 160 ppm). The lower portion of the tephra sequence has Zr

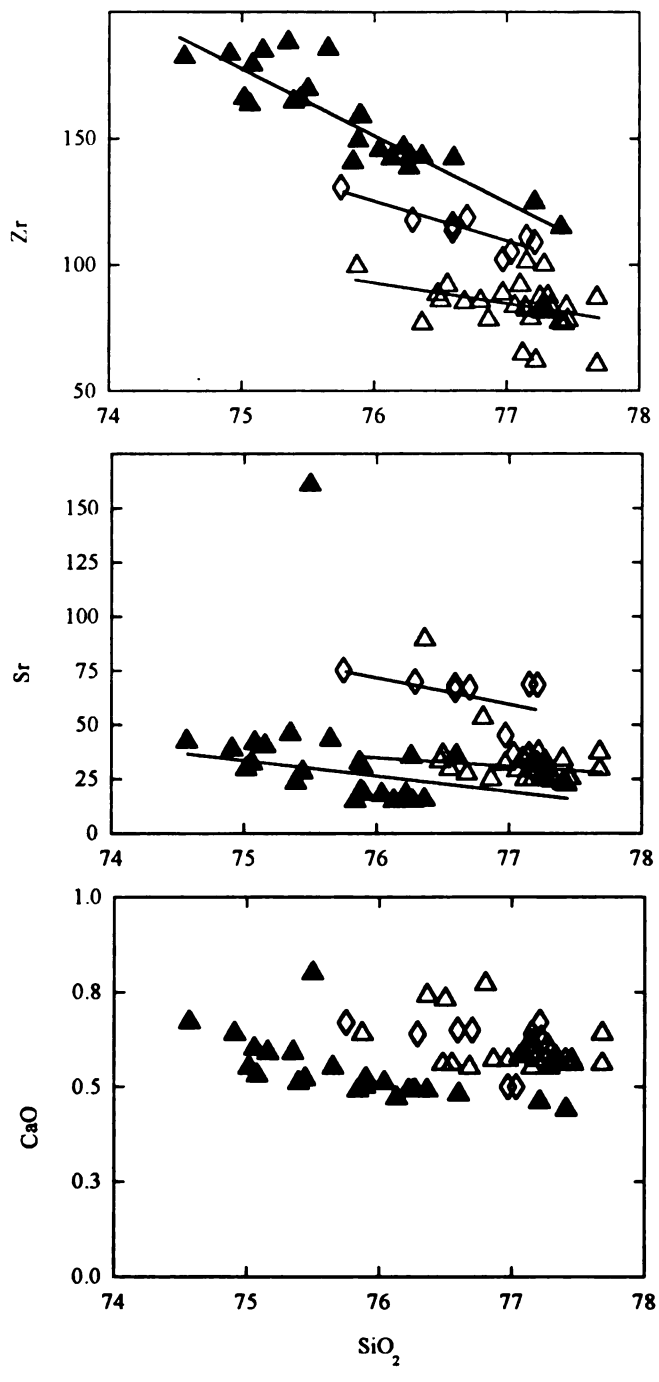

△ = upper Post-grouse Canyon tephra sequence
▲ = middle Post-grouse Canyon tephra sequence
◊ = lower Post-grouse Canyon tephra sequence

Figure 25. Variation diagrams of Zr, CaO, and Sr vs. SiO_2, illustrating distinct trends for the lower, middle, and upper portions of the Post-Grouse Canyon tephra sequence.

concentrations intermediate between the lower and middle portions of the sequence (mean = 120 ppm). This pattern is not compatible with crystal fractionation relating these groups.

Within any of these chemical groups, the decrease of CaO and Sr with increasing SiO_2 (Figure 25), suggests that crystal fractionation dominated by plagioclase can account for the observed variation.

The high Zr group from the highly variable layer cannot be produced by fractionation of any other chemical group. This group is the least evolved (66-74% SiO_2) of any group from the Post-Grouse Canyon tephra sequence. However, any one of the other chemical groups can be produced by crystal fractionation of the low Zr group from the highly variable layer. Numerous regression models can produce an excellent fit for any of the chemical groups by fractionating combinations of present phenocryst phases. Crystal fractionation models for any group, however, are dominated by plagioclase, and alkali feldspar fractionation (Figure 26). The best multiple linear regression model for each chemical group is reported in Table 2.

PARTIAL MELTING

Reasonable models of magma mixing or crystal fractionation cannot relate the lower, middle, and upper portions of the Post-Grouse Canyon tephra sequence. The presence of the highly variable layer suggests that new magma was introduced into the Post-Grouse Canyon magmatic system at approximately 13.3 Ma. Three possible relationships exist for the series of

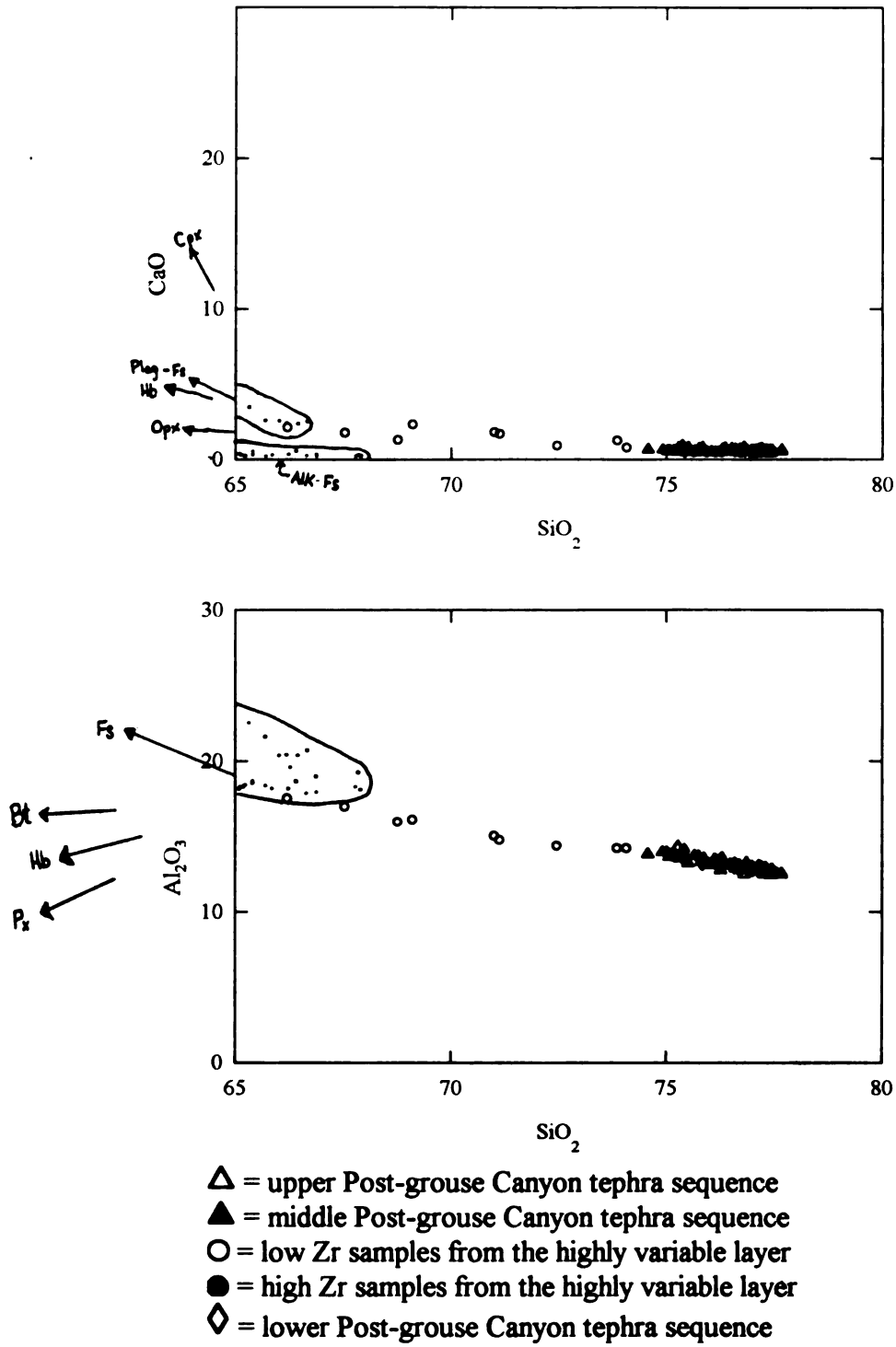

Figure 26. Al_2O_3 and CaO variation diagrams evaluating potential fractionation trends for the Post-Grouse Canyon tephra sequence.

Table 2. Regression analysis of crystal fractionation for the Post-grouse Canyon tephra sequence.

Evaluation of crystal fractionation to produce the lower tephra sequence from the high Zr group of the highly variable layer.

Parent = RM-19R65-211G

Cocf	% Cum	Mineral/Rock & ID
0.044	6.8	m21-7 biotite
0.049	7.6	m21-7 hornblende
0.002	-0.4	m19-10 ilmenite
0.012	1.8	m21-7 magnetite
0.136	20.9	m21-27 orthoclase
0.410	63.2	m21-27 plagioclase
0.349		RM-19R65-4D1=Daughter

	SiO_2	TiO_2	Al_2O_3	FeO	MnO	MgO	CaO	Na_2O	K_2O	P_2O_5
Daughter	77.15	0.13	12.75	0.94	0.05	0.04	0.64	2.32	5.98	0.00
Parent RM-19R65-211G										
Obs. Parent	66.21	0.39	17.51	3.30	0.16	0.76	2.13	5.02	4.44	0.08
Calc. Parent	66.23	0.39	17.22	3.30	0.13	0.79	2.11	5.18	4.49	0.00
Difference (wt %)	-0.01	0.00	0.15	0.00	0.03	-0.03	0.02	0.16	-0.05	0.08
Sum of the squares of the residuals = 0.057										

Table 2 (continued)

Evaluation of crystal fractionation to produce the low Zr group from the high Zr group of the highly variable layer

Parent = RM-19R65-211G

Coef	%Cum	Mineral/Rock
0.022	3.3	m21-7 biotite
0.069	10.3	m21-7 hornblende
0.000	0.0	m19-10 ilmenite
0.010	1.5	m21-7 magnetite
0.196	29.6	m21-27 orthoclase
0.366	55.2	m21-27 plagioclase
0.336		RM-19R65-211E=Daughter

	SiO_2	TiO_2	Al_2O_3	FeO	MnO	MgO	CaO	Na_2O	K_2O	P_2O_5
Daughter	77.51	0.08	12.73	0.89	0.08	0.18	0.47	2.88	5.17	0.01
Parent RM-19R65-211G										
Obs. Parent	66.21	0.39	17.51	3.30	0.16	0.76	2.13	5.02	4.44	0.08
Calc. Parent	66.23	0.39	17.11	3.30	0.16	0.80	2.10	5.25	4.51	0.00
Difference (wt %)	-0.01	0.00	0.20	0.00	0.00	-0.04	0.03	-0.23	0.07	0.08

Sum of the squares of the residuals = 0.107

Evaluation of crystal fractionation to produce the middle tephra sequence from the low Zr group of the highly variable layer.

Parent = RM-19R65-211G

Coef	%Cum	Mineral/Rock
0.037	5.6	m21-7 biotite
0.061	9.2	m21-7 hornblende
0.001	-0.1	m19-10 ilmenite
0.009	1.3	m21-7 magnetite
0.160	24.3	m21-27 orthoclase
0.393	59.7	m21-27 plagioclase
0.340		RM-19R65-236B=Daughter

	SiO_2	TiO_2	Al_2O_3	FeO	MnO	MgO	CaO	Na_2O	K_2O	P_2O_5
Daughter	77.42	0.07	12.45	1.00	0.07	0.01	0.44	2.76	5.77	0.01
Parent RM-19R65-236B										
Obs. Parent	66.21	0.39	17.51	3.30	0.16	0.76	2.13	5.02	4.44	0.08
Calc. Parent	66.22	0.38	17.07	3.30	0.14	0.81	2.10	5.28	4.52	0.00
Difference (wt %)	-0.01	0.01	0.22	0.00	0.02	-0.05	0.03	-0.26	-0.08	0.08

Sum of the squares of the residuals = 0.107

Table 2 (continued)

Evaluation of crystal fractionation to produce the upper tephra sequence from the high Zr group of the highly variable layer.

Parent = RM-19R65-211G

Coef	%Cum	Mineral/Rock
0.043	6.6	m21-7 biotite
0.054	8.1	m21-7 hornblende
0.002	-0.3	m19-10 ilmenite
0.011	1.7	m21-7 magnetite
0.159	24.2	m21-27 orthoclase
0.393	59.7	m21-27 plagioclase
0.339		RM-19R65-25-1-2 = Daughter

	SiO_2	TiO_2	Al_2O_3	FeO	MnO	MgO	CaO	Na_2O	K_2O	P_2O_5
Daughter	77.68	0.07	12.48	0.79	0.06	0.00	0.64	2.73	5.63	0.01
Parent RM-19R65-236B										
Obs. Parent	66.21	0.39	17.51	3.30	0.16	0.76	2.13	5.02	4.44	0.08
Calc. Parent	66.23	0.39	17.10	3.30	0.14	0.80	2.10	5.26	4.52	0.00
Difference (wt %)	-0.01	0.00	0.21	0.00	0.02	-0.04	0.03	-0.24	-0.07	0.08
Sum of the squares of the residuals = 0.107										

spatially related melts that produced the chemical groups of the Post-Grouse Canyon tephra sequence: 1) the chemical groups represent melts related by various degrees of partial melting from a single source that were subsequently erupted to the surface; 2) the chemical groups represent partial melts of the same source that resided separately and subsequently followed separate differentiation paths; 3) the major chemical groups of the Post-Grouse Canyon tephra sequence represent melting of different sources.

It is possible to test whether melts are related by partial melting by comparing observed trace element behavior to predicted behavior of trace elements between liquid and mineral phases in the magma. For this, it is crucial that the partitioning of trace elements between phases is well understood.

Experimental determinations of partition coefficients has been conducted mainly for basaltic systems. However, in recent years, more has been published on the partitioning of trace elements in more silicic systems (Ewart and Griffin, 1994; Sisson, 1994; Sisson, 1991; Michael, 1987; Nash and Crecraft, 1985; Mahood, and Hildreth, 1982;). The consensus is that the partition coefficients in highly silicic systems are significantly more variable than those for basaltic systems. Thus, the application of partition coefficients determined for a particular silicic system to another system is more difficult than in basaltic systems. Because analytically determined partition coefficients are not available for the Post-grouse Canyon magmatic system,

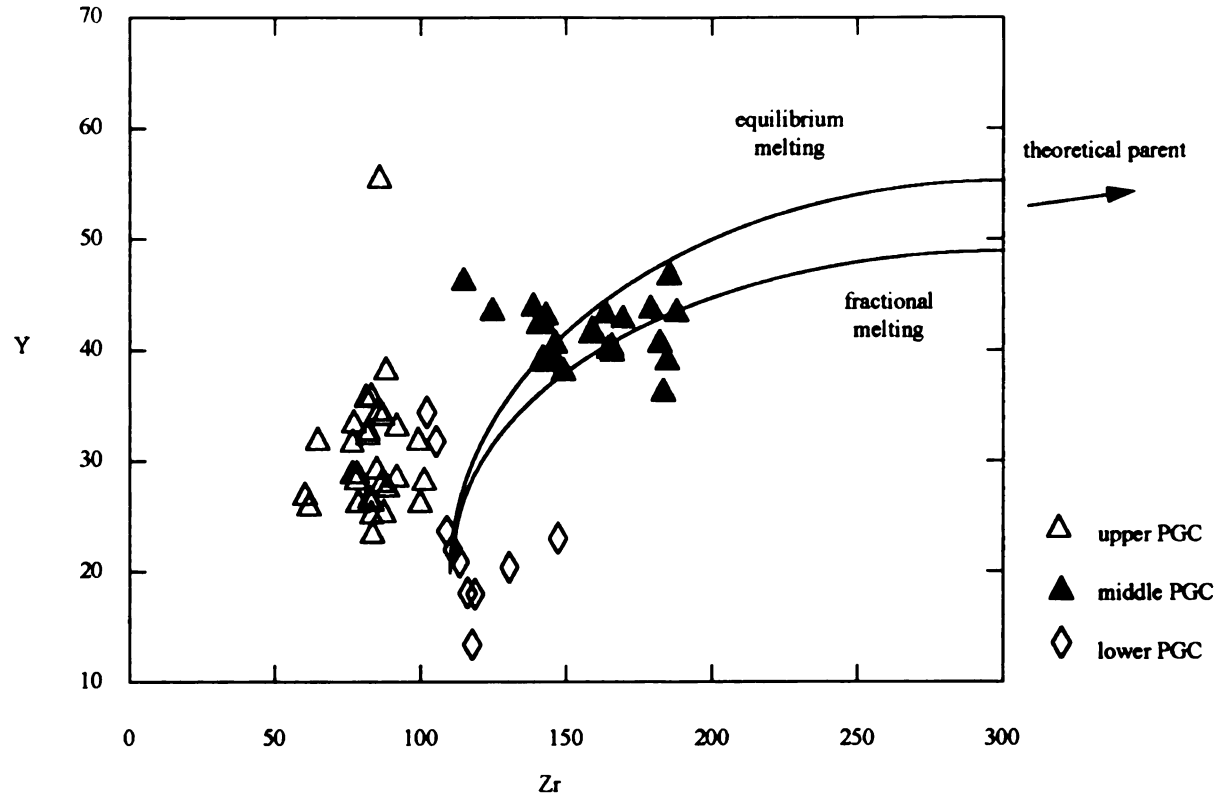

Figure 27. Y vs. Zr discrimination diagram showing that the lower, middle and upper portions of the Post-Grouse Canyon (PGC) tephra sequence cannot be related by partial melting of a single source.

reasonable ranges of partition coefficient values were selected from the literature to determine if the chemical groups could be related by and reasonable means of partial melting. If none of the selected partition coefficient values produced a reasonable fit, the model was rejected.

Rocks related by different degrees of melting of the same parent must lie on a curvilinear trend. A diagram of Y vs. Zr, shows that the chemical groups making up the lower, middle, and upper portions of the tephra sequence three chemical groups do not lie on a single curve (Figure 27) and, therefore, cannot be related by melting of the same source.

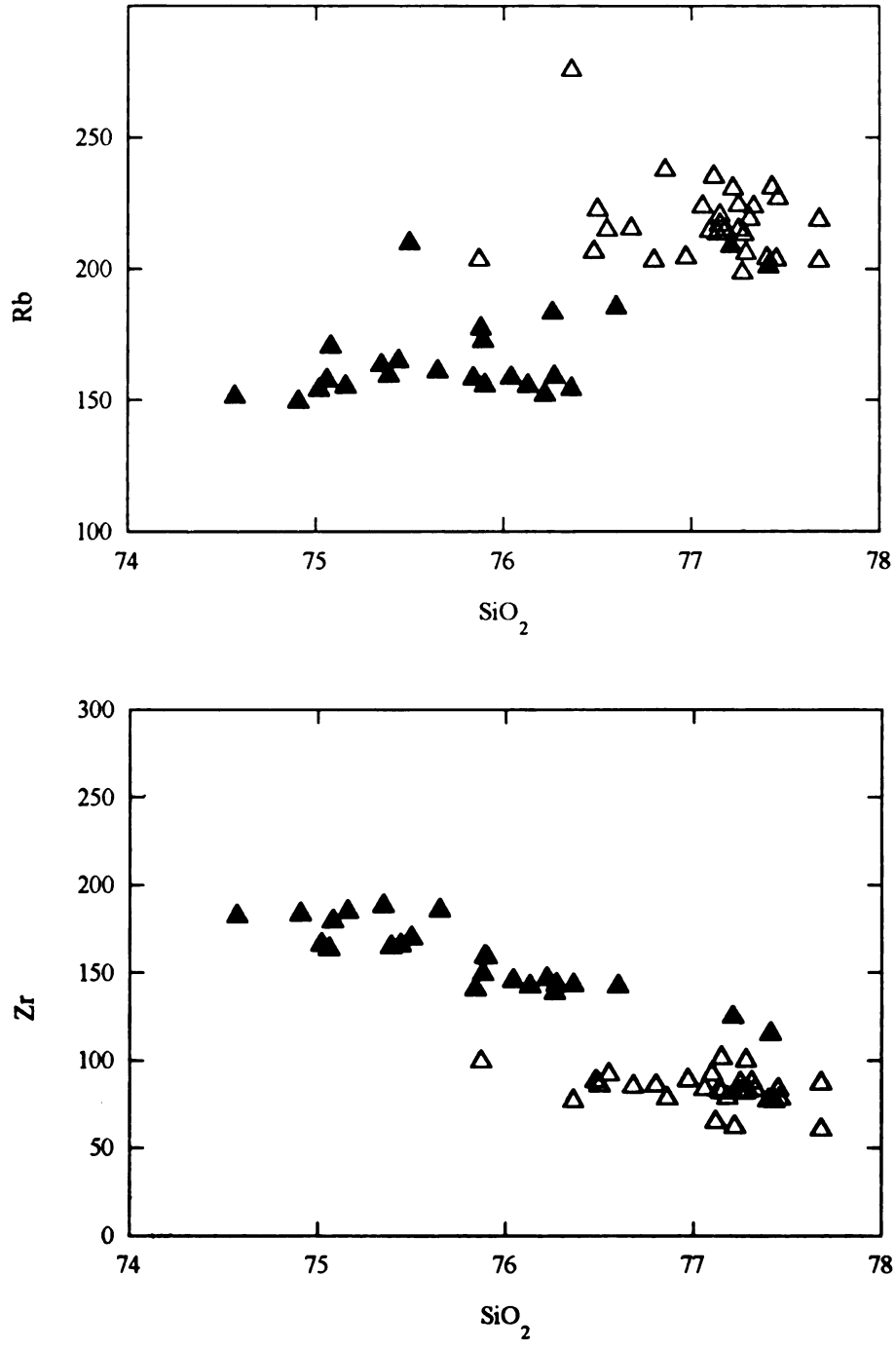

Figure 28. Rb vs. SiO_2 and Zr vs. SiO_2 variation diagrams, evaluating partial melting of a single source, for the middle and upper portions of the Post-Grouse Canyon tephra sequence.

Conceptually, any two of the chemical groups can be related by partial melting of a common source for any given trace element. A comparison of the chemical behavior of more than one trace element, however, indicates that some combinations of melting are unreasonable. The behavior of Zr and Rb with respect to SiO_2 demonstrate this for the chemical groups representing the middle and upper portions of the tephra sequence (Figure 28).

In high-silica systems, Zr acts compatibly. That is, Zr favors the solid phase during crystallization or melting events. The reverse is true for the incompatible behavior of Rb which favors the liquid phase. It is thus reasonable to assume that if the middle and upper portions of the tephra were sequentially produced by partial melting of the same source, that the most primary rocks from the middle tephra sequence would have lower Zr and higher Rb concentrations than the upper tephra sequence. That is, if the middle portion of the tephra represents the first melt produced, it should have the lowest Zr values, and the highest Rb values. The reverse behavior is observed.

These relationships imply that the middle and upper portions of the tephra sequence can be related by partial melting of a single source, but only if the upper portion of the tephra sequence represents an earlier melt than the middle portion of the tephra sequence. Thus, the magma represented by the upper portion of the tephra sequence would have had to reside in the crust until production and eruption of the magma that produced the middle portion of the tephra sequence occurred. This equates to a minimum

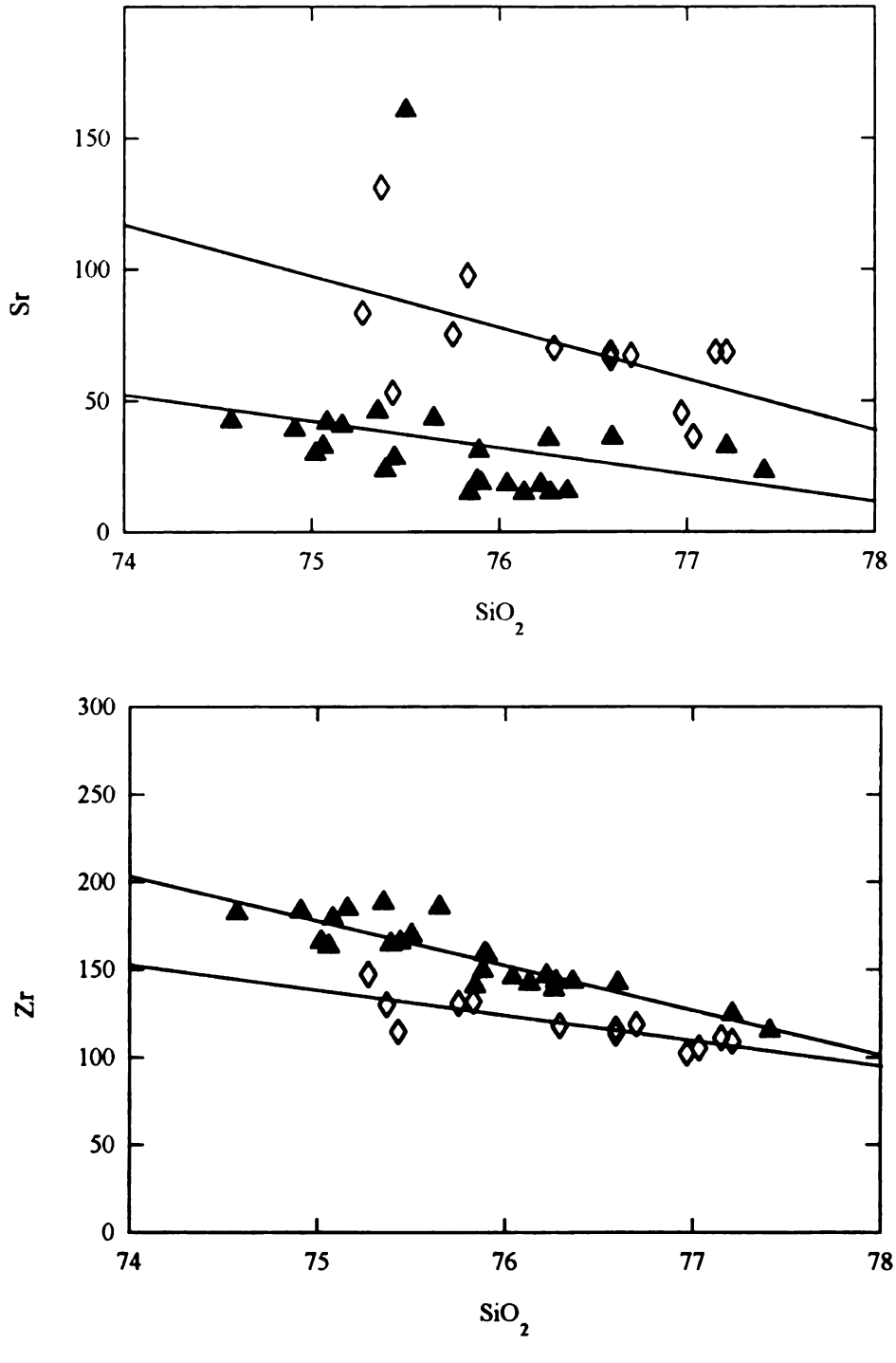

Figure 29. Variation of Sr and Zr with respect to SiO_2, evaluating partial melting of a single source for the origin of the lower and middle portions of the Post-Grouse Canyon tephra sequence.

residence time of at least 200,000 years based on the average age differences between the two.

The lower and middle portions of the Post-Grouse Canyon tephra sequence cannot be related by partial melting based on the chemical behavior of Sr, and Zr with respect to SiO_2 (Figure 29). In very high silica systems, both Zr and Sr act compatibly with respect to silica. In fact within a chemical group, the concentrations of both elements decrease with increasing silica.

If the chemical groups representing the lower and middle portions of the tephra sequence were related by partial melting of the same homogeneous source, the first melt produced should have the lowest Zr concentrations. This would equate with the chemical group that comprises the lower portion of the tephra sequence. However, Sr concentrations should also be low in the earlier melt. In the lower tephra sequence, Sr concentrations are higher than they are in the middle tephra sequence (Figure 25). This behavior is not consistent with the two chemical groups being related by partial melting of the same homogeneous source.

Partial melting of the same source is a permissible relationship between the lower and upper portions of the tephra sequence (Figure 30). In high silica systems, Rb is highly incompatible, and the first melt should be highly enriched in Rb. Likewise, Zr is compatible in high silica systems and the first melt should have lower concentrations than subsequent related

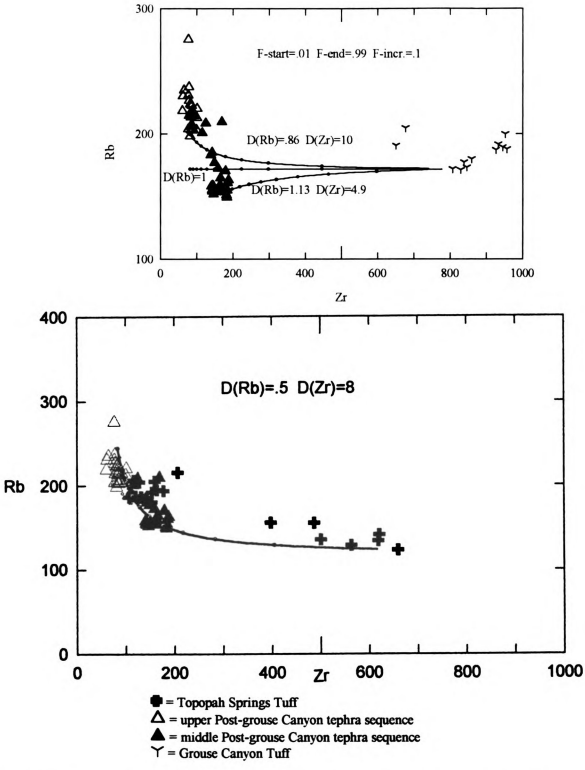

Figure 30. Variation diagram of Rb vs. Zr, and potential melting curves relating the Grouse Canyon Tuff (upper) and the Topopah Springs Tuff (lower) to the middle and upper portions of the Post-Grouse Canyon tephra sequence.

melts. A diagram of Rb vs. Zr shows that the upper portion of the tephra sequence contains higher Rb values and lower Zr values than the lower portion of the tephra sequence. This is consistent with the upper and lower portions of the tephra sequence being related by partial melting, with the upper portion of the tephra sequence representing an earlier melt.
The behavior of other trace elements in the two groups indicate that sequential partial melting could produce the upper and lower portions of the tephra sequence (Figure 30).

Partial melting of a single source cannot relate all three of the lower, middle, and upper portions of the Post-Grouse Canyon tephra sequence. However, partial melting of the same source can relate either the middle and upper portions of the tephra sequence, or the lower and upper portions of the tephra sequence. Either situation requires that the upper portion of the sequence melt first.

Relating the origin of the middle and upper portions of the tephra sequence by partial melting of the same source is far less complex than relating the origin of the lower and upper portions of the sequence by partial melting. If the upper portion of the tephra sequence was related to the lower portion of the tephra sequence, then the upper portion of the sequence would have to form first, and then be stored for 500,000 years. During this period, the lower portion of the tephra sequence, and the unrelated middle portion of

the tephra sequence would have erupted. This sequence of events is very complex and seems unlikely.

Relating the middle and upper portions of the tephra sequence is slightly less complex. In this situation, the storage time for the magma that produced the upper portion of the tephra sequence, is 300,000 years. In addition, an unrelated lower portion of the tephra sequence would erupt before the related middle and upper portions of the sequence, instead of between them.

MAGMATIC SOURCES

Compositions for potential sources are unknown. To date, there are no studies relating xenolith chemistry to potential sources for Nevada ash-flow tuffs. Numerous workers suggest that the Nevada volcanics are ultimately related to melting of the lower crust or lithospheric mantle (Farmer et al., 1991; Hildreth and Moorbath, 1988; Menzies et al., 1983; Farmer, 1989; Cambray et al., 1995). Nd and Sr isotopes and whole rock compositions suggest that intermediate and silicic magmas from the Paintbrush and Timber Mountain Groups may be derived from co-erupted basalts (Farmer et al., 1991). There are no basaltic layers, however, present in the Post-Grouse Canyon tephra sequence.

The specific sources of the Post-Grouse Canyon magmas remain unknown. The middle and upper Post-Grouse Canyon tephra sequence may

be related to either the Grouse Canyon Tuff (erupted prior to the tephra sequence) or the Topopah Springs Tuff (erupted just after the tephra sequence).

There is no reasonable equilibrium or fractional melting model that can relate the Grouse Canyon Tuff and both the middle and upper portions of the tephra sequence (Figure 30). With any combination of bulk distribution values for Rb and Zr, calculated melting paths cannot include these three groups.

Equilibrium partial melting models can produce the Topopah Springs Tuff and the upper and middle portions of the Post-Grouse Canyon tephra sequence. In a diagrams of Rb vs. Zr and Sr vs. Zr (Figure 30b), melting curves are constructed using bulk distribution coefficients ($D_{Rb} = 0.5$; $D_{zr} = 8$; $D_{Sr} = 10$). In this model, partition coefficients consistent with these values are reported for Rb and Sr in Nash and Crecraft (1985), and Hildreth (1977), for sanidine and plagioclase in high-silica rhyolite. As long as sanidine and plagioclase are the main melting phases, reasonable bulk distribution coefficients could be calculated from these partition coefficients. The highest partition coefficients found for Zr, however, are not more than 3.9 (Ewart and Griffin, 1994) for magnetite in dacite, and even less in high silica rhyolite. Zr could have a larger value if one of the main melting phases is zircon. This is unlikely, however, as zircon is a refractory phase and would not participate in initial partial melting events.

The Pre-rainier Mesa tephra sequence

It is clear that the lower (older) portion of the Pre-Rainier Mesa tephra sequence is chemically distinct from the overlying upper (younger) portion of the sequence. Geochemical considerations provide strong evidence that the lower and upper portions of the Pre-Rainier Mesa Tephra Sequence are not related by crystal fractionation (Figure 17). The lower portion of the tephra sequence is also distinct from the underlying Tiva Canyon ash-flow sheet, and the overlying Rainier Mesa ash-flow sheet, although, radiometric $^{40}Ar/^{39}Ar$ ages are indistinguishable between the lower Pre-Rainier Mesa tephra sequence and the Tiva Canyon ash-flow sheet.

From chemical considerations, the lower Pre-Rainier Mesa tephra sequence, is consistent with two models of magma mixing. The best numerical fit is achieved by mixing the low Th/Nb Rainier Mesa magma and the low silica Tiva Canyon magma to produce the lower Pre-Rainier Mesa magma. Alternatively, regression analyses indicate that the low silica Rainier Mesa magma could be mixed with high Th/Nb Rainier Mesa magma to produce another good fit. All other potential mixing models can be eliminated on inspection of trace element ratio diagrams.

Trace element ratios were examined in order to evaluate magma mixing (Langmuir et al., 1977; Cox et al., 1979). This test is not exclusive and a companion plot of one of the original ratios plotted against the ratio of

the denominators provides an additional test for mixing. Here, the end members and the supposed hybrid magma must plot on as a straight line (Langmuir et al., 1977). Rollinson (1993), has shown that plotting elemental ratios often forces trends in unrelated rock suites. This behavior limits the value of interpretations made for rock suites that fit this pattern. However, such plots are extremely useful for eliminating potential solutions.

Most potential mixing combinations for the lower Pre-Rainier Mesa tephra sequence can be eliminated upon inspection by using ratio/ratio plots for comparison. However, two combinations can produce the lower portion of the Pre-Rainier Mesa tephra sequence: 1) a low silica Tiva Canyon magma mixing with low Th/Nb Rainier Mesa magma; and, 2) low silica Rainier Mesa magma mixing with the high Th/Nb Rainier Mesa group, to produce the lower portion of the Pre-Rainier Mesa tephra sequence.

Regression analyses provides another quantitative means by which to evaluate magma mixing. For each test of magma mixing, multiple linear regressions were performed on two parent samples, one from the Tiva Canyon ash-flow sheet, and one from the Rainier Mesa ash-flow sheet, to produce a representative hybrid magma selected from the lower Pre-Rainier Mesa tephra sequence. Sample selection for each regression was based on potential mixing trends observed on chemical variation diagrams. More than one potential mixing trend exists for production of a Pre-Rainier Mesa hybrid magma from a mixture of Tiva Canyon and Rainier Mesa magmas.

Regressions were performed for all possible parent combinations to produce the lower portion of the tephra sequence.

Major oxide concentrations were regressed based on the following equation:

$$1.00\ A = bB + cC$$

where A is the hybrid daughter magma, B and C are parent magmas; and, b and c are the coefficients representing the fraction of magmas B and C to be mixed. Goodness of fit is measured by the sum of the squares of the residuals and by r^2. The sum of the squares of the residuals should be less than one for geologic systems, and r^2 should approach unity.

The best regression results were obtained by mixing 12.2% of the low silica Tiva Canyon (Tiva-1) and 87.8% of the low Th/Nb Rainier Mesa magma (R26-20) to produce the lower Pre-Rainier Mesa magma, 7F (1.00 7F = 0.122 Tiva-1 + 0.878 R26-20). The sum of the squares of the residuals for this regression is 0.171 and $r^2 = 0.98$ (Figure 31).

A good regression analysis was also obtained by mixing 18.6 % of the low silica Rainier Mesa group (R8-16) and 81.4 % of the low Th/Nb Rainier Mesa magma group (R8-21) to produce the lower Pre-Rainier Mesa sample, 7F (1.00 7F = 0.186 R8-16 + 0.814 R8-21). For this regression, the sum of the squares of the residuals is 0.264 and $r^2 = .96$.

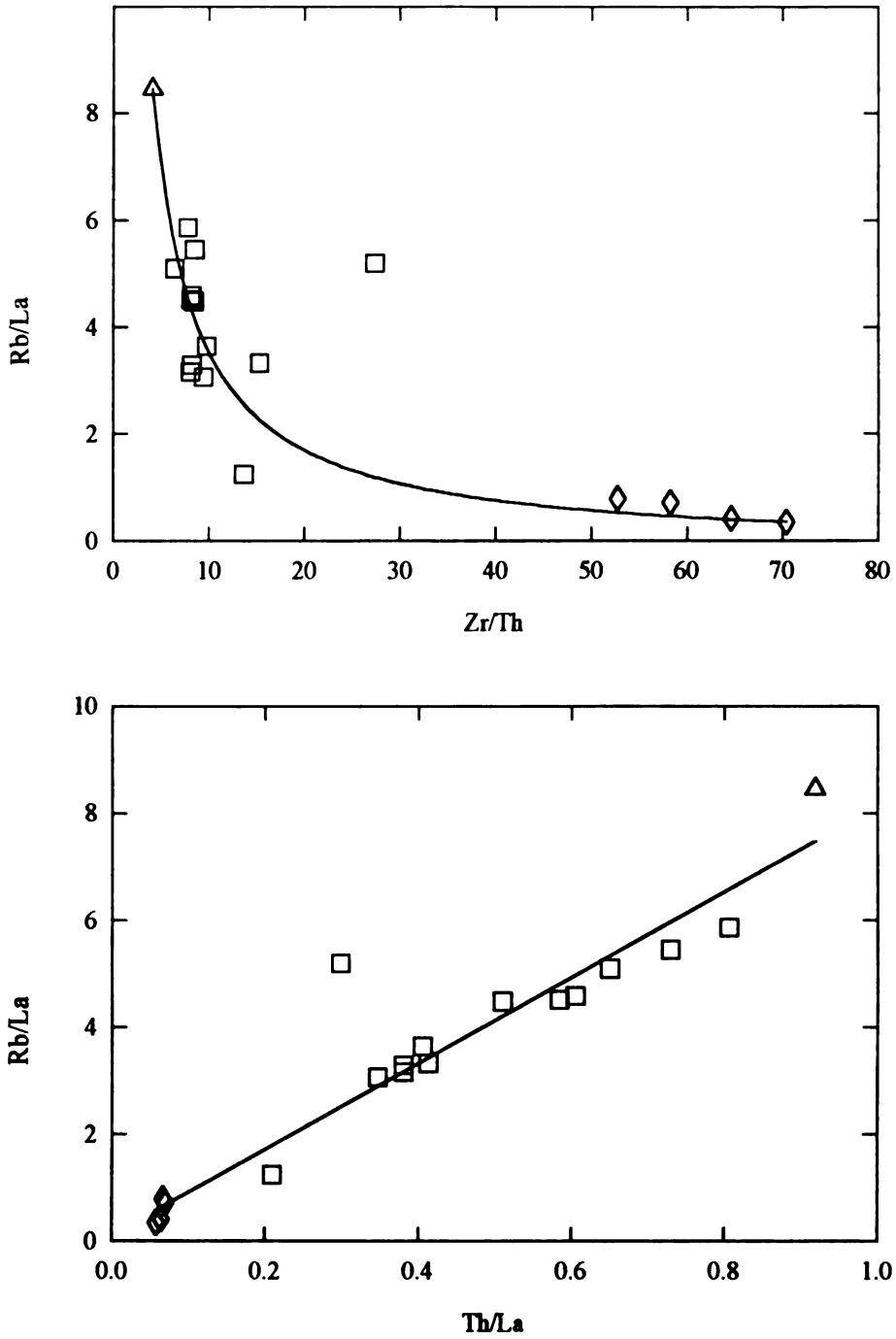

△ = low Th/Nb group from the Rainier Mesa ash-flow sheet
□ = lower Pre-rainier Mesa tephra sequence
◊ = low silica group from the Tiva Canyon ash-flow sheet

Figure 31. Trace element ratio diagram of Rb/La vs. Zr/Th, and companion plot Rb/La vs. Th/La, evaluating mixing of low silica Tiva Canyon magma and low Th/Nb Rainier Mesa magma to produce the lower Pre-Rainier Mesa tephra sequence.

An independent test of magma mixing is the comparison of calculated trace element concentrations determined by regression analysis to the observed trace element concentrations of the hybrid magma. Trace element values calculated for both mixing models, do not differ significantly from the observed values for glassy pumice fragments from the lower Pre-Rainier Mesa Tephra Sequence. Calculated trace element abundance compared with observed trace element values are reported in Table 3.

Two samples were excluded from the comparison because they consistently plot away from the rest of the group making up the lower portion of the tephra sequence. One sample, 8A, is the same sample high silica sample that consistently plotted away from the lower tephra sequence in trace element variation diagrams (Figure 17). The behavior of the other sample, 10A, is not easily explained except to say that weathering has most likely modified its composition.

Although two magma mixing models can account for the chemical variation of the lower Pre-Rainier Mesa tephra sequence, mixing of low silica Tiva Canyon magma with low Th/Nb Rainier Mesa magma is a more geologically viable solution. Because both the Tiva Canyon and Rainier Mesa Tuffs erupted from the same nested caldera, it is reasonable that unerupted low silica Tiva Canyon magma could mix with incoming high silica, low Th/Nb Rainier Mesa magma to produce the lower Pre-Rainier Mesa tephra sequence. This is also consistent with the fact that the upper Pre-Rainier

Table 3. Regression analysis producing sample 7F from two mixing combinations.

Mixture of low SiO_2 Tiva Canyon magma with high silica, low Th/Nb Rainier Mesa magma

	SiO_2	TiO_2	Al_2O_3	FeO	MnO	MgO	CaO	Na_2O	K_2O	P_2O_5
Tiva 1	65.92	0.61	17.14	1.99	0.1	0.77	2.07	4.33	6.66	0.14
R26-20	76.67	0.15	13.25	0.84	0.06	0.27	0.38	3.23	5.14	0.01
Observed 7F	75.16	0.2	13.55	1.13	0.09	0.7	0.54	3.32	5.3	0.01
Calculated 7F	75.12	0.21	13.71	0.98	0.06	0.33	0.58	3.35	5.31	0.03
Difference (wt %)	0.02	-0	-0.08	0.15	0.03	0.37	-0	-0.03	-0	-0.02

Sum of the squares of the residuals (SSR) = 0.171

r^2 = .86

	Tiva 1	R26-20	Observed 7F	Calculated 7F	Residual
Rb	76.5	215.5	204	197.9	6.1
Zr	887.7	96.0	195.4	191.9	3.5
La	218.3	25.5	45.5	48.9	-3.4
Lu	0.3	0.5	0.5	0.5	0.0
Yb	3.0	3.3	2.9	3.3	-0.4
Ce	386.9	60.2	84.8	99.8	-15
Eu	5.2	0.2	0.8	0.8	0.0
Hf	16.5	4.4	6.9	5.8	1.0
Tb	0.9	0.7	1.0	0.8	0.3
Th	12.6	23.4	23.2	22.0	1.2

Mixture of low silica Rainier Mesa magma with high silica, high Th/Nb magma

	SiO_2	TiO_2	Al_2O_3	FeO	MnO	MgO	Na_2O	CaO	K_2O	P_2O_5
R8-16	76.88	0.13	13.40	0.77	0.08	0.54	0.43	2.62	5.13	0.02
R8-21	67.35	0.47	16.86	2.38	0.09	0.76	2.14	4.52	5.28	0.15
Observed 7F	75.16	0.20	13.55	1.13	0.09	0.70	0.54	3.32	5.30	0.01
Calculated 7F	75.15	0.19	14.05	1.07	0.08	0.58	0.75	2.98	5.16	0.04
Difference (wt %)	0.00	0.01	-.0.25	0.06	0.01	0.12	-0.21	0.34	0.14	-0.03

Sum of the squares of the residuals = 0.264

r^2 = .96

	R8-16	R8-21	Observed 7F	Calculated 7F	Residual
Rb	252	90	204	222	-18
Sr	14	453	61	95.8	-34.8
Y	46	21	35.5	41.4	-5.9
Zr	107	497	195.4	179.7	15.7
Nb	26	16	23.9	24.2	-0.3
La	16.3	125	45.5	36.6	8.9
Lu	0.5	0.2	0.5	0.4	0
Yb	4.0	1.7	2.9	3.6	-0.7
Ce	61.2	194.1	84.8	86	-1.2
Eu	0.3	1.9	0.8	0.6	0.2
Hf	4	11	6.9	5.3	1.5
Sc	3.6	3.7	2.6	3.6	-1.0
Tb	0.6	0.6	1	0.6	0.4
Th	24.4	29	23.2	25.3	-2.1

Mesa tephra sequence is chemically equivalent to the low Th/Nb group from the Rainier Mesa Tuff.

It is far more unlikely that low silica Rainier Mesa magma and high Th/Nb Rainier Mesa magma would mix and erupt immediately after the Tiva Canyon with no contribution from Tiva Canyon magma. It would also be difficult to account for the fact that the upper Pre-Rainier Mesa tephra sequence is chemically equivalent to the low Th/Nb Rainier Mesa Tuff.

The Pre-Ammonia Tanks tephra sequence

The Pre-Ammonia Tanks tephra sequence is the only one that does not vary chemically with stratigraphic position. In this sequence the entire chemical variation (66 to 78 wt.% SiO_2) is observed throughout the sequence. Any model explaining the magmatic history of the Pre-Ammonia Tanks magmatic system must account for the full chemical variation present throughout the tephra sequence.

The chemical variation of the Pre-Ammonia Tanks tephra sequence is very similar to that of the overlying Ammonia Tanks Tuff. Nb concentrations of the high silica portion of the Pre-Ammonia Tanks tephra sequence span the compositional range of both the Ammonia Tanks Tuff, and the underlying Rainier Mesa Tuff. The lower-silica portion of the tephra sequence consistently fills a compositional gap between the low silica and high silica portions of the Ammonia Tanks ash-flow sheet.

Radiometric $^{40}Ar/^{39}Ar$ ages for the Pre-Ammonia Tanks tephra sequence are not able to distinguish a clear age difference between the base and the top of the tephra sequence due to overlapping ages and to large errors associated with absolute age values. The latter is most likely due to secondary hydrothermal alteration of the sequence. Higher average age values for the base of the sequence and very small overlaps between the base and the top of the sequence, suggest of an age difference of approximately 200,000 years between the base and the top of the sequence. This age difference, if real, and the chemical similarity of the Pre-Ammonia Tanks tephra sequence to the overlying Ammonia Tanks ash-flow sheet, may indicate that the Ammonia Tanks magma is also a long lived system.

The best examples of the chemical variations and inferred age differences noted between the base and top of the sequence, are where high silica and lower silica magma (down to about 66 wt.% silica) were apparently emplaced immediately after the eruption of the Rainier Mesa ash-flow sheet. In this scenario, there are no restrictions on the time of emplacement for the Ammonia Tanks low silica compositional range. If the entire compositional range was emplaced at this time, subsequent eruptions tapped only down to 66 wt.% SiO_2. It is unclear whether the entire chemical range of the Pre-Ammonia Tanks tephra sequence was tapped periodically, until the eruption of the overlying Ammonia Tanks ash-flow sheet occurred, or all eruption ceased until just before the eruption of the Ammonia Tanks Tuff. Age

determinations from only the base and top of this tephra sequence limit the possible interpretations of this sequence.

The absence of changing compositions from the base to the top of the Pre-ammonia Tanks tephra sequence, and inconclusive radiometric ages did not allow magmatic evolution rates to be calculated for this sequence . However, chemical and age data are interpreted to represent a long lived Ammonia Tanks magma body that contained highly evolved, high silica, Ammonia Tanks magma, and lower silica magma injected into the system near or at the time of emplacement.

Chapter 7

CONCLUSIONS

The Post-Grouse Canyon tephra sequence

Although radiometric age differences match chemical changes within the Post-Grouse Canyon tephra sequence, rates for specific magmatic process that produce chemical change within the pre-eruptive magmatic system cannot be calculated. This is because at least three out of the four chemical groups present were likely produced by the eruption of unrelated magmas.

It is possible to relate a) the middle and upper portion of the tephra sequence, or b) the lower and upper portions of the tephra sequence by partial melting of a single source, provided that in both cases the upper portion of the tephra sequence represents an earlier melt. The former is geologically more reasonable. In this scenario, the upper portion of the tephra sequence must have resided in the crust for at least 300 ka prior to eruption, based on average radiometric age differences between the middle and upper portions of the sequence. For this to occur a) the crust into which the melt resided was hot enough so that the closure temperature of Ar in sanidine was not reached, b) the magma was still fluid enough for eruption to occur, and c) the magma did not accumulate more than about 5% phenocrysts (the total phenocryst content of glassy pumice from the sequence).

The eruption of the Post-Grouse Canyon precedes the most intense period of eruptive activity in the history of Cenozoic volcanism in the southwest Nevada volcanic field. One hundred thousand years after the eruption of the Post-Grouse Canyon tephra sequence, more than 4400 km^3 of volcanic material was erupted over a time span of less than 2 million years. An elevated thermal budget was most likely already present in the crust produced by the Grouse Canyon and preceding magmatic systems. If the Paintbrush magmas were already working their way through the crust, they would also contribute to elevated crustal temperatures.

The alternative is that the middle and upper portions of the tephra sequence, like the other chemical groups within the sequence, represent partial melting of separate sources. This is possibly the most reasonable explanation as it eliminates problems of a long storage period for the upper sequence while the middle sequence is emplaced and erupted.

Whether or not the upper and middle portions of the tephra sequence are related by partial melting of a single source, the dominant relationship is that numerous unrelated magmas erupted one after another in the same place. One reason for focusing on the tephra sequences in this study was the belief that the small volume eruptive deposits represented a series of intermediate steps in the evolutionary history of a larger-volume magmatic system. It is remarkable to consider that a sequence of smaller-volume deposits, closely associated in time and place, are unrelated to one another.

This is the same relationship that has been interpreted to relate the chemical groups in some of the very large-volume ash-flow sheets (Saltoun, 1996; Cambray et al., 1995; Mills, 1991).

Prior to the eruption of the Post-Grouse Canyon tephra sequence, elevated temperatures in the crust coupled with the possible emplacement of Paintbrush magma may have produced a series of partial melts from the melting of separate sources or of a single heterogeneous source. Separate sources may have been tapped if partial melting occurred at various levels in the crust as the Paintbrush magma was emplaced at higher levels. Once formed, if these melts were isolated, each would follow its own differentiation path. Cambray et al. (1995) suggested that magma bodies which produced the large-volume ash-flow sheets of the Paintbrush and Timber Mountain Tuffs were stored along series of releasing steps created during periods of extension. This model provides a mechanism for magmas to be transported through the crust as well as a simple method for producing separate evolutionary paths. The interpreted relationships among the chemical groups in the Post-Grouse Canyon tephra sequence support this model.

The purpose of this study was to determine rates of magmatic processes leading to the chemical variation of large-volume magmatic systems in the Southwest Nevada Volcanic Field. This effort results in the general conclusion that magmatic processes accounting for chemical variation of the tephra sequences, are dominated by, (1) the emplacement of

often unrelated melts and (2) magma mixing that takes place over time scales too short to be measured by $^{40}Ar/^{39}Ar$ dating.

The Pre-Rainier Mesa tephra sequence

Radiometric age, stratigraphic position, and chemical groups divide the Pre-Rainier Mesa tephra sequence into two distinct magma types. The upper Pre-Rainier Mesa tephra sequence is the compositional and age equivalent of the high silica, low Th/Nb magma group defined by Cambray et al. (1995) and Saltoun (1996) from the overlying Rainier Mesa ash-flow sheet. It is interesting to note that no evidence of the high Th/Nb Rainier Mesa group is observed in this sequence.

Ages of the lower portion of the tephra sequence and the underlying Tiva Canyon ash-flow sheet are the same. However, the lower portion of the Pre-Rainier Mesa tephra sequence is chemically distinct from the Tiva Canyon ash-flow sheet. Regression analysis indicates that the lower portion of the Pre-Rainier Mesa tephra sequence is most consistent with mixing of 12.8 % of the low silica Tiva Canyon magma with 87.2% of the high silica, low Th/Nb Rainier Mesa magma.

There is no evidence that any Rainier Mesa magma was present during the eruption of the Tiva Canyon Tuff. Samples with the composition of the Rainier Mesa Tuff have not been observed in the Tiva Canyon ash-flow sheet. However, age relationships presented here indicate that magma with

Rainier Mesa Tuff composition must have entered the magma chamber almost immediately after eruption of the Tiva Canyon ash-flow sheet, to mix with low silica Tiva Canyon magma.

In this situation, the magma that produced the Rainier Mesa Tuff, immediately filled the same chamber from which the Tiva Canyon magma erupted. Rapid mixing of these two end member magmas must have occurred to form the completely mixed magma of the lower Pre-Rainier Mesa tephra sequence. As space was created by the eruption of the Tiva Canyon Tuff, and Rainier Mesa magma entered the chamber, high energy, turbid conditions for complete mixing of the two end member magmas would be produced.

The most important implication of mixing Rainier Mesa and Tiva Canyon end members, to form the lower Pre-Rainier Mesa magma, is that the high silica Rainier Mesa magma (or a Rainier Mesa-like magma) must have existed at the time of eruption of the lower Pre-Rainier Mesa tephra sequence (1.1 million years before the Rainier Mesa Tuff was erupted). This is evidence for a long-lived, already developed, high silica, low Th/Nb Rainier Mesa magma body that was emplaced from deeper levels in the crust when the Tiva Canyon ash-flow sheet was erupted.

The lack of evidence that the high Th/Nb Rainier Mesa magma was erupted with the upper Pre-Rainier Mesa tephra sequence, suggests that it was not present at the time the upper portion of the tephra sequence was

erupted (11.6 Ma). In this case, the high Th/Nb magma must have been emplaced very quickly to have been erupted with the overlying Rainier Mesa Tuff.

Alternatively, the high Th/Nb magma may have resided at deeper levels in the chamber. This is consistent with Fe-Ti oxide temperatures for the two Th/Nb groups from the Rainier Mesa Tuff (Figure 19) [Saltoun, 1996; Mills et al. (in review)], where temperatures from the low Th/Nb group have an average Fe-Ti oxide temperature 54°C lower than the high Th/Nb group. If Fe-Ti oxide temperatures in the Rainier Mesa Tuff reflect temperature gradients in the pre-eruptive magma chamber, the low Th/Nb group would have resided at a higher level than the high Th/Nb group. Eruptions that produced the smaller volume, upper Pre-Rainier Mesa tephra sequence, may not have tapped deep enough into the chamber to sample the high Th/Nb magma.

A thin layer of basaltic ash, present at the top of the sequence, suggests that the low silica Rainier Mesa magma was present during the final eruption of the Pre-Rainier Mesa tephra sequence. Mills (1991), suggests that injection of low silica magma may have triggered eruption of the Rainier Mesa ash-flow sheet. However, the low silica portion of the Rainier Mesa ash-flow sheet is present only in the upper 10% of the ash-flow sheet. It is difficult to reconcile how basaltic ash was able to erupt just prior to the Rainier Mesa ash-flow sheet, and not again until 90% of the ash flow

had been erupted. As no chemical analyses of this basaltic layer have been made, and there is some uncertainty as to how (or whether) this layer is related to the low silica portion of the Rainier Mesa ash-flow sheet, no attempt is made here to resolve the dynamics of its eruption or its relationship to the rest of the sequence.

Evidence for magma mixing recorded in the Pre-Rainier Mesa tephra sequence occurs over a time scale that is too short to be measured by $^{40}Ar/^{39}Ar$ age dating techniques. However, the interpretation that the low Th/Nb Rainier Mesa magma was present at 12.7 Ma, and the fact that the high Th/Nb Rainier Mesa magma is not observed in the Pre-Rainier Mesa tephra sequence, places constraints on the origin of the high silica portion of the Rainier Mesa Tuff. This evidence also indicates that the low Th/Nb magma was long lived, and was highly evolved before emplacement into the crustal level from which it was erupted.

The Pre-ammonia Tanks tephra sequence

The Pre-Ammonia Tanks tephra sequence, though characterized by a large chemical range, does not display systematic compositional changes from the base to the top of the sequence. This suggests little, if any, chemical modification of the Pre-Ammonia Tanks system between the first and last eruptions. Chemical variation of the Pre-Ammonia Tanks tephra sequence is consistent with the overlying Ammonia Tanks Tuff.

Ages for the Pre-Ammonia Tanks tephra sequence are not well constrained. This is most likely due to hydrothermal alteration of the sequence. However, the base of the Pre-Ammonia Tanks tephra sequence is generally more consistent with the age of the Rainier Mesa Tuff than with the age of the overlying Ammonia Tanks Tuff. This lends support to the idea that emplacement of Ammonia Tanks magma occurred very quickly during, or just after, eruption of the Rainier Mesa Tuff. The Pre-Ammonia Tanks tephra sequence is interpreted to represent a series of small eruptions from a long-lived Ammonia Tanks magma body that was emplaced almost immediately after eruption of the Rainier Mesa ash-flow sheet.

APPENDICES

APPENDIX 1

APPENDIX 1

ANALYTICAL TECHNIQUES

X-ray fluorescence (XRF)

Whole rock abundance for ten major element oxides and eleven trace elements were obtained by X-ray fluorescence (XRF) at Michigan State University. Fused disks were prepared for analysis at Michigan State University using methods described, in detail, by Mills, 1991. Major and trace element analysis abundance's were collected with a Rigaku S-max X-ray fluorescence spectrometer. Matrix absorption was corrected for all major elements were corrected using Criss parameters (Criss, 1980). Trace elements were calculated using multiple linear regression of USGS bulk rock standards. Standards were run as known calibration standards and as unknown. Analyses of 'unknown' standards were compared with known concentrations to determine if analyses were within acceptable error limits. Standard deviations for major oxides is ± 1%. Detection limits and standard deviations for trace elements are reported in Table 4.

Table 4. Detection limits and standard deviations for trace element analyses.

Element	Detection limit (ppm)	Relative standard deviation (%)
Ba	100	10
La	48	10
Cr	63	5
Ni	25	4
Zn	14	6
Rb	13	6
Sr	12	5
Y	14	6
Nb	15	6
Zr	14	6

Instrumental Neutron Activation Analysis (INAA)

Trace element analyses for rare earth elements and 6 additional trace elements, were obtained by instrumental neutron activation analysis (INAA) at the University of Michigan, Ann Arbor.

Samples were prepared for INAA by encapsulating between 0.2 g and 0.25 g of rock flour in high purity quartz vials. Samples were irradiated with a blank, internal standards from the Phoenix Lab at the University of Michigan, and four USGS whole rock standards, coded as unknowns. Standard errors for trace element analysis and deviations of INAA analyses from USGS published concentrations are reported in Table 5.

Table 5. Standard errors for INAA analyses.

Element	1-sigma % error
Ba	8.16
La	9.54
Lu	16.26
Nd	18.58
Sm	8.85
Y	9.78
Ce	4.18
Cs	7.36
Cr	3.69
Eu	5.67
Hf	5.42
Sc	7.69
Ta	11.96
Tb	13.06
Th	1.81
Zn	5.75

Electron Microprobe Analyses

Phenocryst compositions were analyzed on a Cameca Microprobe at the University of Michigan, Ann Arbor.

Grain mounts were prepared for analyses by course crushing the sample with a mortar and pestle, and then separating heavy minerals from feldspar, quartz, and glass by tungsten salt, heavy liquid separation. Feldspars were further separated from glass by hand picking individual crystals.

During analysis, grains were checked for homogeneity by analyzing three spots accross the grain. If grains were zoned, three to eight spots were analyzed across the grain, depending on the intensity of zonation.

APPENDIX 2

APPENDIX 2. Major Oxide and Trace Element Analyses (normalizized to 100%)

Grouse Canyon Tuff (glassy pumice)														
	R65-1A	R65-1A1	R65-1A2	R65-1A3	R65-1C1	R65-1C2	R65-1C3	R65-1C7-1	R65-1C8	R65-1C9	R65-1E1	R65-1E2	R65-2G	
Weight Percent Oxide (wt. %)														
SiO[2]	73.97	74.54	74.64	75.25	76.81	75.96	75.66	75.81	76.38	76.22	76.81	76.3	77.03	
TiO[2]	0.24	0.24	0.24	0.24	0.21	0.24	0.22	0.24	0.21	0.22	0.15	0.15	0.09	
Al[2]O[3]	11.83	11.96	11.92	11.6	10.54	11.05	10.74	11.87	10.61	10.93	12.12	11.97	12.86	
FeO	3.52	3.67	3.67	3.61	3.49	3.68	3.63	3.55	3.51	3.59	2.1	2.09	0.82	
MnO	0.18	0.18	0.18	0.17	0.15	0.16	0.16	0.18	0.15	0.16	0.09	0.09	0.09	
MgO	0.05	0.03	0.02	0.02	0.03	0.11	0	0.14	0.06	0.15	0.02	0.19	0.32	
CaO	0.28	0.23	0.22	0.21	0.2	0.19	0.18	0.27	0.19	0.2	0.26	0.24	0.5	
Na[2]O	4.08	3.23	3.24	3.15	3.48	2.92	3.65	2.84	3.62	3.13	2.64	3.41	3.17	
K[2]O	5.85	5.91	5.86	5.76	5.09	5.69	5.77	5.1	5.27	5.4	5.81	5.56	5.12	
P[2]O[5]	0.01	0.01	0	0	0	0	0	0	0	0	0	0.01	0	
X-ray Fluorescence (ppm)														
Cr	0	0	2.4	0	0	0	0	0	0	0	0	0	1.4	
Ni	12	22.1	9.2	1.2	1.6	2.2	5.4	0	0	6.3	0	27.6	0	
Cu	0	0	0	0	0	5	0	0	0	0	0	0	0	
Zn	205.5	191.8	194.3	231.3	210.6	207.6	215.3	226.2	214.8	212.8	145.3	141	57.7	
Rb	173.5	177.5	180.1	171.4	187.3	200	192	172.1	188.1	189.5	204.9	190.9	179.6	
Sr	7.5	2.7	7.6	9	4.3	7.2	2.9	6	0.2	4.5	5.5	0.5	36.4	
Y	91	91.1	90.2	93.9	98	107.2	96.2	87.5	96.3	98.5	70.9	70.7	31.8	
Zr	846.6	838.6	859.4	829.6	926.6	952.5	932.9	807	957.3	945.2	676.9	650.5	105.3	
Nb	69	60.6	66.5	66.7	63.2	69.1	71.3	57.8	62.6	73	54.9	52.6	31	
La	0	0	0	0	0	0	0	0	0	0	0	0	0	
Ba	83.8	106.4	127	164.8	132.1	141.2	101.5	169.5	179.7	74.3	6	0	98.8	

APPENDIX 2. (Continued)

Post-grouse Canyon tephra sequence (glassy pumice)												
	PMR-SURGE-E	PMR-SURGE-F	PMR-1A	PMR-1B	PMR-2.1A	PMR-2.1B	PMR-2.3A	PMR-2.3B	PMR-3.1A	PMR-3.1B		
Weight Percent Oxide (wt. %)												
SiO[2]	76.5	75.87	76.55	77.68	77.31	77.45	76.97	76.68	77.43	77.25		
TiO[2]	0.08	0.1	0.08	0.08	0.08	0.08	0.08	0.08	0.07	0.07		
Al[2]O[3]	13.14	13.55	13.08	12.55	12.92	12.83	13.01	13.08	12.44	12.51		
FeO	0.76	1.16	1.11	0.62	0.75	0.99	0.85	1.08	0.58	0.92		
MnO	0.06	0.06	0.05	0.05	0.06	0.05	0.06	0.06	0.06	0.06		
MgO	0	0.11	0.02	0	0	0	0	0	0	0		
CaO	0.73	0.64	0.56	0.56	0.56	0.57	0.57	0.55	0.56	0.57		
Na[2]O	3.19	3.22	2.87	3	2.54	2.59	2.95	2.91	3.17	3.35		
K[2]O	5.52	5.25	5.66	5.45	5.76	5.43	5.5	5.54	5.67	5.25		
P[2]O[5]	0.01	0.01	0.01	0.01	0.01	0.01	0.01	0.01	0.01	0.01		
X-ray Fluorescence (ppm)												
Cr	0	0	0	1.3	7	3.9	0	1	6.8	0		
Ni	0	5.2	0.8	0	0	0	0	0	0	0.9		
Cu	58	60.2	62.7	58	56	56.9	59.2	59.3	57.8	59.2		
Zn	24.2	53.4	52.7	31.2	29.6	34.1	30.4	34.3	25.4	42.1		
Rb	222.6	203.4	214.8	202.9	218.9	203.5	204.2	215.4	231	214.9		
Sr	36.1	32.6	29.5	29.5	26.7	25.3	32	27.4	22.4	26.8		
Y	55.4	31.7	28.4	27.9	25.2	25.1	27.5	29.1	28.7	34		
Zr	85.8	99.3	91.9	86.7	87.3	83.2	88.5	85	76.7	87		
Nb	41.5	22.9	21.7	27.2	27	22.3	15.1	17.9	17.9	18.3		
La	0.8	41.2	38.2	22.8	30.2	40.7	41.7	18.7	20.8	45.7		
Ba	123.8	165.1	146.2	72.6	87	78.5	215.8	122.7	171.4	102.6		

APPENDIX 2. (Continued)

Post-grouse Canyon tephra sequence (glassy pumice)											
	PMR-3.1G	PMR-3.2A	PMR-3.2B	PMR-3.3A	PMR-3.3B	PMR-3.4A	PMR-3.4B	PMR-4.1	PMR-4.2D	PMR-4.2G	PMR-4.3A
Weight Percent Oxide (wt. %)											
SiO[2]	77.46	77.1	76.48	77.4	77.14	77.15	77.28	77.33	77.25	76.86	77.18
TiO[2]	0.07	0.08	0.08	0.07	0.07	0.08	0.07	0.07	0.07	0.07	0.07
Al[2]O[3]	12.55	12.68	13.14	12.72	12.86	13.04	12.84	12.69	12.69	13.25	12.75
FeO	0.69	0.93	1.05	0.72	0.83	0.74	0.93	0.76	0.83	0.79	0.76
MnO	0.06	0.06	0.06	0.06	0.05	0.06	0.06	0.06	0.06	0.06	0.06
MgO	0	0	0.03	0	0	0.03	0.05	0	0	0.03	0
CaO	0.56	0.58	0.56	0.57	0.59	0.55	0.55	0.58	0.57	0.57	0.57
Na[2]O	2.86	3.21	3.21	3.07	2.81	2.58	2.49	2.96	2.93	2.69	3.17
K[2]O	5.73	5.34	5.37	5.37	5.63	5.76	5.72	5.53	5.59	5.67	5.42
P[2]O[5]	0.01	0.01	0.01	0.01	0.01	0.01	0.01	0.01	0.01	0.01	0.01
X-ray Fluorescence (ppm)											
Cr	0	1.7	0	9.1	2.2	7.2	0.7	12	0	1.7	0
Ni	0	0	0	0	0	0	0	0	0	0	0
Cu	56.4	57.5	58.9	57.2	56.8	57.2	56.6	56.3	57.8	55.4	55.5
Zn	35.7	24.7	26.7	21.5	32.7	32.5	31.7	30.8	28.8	26.3	23.6
Rb	226.8	214.4	206.5	204	213.4	220.3	213.1	223.6	224.1	237.6	214.7
Sr	25.4	34.4	33.3	34	35.5	29	24.9	24.3	25.7	25	24.9
Y	28.2	33	38.1	33.3	35.7	28.1	26.1	26.2	32.2	28.7	26.1
Zr	78	91.9	88.2	77.1	83.1	101.2	99.9	83.3	81.8	78.3	78.6
Nb	26	29.3	29.7	29.4	34.4	24.2	31.9	30.2	34.5	33	31.7
La	42.2	12.6	14	9.2	0.2	29.8	30.7	30.1	39.8	36	37.8
Ba	322.4	78.4	96	124.2	58.9	145.3	159	157.2	10.8	136.3	119.2

APPENDIX 2. (Continued)

Post-grouse Canyon tephra sequence (glassy pumice)										
	PMR-4.3C	PMR-5B	PMR-5E	RM-19R65-2G	RM-19R65-4D1	RM-19R65-20B	RM-19R65-20D	RM-19R65-211C	RM-19R65-211D	
Weight Percent Oxide (wt. %)										
SiO[2]	77.06	77.29	77.15	76.97	77.15	76.82	77.01	76.61	71.12	
TiO[2]	0.07	0.07	0.07	0.08	0.13	0.09	0.08	0.12	0.42	
Al[2]O[3]	12.86	12.65	12.78	12.99	12.75	12.9	12.71	13	14.78	
FeO	0.81	0.86	0.84	0.79	0.94	0.96	0.92	1.1	2.68	
MnO	0.06	0.06	0.06	0.08	0.05	0.09	0.08	0.09	0.11	
MgO	0	0	0.05	0.3	0.04	0.23	0.11	0.28	0.64	
CaO	0.58	0.59	0.62	0.5	0.64	0.48	0.5	0.63	1.71	
Na[2]O	3.02	3.39	3.16	3.18	2.32	3.16	3.31	3.24	3.87	
K[2]O	5.53	5.09	5.28	5.1	5.98	5.25	5.28	4.89	4.56	
P[2]O[5]	0.01	0.01	0.01	0.01	0	0.01	0	0.02	0.11	
X-ray Fluorescence (ppm)										
Cr	0	1.5	5.7	0	0	0	0	0	0	
Ni	0	0	0	0	0	0	0	0	0	
Cu	56.9	57.1	57.1	0	3.2	0	0	0	8.2	
Zn	41.4	31	34.7	56.7	30.5	57.6	59.1	60.1	71.3	
Rb	223.7	206	216.7	167.8	141.9	179.8	179.5	176.2	130.2	
Sr	28.8	29.4	36.8	45.2	68.6	43.1	43.1	78.2	207.6	
Y	23.3	26.5	32.6	34.4	22	30.3	31.6	28.4	34.9	
Zr	83.5	82.5	81.9	102.2	111.1	107.8	111.5	130.1	264.2	
Nb	30.5	31	32.4	19.6	14.3	20.8	22.9	22.8	9.1	
La	19.1	39.4	26.3	80.2	71.4	67.8	55.2	63.4	104.4	
Ba	98.1	104.7	133.7	179.2	464.5	269.3	171.1	291.7	815.7	

APPENDIX 2. (Continued)

Post-grouse Canyon tephra sequence (glassy pumice)								
	RM-19R65-211E	RM-19R65-211H	RM-19R65-211I	RM-19R65-211J	RM-19R65-212I	RM-19R65-212H	RM-19R65-4A	
Weight Percent Oxide (wt. %)								
SiO[2]	77.5	75.89	69.1	76.95	77.18	76.93	76.29	
TiO[2]	0.08	0.12	0.61	0.1	0.08	0.08	0.13	
Al[2]O[3]	12.73	13.3	16.13	12.78	12.95	13.09	13.53	
FeO	0.89	1.18	3.27	1	0.8	0.81	1.06	
MnO	0.08	0.09	0.1	0.08	0.08	0.08	0.05	
MgO	0.18	0.09	0.78	0.18	0.43	0.32	0.12	
CaO	0.47	0.84	2.32	0.53	0.48	0.53	0.64	
Na[2]O	2.88	3.27	3.66	3.26	2.97	3.08	2.38	
K[2]O	5.17	5.4	3.86	5.11	5	5.07	5.79	
P[2]O[5]	0.01	0.02	0.17	0.01	0.01	0.01	0.01	
X-ray Fluorescence (ppm)								
Cr	0	0	0	0	0	0	0	
Ni	0	0	0	2.4	0	0	0	
Cu	4.4	0.5	4.9	11.7	0	0	0	
Zn	54.1	57.6	88.9	56.3	53	54.6	88.3	
Rb	166.4	168.3	103.4	164.7	164.5	166.8	149	
Sr	33.6	101	334.7	42.1	41.2	46.7	69.9	
Y	34.1	35.2	33.1	34.1	33.4	32.7	13.4	
Zr	96.5	143	316.7	104.9	93.9	102	117.9	
Nb	20.3	18.8	18.7	19.6	23.8	11.1	13.6	
La	74.6	91.3	145.8	86.6	55	79.1	105	
Ba	160	374.7	887.2	319	161.6	135.6	555.4	

	Post-grouse Canyon tephra sequence (glassy pumice)							
	RM-19R65-4B	RM-19R65-4C-1	RM-19R65-4C-2	RM-19R65-4D-2	RM-19R65-4F	RM-19R65-13A	RM-19R65-20C	RM-19R65-20E
	Weight Percent Oxide (wt. %)							
SiO[2]	76.7	76.59	76.59	75.75	77.21	75.27	76.67	76.92
TiO[2]	0.13	0.13	0.14	0.16	0.12	0.16	0.08	0.08
Al[2]O[3]	13.07	13.17	13.01	13.64	12.79	14.32	12.86	12.99
FeO	0.93	0.97	1	1.27	0.85	1.36	0.82	0.84
MnO	0.05	0.05	0.05	0.05	0.05	0.07	0.08	0.08
MgO	0.08	0.09	0.07	0.2	0.05	0.68	0.04	0.25
CaO	0.65	0.65	0.65	0.67	0.67	0.72	0.51	0.49
Na[2]O	2.47	2.46	2.61	2.68	2.49	2.73	3.65	3.05
K[2]O	5.9	5.87	5.86	5.57	5.76	4.67	5.27	5.29
P[2]O[5]	0.01	0.01	0.01	0.01	0.01	0.01	0	0.01
	X-ray Fluorescence (ppm)							
Cr	0	0	0	0	1.3	0	0	0
Ni	0	0	0	6.7	0	0	0	0
Cu	12.9	8.1	0	55.6	0	13.3	1	0
Zn	32.8	35.4	34.8	40.5	32.7	46.7	49.9	61.4
Rb	154.8	154.1	155.3	160.6	143.3	158	182.2	186.9
Sr	67.4	68.4	66.1	75.2	68.6	83.4	45.4	38
Y	18	20.9	18.1	20.4	23.7	23.1	31.5	30
Zr	118.8	113.6	116.1	130.6	109	147.2	114.2	113.1
Nb	16.7	17.5	14.2	16.5	18.2	10.9	21.3	23.1
La	89.4	63.9	78	76.6	59.5	58.8	61	65.6
Ba	360.4	369.1	377.1	352.3	414.7	183.6	155.2	143.5

APPENDIX 2. (Continued)

Post-grouse Canyon tephra sequence (glassy pumice)								
	RM-19R65-211A	RM-19R65-211B	RM-19R65-211F	RM-19R65-211G	RM-19R65-212A	RM-19R65-212B	RM-19R65-212C	
Weight Percent Oxide (wt. %)								
SiO[2]	77.19	73.85	68.76	66.2	75.92	75.37	75.23	
TiO[2]	0.08	0.27	0.42	0.39	0.1	0.12	0.13	
Al[2]O[3]	12.76	14.25	15.98	17.51	13.35	13.69	13.6	
FeO	0.83	1.57	3.21	3.3	1.1	1.22	1.19	
MnO	0.09	0.04	0.19	0.16	0.08	0.08	0.08	
MgO	0.08	0.25	0.5	0.76	0.05	0.02	0.04	
CaO	0.54	1.27	1.29	2.13	0.5	0.52	0.58	
Na[2]O	3.25	4.08	4.4	5.02	3.48	3.54	3.59	
K[2]O	5.15	4.37	5.16	4.44	5.4	5.43	5.56	
P[2]O[5]	0.01	0.04	0.08	0.08	0	0.01	0.01	
X-ray Fluorescence (ppm)								
Cr	0	0	0	0	0	0	0	
Ni	0	0	4.8	0	0	0	23.7	
Cu	6	0	28.7	0	0	0	0	
Zn	53.7	57.5	113	110.2	53.2	58.8	61.3	
Rb	192.2	177.3	124.8	136.8	154.3	157.5	165.1	
Sr	33.9	74.5	179.6	367.4	17.9	28	46	
Y	36.7	28.1	56	51.8	42	37.8	38.9	
Zr	100.3	162.2	686.1	453.8	148.5	165	171.1	
Nb	22	21.3	21	18.6	27.6	26.1	27.1	
La	41.9	103.2	257	301.5	119.2	129.7	130.2	
Ba	0	214.7	483.9	674.5	11.4	67.5	164.1	

APPENDIX 2. (Continued)

Post-grouse Canyon tephra sequence (glassy pumice)							
	RM-19R65-212F	RM-19R65-212K	RM-19R65-213B	RM-19R65-213C	RM-19R65-221B	RM-19R65-221C	RM-19R65-221E
Weight Percent Oxide (wt. %)							
SiO[2]	75.16	76.73	76.96	76.94	75.16	74.91	76.04
TiO[2]	0.12	0.09	0.09	0.09	0.11	0.14	0.1
Al[2]O[3]	13.67	12.87	12.62	12.81	13.87	13.96	13.12
FeO	1.27	0.89	0.94	0.86	1.24	1.33	1.05
MnO	0.08	0.09	0.09	0.09	0.08	0.08	0.08
MgO	0.03	0.28	0.03	0.1	0.1	0.06	0.03
CaO	0.58	0.5	0.51	0.55	0.59	0.64	0.51
Na[2]O	3.55	3.36	3.36	3.39	3.41	3.54	3.62
K[2]O	5.55	5.17	5.38	5.15	5.42	5.32	5.43
P[2]O[5]	0.01	0.01	0.01	0.01	0.01	0.01	0.01
X-ray Fluorescence (ppm)							
Cr	0	0	0	0	11.3	7.1	6.3
Ni	0	0	0	0	0	0	0
Cu	1.3	0	0	0	0	0	0
Zn	54.7	48.9	47.6	55.8	70.8	61.1	57.4
Rb	158.8	150.6	171.7	187.2	155	149.4	158.4
Sr	30.6	32.9	36	42.6	40.3	38.8	18
Y	40.8	31.3	29.8	42	38.9	36.1	39.4
Zr	174.4	96.4	91.1	118.2	184.7	183.3	145.4
Nb	11.3	20.1	20.5	22.1	20.1	21.7	27
La	116.5	65.9	78.8	78.1	72.6	61.8	18.7
Ba	149.7	158.2	62.4	0	168.8	191	119.7

APPENDIX 2. (Continued)

Post-grouse Canyon tephra sequence (glassy pumice)							
	RM-19R65-22-3-1	RM-19R65-22-3-2	RM-19R65-22-3-3	RM-19R65-22-3-4	RM-19R65-22-3-5	RM-19R65-22-3-6	RM-19R65-22-4-1
Weight Percent Oxide (wt. %)							
SiO[2]	75.5	75.44	76.36	75.9	76.27	75.84	75.39
TiO[2]	0.11	0.12	0.09	0.1	0.1	0.09	0.1
Al[2]O[3]	13.25	13.58	13.14	13.4	13.13	13.42	13.8
FeO	1.16	1.13	1.05	1.15	1.08	1.08	1.14
MnO	0.08	0.08	0.08	0.08	0.08	0.08	0.08
MgO	0.02	0.13	0.05	0.03	0.03	0.07	0.25
CaO	0.8	0.52	0.49	0.52	0.49	0.49	0.51
Na[2]O	3.25	3.4	3.41	3.54	3.53	3.53	3.39
K[2]O	5.81	5.6	5.32	5.26	5.28	5.37	5.31
P[2]O[5]	0.01	0.01	0.01	0.01	0.01	0.01	0.01
X-ray Fluorescence (ppm)							
Cr	3.1	0.4	10.9	3.7	6.1	0	4.6
Ni	5.1	0	1.8	1.3	0	1.8	3.6
Cu	6.4	0	0	0.9	0	0	0
Zn	57.3	62.1	55.8	57.4	64	61.4	62.3
Rb	209.7	164.9	154.2	155.7	158.8	158.2	159.2
Sr	160.7	28.1	15.4	18.5	14.9	14.8	23.5
Y	42.7	40.2	38.8	41.4	43	42.2	40
Zr	169.4	165.5	142.9	158.8	143.1	140.5	164.4
Nb	21.8	26.2	12.6	22.2	21.3	23.6	22.7
La	51.9	64.2	39.4	42.4	35.4	32.6	49.5
Ba	155.4	0	129.8	25.2	115.9	59.9	0

APPENDIX 2. (Continued)

Post-grouse Canyon tephra sequence (glassy pumice)							
	RM-19R65-22-4-2	RM-19R65-22-4-3	RM-19R65-22-4-5	RM-19R65-22-4-6	RM-19R65-23-1-1	RM-19R65-23-1-1	RM-19R65-25-1-1
Weight Percent Oxide (wt. %)							
SiO[2]	75.88	76.13	75.02	76.22	75.06	74.57	77.12
TiO[2]	0.09	0.09	0.1	0.09	0.09	0.12	0.06
Al[2]O[3]	13.4	13.49	13.98	13.37	13.67	13.83	12.89
FeO	1.07	1.05	1.22	1.11	1.17	1.32	0.66
MnO	0.08	0.08	0.08	0.08	0.08	0.08	0.07
MgO	0.17	0.23	0.18	0.25	0.05	0.06	0
CaO	0.51	0.47	0.55	0.49	0.6	0.67	0.61
Na[2]O	3.2	3.26	3.49	3.18	3.97	4.05	3.1
K[2]O	5.57	5.19	5.37	5.19	5.29	5.28	5.47
P[2]O[5]	0.01	0.01	0.01	0.01	0.01	0.01	0.01
X-ray Fluorescence (ppm)							
Cr	4.2	20.2	11.9	13.4	18.8	14	13.9
Ni	0	0	0	0	5.3	0	0
Cu	3.2	0	2.8	17.8	0	0.7	2.2
Zn	53.9	61	57.5	97	66.1	54.9	31.5
Rb	177.2	155.2	153.9	151.9	157.5	151.3	235.1
Sr	19.3	14.8	29.7	17.9	32.3	42.2	24.9
Y	37.9	39.1	39.7	40.4	43.2	40.5	31.7
Zr	149.1	142	165.9	148.4	163.4	182.1	64.6
Nb	25.7	24.6	23.5	25.8	22.9	10.3	15
La	46.9	15.8	53.2	29.8	18	102.7	2.5
Ba	0	88.4	256.2	49.1	41.4	48.3	0

APPENDIX 2. (Continued)

Post-grouse Canyon tephra sequence (glassy pumice)							
RM-19R65-25-1-2	RM-19R65-25-1-3	RM-19R65-7PRA	RM-19R65-7PRG	RM-19R65-13C	RM-19R65-14A	RM-19R65-14B	
Weight Percent Oxide (wt. %)							
SiO[2]	77.68	77.22	77.27	76.8	75.43	75.83	75.37
TiO[2]	0.07	0.06	0.08	0.07	0.14	0.13	0.14
Al[2]O[3]	12.48	12.71	12.56	12.49	14.06	13.23	13.7
FeO	0.7	0.71	0.83	1.04	1.25	1.36	1.24
MnO	0.06	0.06	0.06	0.06	0.13	0.06	0.07
MgO	0	0	0.25	0.16	0.49	0.25	0.37
CaO	0.84	0.83	0.81	0.77	0.82	0.75	0.88
Na[2]O	2.73	3.08	2.92	3.16	2.88	3.11	3.13
K[2]O	5.63	5.51	5.4	5.45	4.99	5.27	5.08
P[2]O[5]	0.01	0.01	0.01	0.01	0.01	0.01	0.01
X-ray Fluorescence (ppm)							
Cr	7.2	8.4	6.5	6	2.6	0	2.4
Ni	0	0	0	5.8	0.2	10.8	0
Cu	0	2.3	60.2	61.4	60.3	65	60
Zn	31.5	27.9	33.3	27.6	45.4	66.2	45.6
Rb	218.7	230.4	198.3	203.1	185.3	195.3	193.6
Sr	37.1	37.4	33.1	53.1	53	97.8	131.3
Y	26.8	25.8	35.6	34.4	48.4	39.3	38.5
Zr	60.3	61.8	81.3	85.6	114.6	132	130
Nb	16.4	17.7	30.7	12.8	26.8	20.7	29.2
La	36	28.9	21.3	20	18.7	24.7	22.2
Ba	0	61.9	175.8	218.7	421.5	377.4	317.5

APPENDIX 2. (Continued)

Post-grouse Canyon tephra sequence (glassy pumice)								
	RM-19R65-20B	RM-19R65-20F	RM-19R65-20G	RM-19R65-211A	RM-19R65-211D	RM-19R65-212D	RM-19R65-212E	
Weight Percent Oxide (wt. %)								
SiO[2]	76.25	76.72	76.57	76.22	71	75.64	76.13	
TiO[2]	0.08	0.08	0.09	0.1	0.42	0.1	0.1	
Al[2]O[3]	13	12.7	12.84	13.02	15.08	13.34	13.39	
FeO	1	0.98	0.77	1.24	2.61	1.13	0.84	
MnO	0.08	0.08	0.08	0.09	0.09	0.08	0.08	
MgO	0.22	0.01	0.19	0.09	0.56	0.05	0.05	
CaO	0.5	0.53	0.5	0.59	1.81	0.5	0.49	
Na[2]O	3.71	3.75	3.65	3.43	3.84	3.77	3.51	
K[2]O	5.14	5.13	5.29	5.2	4.47	5.38	5.39	
P[2]O[5]	0.01	0.01	0.01	0.01	0.12	0.01	0.01	
X-ray Fluorescence (ppm)								
Cr	6.9	0	7.3	4.3	6.9	3.8	0	
Ni	8	3.7	0	9.9	9	0	0	
Cu	63.3	60.5	57	61.6	64	59.6	58.6	
Zn	55.5	52.8	48.6	58.5	79.3	72	52.7	
Rb	192.2	190.7	185.4	187.3	147.4	160.5	164.6	
Sr	53	49	46.8	67.6	249.7	28.2	27.1	
Y	40.1	40.4	40.6	38.3	37.9	39.9	38.1	
Zr	105	92.8	95.6	116.3	279.8	150.4	149.3	
Nb	33	24	27.9	32.6	16.5	23.2	18.6	
La	35.1	59.9	37.7	43.4	82.5	37.4	54.2	
Ba	237	248.1	284	370.1	639.8	168	130.7	

APPENDIX 2. (Continued)

Post-grouse Canyon tephra sequence (glassy pumice)								
	RM-19R65-213E	RM-19R65-213F	RM-19R65-214D	RM-19R65-216J	RM-19R65-216Q	RM-19R65-221D	RM-19R65-221E	
Weight Percent Oxide (wt. %)								
SiO[2]	77.09	76.71	67.53	74.07	72.45	75.65	75.08	
TiO[2]	0.08	0.08	0.39	0.2	0.22	0.11	0.11	
Al[2]O[3]	12.92	12.74	17	14.25	14.39	13.73	13.78	
FeO	0.83	1.16	2.68	1.46	1.33	1.02	1.5	
MnO	0.09	0.08	0.15	0.08	0.09	0.08	0.08	
MgO	0.53	0.1	0.61	0.19	0.25	0.04	0.07	
CaO	0.48	0.52	1.79	0.8	0.92	0.55	0.53	
Na[2]O	3.16	3.53	4.98	3.86	5.36	3.46	3.51	
K[2]O	4.8	5.05	4.86	5.06	4.97	5.35	5.32	
P[2]O[5]	0.01	0.01	0.01	0.02	0.03	0.01	0.01	
X-ray Fluorescence (ppm)								
Cr	8.3	2.6	6.5	0	8.8	16.1	14.8	
Ni	0	20.3	0	0.8	0	0	4.9	
Cu	59.4	59.8	59	61.6	57.4	56.3	62.7	
Zn	68.2	56	103.9	52.6	44.9	52	53.6	
Rb	166.3	180	164.2	157.5	160.7	160.9	170.4	
Sr	47.3	50.9	307.8	97.8	130.7	43	41.6	
Y	41.9	41.1	42.7	34.7	35	46.6	43.6	
Zr	125.5	99.1	505.7	219.2	249.4	185.4	179.1	
Nb	17.5	23.9	16.6	24.6	23.2	34.2	39.8	
La	43.2	44.2	130.4	92.4	58.7	55.2	89.1	
Ba	231.2	231.5	937.7	540.5	683.2	241	286.5	

APPENDIX 2. (Continued)

Post-grouse Canyon tephra sequence (glassy pumice)								
	RM-19R65-224A	RM-19R65-224B	RM-19R65-236A	RM-19R65-236B	RM-19R65-242A	RM-19R65-242E	RM-19R65-251	
Weight Percent Oxide (wt. %)								
SiO[2]	75.89	75.35	77.21	77.41	76.26	76.6	76.36	
TiO[2]	0.09	0.13	0.07	0.07	0.08	0.08	0.09	
Al[2]O[3]	13.26	13.68	12.97	12.45	12.74	12.87	13.25	
FeO	1.07	1.05	0.74	1	1.25	1.27	0.75	
MnO	0.08	0.08	0.07	0.07	0.07	0.07	0.06	
MgO	0.06	0.04	0.09	0.01	0.01	0	0.09	
CaO	0.5	0.59	0.46	0.44	0.49	0.48	0.74	
Na[2]O	3.73	3.55	3	2.76	3.57	2.93	2.88	
K[2]O	5.31	5.51	5.37	5.77	5.51	5.69	5.76	
P[2]O[5]	0.01	0.02	0.01	0.01	0.01	0.01	0.01	
X-ray Fluorescence (ppm)								
Cr	14.2	15.6	22.6	14.5	20.5	10.7	7.5	
Ni	0	0	0	2.4	0.9	0	0	
Cu	58.9	58	56.3	58.9	61	59.6	58.4	
Zn	59.7	52.4	58.8	52.7	57.8	51	23.5	
Rb	172.5	163.2	208.6	200.9	183.2	185.2	275.6	
Sr	30.8	45.7	32.3	23	35.3	35.8	89.3	
Y	41.7	43.3	43.4	46.1	43.8	42.4	31.5	
Zr	159	188	124.6	114.8	138.6	142.1	76.6	
Nb	36.2	36.9	14.2	31.9	28.1	36.5	33.1	
La	32.8	62.9	20.3	34.3	55.5	40	21.9	
Ba	270.6	210	179.7	100.2	19.9	227.7	271.6	

APPENDIX 2. (Continued)

Post-grouse Canyon tephra sequence (bulk tephra)											
	M18-62	M19-10	M19-20	M21-7	M21-27	RM-19I	RM-19P	RM-19P65-19;9	RM-19P65-19;1.5	RM-19P65-23;9	
Weight Percent Oxide (wt. %)											
SiO[2]	75.23	75.45	75.78	72.88	74.75	74.63	74.6	74.88	75.49	74.15	
TiO[2]	0.18	0.19	0.16	0.25	0.17	0.2	0.19	0.23	0.17	0.17	
Al[2]O[3]	13.75	13.65	13.56	15.07	14.31	13.95	13.98	13.82	13.53	14.18	
FeO	1.42	1.58	1.31	1.68	1.35	1.7	1.52	1.88	1.35	1.51	
MnO	0.09	0.08	0.08	0.09	0.08	0.09	0.08	0.09	0.09	0.09	
MgO	0.29	0.16	0.19	0.22	0.22	0.19	0.1	0.02	0.21	0.47	
CaO	1.07	0.95	0.93	0.99	0.74	1.09	1.1	1.02	0.9	0.73	
Na[2]O	3.2	3.36	3.4	3.73	3.4	3.5	3.75	3.38	3.49	3.46	
K[2]O	4.74	4.57	4.56	5.08	4.98	4.63	4.67	4.67	4.75	5.23	
P[2]O[5]	0.03	0.01	0.01	0.02	0.01	0.02	0.01	0.01	0.02	0.01	
X-ray Fluorescence (ppm)											
Cr	0	0	0	0	0	0	0	0	0	0	
Ni	0	0	0	0	0	0	0	0	0	0	
Cu	0	0	0	0	0	16.1	0	2.4	0	0	
Zn	47.5	50.2	44.2	49.5	41	63.1	56	60	57	61.6	
Rb	169.4	164.8	157.7	154.6	157.3	151	155.4	158.6	163.1	152.4	
Sr	187.8	161	151.5	131.3	76.1	191.5	191	170.3	152.5	86.5	
Y	31.4	30.3	27.9	30.3	29.5	30.7	35.4	32.7	33	38.9	
Zr	160.1	183.4	165.5	261	197.8	201	192.7	207.4	167.1	189.9	
Nb	18.6	18.4	16	28	23.9	10.7	7.4	3.7	16.2	21.7	
La	0	0	0	0	0	0	0	0	0	0	
Ba	539.8	451.4	479.2	463.9	390.2	241.1	282.8	190	158.6	146.3	

APPENDIX 2. (Continued)

Post-grouse Canyon tephra sequence (bulk tephra)							
	RM-19P65-23;4	RM-19P65-23;0	RM-19P65-24;27	RM-19P65-24;15	RM-19P65-24;7	RM-19P65-24;1.5	RM-19P65-24A;7
Weight Percent Oxide (wt. %)							
SiO[2]	73.78	73.82	77.18	77	76.5	76.12	77.48
TiO[2]	0.19	0.2	0.08	0.09	0.12	0.14	0.1
Al[2]O[3]	14.31	14.22	12.61	12.68	12.98	13.05	12.38
FeO	1.64	1.62	1.11	1.04	1.18	1.4	1.02
MnO	0.1	0.1	0.07	0.08	0.08	0.08	0.07
MgO	0.45	0.41	0.12	0.07	0.09	0.14	0.16
CaO	0.76	0.75	0.45	0.51	0.57	0.65	0.51
Na[2]O	3.47	3.69	3.06	3.21	3.23	3.23	3.13
K[2]O	5.28	5.17	5.31	5.31	5.24	5.18	5.14
P[2]O[5]	0.02	0.02	0.01	0.01	0.01	0.01	0.01
X-ray Fluorescence (ppm)							
Cr	0	0	0	0	0	0	0
Ni	0	0	0	0	0	0	0
Cu	11.3	5.9	1.7	0	0	22.6	0
Zn	64	71.1	62	57.5	59.3	62.6	56.9
Rb	152.5	151.2	171.5	172.9	171.9	173.2	172.1
Sr	92.2	95.2	19.4	37.2	48.1	66.7	30.9
Y	41.1	34.8	43.3	42.5	38.8	39.5	43.7
Zr	216.8	212.1	130.9	138.5	134.2	154.6	130.9
Nb	16.6	15.9	24.8	22.5	18.6	27.2	28.2
La	0	0	0	0	0	0	0
Ba	57.1	69.2	0	188.2	0	69.8	45.4

APPENDIX 2. (Continued)

Post-grouse Canyon tephra sequence (bulk tephra)							
	RM-19P65-24A;7	RM-19P65-24A;2	RM-19P61-3;12	RM-19P61-3;6	RM-19P61-3;0	RM-19P61-2;8	RM-19P61-2;2
Weight Percent Oxide (wt. %)							
SiO[2]	77.3	75.5	76.72	77.3	76.82	77.71	77.39
TiO[2]	0.09	0.23	0.08	0.08	0.12	0.07	0.08
Al[2]O[3]	12.41	12.78	12.95	12.59	12.86	12.53	12.59
FeO	1.11	1.98	0.93	0.83	1.05	0.8	0.94
MnO	0.07	0.08	0.06	0.06	0.07	0.06	0.06
MgO	0.2	0.49	0.34	0.13	0.14	0.02	0.01
CaO	0.49	1.02	0.59	0.6	0.68	0.58	0.61
Na[2]O	3.24	3.08	2.85	2.96	2.86	2.99	3.12
K[2]O	5.08	4.82	5.47	5.43	5.38	5.23	5.2
P[2]O[5]	0.01	0.02	0.01	0.02	0.02	0.01	0
X-ray Fluorescence (ppm)							
Cr	0	0	0	0	0	0	0
Ni	0	30.9	0	0	54.4	0	2.7
Cu	9.4	8.8	7.4	0	0	0	2.4
Zn	57.1	63.9	33.1	35.6	35.9	35.1	29.7
Rb	167.8	160.2	190.1	183.2	190.9	190.7	185.1
Sr	23.4	86	44.1	37.4	55.8	24.9	28.5
Y	41.5	42.2	30.5	30.6	30.8	32	22
Zr	122.1	133.1	89.1	87.4	92.6	77.9	84.6
Nb	28.1	26.9	15.5	14	12.4	12.1	21.8
La	0	0	0	0	0	0	0
Ba	0	18.1	0	0	17.5	0	0

	Post-grouse Canyon tephra sequence (bulk tephra)							
	RM-19P61-2;6	RM-19P61-1;25	RM-19P61-1;20	RM-19P61-1;10.	RM-19P61-1;6	RM-19P61-1;3	RM-19P61-1;0.	RM-19P61-0;6
	Weight Percent Oxide (wt. %)							
SiO[2]	77.85	77.36	77.53	76.65	75.94	77.33	77.1	76.88
TiO[2]	0.07	0.09	0.09	0.12	0.17	0.1	0.1	0.09
Al[2]O[3]	12.57	12.72	12.6	13.06	13.49	12.58	12.8	13.48
FeO	0.69	0.82	0.93	1.15	1.34	0.91	0.93	0.93
MnO	0.06	0.06	0.06	0.06	0.07	0.06	0.06	0.06
MgO	0	0.05	0.05	0.16	0.23	0.07	0.08	0
CaO	0.56	0.61	0.59	0.75	0.77	0.66	0.65	0.58
Na[2]O	3.05	2.97	2.9	2.96	2.93	3.1	3.08	2.74
K[2]O	5.15	5.31	5.25	5.08	5.04	5.18	5.19	5.23
P[2]O[5]	0	0.01	0	0.01	0.02	0.01	0.01	0.01
	X-ray Fluorescence (ppm)							
Cr	0	0	0	0	0	0	0	0
Ni	0	9.3	1.6	31.5	6.1	5.7	6.3	3
Cu	0	0	0	0	0	0	0	0
Zn	24.1	23.6	28.6	27.2	30.7	26.5	29.5	23.9
Rb	186.9	182.7	180.8	167.2	166.2	169.3	179.1	175.3
Sr	14.5	37.9	37.1	64.5	85.6	43.2	43.8	22.6
Y	28.1	19.2	21.6	29.2	32.8	28.3	28.6	23.9
Zr	77.7	95	99.8	93.6	114.5	94.7	98.8	87
Nb	20.9	19.3	23.1	16.7	15.4	18	20	18.3
La	0	0	0	0	0	0	0	0
Ba	68.7	75.3	0	166.7	154.1	191.6	75.8	178.8

APPENDIX 2. (Continued)

Post-grouse Canyon tephra sequence (bulk tephra)		
	RM-19P61-0;3	RM-19P61-0;0.5
Weight Percent Oxide (wt. %)		
SiO[2]	75.47	74.04
TiO[2]	0.14	0.17
Al[2]O[3]	14.08	15.04
FeO	1.15	1.52
MnO	0.06	0.07
MgO	0.18	0.27
CaO	0.74	0.75
Na[2]O	3.2	3.48
K[2]O	4.97	4.65
P[2]O[5]	0.01	0.01
X-ray Fluorescence (ppm)		
Cr	0	0
Ni	6.4	12.1
Cu	0	1.4
Zn	27.3	37
Rb	171.8	166.3
Sr	63.1	71.4
Y	27.3	26.9
Zr	102	119
Nb	17.3	15.2
La	0	0
Ba	54.1	12.1

APPENDIX 2. (Continued)

	Pre-rainier Mesa tephra sequence (bulk tephra)							
	17A;1	17A;13	17A;12	17A;11	17A;7	17A;2	17A;24	17B;11
	Weight Percent Oxide (wt %)							
SiO_2	69.47	69.35	68.72	69.85	70.4	70.67	74.12	70.78
TiO_2	0.37	0.54	0.59	0.48	0.38	0.35	0.22	0.4
Al_2O_3	16.17	15.98	17.09	15.85	15.61	15.65	14.39	15.69
FeO	2.25	3.21	3.03	2.66	2.07	2.02	1.19	1.71
MnO	0.08	0.13	0.14	0.12	0.08	0.08	0.12	0.11
MgO	0.77	1.11	1	1.09	0.84	0.76	0.37	0.45
CaO	2.01	1.7	1.44	1.64	1.9	1.7	0.49	1.06
Na_2O	3.81	3.54	3.6	3.76	3.63	3.63	3.49	3.52
K_2O	5.04	4.41	4.35	4.51	5.05	5.1	5.61	6.21
P_2O_5	0.03	0.03	0.04	0.03	0.03	0.03	0.01	0.05
	X-ray Fluorescence (ppm)							
Cr	1.31	0	0	0	0	0	0	2.63
Ni	6.81	1	1.43	6.83	0	4.78	0	16.82
Cu	0.54	0	0	0	0	0	0	0
Zn	47.92	79.61	72.6	73.59	44.23	48.37	66.42	62.37
Rb	133.89	136.16	122.75	146.71	145.33	153.02	165.66	158.98
Sr	380.09	292.72	313.53	280.41	337.39	303.5	72.69	121.18
Y	32.27	36.58	38.99	41.98	32.37	28.58	38.04	31.21
Zr	246.13	359.2	545.62	339.97	244.87	245.04	239.64	359.31
Nb	6.6	20.62	20.16	17.45	13.03	22.1	24.45	12.36
La	94.42	73.39	110.98	67.49	73.03	71.73	66.12	68.15
Ba	1187.88	838.01	1980.01	791.4	938.75	951.97	281.2	823.67
	Instrumental Neutron Activation Analyses (ppm)							
As			2.76	5.09		3.93	3.46	1.9
La			98.47	64.68		66.54	51.37	123.17
Lu			0.46	0.52		0.37	0.52	0.43
Mo			3.74	3.54		3.32	6	3.41
Sm			11.61	9.61		8.16	8.97	13.03
U			2.5	3.37		3.08	3.89	2.48
Yb			3.82	3.19		2.63	3.4	3.02
Ba			1767.74	720.6		1062.51	460.63	1199.04
Ce			208.43	124.54		122.13	99.61	229.4
Cs			4.03	5.09		4.33	4.46	3.8
Cr			6.63	13.36		7.42	2.21	4.01
Eu			2.4	1.23		1.33	0.82	2.56
Hf			13.93	9.82		7.39	8.39	10.31
Nd			63.31	49.76		38.18	34.66	132.42
Sc			6.7	5.75		4.48	2.42	6.07
Ta			1.18	1.38		1.2	1.6	1.24
Tb			1.26	1.33		0.92	1.19	1.3
Th			21.82	20.55		19.09	23.2	20.92
Zn			78.26	87.39		62.32	81.73	88.13

APPENDIX 2. (Continued)

	Pre-rainier Mesa tephra sequence (bulk tephra)							
	17B;7	17B;5.5	17B;4.5	17B;3.5	17B;2	17B;0	16;2	15;0
	Weight Percent Oxide (wt %)							
SiO_2	70.64	72.13	72.36	71.88	70.35	67.09	74.98	73.21
TiO_2	0.45	0.35	0.32	0.37	0.45	0.59	0.24	0.3
Al_2O_3	15.74	15.29	15.28	15.2	15.7	16.87	13.51	14.35
FeO	1.88	1.55	1.61	2.01	2.2	3.24	1.25	1.58
MnO	0.11	0.1	0.1	0.09	0.1	0.09	0.07	0.07
MgO	0.45	0.49	0.52	0.44	0.64	1.05	0.33	0.53
CaO	0.98	0.81	0.82	1.08	1.36	2.52	0.74	0.9
Na_2O	3.57	3.29	3.24	3.34	3.54	3.52	3.2	3.55
K_2O	6.11	5.95	5.71	5.55	5.59	4.9	5.65	5.51
P_2O_5	0.05	0.02	0.03	0.04	0.05	0.12	0.01	0.01
	X-ray Fluorescence (ppm)							
Cr	0	0	4.85	0	0	11.87	0	0
Ni	0	4.42	7.35	0	0	1.72	0	0
Cu	4.06	0	0	3.1	0	16.04	0	0
Zn	69.47	54.25	67.52	73.57	72.27	65.88	1247.1	47.14
Rb	167.43	177.46	177.33	164.18	157.19	145.3	176.4	174.6
Sr	121.22	96.19	101.26	143.94	168.38	395.08	72.9	105.89
Y	36.1	34.18	32.31	37.5	32.99	34.19	33.88	39.51
Zr	394.55	323.96	269.87	295.59	356.91	293	188.99	207.19
Nb	7.24	24.29	23.44	18.07	17.88	16.84	25.91	22.71
La	90.17	92.57	53.74	60.61	88.41	60.64	60.24	75.97
Ba	857.44	677.04	444.23	427.27	529.5	768.04	254.61	358.32
	Instrumental Neutron Activation Analyses (ppm)							
As		2.27		4.16		5.15		4.49
La		113.4		102.05		99.19		66.02
Lu		0.47		0.51		0.42		0.52
Mo		3.6		4.74		4.77		4.4
Sm		11.53		12.01		11.14		9.48
U		3.03		3.96		3.67		4.13
Yb		2.77		3.22		2.76		3.57
Ba		887.16		709.33		1104.34		454.15
Ce		218.6		185.1		189.39		121.33
Cs		4.09		4.57		5.11		4.91
Cr		4.17		6.25		17.19		5.02
Eu		1.89		1.56		2.04		1.14
Hf		9.82		8.58		9.09		6.83
Nd		83.79		119.81		104.97		49.56
Sc		4.73		4.23		7.59		3.62
Ta		1.33		1.46		1.36		1.68
Tb		1.16		1.4		1.15		1.05
Th		22.49		22.96		23.45		22.52
Zn		83.77		56.44		110.14		45.13

APPENDIX 2. (Continued)

	Pre-rainier Mesa tephra sequence (bulk tephra)							
	14;7	14;5.5	14;4	14;1.5	13;18.5	13;9	13;3.5	13;0.5
	Weight Percent Oxide (wt %)							
SiO_2	72.24	71.93	72.41	72.01	71.62	71.86	72.33	72.27
TiO_2	0.4	0.39	0.36	0.38	0.29	0.3	0.28	0.29
Al_2O_3	14.38	14.57	14.74	14.6	15.94	15.97	15.65	15.4
FeO	2.15	2.05	1.92	2.18	1.5	1.5	1.44	1.51
MnO	0.08	0.09	0.08	0.09	0.08	0.08	0.08	0.09
MgO	0.78	0.71	0.69	0.81	0.32	0.56	0.44	0.48
CaO	1.4	1.4	1.33	1.5	1.1	0.97	0.96	1.01
Na_2O	3.51	3.68	3.25	3.34	3.29	3.15	3.29	3.41
K_2O	5.03	5.13	5.17	5.03	5.81	5.57	5.51	5.51
P_2O_5	0.03	0.04	0.03	0.05	0.04	0.04	0.02	0.03
	X-ray Fluorescence (ppm)							
Cr	3.34	0	9.08	0	0	4.58	19.41	7
Ni	0	0	1.54	0.92	0	0	0	0
Cu	21.44	7.31	5.84	0	5.86	0	2.9	4.31
Zn	139.65	85.87	58.81	57.04	56.37	59.71	53.96	57.4
Rb	160.12	160.59	158.28	149.97	173.54	174.4	176.71	163.49
Sr	193.83	187.47	168.99	207.48	148.52	123.17	111.7	126.55
Y	38.09	41.06	36.34	40.32	36.66	39.45	31.8	35.8
Zr	216.47	210.87	187.56	197.36	222.36	229.57	223.96	228.03
Nb	22.35	20.9	26.55	12.18	29.22	26.26	23.61	7.41
La	57.13	88.89	61.01	70.52	53.69	85.14	55.3	58.33
Ba	453.86	292.34	68.85	342.12	327.27	292.3	5.61	157.67
	Instrumental Neutron Activation Analyses (ppm)							
As	4.45		4.83			3.85	3.33	
La	58.34		60.8			70.12	63.93	
Lu	0.47		0.46			0.5	0.46	
Mo	4.46		6.76			3.62	3.66	
Sm	9.19		8.99			10.19	8.93	
U	4.05		3.76			3.66	3.95	
Yb	3.22		3.12			3.23	3.04	
Ba	397.907		504.92			468.99	512.16	
Ce	110.69		116.69			145.29	129.9	
Cs	5.19		4.85			5.64	5.56	
Cr	12.62		8.86			4.44	2.65	
Eu	1.1		1.16			1.22	1.21	
Hf	7.15		6.46			7.62	7.73	
Nd	91.82		41.69			46.66	39.56	
Sc	4.71		4.55			3.51	3.42	
Ta	1.46		1.43			1.8	1.45	
Tb	1.29		1.16			1.14	1.12	
Th	21.31		20.54			23.64	23.76	
Zn	144.79		78.93			48.35	70.8	

APPENDIX 2. (Continued)

	Pre-rainier Mesa tephra sequence (bulk tephra)							
	12;26	12;22	12;18	12;15	12;13	12;7.5	12;1.75	12;0
	Weight Percent Oxide (wt %)							
SiO_2	72.51	72.26	72.17	71.24	70.4	71.44	69.9	70.46
TiO_2	0.34	0.35	0.34	0.36	0.43	0.37	0.46	0.43
Al_2O_3	14.92	14.94	15.12	15.57	16.12	15.43	16.07	15.76
FeO	1.72	1.88	1.75	1.96	2.37	2.14	2.76	2.64
MnO	0.09	0.08	0.09	0.09	0.1	0.1	0.1	0.1
MgO	0.59	0.72	0.7	0.82	1.14	0.88	0.8	0.68
CaO	1.14	1.34	1.28	1.31	1.28	1.3	1.55	1.42
Na_2O	3.4	3.43	3.46	3.63	3.51	3.47	3.63	3.64
K_2O	5.26	4.97	5.06	4.98	4.62	4.82	4.69	4.85
P_2O_5	0.03	0.02	0.03	0.03	0.03	0.03	0.03	0.03
	X-ray Fluorescence (ppm)							
Cr	11.12	7.22	9.73	10.02	23.38	5.11	1.18	0
Ni	0	0	0	0	20.03	4.25	4.96	7.02
Cu	2.03	3.64	0	12.23	9.46	1.57	0	0
Zn	57.52	53.9	53.65	63.48	69.07	56.68	91.18	77.43
Rb	150.42	155.34	147.18	155.41	156.61	151.47	133.95	132.94
Sr	146.01	173.28	166.42	175.48	169.53	171.18	201.81	177.25
Y	35.75	34.47	39.61	38.47	46.44	46.58	53.6	56.9
Zr	223.8	214.43	217.66	233.28	271.78	210.71	257.91	243.5
Nb	28.36	34.82	29.97	24.99	18.89	19.08	22.78	17.06
La	44.7	57.86	63.3	66.2	64.9	14.82	43.51	35.44
Ba	138.57	162.83	278.79	207.79	165.81	25.83	135.72	177.66
	Instrumental Neutron Activation Analyses (ppm)							
As		3.39	3.79	4.07	3.89	4.67		
La		62	62.39	70.22	75.27	59.4		
Lu		0.5	0.5	0.47	0.58	0.54		
Mo		5.07	5.17	4.07	3.86	4.39		
Sm		9.86	9.87	9.52	12.5	10.2		
U		4.66	4.15	3.3	3.52	3.89		
Yb		3.31	3.18	3.09	3.94	3.68		
Ba		411.04	510.96	429.12	466.51	396.33		
Ce		127.81	128.65	132.25	160.56	126.82		
Cs		4.68	4.98	4.84	5.61	5.76		
Cr		9.97	9.35	8.96	10.72	11.09		
Eu		1.26	1.34	1.22	1.51	1.05		
Hf		7.31	7.56	7.84	9.38	7.3		
Nd		108.31	44.74	50.54	58.51	47.05		
Sc		4.46	4.4	4.44	5.46	4.8		
Ta		1.52	1.31	1.55	1.63	1.7		
Tb		1.07	1.4	1.08	1.41	1.18		
Th		21.3	22.18	21.29	24.74	24.21		
Zn		70.17	79.08	58.95	71.23	81.57		

APPENDIX 2. (Continued)

	Pre-rainier Mesa tephra sequence (bulk tephra)							
	3;200	3;188	3;156	3;120	3;58	3;3	2;30	1;129
	Weight Percent Oxide (wt %)							
SiO_2	77.01	77.24	76.11	76.7	76.88	76.39	77.52	78.24
TiO_2	0.1	0.11	0.15	0.21	0.19	0.22	0.1	0.11
Al_2O_3	13.09	12.79	13.42	12.88	12.74	12.95	12.66	12.13
FeO	0.72	0.73	0.95	1.3	1.16	1.37	0.71	0.71
MnO	0.07	0.07	0.07	0.06	0.07	0.07	0.06	0.07
MgO	0.64	0.71	0.96	0.78	0.44	0.68	0.2	0.15
CaO	0.48	0.5	0.62	0.74	0.68	0.7	0.44	0.49
Na_2O	3	2.94	3.09	3.02	3.16	3.17	3.42	3.23
K_2O	4.88	4.89	4.63	4.29	4.67	4.43	4.88	4.86
P_2O_5	0.01	0.01	0.01	0.02	0.02	0.02	0.01	0.01
	X-ray Fluorescence (ppm)							
Cr	0	0	0	0	0	0	0	0
Ni	0	0	0	0	0	6.73	1.29	0
Cu	0	0	0	0	0	0	0	0
Zn	39.15	30.72	32.33	43	45.9	52.17	20.59	22.39
Rb	238.96	224.6	212.13	198.82	226.11	213.74	246.52	235.4
Sr	17.71	22.37	51.18	83.2	68.72	76.33	14.69	15.99
Y	23.77	21.13	21.97	25.03	30.81	32.93	28.32	32.26
Zr	88.81	78.99	102.05	115.25	107.49	133.08	80.72	80.61
Nb	28.11	26.63	28.79	27.5	26.32	24.19	23.55	21.64
La	15.51	31.46	31.28	34.51	18.59	51.76	9.69	40.53
Ba	33.99	117.07	185.67	219.36	267.5	195.87	0	80.66
	Instrumental Neutron Activation Analyses (ppm)							
As		4.35				5.18		6.23
La		24.52				30.63		21.3
Lu		0.41				0.47		0.49
Mo		6.78				6.8		9.22
Sm		4.09				4.65		3.97
U		4.62				5.74		6.4
Yb		2.41				2.84		2.9
Ba		219.25				334.96		175.78
Ce		51.98				61.1		47.31
Cs		4.83				11.01		9.95
Cr		2.2				6.47		2.51
Eu		0.17				0.34		0.13
Hf		3.34				4.67		3.67
Nd		13.76				41.83		13
Sc		2.89				4.26		3.65
Ta		1.95				2.29		2.43
Tb		0.73				1.1		0.68
Th		20.24				19.96		17.71
Zn		39.03				65		34.77

APPENDIX 2. (Continued)

	Pre-rainier Mesa tephra sequence (bulk tephra)							
	1;117	1;94	1;78	1;54	1;31	1;18	1;14	1;1
	Weight Percent Oxide (wt %)							
SiO_2	77.7	77.27	77.07	76.77	77.91	77.15	77.89	77.26
TiO_2	0.11	0.12	0.14	0.15	0.12	0.17	0.16	0.18
Al_2O_3	12.49	12.77	12.86	12.84	12.33	12.69	12.26	12.51
FeO	0.74	0.86	0.81	1	0.93	1.1	1.09	1.26
MnO	0.06	0.06	0.06	0.07	0.06	0.07	0.04	0.05
MgO	0.27	0.24	0.29	0.32	0.24	0.54	0.36	0.43
CaO	0.47	0.52	0.53	0.6	0.56	0.67	0.64	0.65
Na_2O	3.33	3.32	3.41	3.54	3.19	3.1	3.01	3.15
K_2O	4.81	4.84	4.81	4.7	4.64	4.48	4.53	4.49
P_2O_5	0.01	0.01	0.01	0.01	0.01	0.03	0.02	0.02
	X-ray Fluorescence (ppm)							
Cr	0	0	0	0	0	16.05	0	0
Ni	6.14	29.4	6.8	8.4	8.58	0	5.73	6.99
Cu	0	1.66	0	0	0.21	0	0	12.96
Zn	26.75	74.71	283.55	1134.93	26.36	35.77	22.97	692.77
Rb	224.86	237.02	233.02	224.24	211.82	185.87	176.76	179.59
Sr	15.15	30.42	31.6	46.63	36.49	85.05	68.69	85.59
Y	29.64	30.18	28.49	31.27	22.56	30.82	20.05	21.03
Zr	78.78	91.76	86.81	82.4	78.57	100.65	86.6	99.38
Nb	22.52	20.94	19.46	18.55	20.03	15.11	16.96	15.06
La	51.74	40.7	73.84	45.2	35.21	8.31	47.42	42.92
Ba	82.84	94.63	0	34.14	19.87	37.8	118.68	192.36
	Instrumental Neutron Activation Analyses (ppm)							
As	5.44	5.63	5.3		6.02			3.54
La	22.7	21.21	22.69		20.75			23.34
Lu	0.51	0.48	0.47		0.46			0.36
Mo	9.71	9.26	9.18		8.44			6.15
Sm	4.18	3.98	4.17		3.57			3.61
U	6.04	6.49	6.31		6.23			4.59
Yb	2.96	3.28	2.98		2.71			2.53
Ba	144.43	199.55	271.7		65.65			288.61
Ce	52.45	49.83	51.34		46.23			50.43
Cs	9.84	11.34	11.32		9.86			12.99
Cr	2.41	1.52	2.5		3.64			8.59
Eu	0.19	0.19	0.2		0.19			0.31
Hf	3.58	3.62	3.77		3.55			3.47
Nd	17.04	11.42	9.11		9.01			14.45
Sc	3.71	3.86	3.98		3.51			3.65
Ta	2.51	2.45	2.51		2.25			1.9
Tb	1.04	0.92	0.81		0.53			0.68
Th	19.85	18.12	19.28		16.89			16.58
Zn	38.53	31.52	25.49		35.65			58.53

APPENDIX 2. (Continued)

	Pre-rainier Mesa tephra sequence (bulk tephra)					
	592-802-3	592-802-23	592-802-40	592-802-33	292-802-70	592-802-13
	Weight Percent Oxide (wt %)					
SiO_2	73.3	72.3	72.95	73.36	76.03	72.48
TiO_2	0.16	0.19	0.14	0.15	0.13	0.19
Al_2O_3	13.08	13.06	12.79	12.7	12.42	13.05
FeO	1.02	1.28	0.9	1.01	0.84	1.26
MnO	0.07	0.07	0.06	0.07	0.07	0.07
MgO	0.73	0.84	0.56	0.66	0.21	0.83
CaO	0.65	0.71	0.58	0.6	0.57	0.69
Na_2O	2.82	2.99	3.04	3.13	3.15	2.83
K_2O	4.71	4.62	4.91	4.69	4.89	4.61
P_2O_5	0.04	0.02	0.02	0.02	0.02	0.02
	X-ray Fluorescence (ppm)					
Cr	48.03	48.43	44.58	48.68	21.74	36.55
Ni	0	0	0	0	0	0
Cu	0	0	0	0	0	0
Zn	26.04	27.21	24.64	22.15	26.46	33.1
Rb	232.42	237.22	250.33	231.89	248.64	229.56
Sr	64.2	85.52	51.99	46.65	26	69.01
Y	22.64	19.3	21.74	18.61	28.93	24.3
Zr	92.15	113.51	90.67	82.67	72.74	104.66
Nb	15.75	16.07	14.76	11.34	16.49	15.32
La	33.12	25.28	18.81	13.47	34.5	36.43
Ba	154.97	232.53	170.5	111.68	191.59	203.28
					Instrumental Neutron Activation Anal	
As						
La						
Lu						
Mo						
Sm						
U						
Yb						
Ba						
Ce						
Cs						
Cr						
Eu						
Hf						
Nd						
Sc						
Ta						
Tb						
Th						
Zn						

APPENDIX 2. (Continued)

	Pre-rainier Mesa tephra sequence (glassy pumice)							
	2B	2D	3A	6D	7E	7F	8A	11A
	Weight Percent Oxide (wt %)							
SiO_2	77.39	77.23	77.54	74.08	69.99	75.15	77.84	75.68
TiO_2	0.09	0.09	0.09	0.23	0.34	0.2	0.19	0.16
Al_2O_3	12.8	12.88	12.76	13.99	16.31	13.55	12.3	13.57
FeO	0.56	0.6	0.48	1.63	1.44	1.13	0.91	0.89
MnO	0.07	0.07	0.07	0.13	0.14	0.09	0.08	0.12
MgO	0.07	0.17	0.11	1.15	2.73	0.7	0.65	0.31
CaO	0.41	0.42	0.41	0.57	1.33	0.54	0.44	0.3
Na_2O	3.4	3.42	3.46	3.3	3.79	3.32	2.81	3.13
K_2O	5.19	5.09	5.05	4.9	3.49	5.3	4.76	5.85
P_2O_5	0.01	0.02	0.02	0.02	0.43	0.01	0.01	0.01
	X-ray Fluorescence (ppm)							
Cr	5.9	11.2	9.2	10.6	23.5	18.1	17.1	0
Ni	0	6.9	1.3	4.2	0	0	0	0
Cu	56.7	58.5	57.5	61.8	59.7	58.1	56.9	57.2
Zn	55.6	34.2	44.3	74.6	76	61.6	51.5	63.5
Rb	290.5	282	283.5	207.5	126.7	204	184	191.8
Sr	19.7	23	15.5	75.4	131.7	61	38.4	24.6
Y	41.1	37.2	36.9	41.1	55.4	35.5	39.8	48.9
Zr	68.1	65.6	62.4	218.2	292.4	195.4	150.9	204.6
Nb	30.4	26.3	30.5	24.5	18.5	23.9	26.6	25.1
La	29.2	0.2	14	71.5	91.5	40.5	34.9	16.3
Ba	202.3	240.5	82.3	280	1106.1	385.6	159.4	138.5
	Instrumental Neutron Activation Analyses (ppm)							
As	6.23	7.11	655	4.37	10.22	2.72	2.66	3.45
La	16.81	17.4	16.85	45.97	102.1	45.51	36.14	32.71
Lu	0.49	0.55	0.56	0.53	0.61	0.45	0.49	0.5
Mo	9.83	11.93	10.57	4.95	3.27	5.91	6.95	5.26
Sm	3.65	3.77	3.74	8.34	12.34	7.25	7.44	6.56
U	8.81	8.06	7.39	3.96	2.5	3.92	4.7	4.31
Yb	3.57	3.81	3.73	3.33	4.72	2.87	3.22	3.3
Ba	170.27	180.39	185.72	157.8	997.95	353.53	129.58	104.84
Ce	37.94	38.62	41.67	96.98	158.62	84.77	82.52	68.33
Cs	10.66	11.4	8.2	5.2	2.72	4.4	5	5
Cr	2.34	2.46	2.36	4.78	2.88	2.34	2.49	1.01
Eu	0.09	0.12	0.12	0.61	1.86	0.79	0.49	0.34
Hf	3.22	3.13	3.3	7.69	8	6.85	5.78	8.03
Nd	8.09	6.5	6.88	28.44	58.81	28.09	25.44	23.37
Sc	3.73	3.9	3.97	2.76	4.29	2.56	2.37	1.78
Ta	2.59	2.58	2.68	1.58	1.3	1.31	1.62	1.74
Tb	0.76	0.96	0.88	1.11	1.27	1.02	1.16	0.98
Th	17.75	17.49	18.63	26.89	21.4	23.22	23.52	26.39
Zn	24.87	14.57	39.53	72.75	56.16	64.66	47.21	76.97

APPENDIX 2. (Continued)

	Pre-rainier Mesa tephra sequence (glassy pumice)						
	11F	12F	14B	15A	16A	17G	17H
	Weight Percent Oxide (wt %)						
SiO_2	75.88	73.51	73.81	74.67	73.87	72.49	75.84
TiO_2	0.16	0.26	0.28	0.23	0.25	0.27	0.17
Al_2O_3	13.28	14.46	14.44	13.86	14.48	14.87	13.08
FeO	0.79	1.37	1.24	1.04	1.26	1.28	1
MnO	0.12	0.08	0.09	0.08	0.09	0.13	0.11
MgO	0.16	0.55	0.48	0.31	0.37	0.39	0.13
CaO	0.3	0.82	0.75	0.65	0.68	0.66	0.32
Na_2O	3.48	3.16	3.02	3.06	2.97	3.96	3.58
K_2O	5.83	5.78	5.86	6.07	5.99	5.92	5.75
P_2O_5	0.01	0.01	0.02	0.02	0.03	0.03	0.01
	X-ray Fluorescence (ppm)						
Cr	0.3	0	0	0	2.1	0	2.6
Ni	0	0	0	0	0	0	0
Cu	57	58.1	58.1	57.4	57.9	56.4	57.2
Zn	63.9	50.8	44.4	55.5	42	64.9	74.1
Rb	187.3	207.8	192	203.2	192.3	167.2	187.6
Sr	21.5	102	79.8	63	60.8	74.8	25.4
Y	44.3	48.1	41.5	43.5	47.7	55	47.1
Zr	213.1	222.5	209.2	193.8	187.2	318.9	202.5
Nb	26.7	26.5	22.3	24.2	21.7	22.3	24.8
La	0	29.3	29.7	19.3	31.2	12.5	35.1
Ba	83	436.5	344.5	189.6	205.3	282.3	115.8
	Instrumental Neutron Activation Analyses (ppm)						
As	3.34	3.98	3.97	3.81	3.54	3.76	3.74
La	34.4	67.86	52.67	61.87	60.88	50.34	40.91
Lu	0.5	0.5	0.49	0.48	0.49	0.52	0.54
Mo	6.98	4.1	4.87	6.92	5.27	4.89	7.74
Sm	6.57	9.59	7.48	8.72	8.99	13.25	7.54
U	4.18	3.89	4.19	4.22	4.19	3.45	4.48
Yb	3.37	3.17	3.35	3.76	3.27	3.57	3.62
Ba	116.45	389.63	303.14	335.9	321.39	367.84	184.28
Ce	76.8	119.71	101.11	117.26	114.71	119.34	73.43
Cs	4.86	5.02	4.8	4.85	4.47	4.16	4.93
Cr	1.54	2.64	2.39	2.62	3.32	4.6	2.29
Eu	0.39	1.17	0.86	1.02	1	0.81	0.44
Hf	8	7.15	6.24	6.21	6.29	9.29	7.65
Nd	18.41	36.27	35.85	32.92	73.6	49.22	22.9
Sc	1.77	3.31	3.02	2.98	2.86	2.25	1.82
Ta	1.51	1.43	1.33	1.5	1.53	1.42	1.49
Tb	1.25	1.12	0.85	1.08	1.25	1.63	1.17
Th	25.12	23.55	21.39	23.57	23.18	20.82	24.79
Zn	68.55	72.77	60.58	40.45	45.69	80.41	85.25

	Pre-ammonia Tanks tephra sequence (glassy pumice)										
	WW8-1-A	WW8-1-B	WW8-1-C	WW8-1-D	WW8-1B-A	WW8-1B-B	WW8-1B-C	WW8-1B-D	WW8-2A	WW8-2C	WW8-2D
	Weight Percent Oxide (wt. %)										
SiO_2	77.42	72.24	76.87	77.1	73.05	76.61	76.48	77.05	76.63	74.72	73.79
TiO_2	0.17	0.35	0.11	0.11	0.32	0.15	0.09	0.08	0.17	0.22	0.3
Al_2O_3	12.34	15.58	13.08	12.81	14.68	12.65	13.21	12.7	12.84	13.86	14.34
FeO	0.81	1.69	0.82	0.62	1.4	0.9	0.49	0.87	0.74	1.15	1.17
MnO	0.04	0.1	0.07	0.06	0.11	0.1	0.06	0.06	0.06	0.08	0.11
MgO	0.24	0.46	0.14	0.07	0.23	0	0	0	0.11	0.13	0.2
CaO	0.53	0.76	0.55	0.47	0.79	0.25	0.49	0.63	0.68	0.83	0.72
Na_2O	2.63	3.13	2.67	2.89	3.14	3.17	3.55	3.12	3.01	3.14	3
K_2O	5.8	5.66	5.69	5.85	6.27	6.17	5.61	5.48	5.73	5.85	6.36
P_2O_5	0.01	0.03	0.01	0	0.02	0	0.01	0	0.02	0.02	0.02
	X-ray Fluorescence										
Cr	0	0	0	0	0	0	0	0	0	0	0
Ni	0.5	13.7	14	9.4	13.5	17.3	11.6	4.7	1.5	12.4	0
Cu	4.2	2.8	6.2	3.3	2.3	1.4	3.8	5.9	4.8	7.4	2
Zn	148.7	115.6	79.6	69.6	122.3	106.5	127.2	1007	308.1	105.7	217
Rb	150.5	161.1	198.6	227	170.4	197.2	246.8	204.1	187.9	192.3	157.2
Sr	38.2	95.6	36.4	17.4	83.3	19.8	18.3	36.4	75.8	90	60.3
Y	41.1	59.4	37.7	47	52.2	55.7	47.6	47.6	37.4	49.1	39.3
Zr	139.5	295.9	108.9	97.8	285.3	190.9	83.9	103.4	159.7	196.4	274.8
Nb	13.9	20.4	21.8	37.1	24.1	28.8	34.3	26.9	32.9	30.7	25
La	53.9	109.1	28.9	15.7	75.9	16.4	18.6	26.1	42	53.9	91.3
Ba	4.2	1270.1	3.3	0	1209.8	10.2	0	62.1	288.1	562	981.1

APPENDIX 2. (Continued)

Pre-ammonia Tanks tephra sequence (glassy pumice)									
	WW8-3A-A	WW8-3A-B	WW8-3A-C	WW8-3B-A-a	WW8-3B-A	WW8-3B-B	WW8-3B-C	WW8-3B-D	WW8-3B-E
Weight Percent Oxide (wt. %)									
SiO_2	75.68	76.83	77.47	77.24	77.04	70.78	76.67	76.64	77.36
TiO_2	0.21	0.07	0.09	0.16	0.16	0.4	0.15	0.15	0.1
Al_2O_3	13.18	12.81	12.46	12.41	12.48	15.21	12.65	12.69	12.58
FeO	1.04	0.79	0.61	0.77	0.8	1.87	0.87	0.84	0.65
MnO	0.06	0.06	0.07	0.04	0.04	0.07	0.12	0.1	0.07
MgO	0.16	0	0	0.07	0.08	0.58	0	0	0
CaO	0.88	0.6	0.4	0.6	0.59	1.39	0.3	0.35	0.42
Na_2O	2.96	3.09	3.26	2.81	2.84	3.58	2.89	3.18	3.01
K_2O	5.8	5.74	5.63	5.88	5.97	6.02	6.35	6.05	5.79
P_2O_5	0.03	0	0.01	0.01	0.01	0.09	0	0	0.01
X-ray Fluorescence									
Cr	0	0	0	0	0	0	0	0	0
Ni	8.1	12.4	11.8	0	6.9	12.1	12.9	9.1	21
Cu	5	1.7	0	0.7	0.4	3.2	1.3	0.5	2.8
Zn	54.6	1095.5	770.1	54.8	244.1	104.9	108.3	394.9	61.1
Rb	164.4	195	247.8	148.2	145.5	133.9	189.5	172.9	242.8
Sr	89.6	28.7	12.7	39.9	41.4	232.6	16.8	20.6	11.7
Y	31.5	32.1	35	25.7	24	30.1	49.7	40.3	39.8
Zr	181.8	105.4	87.1	120.7	127.1	345.7	196.2	190.8	87
Nb	29.6	32.2	41.1	24.5	23.7	20.7	28.8	34.3	38.5
La	69.3	22.4	32.3	57.4	40.3	97.3	31.5	34.6	22.4
Ba	211.6	0	48.8	132.1	151.9	881.5	67	129.4	82.1

APPENDIX 2. (Continued)

Pre-ammonia Tanks tephra sequence (glassy pumice)										
	WW8-3B-F	WW8-3C-A	WW8-3C-B	WW8-3C-C	WW8-3C-D	WW8-3C-F	WW8-3D-A	WW8-3D-B	WW8-3D-D	WW8-4A
Weight Percent Oxide (wt. %)										
SiO_2	75.26	77.25	76.73	77.04	77.55	75.67	77.49	77.11	74.63	74.17
TiO_2	0.11	0.12	0.08	0.1	0.1	0.17	0.11	0.1	0.23	0.25
Al_2O_3	13.03	12.49	13.05	12.92	12.49	13.45	12.48	12.64	13.85	14.29
FeO	0.54	0.63	1.03	0.62	0.62	0.91	0.5	0.74	1.09	1.08
MnO	0.08	0.09	0.08	0.08	0.07	0.06	0.06	0.07	0.08	0.08
MgO	0	0	0	0.02	0.01	0.11	0	0	0.07	0.37
CaO	0.5	0.41	0.57	0.41	0.4	0.81	0.45	0.44	0.75	0.83
Na_2O	3.13	2.79	2.67	2.84	2.86	2.78	3.22	2.96	3.04	3.01
K_2O	7.35	6.22	5.79	5.98	5.88	6	5.68	5.93	6.23	5.89
P_2O_5	0.01	0.01	0.01	0.01	0.01	0.03	0.01	0.01	0.02	0.02
X-ray Fluorescence										
Cr	0	0	0	0	0	0	0	0	0	0
Ni	27.4	17.5	16.1	10.3	20.6	2.9	3.7	27.4	16.7	20.8
Cu	5.7	1.5	5.1	6.6	4.6	2.9	2.2	7.1	5.4	5
Zn	324.8	518.7	67.2	121.1	74.7	172.7	192.4	179.6	136.8	89.9
Rb	322.9	195.3	201.9	257.5	261.5	196.9	239.7	262	172.1	181
Sr	13.1	17	26.5	11.2	10.2	85.7	20.4	17.5	88.7	95.1
Y	57.8	31.5	41.4	43.8	46.2	38.4	42.1	44.2	46.8	52
Zr	116.4	132.5	110	93.9	92.8	139.3	87.6	88.5	213	212
Nb	35.9	17.4	18.1	32.2	30.6	10.9	26.4	31.6	21.6	23.3
La	50.6	45.6	49	37.5	26.3	57.9	41.1	28.5	78.3	84.6
Ba	183.3	90.1	227.7	145	150.2	498.1	104	140.8	843.2	337.8

	Pre-ammonia Tanks tephra sequence (glassy pumice)									
	WW8-4C	WW8-4D	WW8-4E	WW8-5B-A	WW8-5B-B	WW8-5B-C	WW8-5A-A	WW8-5A-B	WW8-5A-C	WW8-5A-D
	Weight Percent Oxide (wt. %)									
SiO_2	71.17	75.25	73.4	77.28	76.95	77.33	77.31	76.39	77.25	77.24
TiO_2	0.47	0.18	0.29	0.11	0.1	0.13	0.13	0.21	0.1	0.08
Al_2O_3	14.93	13.76	14.8	12.69	12.85	12.56	12.52	12.94	12.66	12.56
FeO	2.17	0.83	1.39	0.51	0.73	0.69	0.73	0.97	0.5	0.92
MnO	0.08	0.06	0.1	0.07	0.06	0.05	0.05	0.04	0.07	0.06
MgO	0.68	0.13	0.34	0	0.07	0.09	0.04	0.22	0	0
CaO	1.34	0.69	0.83	0.41	0.42	0.56	0.49	0.66	0.42	0.6
Na_2O	3.31	2.96	2.95	3.12	3.25	2.67	2.74	2.57	3.46	2.79
K_2O	5.77	6.13	5.89	5.8	5.55	5.89	5.98	5.98	5.52	5.73
P_2O_5	0.07	0.02	0.02	0.01	0.01	0.01	0.01	0.02	0.01	0.01
	X-ray Fluorescence									
Cr	0	0	0	0	0	0	0	0	0	0
Ni	13.8	19.7	18.9	17	28.7	31.7	20.1	0	15.3	15.1
Cu	7.3	0.9	7.6	2.7	5	2.1	2.8	2.5	1.5	4.3
Zn	72.4	240.3	102	209.2	388.4	159.9	116.4	218.4	63.4	63.3
Rb	173.9	200.9	159.4	247.5	245.1	170.5	199	140.8	258.6	193.4
Sr	180.1	88.6	98.1	11.6	14.1	27.6	18.1	46.1	10	23.8
Y	24.2	24.6	33.4	33.5	30.7	25.1	31.3	20.7	31.6	33.8
Zr	396.2	153.3	259.8	87.2	87	108.8	103.4	167.8	96	105.3
Nb	12.9	19.8	20.3	34.5	25.3	6.8	21.6	8.6	34	21.9
La	123.8	65.4	89.2	35.9	57.5	58.8	72.3	61.3	39.4	59.7
Ba	642.6	390.5	1258	170.9	0	67.3	217.4	155.7	153.1	175.3

	Pre-ammonia Tanks tephra sequence (glassy pumice)							
	ATRP1UC-1	ATRP2UC-1	AT20-103-p-3a	AT20-103-p-3b	AT20-103-p4	AT20-103-p-5a	AT20-103-p-5b	AT20-103-p-5c
	Weight Percent Oxide (wt. %)							
SiO_2	75.66	76.68	77.24	77.02	77.42	72.74	77.4	76.97
TiO_2	0.16	0.16	0.16	0.14	0.14	0.34	0.15	0.18
Al_2O_3	13.94	13.11	12.55	12.48	12.39	14.56	12.64	12.64
FeO	1.04	0.87	0.67	0.9	0.93	1.4	0.57	0.93
MnO	0.09	0.09	0.08	0.08	0.08	0.07	0.08	0.07
MgO	0.01	0	0.13	0.08	0.21	0.52	0.24	0.1
CaO	0.33	0.34	0.36	0.35	0.28	1.14	0.36	0.45
Na_2O	3.2	3.3	3.63	3.73	3.45	4.29	3.18	3.64
K_2O	5.57	5.45	5.16	5.2	5.09	4.86	5.38	5.01
P_2O_5	0	0	0.01	0.01	0.01	0.06	0.01	0.01
	X-ray Fluorescence							
Cr	0	0	0	0	0	0	0	0
Ni	7	0	0	0	1.6	0	0	0
Cu	60.8	56	56.9	59.6	59.7	56.8	55.9	58.7
Zn	55.4	65.3	60.7	48.6	61.4	43.2	54.3	99.5
Rb	237.6	223.6	230.3	223.1	224.9	147.1	235.8	201.5
Sr	13.3	15.9	18.2	13.9	12.4	231.5	16.4	43
Y	41.4	41.5	42	34.1	35.3	34.6	38.5	37.2
Zr	138.2	140.9	144.5	134.5	129.8	268.7	126.5	147.8
Nb	44.3	48	46.7	56.8	51.9	16.6	50.2	39.4
La	5.5	2.6	17	5.2	7.3	25	19.7	12.2
Ba	243.6	186.6	139.1	218.6	147.8	1021.7	59.9	499.5

	Pre-ammonia Tanks tephra sequence (glassy pumice)					Pre-ammonia Tanks tephra sequence (bulk)		
	AT20-103-p-5d	AT20-103-p-5e	AT20-103-p-5f	AT20-103-p-6a	AT20-103-p-6b	AT92-728-(-21)	AT92-728-(-18)	AT92-728-(-1)
	Weight Percent Oxide (wt. %)					Weight Percent Oxide (wt. %)		
SiO_2	72.08	76.25	72.34	77.05	76.97	75.2	74.52	74.56
TiO_2	0.36	0.2	0.38	0.16	0.15	0.25	0.26	0.29
Al_2O_3	14.68	13.12	14.78	12.82	12.86	14.04	14.58	14.09
FeO	2.03	0.77	1.69	0.74	0.87	1.5	1.55	1.67
MnO	0.08	0.07	0.07	0.08	0.08	0.08	0.08	0.09
MgO	0.61	0.33	0.67	0.29	0.43	0.29	0.46	0.52
CaO	1.28	0.46	1.16	0.34	0.38	0.43	0.46	0.65
Na_2O	4.13	3.25	4.03	3.54	3.1	3.22	3.12	3.01
K_2O	4.67	5.52	4.82	4.98	5.15	5	4.99	5.12
P_2O_5	0.07	0.02	0.06	0	0.01	0	0	0
	X-ray Fluorescence					X-ray Fluorescence		
Cr	0	0	0	0	0	0	0	0
Ni	0	0	0	0	1.8	5.87	0	0.03
Cu	60.3	55.3	57	56.3	56.5	14.8	8.73	15.87
Zn	57.4	48.6	53.8	48.7	53.8	64.9	62.9	61.4
Rb	148.8	196.9	149.9	209.3	233.3	175.49	189.33	214.04
Sr	274.4	29.8	234.1	9.2	18.1	45.91	46.96	111.68
Y	30.9	46	25	31.3	27.3	43.27	39	41.62
Zr	281	190.9	292.1	131.6	115.8	191.75	193.48	198.79
Nb	33.4	48.1	22.7	42.8	42.1	20.65	27.19	27.26
La	32.8	13.8	56.1	25.4	41.9	72.54	67.65	60.36
Ba	1182.7	327.4	1067.3	140.9	233.3	295.45	395.04	305.69

	Pre-ammonia Tanks tephra sequence (bulk tephra)								
	AT92-728-1	AT92-728-1.5	AT92-728-12	AT92-728-21	AT92-728-28	AT92-728-30	AT92-728-34	AT92-728-48	AT92-728-57
	Weight Percent Oxide (wt. %)								
SiO_2	75.4	76.02	70.04	76.34	72.97	75.92	75.89	75.01	75.29
TiO_2	0.23	0.19	0.53	0.24	0.35	0.27	0.27	0.29	0.3
Al_2O_3	14.23	13.81	17.22	12.78	15.35	13.16	13.2	13.88	13.39
FeO	1.45	1.28	2.67	1.29	1.95	1.52	1.5	1.88	1.8
MnO	0.08	0.08	0.1	0.09	0.08	0.1	0.11	0.08	0.08
MgO	0.3	0.26	0.67	0.27	0.34	0.4	0.32	0.44	0.37
CaO	0.41	0.44	0.97	0.73	0.65	0.74	0.74	0.7	0.79
Na_2O	3.03	2.97	3.57	3.23	3.44	3.04	3.01	2.94	3.01
K_2O	4.86	4.94	4.23	5.05	4.87	4.87	4.97	4.78	4.98
P_2O_5	0	0	0.02	0	0	0	0	0	0
	X-ray Fluorescence								
Cr	0	0	0	0	0	0	0	0	0
Ni	0.13	0	19.83	0	0	0	4.23	15.09	13.33
Cu	13.67	13.65	13.47	10.16	14.32	12.66	8.21	10.72	10.43
Zn	63.77	55.71	92.12	54.94	70.88	60.75	57.75	64.39	57.2
Rb	205.04	226.38	103.75	210.95	177.34	213.79	212.48	200.97	227.81
Sr	54.13	72.87	203.33	80.27	97.98	102.51	99.63	89.98	94.85
Y	34.3	31.92	71.86	37.61	51.33	35.52	35.7	45.3	44.35
Zr	160.44	148.23	305.19	166.09	232.93	182.58	180.92	213.38	246.25
Nb	33.26	25.6	19.71	26.95	26.98	21.8	26.87	37.47	33.56
La	33.51	55.41	114.73	59.82	13.48	97.02	44.02	65.51	82.41
Ba	533.02	361.57	735.92	374.19	459.57	389.7	549.56	315.44	348.21

	Pre-ammonia Tanks tephra sequence (bulk tephra)									
	AT92-728-61	AT92-728-66	AT92-728-69	AT92-728-81	AT-19-11	AT-19-38	AT-19-63	AT-19-87	AT-19-110	AT-19-126
	Weight Percent Oxide (wt. %)									
SiO_2	75.26	74.96	74.96	74.8	74.02	73.45	73.53	69.18	70.47	71.95
TiO_2	0.3	0.29	0.31	0.31	0.36	0.31	0.28	0.53	0.44	0.4
Al_2O_3	13.38	13.83	13.9	14.19	13.59	14.61	14.58	15.92	15.71	15.05
FeO	1.85	1.96	2.01	1.93	1.73	1.32	1.3	3.11	2.34	1.94
MnO	0.08	0.08	0.09	0.09	0.09	0.08	0.08	0.09	0.09	0.09
MgO	0.39	0.45	0.47	0.43	0.56	0.77	0.46	1.01	0.84	0.6
CaO	0.78	0.7	0.71	0.67	0.88	0.94	0.92	2.29	1.86	1.43
Na_2O	3.04	2.94	2.86	2.95	3.64	3.47	3.47	3.82	3.91	3.82
K_2O	4.93	4.79	4.69	4.62	5.08	5.01	5.34	3.97	4.25	4.66
P_2O_5	0	0	0	0.01	0.04	0.04	0.04	0.08	0.08	0.06
	X-ray Fluorescence									
Cr	0	0	0	0	22.6	17.34	15.43	45.91	40.27	19.89
Ni	5.49	17.8	8.8	9.87	0	0	0	3.57	16.99	0
Cu	9.47	6.52	10.1	10.17	0	0	0	0	0	0
Zn	63.47	64.04	69.37	86.26	46.88	40.85	42.06	80.88	73.7	54.01
Rb	226.76	211.18	208.59	192.77	181.74	169.54	186.04	124.45	175.54	165.06
Sr	100.01	91.34	84.69	91.6	99.81	116.98	121.04	443.63	415.7	282.13
Y	52.04	53.94	57.57	71.61	37.94	37.38	32.78	26.65	28.2	28.8
Zr	230.35	225.11	225.51	221.12	263.1	209.94	211.91	297.84	303.86	327.35
Nb	33.38	31.46	31.96	34.76	26.77	25.68	22.93	14.36	22.04	23.18
La	71.31	86.85	108.46	98.82	55.74	118.63	67.43	49.92	82.32	95.46
Ba	417.91	390.6	375.38	367.62	144.96	319.53	236.51	869.03	84.91	761.84

	Pre-ammonia Tanks tephra sequence (bulk tephra)										
	AT-19-162	AT-19-170	AT-19-176	AT-19-180	AT-19-202	AT-19-234	AT-19-250	AT-19-258	AT-19-272	AT-19-287	AT-19-291
	Weight Percent Oxide (wt. %)										
SiO_2	75.89	75.39	75.29	73.78	76.15	73.96	74.86	74.75	75	73.82	75.56
TiO_2	0.22	0.22	0.26	0.3	0.22	0.27	0.29	0.28	0.25	0.31	0.2
Al_2O_3	13.29	13.66	13.4	14.16	13.11	14.22	13.63	13.69	13.76	14.26	13.92
FeO	1.03	1.04	1.14	1.27	1.05	1.21	1.29	1.31	1.2	1.44	1.39
MnO	0.09	0.09	0.09	0.08	0.09	0.08	0.1	0.08	0.08	0.09	0.07
MgO	0.26	0.37	0.24	0.26	0.15	0.2	0.96	0.5	0.53	0.89	0.49
CaO	0.59	0.53	0.65	0.94	0.56	0.84	0.55	0.85	0.71	0.76	0.41
Na_2O	3.32	3.33	3.48	3.87	3.21	3.78	3.2	3.35	3.34	3.66	3.41
K_2O	5.27	5.34	5.41	5.3	5.42	5.39	5.08	5.14	5.1	4.7	4.52
P_2O_5	0.03	0.03	0.03	0.04	0.03	0.05	0.04	0.04	0.04	0.06	0.02
	X-ray Fluorescence										
Cr	21.26	9.38	15.67	24.82	18.65	17.95	18.74	24.86	23.19	18.29	37.41
Ni	0	0	0	0	0	0	0	0	0	0	8.43
Cu	0	0	44.58	0	0	0.94	0	0	37.67	0	0
Zn	42.8	43.86	45.68	60.46	58.23	47.19	70.12	59.3	49.47	42.39	66.98
Rb	205.56	213.9	203.93	171.34	208.23	178	208.63	179.95	188.39	179.14	168.8
Sr	67.36	47.06	79	151.96	50.01	130.36	53.99	113.41	82.36	134.85	27
Y	29.45	30.68	26.77	29.42	26	29.34	30.21	25.9	30.37	32.23	24.76
Zr	210.8	214.4	230.7	373.69	202.46	234.03	253.31	204.51	226.67	269.62	157.3
Nb	28.28	25.82	31.35	29.18	32.06	28.17	36	21.48	25.68	30.5	25.39
La	100.78	73.29	49.93	60.5	27.6	72.01	60.86	41.17	82.55	104.47	27.31
Ba	371.57	236.61	384.86	513.58	239.66	497.45	157.88	307.97	398.05	514.27	177.36

APPENDIX 2 (Continued)

Pre-ammonia Tanks tephra sequence (bulk tephra)							
	AT-19-304	AT-19-317	AT-19-327	AT-19-333	AT-19-344	AT-19-352	AT-19-360
Weight Percent Oxide (wt. %)							
SiO_2	71.89	76.08	72.79	74.4	73.51	75.69	74.63
TiO_2	0.34	0.22	0.44	0.25	0.31	0.23	0.31
Al_2O_3	15.12	13.14	14.27	14.01	14.77	13.19	13.91
FeO	1.6	1.09	1.92	1.27	1.52	1.07	1.43
MnO	0.08	0.07	0.09	0.08	0.08	0.07	0.08
MgO	0.45	0.22	0.39	0.25	0.28	0.13	0.31
CaO	1.19	0.66	0.99	0.65	0.79	0.64	0.76
Na_2O	4.01	3.55	3.8	4.05	3.64	3.82	3.34
K_2O	5.26	4.93	5.25	4.99	5.05	5.12	5.16
P_2O_5	0.06	0.03	0.06	0.04	0.04	0.04	0.06
X-ray Fluorescence							
Cr	13.55	15.52	24.46	9.42	12.24	15.09	10.29
Ni	0	0	0	0	0	0	0
Cu	208.78	0	0	327.13	0	42.21	0
Zn	2059.17	42.16	55.52	2421.66	46.05	52.16	46.52
Rb	142.05	167.85	164.1	171.05	154.85	188.23	202.6
Sr	215.27	79.73	147.96	69.24	107.84	84.62	121.63
Y	29.7	29.44	40.38	28.37	36.48	31.71	32.91
Zr	265.94	203.69	323.42	224.46	263.01	189.02	280.43
Nb	22.52	31.84	28.5	30.11	30.91	32.77	32.07
La	92.04	59.42	93.81	50.08	85.96	28.42	69.34
Ba	988.41	253.39	688.7	307.37	494.22	399.58	604.27

APPENDIX 3

FELDSPAR ANALYSES

Post-grouse Canyon tephra sequence

	Na_2O	MgO	Al_2O_3	SiO_2	K_2O	CaO	FeO	BaO	SrO	total	An	Ab	Or	Cn
p65-24-1.5-1c-or	4.88	0.00	18.18	65.85	9.60	0.30	0.01	0.00	0.00	98.83	1.46	42.95	55.59	0.00
p65-24-1.5-1m-or	4.98	0.00	18.52	65.39	9.52	0.32	0.01	0.03	0.00	98.79	1.55	43.58	54.82	0.05
p65-24-1.5-1e-or	4.88	0.00	18.33	65.19	9.75	0.26	0.01	0.00	0.00	98.43	1.26	42.66	56.08	0.00
p65-24-1.5-2c-pl	9.34	0.00	20.36	63.60	1.65	2.37	0.03	0.03	0.00	97.39	11.15	79.55	9.25	0.05
p65-24-1.5-2m-pl	9.21	0.00	20.37	63.66	1.63	2.46	0.00	0.00	0.00	97.32	11.68	79.11	9.21	0.00
p65-24-1.5-2e-pl	9.06	0.00	20.21	64.63	1.85	2.26	0.01	0.00	0.00	98.01	10.84	78.60	10.56	0.00
p65-24-1.5-3c-or	7.84	0.00	19.60	66.28	4.54	1.49	0.02	0.00	0.00	99.76	7.07	67.29	25.64	0.00
p65-24-1.5-3m-or	5.81	0.01	18.67	65.39	8.28	0.54	0.02	0.05	0.00	98.76	2.58	50.23	47.10	0.09
p65-24-1.5-3m-or	5.65	0.00	18.51	64.41	8.44	0.54	0.00	0.03	0.00	97.57	2.59	49.10	48.26	0.05
p65-24-1.5-3e-or	4.61	0.00	17.62	64.39	9.72	0.25	0.02	0.00	0.00	96.61	1.24	41.37	57.39	0.00
p65-24-1.5-3c-or	7.74	0.00	19.62	64.25	4.37	1.44	0.00	0.00	0.00	97.43	6.97	67.83	25.20	0.00
p65-24-1.5-4c-pl	9.02	0.00	20.37	66.45	1.70	2.36	0.00	0.00	0.00	99.90	11.40	78.83	9.77	0.00
p65-24-1.5-4c-pl	9.12	0.00	20.38	66.02	1.65	2.55	0.00	0.05	0.00	99.76	12.12	78.45	9.34	0.09
p65-24-1.5-4m-pl	9.34	0.00	20.41	66.18	1.69	2.42	0.00	0.03	0.00	100.08	11.34	79.18	9.43	0.05
p65-24-1.5-4e-pl	9.40	0.00	20.70	66.66	1.61	2.53	0.00	0.00	0.00	100.91	11.79	79.28	8.93	0.00
p65-24-1.5-5c-or	4.70	0.01	17.86	66.64	9.89	0.27	0.02	0.00	0.00	99.40	1.31	41.39	57.30	0.00
p65-24-1.5-5m-or	4.65	0.00	17.93	66.88	10.00	0.25	0.01	0.00	0.00	99.72	1.22	40.91	57.88	0.00
p65-24-1.5-5e-or	4.93	0.00	18.10	67.90	9.85	0.25	0.00	0.01	0.00	101.04	1.20	42.68	56.11	0.02
p65-24-27-1c-pl	8.75	0.00	20.99	62.83	1.16	3.30	0.00	0.07	0.00	97.11	16.07	77.09	6.72	0.12
p65-24-27-1c-pl	8.49	0.00	20.90	63.03	1.26	3.38	0.00	0.00	0.00	97.06	16.70	75.89	7.41	0.00
p65-24-27-2c-or	5.05	0.07	18.26	64.64	9.53	0.36	0.14	0.20	0.00	98.26	1.72	43.69	54.24	0.35
p65-24-27-2m-or	5.08	0.10	18.26	65.11	9.41	0.34	0.17	0.31	0.00	98.79	1.63	44.09	53.73	0.54
p65-24-27-2e-or	5.23	0.08	18.97	66.87	9.33	0.35	0.17	0.14	0.00	101.16	1.67	45.12	52.96	0.24
p65-24-27-4c-or	5.96	0.09	18.70	64.97	8.02	0.59	0.10	0.17	0.00	98.60	2.81	51.39	45.50	0.30
p65-24-27-4m-or	5.91	0.09	18.61	64.55	7.93	0.57	0.16	0.19	0.00	98.02	2.74	51.48	45.44	0.33
p65-24-27-4e-or	5.96	0.09	18.37	64.58	7.50	0.71	0.13	0.21	0.00	97.56	3.46	52.61	43.56	0.37
p65-24-27-5c-or	4.96	0.08	18.38	64.78	9.70	0.37	0.13	0.20	0.00	98.61	1.76	42.81	55.08	0.35
p65-24-27-5m-or	4.95	0.09	18.14	65.08	9.52	0.38	0.16	0.19	0.00	98.52	1.83	43.19	54.65	0.33
p65-24-27-5e-or	4.96	0.08	18.19	66.23	9.54	0.35	0.18	0.13	0.00	99.67	1.69	43.29	54.79	0.23
p65-24-27-6c-pl	8.59	0.08	22.24	61.12	0.77	4.48	0.10	0.19	0.00	97.58	21.32	73.98	4.36	0.33
p65-24-27-6m-pl	8.47	0.09	22.42	61.23	0.81	4.41	0.14	0.26	0.00	97.83	21.20	73.70	4.64	0.46

APPENDIX 3. (Continued)

Post-grouse Canyon tephra sequence															
	Na_2O	MgO	Al_2O_3	SiO_2	K_2O	CaO	FeO	BaO	SrO	total	An	Ab	Or	Cn	
p85-24-27-6e-pl	9.45	0.08	20.85	63.59	1.39	2.58	0.15	0.26	0.00	98.36	12.04	79.80	7.72	0.44	
p85-24-27-6e-pl	9.64	0.08	20.87	63.54	1.51	2.51	0.17	0.15	0.00	98.49	11.51	79.99	8.24	0.25	
p85-24-7-1c-or	5.47	0.02	19.26	67.84	9.11	0.32	0.02	0.01	0.00	102.05	1.52	46.98	51.48	0.02	
p85-24-7-1m-or	5.54	0.00	18.65	66.40	8.47	0.56	0.02	0.02	0.00	99.67	2.71	48.49	48.77	0.04	
p85-24-7-1e-or	4.73	0.00	18.30	67.78	9.88	0.22	0.02	0.05	0.00	100.99	1.07	41.63	57.21	0.09	
p85-24-7-2c-or	4.63	0.00	18.42	65.22	10.03	0.25	0.01	0.00	0.00	98.56	1.22	40.73	58.05	0.00	
p85-24-7-2m-or	4.65	0.00	18.38	65.69	9.90	0.23	0.02	0.14	0.00	99.01	1.12	41.08	57.55	0.25	
p85-24-7-2e-or	4.55	0.00	18.43	64.90	9.75	0.25	0.02	0.00	0.00	97.90	1.24	40.98	57.78	0.00	
p85-24-7-3c-pl	9.11	0.00	20.71	63.83	1.71	2.34	0.00	0.02	0.00	97.73	11.21	79.00	9.76	0.04	
p85-24-7-3m-pl	9.33	0.01	21.14	64.78	1.67	2.38	0.04	0.00	0.00	99.35	11.20	79.45	9.36	0.00	
p85-24-7-3e-pl	8.85	0.00	20.31	61.03	1.75	2.24	0.01	0.05	0.00	94.24	11.00	78.67	10.24	0.09	
p85-24-7-3e-pl	8.96	0.01	20.66	63.79	1.66	2.34	0.03	0.00	0.00	97.44	11.40	78.98	9.63	0.00	
p85-24-7-4c-pl	9.10	0.00	20.66	64.71	1.55	2.61	0.02	0.00	0.00	98.65	12.47	78.71	8.82	0.00	
p85-24-7-4m-pl	9.34	0.01	21.02	64.91	1.43	2.81	0.00	0.05	0.00	99.56	13.11	78.86	7.94	0.09	
p85-24-7-4e-pl	9.53	0.00	21.60	65.69	1.49	2.59	0.04	0.00	0.00	100.94	11.99	79.81	8.21	0.00	
p85-24-7-5c-pl	7.59	0.00	24.38	58.33	0.50	6.52	0.01	0.00	0.00	97.33	31.27	65.87	2.86	0.00	
p85-24-7-5m-pl	7.90	0.01	24.09	59.24	0.58	6.09	0.00	0.07	0.00	97.98	28.86	67.75	3.27	0.12	
p85-24-7-5e-pl	9.41	0.01	22.52	65.31	1.10	3.47	0.02	0.00	0.00	101.84	15.91	78.08	6.01	0.00	
p85-24-7-5m-pl	8.19	0.03	21.87	62.00	0.84	4.34	0.00	0.01	0.00	97.29	21.52	73.50	4.96	0.02	
p85-24-7-5m-pl	7.89	0.01	24.29	60.78	0.55	6.01	0.04	0.01	0.00	99.57	28.69	68.16	3.13	0.02	
p85-24-7-5c-pl	7.65	0.00	24.02	59.17	0.58	6.07	0.03	0.08	0.00	97.61	29.42	67.09	3.35	0.14	
m21-27-1c-or	4.85	0.01	19.24	64.20	9.29	0.44		0.47		98.63	2.15	42.92	54.09	0.84	
m21-27-1e-or	4.61		18.90	64.53	9.34	0.46		0.52		98.52	2.29	41.48	55.29	0.95	
m21-27-2c-or	4.29		19.06	64.82	10.20	0.30		0.22		99.03	1.48	38.27	59.86	0.40	
m21-27-2e-or	4.48		19.28	65.30	9.98	0.30		0.16		99.66	1.47	39.84	58.40	0.29	
m21-27-3c-or	4.26		18.83	64.04	10.08	0.36		0.26		97.98	1.79	38.23	59.51	0.47	
m21-27-3e-or	4.51		19.54	64.75	10.06	0.32		0.49		99.81	1.55	39.55	58.04	0.87	
m21-27-4c-pl	8.32		22.67	61.01	1.44	3.81		0.05		97.51	18.50	73.09	8.32	0.09	
m21-27-4e-pl	9.02		22.84	64.77	1.53	3.30		0.11		101.77	15.36	75.97	8.48	0.19	
m21-27-5c-pl	8.43		22.55	61.53	1.37	3.87		0.12		98.11	18.61	73.34	7.84	0.21	
m21-27-5e-pl	8.69		23.27	61.62	1.24	4.18		0.08		99.28	19.52	73.45	6.90	0.14	
m19-6-1c-pl	8.65		22.34	62.97	1.29	3.36		0.10		98.88	16.32	76.04	7.46	0.18	

Post-grouse Canyon tephra sequence															
	Na_2O	MgO	Al_2O_3	SiO_2	K_2O	CaO	FeO	BaO	SrO	total	An	Ab	Or	Cn	
m19-6-1e-pl	8.71		22.14	64.02	1.37	3.36		0.11		99.88	16.16	75.80	7.84	0.19	
m19-6-3c-or	3.82		19.06	63.58	10.95	0.25		0.56		98.36	1.23	33.88	63.89	1.00	
m19-6-3e-or	4.05		19.53	64.59	10.76	0.24		0.63		99.95	1.16	35.56	62.16	1.12	
m19-6-4c-pl	8.76		22.08	62.92	1.35	3.13		0.00		98.43	15.20	76.99	7.81	0.00	
m19-6-4e-pl	9.12		22.48	63.58	1.32	3.36		0.02		100.07	15.67	76.97	7.33	0.03	
m23a-9-3c-pl	7.62		23.98	59.41	1.17	5.51		0.39		98.55	26.45	66.18	6.69	0.68	
m23a-9-3e-pl	8.03		23.97	61.74	1.24	5.22		0.43		101.18	24.41	67.95	6.90	0.74	
m23a-9-3c-or	5.13		19.17	63.04	9.44	0.44		0.59		98.14	2.08	43.83	53.07	1.02	
m23a-9-4c-or	4.67		19.06	63.62	9.81	0.41		0.52		98.45	1.98	40.76	56.34	0.92	
m23a-9-4e-or	5.04		19.71	65.36	9.84	0.51		0.56		101.36	2.37	42.32	54.36	0.95	
p61-0-3-3c-or	3.46	0.01	18.62	61.93	11.51	0.19	0.09	0.17	0.00	95.99	0.94	30.97	67.78	0.31	
p61-0-3-3c-or	3.39	0.00	18.27	65.53	11.72	0.14	0.08	0.05	0.00	99.21	0.69	30.30	68.92	0.09	
p61-0-3-3m-or	3.37	0.00	18.12	66.05	11.93	0.15	0.03	0.00	0.00	99.66	0.73	29.82	69.45	0.00	
p61-0-3-3e-or	3.60	0.00	18.47	65.93	11.60	0.17	0.05	0.02	0.00	99.84	0.83	31.77	67.36	0.04	
p61-0-3-4c-or	3.31	0.00	18.21	64.83	11.80	0.12	0.03	0.01	0.00	98.31	0.60	29.71	69.68	0.02	
p61-0-3-4m-or	3.30	0.01	18.04	65.16	11.80	0.10	0.05	0.00	0.00	98.47	0.50	29.68	69.82	0.00	
p61-0-3-4e-or	3.33	0.00	17.80	64.45	12.22	0.11	0.03	0.07	0.00	98.01	0.53	29.10	70.25	0.12	
p61-0-3-5c-pl	8.81	0.00	21.97	63.17	1.28	3.62	0.08	0.00	0.00	98.93	17.17	75.61	7.23	0.00	
p61-0-3-5m-pl	8.64	0.00	21.98	63.17	1.22	3.56	0.05	0.00	0.00	98.62	17.24	75.72	7.03	0.00	
p61-0-3-5e-pl	7.80	0.00	21.59	58.77	0.99	4.57	0.10	0.00	0.00	93.84	23.01	71.06	5.93	0.00	
p61-0-3-5e-pl	8.72	0.00	22.15	63.34	1.26	3.63	0.14	0.00	0.00	99.26	17.36	75.47	7.17	0.00	
p61-0-3-6c-or	3.24	0.00	17.16	61.89	11.89	0.13	0.07	0.00	0.00	94.39	0.65	29.10	70.26	0.00	
p61-0-3-6c-or	3.35	0.00	18.18	64.23	11.93	0.14	0.06	0.07	0.00	97.97	0.69	29.67	69.52	0.13	
p61-0-3-6m-or	3.28	0.00	18.28	64.40	11.81	0.14	0.05	0.08	0.00	98.06	0.69	29.43	69.73	0.15	
p61-0-3-6e-or	3.22	0.00	17.76	64.77	11.75	0.15	0.04	0.07	0.00	97.77	0.75	29.15	69.98	0.13	
p61-0-3-7c-pl	8.34	0.01	22.56	61.48	1.08	4.48	0.10	0.00	0.00	98.06	21.48	72.36	6.16	0.00	
p61-0-3-7m-pl	8.65	0.00	22.79	60.98	1.09	4.36	0.12	0.03	0.00	98.04	20.45	73.41	6.09	0.05	
p61-0-3-7e-pl	8.05	0.00	22.23	56.16	1.00	4.69	0.13	0.00	0.00	92.27	22.94	71.24	5.82	0.00	
p61-0-6-1c-pl	8.75	0.00	21.81	61.65	1.38	3.33	0.02	0.00	0.00	96.93	16.00	76.10	7.90	0.00	
p61-0-6-1c-pl	8.95	0.00	21.73	61.75	1.23	3.37	0.06	0.00	0.00	97.09	16.02	77.01	6.96	0.00	
p61-0-6-1-pl	8.46	0.00	21.59	65.75	1.33	3.60	0.15	0.05	0.00	100.95	17.55	74.64	7.72	0.09	
p61-0-6-1m-pl	8.55	0.00	21.90	63.68	1.26	3.72	0.12	0.09	0.00	99.34	17.95	74.65	7.24	0.16	

APPENDIX 3. (Continued)

Post-grouse Canyon tephra sequence															
	Na_2O	MgO	Al_2O_3	SiO_2	K_2O	CaO	FeO	BaO	SrO	total	An	Ab	Or	Cn	
p61-0-6-1e-pl	8.40	0.00	21.37	62.92	1.30	3.68	0.11	0.00	0.00	97.80	18.01	74.41	7.58	0.00	
p61-0-6-2c-or	3.23	0.00	18.14	66.97	11.68	0.22	0.09	0.09	0.00	100.43	1.10	29.22	69.52	0.16	
p61-0-6-2m-or	3.21	0.01	18.28	67.21	11.85	0.19	0.10	0.24	0.00	101.10	0.94	28.76	69.86	0.43	
p61-0-6-2e-or	3.07	0.00	17.77	63.47	11.79	0.19	0.08	0.29	0.00	96.66	0.96	27.93	70.58	0.53	
p61-0-6-3c-or	3.21	0.00	18.32	66.84	11.98	0.19	0.12	0.29	0.00	100.97	0.93	28.50	70.04	0.52	
p61-0-6-3m-or	3.36	0.00	18.26	67.74	11.92	0.17	0.08	0.19	0.00	101.72	0.83	29.84	69.19	0.34	
p61-0-6-3e-or	3.76	0.01	19.25	71.25	11.50	0.17	0.08	0.05	0.00	106.06	0.82	32.90	66.19	0.09	
p61-0-6-3-or	3.76	0.01	19.36	67.30	11.46	0.15	0.10	0.13	0.00	102.29	0.73	32.96	66.09	0.23	
p61-0-6-4c-pl	8.49	0.01	22.10	62.35	1.17	3.90	0.20	0.00	0.00	98.24	18.88	74.38	6.74	0.00	
p61-0-6-4m-pl	8.55	0.02	21.95	62.35	1.06	3.98	0.13	0.00	0.00	98.05	19.21	74.69	6.09	0.00	
p61-0-6-4e-pl	8.49	0.00	21.93	59.87	1.05	4.18	0.13	0.00	0.00	95.46	20.10	73.89	6.01	0.00	
p61-0-6-4e-pl	8.65	0.01	21.44	63.84	1.20	3.50	0.14	0.00	0.00	98.79	17.01	76.05	6.94	0.00	
p61-2-2-1c-or	3.58	0.00	18.56	65.92	12.03	0.16	0.11	0.13	0.00	100.50	0.78	30.84	68.18	0.23	
p61-2-2-1c-or	3.52	0.00	18.27	64.58	11.90	0.18	0.05	0.29	0.00	98.79	0.86	30.59	68.04	0.51	
p61-2-2-1e-or	3.19	0.00	17.52	61.95	12.09	0.17	0.10	0.23	0.00	95.25	0.83	28.27	70.49	0.41	
p61-2-2-2c-or	3.46	0.00	18.14	64.31	11.82	0.21	0.07	0.40	0.00	98.41	1.01	30.26	68.02	0.71	
p61-2-2-2m-or	3.46	0.00	17.95	64.81	11.66	0.18	0.12	0.33	0.00	98.52	0.88	30.63	67.90	0.59	
p61-2-2-2e-or	3.40	0.00	18.04	62.41	12.08	0.20	0.13	0.15	0.00	96.43	0.96	29.59	69.18	0.26	
p61-2-2-3c-pl	8.88	0.01	22.11	62.87	1.24	3.94	0.10	0.06	0.00	99.21	18.32	74.71	6.86	0.10	
p61-2-2-3m-pl	8.90	0.00	22.24	61.62	1.24	4.08	0.11	0.00	0.00	98.20	18.83	74.35	6.82	0.00	
p61-2-2-3e-pl	8.49	0.00	21.94	60.55	1.21	4.13	0.09	0.08	0.00	96.52	19.70	73.29	6.87	0.14	
p61-2-2-4c-pl	9.22	0.01	22.05	61.96	1.16	3.53	0.18	0.05	0.00	98.18	16.33	77.19	6.39	0.08	
p61-2-2-4m-pl	9.14	0.01	21.78	62.62	1.18	3.48	0.11	0.00	0.00	98.33	16.24	77.20	6.56	0.00	
p61-2-2-4m-pl	8.69	0.00	21.13	58.20	1.19	3.56	0.13	0.07	0.00	91.00	17.17	75.87	6.84	0.12	
p61-2-2-4e-pl	8.90	0.00	21.21	59.61	1.16	3.45	0.14	0.00	0.00	94.48	16.48	76.93	6.60	0.00	
p61-2-2-1c-pl	8.80	0.00	21.96	62.81	1.23	4.16	0.12	0.00	0.00	99.08	19.30	73.90	6.80	0.00	
p61-2-2-1m-pl	8.70	0.00	21.88	62.93	1.22	4.03	0.12	0.00	0.00	98.89	18.99	74.17	6.84	0.00	
p61-2-2-1e-pl	8.73	0.00	22.07	63.50	1.19	4.13	0.12	0.00	0.00	99.75	19.35	74.01	6.64	0.00	
p61-2-2-2c-or	3.30	0.00	18.03	65.36	11.91	0.19	0.00	0.00	0.00	98.80	0.93	29.36	69.71	0.00	
p61-2-2-2-or	3.31	0.00	18.26	64.73	11.89	0.20	0.00	0.00	0.00	98.39	0.98	29.44	69.58	0.00	
p61-2-2-2e-or	3.17	0.00	18.31	64.79	12.05	0.19	0.00	0.00	0.00	98.51	0.94	28.30	70.77	0.00	
p61-2-2-3c-or	3.28	0.00	18.14	64.95	11.92	0.21	0.00	0.00	0.00	98.50	1.03	29.19	69.78	0.00	

APPENDIX 3. (Continued)

Post-grouse Canyon tephra sequence															
	Na_2O	MgO	Al_2O_3	SiO_2	K_2O	CaO	FeO	BaO	SrO	total	An	Ab	Or	Cn	
p61-2-2-3m-or	3.29	0.00	18.38	63.85	11.88	0.18	0.00	0.00	0.00	97.58	0.89	29.36	69.75	0.00	
p61-2-2-3e-or	3.30	0.01	18.44	63.84	11.88	0.19	0.00	0.00	0.00	97.46	0.94	29.41	69.66	0.00	
p61-2-2-4c-or	3.15	0.00	18.10	63.43	12.05	0.15	0.00	0.00	0.00	96.88	0.74	28.22	71.03	0.00	
p61-2-2-4c-or	3.33	0.00	17.96	66.57	12.16	0.13	0.00	0.06	0.00	100.19	0.63	29.17	70.09	0.11	
p61-2-2-4m-or	3.22	0.00	17.97	66.39	12.06	0.14	0.00	0.12	0.00	99.89	0.69	28.61	70.49	0.22	
p61-2-2-4e-or	3.30	0.00	17.89	65.70	11.88	0.16	0.01	0.06	0.00	99.00	0.79	29.42	69.68	0.11	
p61-2-2-5c-pl	9.06	0.00	22.56	63.45	1.11	4.11	0.00	0.00	0.00	100.28	18.83	75.12	6.05	0.00	
p61-2-2-5m-pl	8.83	0.00	22.58	63.45	0.99	4.21	0.00	0.06	0.00	100.12	19.68	74.70	5.51	0.10	
p61-2-2-5e-pl	8.37	0.00	21.28	61.66	1.10	3.96	0.00	0.09	0.00	96.46	19.37	74.07	6.40	0.16	
p61-1-25-1c-or	4.89	0.00	18.73	66.29	9.27	0.51	0.09	0.24	0.00	100.03	2.49	43.20	53.88	0.43	
p61-1-25-1c-or	4.68	0.00	18.38	65.73	9.45	0.34	0.09	0.09	0.00	98.75	1.69	42.15	56.00	0.16	
p61-1-25-1e-or	4.93	0.01	18.75	66.69	9.56	0.35	0.13	0.13	0.00	100.55	1.69	43.10	54.98	0.23	
p61-1-25-2c-or	3.32	0.00	17.92	65.62	11.86	0.12	0.09	0.05	0.00	98.99	0.59	29.64	69.67	0.09	
p61-1-25-2m-or	3.43	0.00	18.03	65.44	11.60	0.17	0.09	0.14	0.00	98.90	0.84	30.67	68.24	0.25	
p61-1-25-2e-or	3.62	0.00	18.24	66.83	11.58	0.17	0.05	0.06	0.00	100.56	0.83	31.91	67.16	0.11	
p61-1-25-3c-pl	8.51	0.00	21.96	63.21	1.20	4.06	0.18	0.00	0.00	99.12	19.44	73.72	6.84	0.00	
p61-1-25-3m-pl	8.57	0.00	21.68	63.50	1.23	3.88	0.14	0.00	0.00	99.01	18.61	74.37	7.02	0.00	
p61-1-25-3e-pl	8.48	0.00	21.46	65.02	1.21	3.76	0.10	0.01	0.00	100.05	18.30	74.67	7.01	0.02	
p61-1-25-4c-or	3.37	0.01	18.20	65.64	11.80	0.18	0.13	0.24	0.00	99.58	0.88	29.87	68.82	0.43	
p61-1-25-4m-or	3.46	0.00	18.20	65.09	11.81	0.17	0.08	0.09	0.00	98.90	0.83	30.51	68.51	0.16	
p61-1-25-4e-or	3.48	0.00	18.35	66.74	11.67	0.19	0.09	0.02	0.00	100.55	0.93	30.89	68.15	0.04	
p61-1-25-4e-or	3.38	0.00	18.16	65.06	11.52	0.18	0.10	0.13	0.00	98.54	0.90	30.49	68.37	0.24	
p61-1-25-5c-pl	8.37	0.00	22.09	63.32	1.05	4.17	0.18	0.00	0.00	99.20	20.28	73.65	6.08	0.00	
p61-1-25-5m-pl	8.49	0.00	21.80	63.27	1.24	3.69	0.10	0.00	0.00	98.40	17.97	74.84	7.19	0.00	
p61-1-25-5e-pl	8.58	0.00	22.27	63.85	1.03	4.16	0.10	0.00	0.00	99.99	19.89	74.24	5.86	0.00	
p61-1-20-1c-or	3.50	0.00	18.93	64.93	11.38	0.19	0.07	0.28	0.00	99.30	0.94	31.39	67.16	0.51	
p61-1-20-1m-or	3.44	0.01	18.03	65.37	11.13	0.17	0.06	0.23	0.00	98.46	0.86	31.55	67.16	0.43	
p61-1-20-1e-or	3.42	0.02	18.18	66.05	11.27	0.12	0.04	0.15	0.00	99.25	0.61	31.29	67.83	0.28	
p61-1-20-2c-or	3.40	0.00	17.92	64.59	11.31	0.19	0.04	0.16	0.00	97.63	0.96	30.97	67.78	0.29	
p61-1-20-2m-or	3.36	0.00	18.01	64.46	11.14	0.17	0.05	0.24	0.00	97.43	0.87	31.02	67.67	0.45	
p61-1-20-2e-or	3.36	0.00	17.70	65.08	11.29	0.18	0.08	0.16	0.00	97.87	0.91	30.77	68.02	0.30	
p61-1-6-1c-or	3.51	0.00	18.61	65.00	11.66	0.17	0.00	0.07	0.08	99.26	0.83	31.09	67.95	0.13	

Post-grouse Canyon tephra sequence														
	Na_2O	MgO	Al_2O_3	SiO_2	K_2O	CaO	FeO	BaO	SrO	total	An	Ab	Or	Cn
p61-1-6-1m-or	3.40	0.01	18.56	64.62	11.83	0.16	0.00	0.11	0.00	98.78	0.78	30.10	68.92	0.20
p61-1-6-1e-or	3.09	0.00	17.62	62.73	11.64	0.15	0.00	0.19	0.07	95.63	0.76	28.43	70.46	0.35

Pre-rainier Mesa tephra sequence														
	Na_2O	MgO	Al_2O_3	SiO_2	K_2O	CaO	FeO	BaO	SrO	total	An	Ab	Or	Cn
r8-12-26-1c-or	4.32	0.00	17.96	65.27	9.99	0.29	0.15	0.78	0.00	98.78	1.43	38.54	58.63	1.41
r8-12-26-1m-or	4.15	0.00	17.93	64.37	10.05	0.30	0.16	0.56	0.00	97.54	1.50	37.59	59.89	1.02
r8-12-26-1e-or	4.46	0.00	17.99	63.05	9.84	0.29	0.13	0.40	0.00	96.16	1.43	39.91	57.93	0.72
r8-12-26-2c-or	4.45	0.00	18.15	65.20	9.90	0.27	0.17	0.22	0.00	98.38	1.34	39.88	58.38	0.40
r8-12-26-2m-or	4.47	0.00	18.05	65.58	9.93	0.29	0.18	0.36	0.00	98.87	1.43	39.78	58.14	0.65
r8-12-26-2e-or	4.46	0.00	18.32	65.15	9.95	0.30	0.17	0.26	0.00	98.62	1.48	39.73	58.32	0.47
r8-12-26-3c-or	4.41	0.00	18.14	65.14	9.74	0.39	0.17	0.26	0.00	98.26	1.94	39.78	57.80	0.47
r8-12-26-3m-or	4.51	0.00	17.85	65.00	9.84	0.38	0.14	0.16	0.00	97.91	1.87	40.17	57.67	0.29
r8-12-26-3e-or	4.48	0.00	17.72	64.92	9.67	0.36	0.17	0.28	0.00	97.63	1.79	40.37	57.33	0.51
r8-12-26-4c-pl	8.54	0.00	20.61	63.43	1.41	3.35	0.19	0.23	0.00	97.78	16.29	75.14	8.16	0.41
r8-12-26-4m-pl	8.55	0.00	21.31	62.71	1.19	3.90	0.27	0.10	0.00	98.06	18.73	74.29	6.80	0.18
r8-12-26-4e-pl	7.06	0.00	24.92	57.04	0.48	7.43	0.16	0.09	0.00	97.21	35.70	61.39	2.75	0.16
r8-12-26-4m-pl	8.12	0.00	22.12	60.74	0.89	5.18	0.21	0.05	0.00	97.32	24.72	70.13	5.06	0.09
r8-17b-3-1c-pl	8.04	0.00	21.97	61.72	1.61	3.78	0.27	0.58	0.00	98.00	18.48	71.12	9.37	1.04
r8-17b-3-1m-pl	8.38	0.01	22.04	63.56	1.70	3.32	0.27	0.27	0.00	99.58	16.11	73.59	9.82	0.48
r8-17b-3-1e-or	2.33	0.06	14.76	70.57	5.62	0.89	0.68	0.05	0.00	95.03	7.53	35.68	56.63	0.15
r8-17b-3-1e-pl	8.51	0.00	22.26	61.84	1.46	3.56	0.32	0.38	0.00	98.37	17.08	73.91	8.34	0.67
r8-17b-3-2c-or	4.36	0.00	17.76	65.87	9.91	0.17	0.09	0.24	0.00	98.43	0.85	39.56	59.15	0.44
r8-17b-3-2m-or	4.34	0.00	17.53	64.70	9.99	0.21	0.11	0.35	0.00	97.24	1.05	39.10	59.22	0.64
r8-17b-3-2e-or	4.36	0.07	16.83	63.01	9.95	0.34	0.23	0.62	0.00	95.43	1.67	38.86	58.35	1.12
r8-17b-3-3c-or	4.52	0.08	18.39	64.74	9.35	0.62	0.38	1.82	0.00	99.94	3.01	39.71	54.05	3.23
r8-17b-3-3m-or	4.48	0.09	18.48	64.23	9.35	0.71	0.35	1.56	0.00	99.27	3.46	39.51	54.25	2.78
r8-17b-3-3e-or	4.26	0.09	17.93	61.72	9.50	0.65	0.35	1.41	0.00	95.94	3.22	38.19	56.03	2.55
r8-17b-3-4c-or	4.64	0.07	18.10	66.38	9.74	0.36	0.29	0.41	0.00	100.04	1.76	40.95	56.56	0.73
r8-17b-3-4m-or	4.82	0.09	18.21	66.34	9.79	0.32	0.24	0.42	0.00	100.24	1.53	41.83	55.90	0.74
r8-17b-3-4e-or	4.64	0.08	17.50	64.74	9.70	0.33	0.26	0.35	0.00	97.63	1.62	41.15	56.60	0.63
r8-17b-3-5c-pl	6.37	0.11	25.60	56.99	0.51	8.73	0.51	0.50	0.00	99.38	41.48	54.77	2.88	0.87

APPENDIX 3. (Continued)

Pre-rainier Mesa tephra sequence															
	Na_2O	MgO	Al_2O_3	SiO_2	K_2O	CaO	FeO	BaO	SrO	total	An	Ab	Or	Cn	
r8-1-54-2c-pl	8.99	0.00	21.49	64.85	1.37	2.94	0.12	0.05	0.00	99.61	14.10	78.00	7.82	0.09	
r8-1-54-2m-pl	9.01	0.00	21.70	65.19	1.44	2.79	0.09	0.05	0.00	100.27	13.40	78.28	8.23	0.09	
r8-1-54-2e-pl	9.48	0.01	21.97	64.95	1.37	2.84	0.11	0.01	0.00	100.74	13.13	79.31	7.54	0.02	
r8-1-54-3c-or	1.76	0.05	12.41	74.71	4.55	0.27	0.56	0.10	0.00	94.48	3.03	35.75	60.81	0.41	
r8-1-54-4c-or	2.52	0.00	0.00	62.63	5.88	0.00	0.00	0.60	0.00	71.61	0.00	38.79	59.34	1.87	
r8-1-54-4c-or	4.18	0.01	18.39	65.90	10.45	0.18	0.10	0.09	0.00	99.32	0.89	37.41	61.54	0.16	
r8-1-54-4m-or	3.99	0.00	18.27	65.64	10.58	0.17	0.08	0.13	0.00	98.88	0.85	36.04	62.87	0.24	
r8-1-54-4e-or	4.02	0.00	18.61	65.11	10.65	0.17	0.06	0.14	0.00	98.79	0.84	36.06	62.85	0.25	
r8-1-54-5c-pl	8.96	0.00	21.15	65.01	1.35	2.86	0.13	0.02	0.00	99.49	13.82	78.37	7.77	0.04	
r8-1-54-5m-pl	9.01	0.00	21.61	64.86	1.24	2.96	0.11	0.03	0.00	99.83	14.26	78.57	7.11	0.05	
r8-1-54-5e-pl	9.35	0.00	21.90	65.89	1.43	2.67	0.09	0.01	0.00	101.36	12.54	79.45	7.99	0.02	
r8-1-54-6c-pl	8.93	0.00	19.56	64.01	1.42	2.79	0.11	0.02	0.00	96.85	13.51	78.26	8.19	0.04	
r8-1-54-6e-pl	8.83	0.01	19.79	64.93	1.38	2.78	0.14	0.09	0.00	97.96	13.60	78.19	8.04	0.16	
r8-3-154-1c-or	3.59	0.03	17.79	65.93	10.87	0.28	0.09	0.36	0.00	98.95	1.41	32.73	65.20	0.66	
r8-3-154-1e-or	3.31	0.02	17.29	63.36	11.05	0.27	0.11	0.15	0.00	95.57	1.39	30.76	67.57	0.28	
r8-3-154-2c-pl	8.81	0.02	17.55	68.20	6.71	0.00	0.53	0.00	0.00	99.88	0.00	60.67	39.33	0.00	
r8-3-154-2m-pl	8.89	0.02	17.45	66.85	6.57	0.00	0.57	0.00	0.00	98.42	0.00	61.45	38.55	0.00	
r8-3-154-2e-pl	8.47	0.02	15.95	65.14	6.59	0.00	0.55	0.02	0.00	94.80	0.00	59.85	40.11	0.04	
r8-3-154-3c-or	1.22	0.07	11.62	74.51	4.37	0.29	0.43	0.00	0.00	92.57	3.77	28.67	67.56	0.00	
r8-3-154-3c-or	3.46	0.01	17.69	64.36	11.30	0.18	0.13	0.06	0.00	97.21	0.90	31.44	67.55	0.11	
r8-3-154-3c-or	3.48	0.01	17.66	64.88	11.26	0.16	0.09	0.18	0.00	97.72	0.80	31.60	67.27	0.33	
r8-3-154-3m-or	3.56	0.02	17.82	63.96	11.46	0.18	0.07	0.00	0.00	97.08	0.89	31.79	67.32	0.00	
r8-3-154-3e-or	3.53	0.01	18.14	62.64	11.24	0.17	0.09	0.06	0.00	95.90	0.85	32.00	67.04	0.11	
r8-15-0m-or	4.69	0.01	18.58	64.80	9.64	0.34	0.19	0.26	0.00	98.52	1.67	41.60	56.26	0.47	
r8-15-0-1c-or	4.65	0.01	18.48	64.12	9.48	0.38	0.23	0.26	0.06	97.70	1.88	41.71	55.94	0.47	
r8-15-0-1e-or	3.33	0.02	15.44	63.46	9.06	0.36	0.21	0.20	0.00	92.12	2.09	34.94	62.55	0.42	
r8-15-0-2e-or	2.45	0.02	12.06	63.67	8.52	0.51	0.22	0.21	0.00	87.69	3.36	29.24	66.89	0.51	
r8-15-0-2m-pl	5.76	0.01	18.42	64.15	7.25	0.88	0.21	0.22	0.10	97.02	4.40	52.08	43.13	0.40	
r8-15-0-2m-or	4.48	0.00	17.78	65.09	9.57	0.28	0.22	0.25	0.00	97.68	1.41	40.80	57.34	0.46	
r8-15-0-2m-pl	8.96	0.01	20.38	63.42	1.36	3.01	0.32	0.07	0.00	97.56	14.42	77.70	7.76	0.12	
r8-15-0-2m-or	4.23	0.01	17.37	64.47	9.69	0.22	0.23	0.12	0.00	96.36	1.13	39.34	59.30	0.23	
r8-15-0-2m-or	4.25	0.00	17.80	64.28	9.54	0.24	0.18	0.18	0.00	96.49	1.24	39.74	58.68	0.34	

APPENDIX 3. (Continued)

Pre-rainier Mesa tephra sequence															
	Na_2O	MgO	Al_2O_3	SiO_2	K_2O	CaO	FeO	BaO	SrO	total	An	Ab	Or	Cn	
r8-15-0-2e-pl	10.22	0.00	22.27	59.73	1.29	2.68	0.30	0.00	0.01	96.54	11.80	81.44	6.76	0.00	
r8-15-0-3e-pl	6.94	0.00	19.07	50.88	1.58	3.18	0.24	0.01	0.00	81.90	18.07	71.36	10.55	0.02	
r8-15-0-3m-pl	8.60	0.00	20.83	62.39	1.15	3.13	0.19	0.06	0.05	96.41	15.58	77.49	6.82	0.11	
r8-15-0-3m-pl	8.80	0.01	22.11	62.58	1.35	3.58	0.24	0.02	0.00	98.71	16.95	75.40	7.61	0.03	
r8-15-0-3e-pl	7.95	0.00	21.08	53.04	1.24	3.71	0.24	0.04	0.00	87.34	18.94	73.45	7.54	0.07	
r8-15-0-3m-pl	8.46	0.00	22.44	63.78	1.00	4.14	0.18	0.00	0.04	100.05	20.06	74.17	5.77	0.00	
r8-15-0-3c-pl	7.24	0.01	24.94	58.60	0.50	7.07	0.12	0.02	0.09	98.62	34.03	63.07	2.87	0.04	
r8-15-0-3m-pl	7.95	0.00	23.48	60.62	0.74	5.64	0.14	0.00	0.11	98.68	26.98	68.81	4.21	0.00	
r8-15-0-3c-pl	7.14	0.00	25.27	59.22	0.46	7.26	0.06	0.02	0.14	99.57	35.01	62.31	2.64	0.04	
r8-15-0-4e-pl	8.89	0.00	22.41	61.97	1.08	3.90	0.20	0.00	0.00	98.46	18.33	75.62	6.04	0.00	
r8-15-0-4m-pl	8.38	0.01	22.16	62.42	0.85	4.46	0.28	0.00	0.00	98.59	21.61	73.48	4.90	0.00	
r8-15-0-4c-pl	8.19	0.00	22.72	62.09	0.75	5.04	0.19	0.00	0.00	99.00	24.28	71.41	4.30	0.00	
r8-15-0-5e-pl	7.59	0.00	23.70	61.31	0.75	5.72	0.29	0.09	0.12	99.61	28.07	67.39	4.38	0.16	
r8-15-0-5m-pl	7.80	0.01	23.51	61.17	0.74	5.66	0.32	0.27	0.09	99.60	27.27	68.01	4.25	0.48	
r8-15-0-5c-pl	7.48	0.01	24.34	60.34	0.61	6.29	0.37	0.25	0.08	99.81	30.47	65.57	3.52	0.44	
r8-15-0-5c-pl	7.22	0.00	23.84	59.59	0.61	6.42	0.39	0.08	0.06	98.27	31.72	64.55	3.59	0.14	
r8-15-0-8e-or	4.24	0.00	18.13	62.97	9.22	0.26	0.18	0.08	0.00	95.11	1.37	40.51	57.96	0.15	
r8-15-0-8e-or	4.30	0.00	17.88	63.84	9.15	0.29	0.15	0.06	0.00	95.28	1.53	40.98	57.38	0.12	
r8-15-0-8e-or	4.62	0.00	18.03	62.34	10.04	0.27	0.16	0.18	0.05	95.71	1.31	40.49	57.89	0.32	
r8-15-0-8m-or	4.30	0.00	17.62	64.42	10.35	0.25	0.11	0.11	0.05	97.23	1.23	38.15	60.42	0.20	
r8-15-0-8c-or	5.47	0.00	18.47	64.71	8.02	1.08	0.17	0.22	0.04	98.22	5.24	48.03	46.34	0.39	
r8-15-0-8m-pl	8.91	0.02	20.58	63.84	1.57	3.09	0.21	0.05	0.01	98.30	14.64	76.41	8.86	0.09	
r8-15-0-8m-or	4.66	0.00	18.08	65.11	9.76	0.43	0.15	0.21	0.09	98.50	2.09	41.02	56.52	0.37	
r8-1-129-1e-or	0.76	0.05	12.62	75.47	3.59	0.33	0.53	0.07	0.03	93.50	5.50	22.90	71.18	0.43	
r8-1-129-2e-or	3.96	0.01	18.40	65.47	10.71	0.18	0.09	0.22	0.04	99.11	0.89	35.51	63.19	0.40	
r8-1-129-2m-or	4.06	0.01	18.35	65.22	10.78	0.13	0.12	0.05	0.09	98.83	0.64	36.14	63.13	0.09	
r8-1-129-2c-or	3.98	0.00	18.47	65.25	10.56	0.16	0.12	0.20	0.01	98.77	0.80	36.00	62.84	0.37	
r8-1-129-1m-or	1.57	0.06	12.30	73.88	4.24	0.29	0.47	0.04	0.08	92.99	3.54	34.67	61.61	0.18	
r8-1-129-1c-or	1.92	0.06	12.32	73.59	4.51	0.29	0.50	0.11	0.06	93.42	3.16	37.87	58.53	0.44	
r8-1-129-3e-or	1.28	0.04	11.98	74.23	4.53	0.30	0.50	0.14	0.14	93.20	3.72	28.74	66.91	0.64	
r8-1-129-4c-pl	9.12	0.00	21.70	62.46	1.33	2.69	0.07	0.04	0.07	97.49	12.94	79.38	7.62	0.07	
r8-1-129-4m-pl	9.32	0.08	21.17	65.49	1.40	2.76	0.25	0.16	0.21	100.88	12.93	78.99	7.81	0.27	

APPENDIX 3. (Continued)

Pre-rainier Mesa tephra sequence															
	Na2O	MgO	Al2O3	SiO2	K2O	CaO	FeO	BaO	SrO	total	An	Ab	Or	Cn	
r8-1-129-4e-pl	9.53	0.08	21.40	64.25	1.43	2.73	0.27	0.18	0.15	100.05	12.56	79.31	7.83	0.30	
r8-1-129-5e-or	1.29	0.06	12.31	74.75	4.38	0.35	0.46	0.00	0.02	93.69	4.43	29.55	66.02	0.00	
r8-1-12-1m-or	4.64	0.00	18.33	65.65	9.78	0.26	0.06	0.00	0.00	98.72	1.28	41.36	57.36	0.00	
r8-1-12-1m-or	4.77	0.00	18.63	65.16	10.02	0.24	0.13	0.22	0.00	99.19	1.15	41.34	57.13	0.39	
r8-1-12-1c-or	4.64	0.00	18.51	65.75	9.85	0.25	0.12	0.13	0.04	99.31	1.22	41.12	57.43	0.23	
r8-1-12-2e-or	1.16	0.04	11.78	73.82	4.98	0.34	0.60	0.00	0.00	92.78	4.06	25.08	70.85	0.00	
r8-1-12-2m-or	1.45	0.05	11.72	74.66	5.13	0.35	0.58	0.00	0.09	94.09	3.85	28.89	67.25	0.00	
r8-12-1.75-3c-or	5.13	0.01	18.69	64.64	9.09	0.38	0.20	0.21	0.00	98.38	1.85	45.15	52.63	0.37	
r8-12-1.75-3m-or	5.23	0.00	18.67	64.44	9.05	0.38	0.15	0.11	0.03	98.07	1.84	45.81	52.15	0.19	
r8-12-1.75-3e-or	5.27	0.00	18.90	65.43	9.16	0.42	0.21	0.00	0.07	99.49	2.01	45.71	52.27	0.00	
r8-12-1.75-4c-or	6.79	0.02	18.62	65.56	6.88	0.31	0.24	0.06	0.01	98.53	1.49	59.04	39.36	0.11	
r8-12-1.75-4m-or	6.75	0.00	18.42	65.53	6.73	0.31	0.23	0.00	0.08	98.08	1.51	59.48	39.01	0.00	
r8-12-1.75-4e-or	6.85	0.00	18.78	64.54	7.01	0.29	0.25	0.00	0.00	97.72	1.38	58.94	39.68	0.00	
r8-12-1.75-5c-pl	7.53	0.00	24.51	58.40	0.62	6.52	0.17	0.04	0.26	98.06	31.20	65.20	3.53	0.07	
r8-12-1.75-5m-pl	7.48	0.00	24.21	59.31	0.68	6.29	0.17	0.13	0.26	98.54	30.41	65.44	3.91	0.23	
r8-12-1.75-5e-pl	7.44	0.00	24.01	58.93	0.63	6.40	0.18	0.13	0.28	98.02	30.98	65.16	3.63	0.23	
r8-12-1.75-6c-or	4.40	0.00	18.55	64.47	10.24	0.31	0.22	0.53	0.03	98.78	1.50	38.54	59.02	0.94	
r8-12-1.75-6m-or	4.34	0.01	18.58	64.41	10.14	0.32	0.22	0.32	0.01	98.38	1.57	38.57	59.29	0.57	
r8-12-1.75-6e-or	4.17	0.00	18.32	64.11	10.24	0.28	0.16	0.32	0.04	97.66	1.39	37.48	60.55	0.58	

CLINOPYROXENE ANALYSES

	Na_2O	MgO	Al_2O_3	SiO_2	K_2O	CaO	TiO_2	Cr_2O_3	MnO	FeO	Cl	F	total
Post-grouse Canyon tephra sequence													
m23a-9-	0.41	11.13	0.60	51.34	0.00	20.36	0.09	0.07	1.60	12.94			98.59
m23a-9-	0.41	11.52	0.71	53.01	0.00	20.75	0.14	0.00	1.33	12.55			100.41
m19-6-4	0.51	12.97	1.35	51.92	0.00	22.06	0.23	0.03	0.95	9.04			99.06
m19-6-4	0.46	12.46	1.23	51.67	0.01	22.32	0.26	0.00	0.86	8.21			97.47
m19-6-4	0.49	12.97	1.42	51.01	0.01	22.17	0.27	0.03	0.92	9.03			98.32
m21-7-4	0.37	11.47	0.73	52.01	0.01	19.94	0.16	0.00	1.51	13.30			99.49
m21-7-4	0.44	10.77	0.60	50.81	0.00	19.79	0.17	0.00	1.44	12.62			96.63
m21-7-7	0.39	9.49	0.65	52.02	0.01	19.58	0.17	0.00	1.92	16.00			100.23
m21-7-7	0.40	10.32	0.76	52.91	0.01	19.32	0.10	0.00	1.69	15.76			101.27
Pre-rainier Mesa tephra sequence													
r12-1.75	0.51	14.79	1.70	51.43	0.00	19.58	0.80	0.16	0.49	9.82	0.06	0.18	99.51
r12-1.75	2.00	14.64	5.51	46.08	0.54	10.80	1.23	0.22	1.83	11.83	0.08	1.42	96.19
r12-1.75	2.06	15.38	5.70	49.06	0.74	10.88	1.24	0.13	1.84	11.64	0.07	1.54	100.30
r1-54-1-[	0.42	15.04	2.01	51.60	0.09	20.24	1.03	0.24	0.36	9.11	0.07	0.15	100.36
r1-54-1e	0.44	14.86	1.95	51.62	0.10	20.29	1.04	0.24	0.35	9.30	0.07	0.24	100.51
r1-54-2c	0.52	15.25	1.91	52.13	0.10	20.72	0.79	0.18	0.43	8.66	0.06	0.14	100.89
r1-54-2e	0.47	15.77	3.75	48.87	0.10	19.66	1.19	0.17	0.47	9.16	0.06	0.13	99.80
r1-54-3c	0.58	14.45	2.08	45.69	0.11	18.27	0.95	0.23	0.46	10.21	0.08	0.21	93.32

ORTHOPYROXENE ANALYSES

Post-grouse Canyon tephra sequence

	F	Na_2O	MgO	Al_2O_3	SiO_2	Cl	K_2O	CaO	TiO_2	Cr_2O_3	MnO	FeO	total
m23a-3-6c-opx	0.07	0.00	7.86	0.10	46.07	0.02	0.02	2.08	0.08	0.01	4.69	35.08	96.07
m23a-3-6e-opx	0.00	0.02	7.30	0.17	48.26	0.00	0.02	1.22	0.10	0.00	4.76	37.84	99.68
m23a-3-6m-opx	0.00	0.00	8.96	0.22	48.84	0.00	0.02	1.26	0.11	0.00	4.38	35.99	99.80
m23a-3-7c-opx	0.00	0.01	6.97	0.60	46.54	0.00	0.00	1.27	0.11	0.02	5.24	37.49	98.27
m23a-3-7e-opx	0.00	0.04	7.01	0.31	47.75	0.01	0.00	1.65	0.11	0.02	4.97	37.46	99.34
m23a-3-7m-opx	0.02	0.03	6.63	0.15	47.22	0.01	0.03	1.30	0.13	0.01	5.12	38.20	98.86
m21-7-6c-opx	0.00	0.05	17.03	1.60	50.55	0.00	0.02	1.61	0.37	0.00	2.33	24.71	98.28
m21-7-6e-opx	0.00	0.01	14.24	1.27	47.94	0.00	0.02	1.27	0.41	0.03	3.25	27.77	96.21
m21-7-6m-opx	0.00	0.02	15.74	1.49	49.87	0.00	0.02	1.41	0.40	0.00	2.65	26.79	98.38

MAGNETITE AND ILMENITE ANALYSES

Post-grouse Canyon tephra sequence

	MgO	Al_2O_3	SiO_2	CaO	TiO_2	Cr_2O_3	MnO	FeO	V_2O_5	NiO	total
m23a-9-9c-il	0.63	0.02	0.05	0.04	48.98	0.02	2.88	44.88	0.19	0.04	97.73
m23a-9-9e-il	0.56	0.03	0.05	0.02	48.62	0.01	3.01	46.00	0.31	0.00	98.62
m23a-9-11c-il	0.57	0.02	0.03	0.04	49.37	0.00	3.21	45.17	0.25	0.05	98.71
m23a-9-11e-il	0.54	0.02	0.03	0.03	49.36	0.00	3.16	45.46	0.27	0.07	98.95
m23a-36-1c-mt	0.31	0.87	0.17	0.26	12.40	0.07	1.62	77.28	0.06	0.01	93.05
m23a-36-1e-mt	0.22	0.87	0.11	0.08	12.20	0.04	1.58	77.25	0.02	0.05	92.40
m23a-36-2c-mt	0.74	1.61	0.06	0.03	6.71	0.07	1.05	82.21	0.23	0.09	92.80
m23a-36-2e-mt	0.18	1.18	0.11	0.16	7.44	0.06	0.47	79.18	0.16	0.02	88.96
m23a-36-3-mt	0.23	0.83	0.10	0.06	12.85	0.06	1.73	78.71	0.07	0.00	94.63
m23a-36-4c-mt	0.21	0.85	0.10	0.02	12.54	0.07	1.61	80.27	0.03	0.00	95.69
m23a-36-4e-mt	0.21	1.24	0.14	0.06	12.88	0.04	1.80	77.02	0.04	0.02	93.43
m19-7c-mt	0.32	0.96	0.05	0.02	10.17	0.00	1.81	80.69	0.14	0.06	94.21
m19-7e-mt	0.34	1.01	0.06	0.02	9.98	0.01	1.85	80.29	0.11	0.02	93.70
m19-8c-mt	0.37	0.97	0.07	0.06	9.92	0.00	1.64	81.82	0.12	0.00	94.97
m19-8e-mt	0.37	1.14	0.33	0.07	9.77	0.00	1.89	78.55	0.11	0.02	92.25
m19-9c-mt	0.38	0.93	0.05	0.02	10.27	0.00	1.79	82.22	0.17	0.00	95.82
m19-9e-mt	0.38	1.03	0.08	0.06	10.30	0.00	1.69	80.55	0.20	0.00	94.29
m19-10c-il	1.98	0.66	0.04	0.07	28.70	0.00	0.60	61.70	0.40	0.00	94.14
m19-10e-il	2.47	0.18	0.06	0.06	40.50	0.00	0.84	51.24	0.49	0.00	95.84
m19-10c-il	1.37	0.90	0.30	0.31	28.27	0.46	0.80	63.15	0.53	0.41	96.50
m19-11c-mt	1.04	2.56	0.22	0.18	3.30	0.56	0.75	85.93	0.60	0.51	95.65
m19-11e-mt	0.67	1.00	0.27	0.17	0.70	0.52	0.74	89.38	0.54	0.47	94.46
m19-11m-mt	1.24	2.71	0.26	0.18	0.89	0.53	0.73	88.68	0.47	0.46	96.16
m19-12c-mt	1.19	3.11	0.57	0.18	3.94	0.56	0.69	82.72	0.50	0.48	93.94
m19-12e-mt	0.51	0.82	0.25	0.17	1.44	0.51	0.69	89.21	0.56	0.48	94.64
m23a-9-1c-mt	0.00	1.04	0.30	0.16	14.43	0.39	1.91	79.74	0.25	0.47	98.70
m23a-9-1e-mt	0.00	1.04	0.38	0.18	13.61	0.40	1.92	78.12	0.31	0.41	96.38
m23a-9-2c-mt	0.00	1.02	0.63	0.20	14.39	0.43	1.96	77.77	0.31	0.46	97.17
m23a-9-2e-mt	0.00	1.00	0.34	0.19	14.35	0.41	2.23	77.38	0.25	0.45	96.59
m23a-9-3c-mt	0.00	1.12	0.29	0.18	13.91	0.39	1.82	79.73	0.30	0.45	98.19
m23a-9-3c-mt	0.00	1.08	0.28	0.21	13.70	0.42	1.92	79.33	0.36	0.47	97.77

Post-grouse Canyon tephra sequence											
	MgO	Al_2O_3	SiO_2	CaO	TiO_2	Cr_2O_3	MnO	FeO	V_2O_5	NiO	total
m21-7-8c-mt	0.30	0.96	0.20	0.08	12.97	0.03	1.74	77.75	0.11	0.01	94.14
m21-7-8e-mt	0.37	0.99	0.16	0.07	13.24	0.05	1.84	77.71	0.14	0.02	94.58
m21-7-9-mt	0.48	1.12	0.09	0.13	12.38	0.06	1.47	79.19	0.15	0.00	95.05
m21-7-10c-mt	0.35	0.91	0.10	0.13	13.05	0.02	1.76	78.07	0.07	0.05	94.51
m21-7-10e-mt	0.27	0.86	0.08	0.04	13.76	0.00	1.94	77.26	0.05	0.06	94.33

Pre-rainier Mesa tephra sequence											
	MgO	Al_2O_3	SiO_2	CaO	TiO_2	Cr_2O_3	MnO	FeO	V_2O_5	NiO	total
r12-1.75-1c-mt	0.81	0.96	0.24	0.19	5.59	0.46	2.93	83.56	0.00	0.37	95.10
r12-1.75-1e-mt	0.85	0.95	0.22	0.21	5.65	0.44	2.71	83.33	0.27	0.35	94.97
r12-1.75-2c-mt	0.74	0.98	0.22	0.21	5.66	0.40	2.90	83.55	0.29	0.42	95.36
r12-1.75-2e-mt	0.78	0.91	0.23	0.19	5.70	0.42	2.89	82.79	0.32	0.39	94.61
r12-1.75-2-mt	0.84	0.93	0.23	0.17	5.59	0.64	2.91	83.31	0.29	0.38	95.28
r12-1.75-3c-mt	3.41	2.87	0.25	0.19	11.12	0.49	1.35	75.37	0.44	0.41	95.90
r12-1.75-3e-mt	3.39	2.72	0.24	0.19	10.72	0.45	1.47	75.51	0.34	0.41	95.43
r12-1.75-4c-il	1.57	0.22	0.24	0.64	43.01	0.70	5.13	46.46	0.50	0.39	98.86
r12-1.75-5-il	1.58	0.21	0.23	0.77	42.75	1.30	5.47	45.96	0.54	0.38	99.19
r12-1.75-6e-il	1.64	0.23	0.19	0.19	44.91	0.47	5.45	46.45	0.47	0.36	100.36
r12-1.75-6c-il	1.54	0.20	0.21	0.22	44.82	0.76	5.45	46.72	0.45	0.40	100.78
r1-54-1c-mt	0.45	0.94	0.65	0.27	5.93	0.52	4.19	79.84	0.29	0.36	93.45
r1-54-2c-mt	0.61	1.33	0.25	0.18	5.50	0.42	2.05	85.22	0.16	0.39	96.10
r1-54-2e-mt	0.68	1.40	0.24	0.19	5.48	0.90	1.99	84.87	0.24	0.38	96.36
r1-54-3c-mt	0.66	1.32	0.22	0.18	5.47	0.85	2.14	86.02	0.19	0.37	97.42
r1-54-3e-mt	0.63	1.25	0.23	0.21	5.54	1.05	2.02	86.14	0.17	0.39	97.62
r1-54-4-mt	3.54	2.76	0.69	0.49	14.73	1.41	0.51	66.17	0.75	0.41	91.46
r1-54-5-mt	2.26	2.46	0.48	0.44	21.69	1.26	0.48	63.67	0.90	0.36	94.00
r1-54-6-il	5.13	1.85	0.23	0.26	45.23	1.67	0.35	42.66	0.74	0.33	98.44
r1-54-7-mt	2.98	3.65	0.35	0.30	34.31	0.47	0.40	50.70	1.03	0.31	94.50
r1-54-8-mt	2.89	2.18	0.30	0.20	17.44	0.64	0.63	69.58	0.56	0.40	94.81
r1-54-8c-mt	2.87	2.02	0.25	0.20	12.93	0.68	0.68	73.95	0.41	0.39	94.38
r1-54-8e-mt	2.55	1.85	0.31	0.21	24.57	0.70	0.56	62.41	0.64	0.42	94.23

Pre-rainier Mesa tephra sequence											
	MgO	Al_2O_3	SiO_2	CaO	TiO_2	Cr_2O_3	MnO	FeO	V_2O_5	NiO	total
r8-3-156-1c1-il	0.95	0.08	0.02	0.01	41.73	0.01	3.01	43.37	0.27		89.44
r8-3-156-1e1-il	0.69	0.12	0.05	0.03	41.12	0.01	3.04	43.09	0.26		88.42
r8-3-156-2c1-il	2.12	0.08	0.03	0.00	40.46	0.01	4.35	42.43	0.34		89.83
r8-3-156-2e1-il	2.08	0.11	0.03	0.00	40.53	0.00	4.18	42.39	0.32		89.64
r8-3-156-3e1-il	1.02	0.09	0.02	0.00	42.71	0.00	3.58	43.40	0.21		91.03
r8-3-156-3e1-il	1.01	0.10	0.04	0.00	42.20	0.00	3.42	43.03	0.33		90.13
r8-3-156-4e1-il	0.87	0.08	0.02	0.00	42.78	0.00	4.28	41.50	0.27		89.80
r8-3-156-5c1-il	1.11	0.08	0.01	0.00	42.90	0.00	2.90	44.48	0.26		91.74
r8-3-156-5e1-il	1.11	0.09	0.00	0.00	42.70	0.00	2.88	44.37	0.31		91.45
r8-3-156-2c1-mt	0.39	0.99	0.04	0.00	4.84	0.02	1.33	79.19	0.08		86.87
r8-3-156-2e1-mt	0.46	1.11	0.18	0.04	4.96	0.01	1.41	76.06	0.02		84.25
r8-3-156-3c1-mt	0.43	1.09	0.06	0.00	4.84	0.02	1.36	78.21	0.00		86.03
r8-3-156-3e1-mt	0.48	1.20	0.06	0.02	4.90	0.04	1.38	76.36	0.07		84.51
r8-3-156-4e1-mt	0.51	1.24	0.12	0.01	5.50	0.02	1.58	75.58	0.03		84.59
r8-3-156-5c1-mt	0.38	1.40	0.04	0.00	4.83	0.05	1.80	78.00	0.07		86.57
r8-3-156-5e1-mt	0.42	1.18	0.02	0.02	4.46	0.04	1.66	75.93	0.03		83.75
r8-16-2-1c1-il	1.67	0.08	0.01	0.02	43.46	0.03	3.98	48.10	0.19		97.55
r8-16-2-1e1-il	1.63	0.07	0.00	0.01	43.42	0.02	3.96	47.72	0.30		97.12
r8-16-2-1e1-mt	0.73	0.81	0.03	0.00	5.24	0.06	2.13	83.63	0.10		92.74
r8-16-2-2e1-il	1.64	0.08	0.02	0.00	43.22	0.03	4.20	47.67	0.28		97.15
r8-16-2-3e1-il	1.65	0.10	0.00	0.00	42.06	0.05	3.15	49.67	0.23		96.91
r8-16-2-3e1-mt	0.86	0.95	0.04	0.00	5.64	0.07	2.05	83.51	0.12		93.24
r8-16-2-1c1eq-il	1.64	0.14	0.01	0.00	44.15	0.00	4.29	48.13	0.26		98.62
r8-16-2-1e1eq-il	1.56	0.10	0.06	0.00	42.54	0.00	4.53	47.61	0.28		96.69
r8-16-2-1e2eq-il	1.56	0.07	0.02	0.00	43.45	0.00	4.21	47.94	0.28		97.53
r8-16-2-1e3eq-il	1.69	0.08	0.01	0.00	44.13	0.00	4.34	47.67	0.34		98.26
r8-16-2-1e1eq-m	0.77	0.92	0.06	0.00	5.23	0.03	2.40	83.64	0.09		93.13
r8-16-2-1m1eq-m	0.72	0.84	0.04	0.00	5.18	0.02	2.27	83.02	0.12		92.22
r8-16-2-1e2eq-m	0.77	0.92	0.06	0.25	5.52	0.03	2.35	82.71	0.06		92.68

HORNBLENDE ANALYSES

Post-grouse Canyon tephra sequence	F	Na2O	MgO	Al2O3	SiO2	Cl	K2O	CaO	TiO2	Cr2O3	MnO	FeO	total
m23a-9-3c-hb	0.84	2.17	7.19	7.13	45.06	0.09	0.83	9.48	1.81	0.00	1.36	23.88	99.82
m23a-9-5c-hb	0.75	1.94	6.34	6.54	43.17	0.09	0.74	9.16	1.37	0.00	1.53	25.73	97.35
m23a-9-5e-hb	0.80	1.96	6.97	6.45	42.56	0.11	0.79	9.61	1.59	0.00	1.40	23.60	95.83
m23a-9-5m-hb	0.56	1.88	5.93	6.39	42.68	0.11	0.70	9.26	1.30	0.02	1.54	26.00	96.36
m23a-9-10c-hb	0.78	1.86	7.46	6.11	42.99	0.08	0.61	9.14	1.37	0.02	1.55	23.77	95.74
m23a-9-10e-hb	0.73	1.97	7.60	6.59	44.89	0.09	0.67	9.43	1.33	0.04	1.54	23.92	98.79
m23a-9-7c-hb	0.41	2.28	11.89	11.67	38.58	0.00	0.86	10.70	3.01	0.00	0.50	13.19	93.09
m23a-9-7e-hb	0.43	2.41	11.31	11.23	38.71	0.04	0.97	10.52	2.65	0.00	0.71	15.39	94.36
m19-6-1c-hb	0.61	1.77	9.43	6.89	44.93	0.08	0.73	10.06	1.48	0.00	1.43	19.95	97.35
m19-6-1e-hb	0.78	1.82	9.52	7.30	44.72	0.12	0.78	9.94	1.37	0.00	1.41	20.17	97.92
m19-6-2c-hb	0.62	1.89	9.44	6.64	46.05	0.11	0.75	10.03	1.35	0.01	1.55	20.91	99.33
m19-6-2e-hb	0.74	1.73	9.23	6.35	46.48	0.11	0.74	9.88	1.19	0.01	1.49	20.46	98.41
m19-6-3c-hb	0.75	1.78	9.15	6.89	45.10	0.10	0.78	9.92	1.37	0.07	1.50	20.39	97.78
m19-6-3e-hb	0.72	1.73	8.96	6.67	44.24	0.11	0.80	10.04	1.36	0.05	1.65	20.55	96.87
m19-6-3m-hb	0.50	1.77	9.04	6.91	44.37	0.11	0.81	10.12	1.37	0.04	1.49	20.90	97.43
m19-6-6c-hb	0.59	1.70	9.12	6.42	44.06	0.13	0.73	10.14	1.37	0.04	1.69	20.37	96.36
m23a-3-5c-hb	0.36	1.97	6.05	6.67	42.55	0.12	0.76	9.30	1.68	0.00	1.59	25.34	96.38
m23a-3-5e-hb	0.51	1.87	5.76	5.98	42.25	0.10	0.66	8.87	1.49	0.00	1.65	25.50	94.64
m23a-3-7c-hb	0.47	1.94	6.58	7.02	42.14	0.09	0.73	9.52	1.53	0.00	1.45	24.05	95.52
m23a-3-7e-hb	0.49	1.94	6.38	6.41	45.31	0.14	0.73	9.19	1.23	0.00	1.59	24.95	98.35
m23a-3-9c-hb	0.59	2.01	7.44	6.39	44.05	0.09	0.76	9.72	1.52	0.03	1.39	23.44	97.43
m23a-3-9e-hb	0.63	2.24	6.64	7.13	45.01	0.15	0.76	9.48	1.47	0.00	1.48	24.70	99.68
m23a-3-9m-hb	0.56	2.10	7.48	6.89	44.08	0.10	0.82	10.11	1.64	0.00	1.45	22.52	97.75
m21-7-3c-hb	0.41	2.07	7.34	6.95	41.14	0.07	0.86	9.58	1.72	0.00	1.50	23.04	94.68
m21-7-3e-hb	0.49	2.00	7.68	6.90	42.84	0.08	0.74	9.49	1.61	0.00	1.48	23.52	96.85
Pre-rainier Mesa tephra sequence													
r12-1.75-1-hb	0.41	2.58	13.50	12.49	42.08	0.10	0.69	11.02	2.65	0.14	0.35	12.06	98.06
r12-1.75-1e-hb	0.24	2.59	13.58	12.37	41.81	0.09	0.66	11.07	2.70	0.21	0.30	11.91	97.53
r12-1.75-2c-hb	1.50	2.07	15.09	5.80	48.63	0.10	0.62	10.68	1.30	0.18	1.70	11.57	99.23
r12-1.75-2e-hb	1.54	2.09	15.73	5.66	49.70	0.09	0.57	10.68	1.17	0.16	1.89	11.23	100.51

BIOTITE ANALYSES

Post-grouse Canyon tephra sequence	F	Na_2O	MgO	Al_2O_3	SiO_2	Cl	K_2O	CaO	TiO_2	Cr_2O_3	MnO	FeO	total
m19-6-5c-bt	0.92	0.71	8.67	13.40	38.40	0.11	7.56	0.15	3.87	0.02	0.52	18.69	93.03
m19-6-5e-bt	1.11	0.34	8.56	12.71	38.15	0.12	7.98	0.14	4.14	0.05	0.48	18.23	92.02
m19-6-5m-bt	1.01	0.55	8.14	11.63	37.82	0.14	7.55	0.22	4.10	0.03	0.52	18.85	90.56
m19-6-7c-bt	0.30	0.25	5.66	6.95	25.85	0.12	3.75	0.21	2.07	0.00	0.22	11.64	57.01
m19-6-7e-bt	1.01	0.38	8.82	10.41	36.98	0.12	7.27	0.24	4.01	0.01	0.54	18.33	88.10
m19-6-7c-bt	1.11	0.35	9.16	12.12	39.10	0.13	8.01	0.10	4.07	0.03	0.56	19.59	94.32
m19-6-7m-bt	0.85	1.05	8.49	10.23	39.31	0.14	6.47	0.21	3.61	0.00	0.40	18.37	89.12
m23a-3-9c-bt	5.48	0.19	9.87	9.03	45.36	0.18	6.28	0.08	2.09	0.00	0.84	20.13	99.51
m23a-3-9e-bt	8.34	0.25	13.43	11.82	44.40	0.18	8.39	0.17	1.28	0.00	1.13	10.05	99.44
m23a-3-9m-bt	3.72	0.08	6.97	10.86	48.21	0.14	5.25	0.06	1.56	0.00	0.75	12.36	89.96
m23a-3-9m-bt	2.57	0.05	5.58	5.80	62.12	0.08	3.10	0.06	2.61	0.00	0.45	18.71	101.10
m23a-3-9m-bt	2.94	0.10	5.65	5.85	64.62	0.09	4.05	0.03	1.37	0.00	0.56	12.81	98.06
m23a-3-9c-bt	2.86	0.27	3.58	3.43	34.25	0.09	4.34	0.14	1.25	0.00	0.96	30.20	81.38
m21-7-1c-bt	0.55	0.16	7.84	10.62	40.80	0.07	6.97	0.54	4.05	0.01	0.33	18.38	90.31
m21-7-1e-bt	0.52	0.17	7.90	10.49	43.10	0.06	7.56	0.52	3.94	0.00	0.26	17.11	91.63
m21-7-5c-bt	0.45	0.24	7.36	10.39	40.85	0.08	7.26	0.51	4.03	0.00	0.28	18.07	89.51
m21-7-5e-bt	0.50	0.35	8.10	11.83	36.43	0.07	7.99	0.18	4.89	0.00	0.43	20.20	90.97
Pre-rainier Mesa tephra sequence													
r12-1.75-4c-bt	2.36	0.50	15.35	12.46	38.22	0.11	7.38	0.47	3.57	0.14	0.79	14.00	95.35
r12-1.75-4e-bt	2.08	0.43	14.69	12.29	39.73	0.12	7.59	0.35	3.29	0.12	0.83	12.11	93.62
r12-1.75-7-bt	1.74	0.46	14.31	12.44	38.15	0.09	7.55	0.34	3.84	0.15	0.66	13.77	93.50

APPENDIX 4

BIBLIOGRAPHY

APPENDIX 4. $^{40}Ar/^{39}Ar$ Analyses

Key:

Pre-rainier Mesa tephra sequence
- 12R8 series
- AFB series
- *RM92 series

Post-grouse Canyon tephra sequence
- M* series
- P6293 series

Pre-ammonia Tanks tephra sequence
- AT92 series
- 2AT92 series
- AT19 series
- 3EAT92 series
- 7-30-92
- 2EAT92 series

UAF039-15 12R8-0 SWNVF R80-21.TXT

Weighted average of J from standards = 0.000486 +/- 0.000008

Grain #	Cumulative 39Ar	40Ar/39Ar measured	37Ar/39Ar measured	36Ar/39Ar measured	% Atmospheric 40Ar	37Ca/39K	+/-	40*/39K	+/-	Age (Ma)	+/- (Ma)
21	0.172	13.514	0.010	0.001	1.747	0.010	0.000	13.250	0.062	11.572	0.054
22	0.245	14.046	1.145	0.003	6.090	1.145	0.005	13.174	0.071	11.506	0.062
232	0.248	16.624	0.026	0.012	20.901	0.026	0.004	13.127	0.589	11.465	0.513
232	0.382	13.482	0.010	0.000	0.388	0.010	0.000	13.401	0.066	11.704	0.057
241	0.475	14.278	0.013	0.004	7.974	0.013	0.000	13.114	0.066	11.454	0.057
242	0.948	13.393	0.009	0.000	0.174	0.009	0.000	13.341	0.077	11.652	0.067
25	0.997	13.507	0.009	0.001	1.808	0.009	0.000	13.235	0.072	11.559	0.063
26	0.997	14.558	1.152	0.003	6.206	1.153	0.018	13.638	1.992	11.910	1.734
272	1.000	14.177	0.010	0.004	7.975	0.010	0.005	13.020	0.682	11.373	0.593
272	1.000	15.010	0.075	-0.021	-41.172	0.075	0.147	21.151	18.929	18.438	16.417

UAF039-14 12R8-3 SWNVF

Weighted average of J from standards = 0.000486 +/- 0.000008

Grain #	Cumulative 39Ar	40Ar/39Ar measured	37Ar/39Ar measured	36Ar/39Ar measured	% Atmospheric 40Ar	37Ca/39K	+/-	40*/39K	+/-	Age (Ma)	+/- (Ma)
1	0.018	23.272	0.779	0.036	45.193	0.780	0.004	12.746	0.147	11.133	0.128
1	0.019	18.761	0.905	0.024	37.213	0.905	0.057	11.768	6.488	10.282	5.653
12	0.395	16.334	0.005	0.010	18.703	0.005	0.000	13.256	0.072	11.578	0.063
2	0.530	13.680	0.015	0.001	2.040	0.015	0.000	13.373	0.067	11.679	0.058
5	0.623	13.946	0.008	0.002	3.875	0.008	0.000	13.378	0.067	11.684	0.059
6	0.654	20.598	0.493	0.026	37.015	0.494	0.002	12.960	0.109	11.320	0.095
8	0.713	18.718	0.015	0.019	30.069	0.015	0.000	13.070	0.084	11.415	0.073
12	0.714	112.344	0.055	0.363	95.582	0.055	0.032	4.962	3.936	4.343	3.440
19	1.000	17.142	0.047	0.009	14.855	0.047	0.000	14.571	0.076	12.722	0.066

UAF039-12 12R8-4A SWNVF

Weighted average of J from standards = 0.000486 +/- 0.000008

Grain #	Cumulative 39Ar	40Ar/39Ar measured	37Ar/39Ar measured	36Ar/39Ar measured	% Atmospheric 40Ar	37Ca/39K	+/-	40*/39K	+/-	Age (Ma)	+/- (Ma)
12	0.195	19.220	0.015	0.019	28.898	0.015	0.000	13.646	0.081	11.917	0.070
13	0.254	16.062	0.032	0.005	8.932	0.032	0.000	14.601	0.076	12.748	0.066
14	0.285	20.782	0.170	0.021	29.400	0.171	0.001	14.654	0.092	12.794	0.080
15	0.417	17.007	0.014	0.006	9.595	0.014	0.000	15.349	0.083	13.399	0.072
16	0.481	17.484	0.031	0.010	16.183	0.031	0.000	14.631	0.076	12.775	0.067
17	0.592	18.895	0.013	0.013	20.884	0.013	0.000	14.926	0.083	13.031	0.072
18	0.680	15.792	0.026	0.005	9.480	0.026	0.000	14.270	0.072	12.460	0.063
19	0.725	47.634	0.420	0.116	71.767	0.420	0.002	13.444	0.206	11.741	0.179
20	0.783	22.401	0.139	0.025	33.527	0.139	0.001	14.873	0.102	12.985	0.089
21	0.906	21.535	0.044	0.025	34.136	0.044	0.000	14.165	0.095	12.369	0.083
22	1.000	28.335	0.087	0.050	52.257	0.087	0.000	13.515	0.118	11.803	0.102

UAF039-9 12R8-7A SWNFV

Weighted average of J from standards = 0.000486 +/- 0.000008

Grain #	Cumulative 39Ar	40Ar/39Ar measured	37Ar/39Ar measured	36Ar/39Ar measured	% Atmospheric 40Ar	37Ca/39K	+/-	40*/39K	+/-	Age (Ma)	+/- (Ma)
10	0.102	18.287	0.080	0.012	19.338	0.080	0.000	14.728	0.079	12.859	0.069
11	0.178	21.455	0.186	0.023	32.206	0.186	0.001	14.527	0.091	12.684	0.079
1	0.358	15.400	0.021	0.003	4.868	0.021	0.000	14.623	0.088	12.768	0.077
2	0.442	17.280	0.150	0.009	14.849	0.150	0.001	14.691	0.076	12.827	0.066
3	0.613	18.266	0.030	0.013	20.753	0.030	0.000	14.453	0.093	12.619	0.081
4	0.692	34.125	0.343	0.066	57.391	0.343	0.002	14.532	0.147	12.688	0.128
5	0.798	17.006	0.025	0.008	14.086	0.025	0.000	14.586	0.075	12.736	0.065
6	0.809	15.471	0.024	0.009	18.098	0.024	0.000	12.648	0.087	11.048	0.076
1	0.810	4.833	0.125	4.809	29574.001	0.125	0.010	#######	10.289	-2051.714	28.878
2	0.840	28.858	0.022	0.048	49.670	0.022	0.000	14.510	0.121	12.669	0.105
8	0.910	16.378	0.027	0.006	10.545	0.027	0.000	14.625	0.078	12.769	0.068
9	1.000	17.756	0.034	0.010	17.106	0.034	0.000	14.695	0.077	12.830	0.067

UAF039-16 12R8-8-9 SWNVF

Weighted average of J from standards = 0.000486 +/- 0.000008

Grain #	Cumulative 39Ar	40Ar/39Ar measured	37Ar/39Ar measured	36Ar/39Ar measured	% Atmospheric 40Ar	37Ca/39K	+/-	40*/39K	+/-	Age (Ma)	+/- (Ma)
13	0.088	15.529	0.050	0.005	9.038	0.050	0.000	14.099	0.070	12.312	0.061
14	0.159	14.564	0.024	0.000	0.669	0.024	0.000	14.438	0.069	12.606	0.060
15	0.263	14.857	0.022	0.001	2.201	0.022	0.000	14.502	0.068	12.662	0.060
16	0.468	15.624	0.017	0.003	6.224	0.017	0.000	14.625	0.071	12.769	0.062
17	0.744	15.443	0.024	0.002	4.381	0.024	0.000	14.739	0.072	12.869	0.063
19	0.882	17.405	0.047	0.009	14.630	0.047	0.000	14.835	0.077	12.952	0.067
20	0.967	15.200	0.116	0.001	1.984	0.116	0.001	14.872	0.071	12.984	0.062
21	1.000	14.786	0.020	0.001	2.324	0.020	0.000	14.415	0.076	12.586	0.066

UAF039-10 12R8-12-13-16 SWNVF

Weighted average of J from standards = 0.000486 +/- 0.000008

Grain #	Cumulative 39Ar	40Ar/39Ar measured	37Ar/39Ar measured	36Ar/39Ar measured	% Atmospheric 40Ar	37Ca/39K	+/-	40*/39K	+/-	Age (Ma)	+/- (Ma)
27	0.218	14.818	0.021	0.000	0.599	0.021	0.000	14.701	0.080	12.835	0.070
28	0.319	14.851	0.016	0.000	0.426	0.016	0.000	14.760	0.074	12.886	0.064
29	0.557	14.858	0.034	0.000	0.848	0.034	0.000	14.704	0.069	12.838	0.060
30	0.590	41.190	0.039	0.092	66.349	0.039	0.000	13.851	0.170	12.096	0.148
31	0.718	16.924	0.019	0.007	12.455	0.019	0.000	14.791	0.075	12.914	0.065
33	0.742	14.849	0.045	0.001	1.797	0.045	0.000	14.555	0.074	12.708	0.064
35	0.753	15.789	1.595	0.005	8.803	1.597	0.007	14.388	0.091	12.563	0.079
38	0.815	14.934	0.018	0.000	0.779	0.018	0.000	14.790	0.070	12.912	0.061
39	0.841	22.011	1.688	0.027	35.249	1.690	0.007	14.249	0.094	12.442	0.082
40	0.955	15.079	0.017	0.001	1.437	0.017	0.000	14.834	0.081	12.951	0.070
41	1.000	14.818	0.335	0.001	1.002	0.335	0.002	14.645	0.072	12.786	0.062

UAF039-13 12R8-17A SWNVF

Weighted average of J from standards = 0.000486 +/- 0.000008

Grain #	Cumulative 39Ar	40Ar/39Ar measured	37Ar/39Ar measured	36Ar/39Ar measured	% Atmospheric 40Ar	37Ca/39K	+/-	40*/39K	+/-	Age (Ma)	+/- (Ma)
29	0.008	16.576	3.335	0.008	13.621	3.342	0.015	14.324	0.262	12.507	0.228
30	0.177	16.852	0.069	0.007	12.922	0.069	0.000	14.650	0.074	12.791	0.064
312	0.177	22.374	0.385	0.063	83.046	0.385	0.334	3.789	43.980	3.317	38.464
312	0.300	19.031	0.030	0.015	23.862	0.030	0.000	14.468	0.082	12.633	0.071
32	0.365	15.627	0.290	0.004	6.989	0.290	0.001	14.511	0.076	12.670	0.066
332	0.429	15.444	0.025	0.003	5.646	0.025	0.000	14.545	0.077	12.700	0.067
332	0.430	15.391	0.041	0.007	13.271	0.041	0.010	13.324	1.288	11.637	1.121
34	0.574	15.189	0.148	0.002	3.333	0.148	0.001	14.656	0.071	12.797	0.062
35	0.729	16.446	0.052	0.007	12.558	0.052	0.000	14.356	0.073	12.535	0.063
362	0.758	73.025	0.035	0.207	83.594	0.035	0.001	11.976	0.316	10.463	0.276
362	0.806	15.466	0.030	0.003	5.926	0.030	0.000	14.522	0.079	12.680	0.069
371	0.821	73.698	0.046	2.477	993.599	0.046	0.001	-658.331	3.417	-694.942	4.402
372	0.842	16.466	0.040	0.509	915.584	0.040	0.001	-134.067	0.662	-121.468	0.620
38	1.000	17.614	0.047	0.010	17.611	0.047	0.000	14.489	0.078	12.651	0.068

UAF039-11 12R8-17B SWNVF

Weighted average of J from standards = 0.000486 +/- 0.000008

Grain #	Cumulative 39Ar	40Ar/39Ar measured	37Ar/39Ar measured	36Ar/39Ar measured	% Atmospheric 40Ar	37Ca/39K	+/-	40*/39K	+/-	Age (Ma)	+/- (Ma)
39	0.230	14.821	0.023	0.000	0.372	0.023	0.000	14.738	0.072	12.867	0.062
412	0.237	23.099	0.115	0.028	35.803	0.115	0.005	14.812	0.697	12.932	0.606
412	0.375	14.815	0.027	0.000	0.453	0.027	0.000	14.720	0.075	12.851	0.065
432	0.389	15.427	0.029	0.003	6.565	0.029	0.003	14.388	0.363	12.563	0.316
432	1.000	14.781	0.024	0.000	0.247	0.024	0.000	14.716	0.069	12.849	0.060

UAF039-33 AT92-730-20-20-25 SANIDINE SWNVF

Weighted average of J from standards = 0.000486 +/- 0.000008

Grain #	Cumulative 39Ar	40Ar/39Ar measured	37Ar/39Ar measured	36Ar/39Ar measured	% Atmospheric 40Ar	37Ca/39K	+/-	40*/39K	+/-	Age (Ma)	+/- (Ma)
23	0.115	14.038	0.050	0.001	2.592	0.050	0.001	13.646	0.077	11.918	0.067
24	0.188	14.502	0.071	0.002	5.052	0.071	0.002	13.743	0.064	12.001	0.055
25	0.220	14.135	0.078	0.001	2.564	0.078	0.005	13.745	0.065	12.004	0.056
26	0.345	13.921	0.037	0.001	1.413	0.037	0.001	13.696	0.063	11.961	0.055
27	0.457	14.087	0.044	0.001	3.115	0.044	0.002	13.621	0.062	11.895	0.054
28	0.613	14.261	0.042	0.002	4.330	0.042	0.001	13.616	0.062	11.891	0.054
29	0.750	14.448	0.090	0.003	5.739	0.090	0.001	13.593	0.064	11.871	0.056
30	0.792	14.010	0.051	0.001	2.344	0.051	0.004	13.654	0.063	11.925	0.055
31	0.958	19.857	0.160	0.021	30.957	0.160	0.001	13.692	0.085	11.957	0.074
32	0.994	14.964	0.138	0.005	10.358	0.138	0.005	13.389	0.067	11.694	0.058
33	1.000	18.147	3.856	0.020	31.409	3.866	0.032	12.459	0.125	10.884	0.109

UAF039-34 P6293-AD-2 SWNVF

Weighted average of J from standards = 0.000486 +/- 0.000008

Grain #	Cumulative 39Ar	40Ar/39Ar measured	37Ar/39Ar measured	36Ar/39Ar measured	% Atmospheric 40Ar	37Ca/39K	+/-	40*/39K	+/-	Age (Ma)	+/- (Ma)
19	0.044	18.882	0.254	0.016	24.650	0.254	0.001	14.208	0.109	12.406	0.095
20	0.115	20.029	0.046	0.019	28.564	0.046	0.001	14.288	0.092	12.476	0.080
21	0.992	25.253	0.046	0.037	43.655	0.046	0.000	14.213	0.103	12.411	0.090
22	1.000	18.884	0.529	0.015	23.689	0.529	0.005	14.394	0.393	12.568	0.342

UAF039-35 AFB-6 SWNVF

Weighted average of J from standards = 0.000486 +/- 0.000008

Grain #	Cumulative 39Ar	40Ar/39Ar measured	37Ar/39Ar measured	36Ar/39Ar measured	% Atmospheric 40Ar	37Ca/39K	+/-	40*/39K	+/-	Age (Ma)	+/- (Ma)
17	0.271	18.255	0.011	0.016	26.069	0.011	0.000	13.475	0.077	11.768	0.067
18	0.414	14.289	0.008	0.002	3.454	0.008	0.000	13.768	0.089	12.023	0.078
19	0.567	13.940	0.007	0.001	1.456	0.007	0.000	13.709	0.065	11.972	0.056
20	0.628	13.813	0.011	0.000	0.949	0.011	0.000	13.653	0.065	11.924	0.057
21	0.691	14.750	0.011	0.004	7.994	0.011	0.000	13.545	0.067	11.829	0.059
22	0.765	14.192	0.011	0.002	3.508	0.011	0.000	13.667	0.067	11.936	0.058
23	0.853	14.159	0.037	0.002	3.296	0.037	0.000	13.665	0.091	11.934	0.079
24	0.913	15.567	0.132	0.006	11.001	0.132	0.001	13.830	0.071	12.078	0.062
25	1.000	15.259	0.046	0.005	10.205	0.046	0.000	13.676	0.070	11.944	0.061

UAF039-36 AT92-730-0

Weighted average of J from standards = 0.000486 +/- 0.000008

Grain #	Cumulative 39Ar	40Ar/39Ar measured	37Ar/39Ar measured	36Ar/39Ar measured	% Atmospheric 40Ar	37Ca/39K	+/-	40*/39K	+/-	Age (Ma)	+/- (Ma)
34	0.131	14.100	0.148	0.002	4.107	0.148	0.002	13.495	0.064	11.786	0.056
35	0.187	13.844	0.099	0.001	3.085	0.099	0.003	13.390	0.062	11.694	0.054
37	0.360	14.043	0.078	0.002	3.687	0.078	0.001	13.498	0.073	11.789	0.063
38	0.554	14.054	0.086	0.002	3.543	0.086	0.001	13.529	0.063	11.815	0.055
39	0.643	14.158	0.132	0.002	4.104	0.132	0.002	13.551	0.068	11.835	0.060
40	0.823	13.835	0.052	0.001	2.243	0.052	0.001	13.497	0.062	11.788	0.054
42	0.960	14.332	0.118	0.003	5.896	0.118	0.002	13.461	0.064	11.756	0.056
43	1.000	14.687	0.312	0.004	8.360	0.312	0.005	13.435	0.069	11.734	0.060

UAF039-37 2AT92-803-74-76 SWNVF

Weighted average of J from standards = 0.000486 +/- 0.000008

Grain #	Cumulative 39Ar	40Ar/39Ar measured	37Ar/39Ar measured	36Ar/39Ar measured	% Atmospheric 40Ar	37Ca/39K	+/-	40*/39K	+/-	Age (Ma)	+/- (Ma)
22	0.430	16.300	0.142	0.009	16.982	0.142	0.002	13.509	0.077	11.798	0.067
23	0.513	17.634	0.389	0.014	24.073	0.389	0.010	13.371	0.078	11.677	0.068
24	0.890	24.894	0.256	0.038	45.412	0.256	0.002	13.576	0.102	11.856	0.089
25	0.899	15.525	1.210	0.008	14.131	1.211	0.101	13.317	0.290	11.631	0.252
26	0.994	14.071	0.125	0.002	4.863	0.125	0.009	13.360	0.064	11.668	0.056
27	0.995	18.200	0.756	0.023	36.939	0.756	0.694	11.465	1.952	10.018	1.701
28	1.000	13.831	0.084	0.001	2.594	0.084	0.176	13.445	0.498	11.743	0.434

UAF039-38 6RM92-802-1,3 SWNVF

Weighted average of J from standards = 0.000486 +/- 0.000008

Grain #	Cumulative 39Ar	40Ar/39Ar measured	37Ar/39Ar measured	36Ar/39Ar measured	% Atmospheric 40Ar	37Ca/39K	+/-	40*/39K	+/-	Age (Ma)	+/- (Ma)
7	0.102	26.412	0.014	0.041	45.879	0.014	0.000	14.279	0.121	12.468	0.105
8	0.176	16.353	0.016	0.006	10.982	0.016	0.000	14.532	0.078	12.688	0.068
9	0.232	15.730	0.056	0.004	6.836	0.056	0.000	14.629	0.075	12.772	0.065
10	0.300	17.375	0.026	0.009	14.943	0.026	0.000	14.755	0.078	12.882	0.068
11	0.380	17.314	0.029	0.008	14.203	0.029	0.000	14.830	0.077	12.948	0.067
40	0.404	29.374	0.721	0.053	52.737	0.722	0.003	13.876	0.124	12.118	0.108
41	0.542	16.593	0.064	0.007	12.298	0.064	0.000	14.528	0.085	12.685	0.074
42	0.829	16.886	0.013	0.008	13.419	0.013	0.000	14.595	0.076	12.743	0.066
43	0.960	17.584	0.016	0.010	16.443	0.016	0.000	14.669	0.077	12.807	0.067
12	1.000	17.462	0.044	0.009	16.021	0.044	0.000	14.641	0.079	12.783	0.068

UAF039-27 AFB-5-14 SWNVF

Weighted average of J from standards = 0.000486 +/- 0.000008

Grain #	Cumulative 39Ar	40Ar/39Ar measured	37Ar/39Ar measured	36Ar/39Ar measured	% Atmospheric 40Ar	37Ca/39K	+/-	40*/39K	+/-	Age (Ma)	+/- (Ma)
1	0.303	14.209	0.001	0.001	2.455	0.001	0.000	13.832	0.083	12.079	0.072
2	0.478	13.809	0.001	-0.001	-2.425	0.001	0.000	14.114	0.067	12.325	0.059
3	0.588	13.946	-0.009	-0.003	-5.641	-0.009	0.000	14.702	0.070	12.836	0.061
4	0.706	16.491	0.087	0.014	24.329	0.087	0.000	12.458	0.071	10.883	0.062
5	0.844	13.998	0.071	0.001	2.657	0.071	0.000	13.598	0.067	11.876	0.059
6	0.966	14.983	0.059	0.005	10.596	0.059	0.000	13.370	0.072	11.677	0.062
7	0.990	20.228	0.041	0.026	38.247	0.041	0.001	12.474	0.120	10.897	0.104
8	1.000	14.918	0.246	0.005	10.459	0.246	0.002	13.334	0.203	11.646	0.177

UAF039-26 AFB-PRE RAINIER LAVA SWNVF

Weighted average of J from standards = 0.000486 +/- 0.000008

Grain #	Cumulative 39Ar	40Ar/39Ar measured	37Ar/39Ar measured	36Ar/39Ar measured	% Atmospheric 40Ar	37Ca/39K	+/-	40*/39K	+/-	Age (Ma)	+/- (Ma)
17	0.256	17.884	0.029	0.011	18.108	0.029	0.000	14.622	0.079	12.767	0.069
18	0.344	33.663	0.024	0.066	58.025	0.024	0.000	14.118	0.142	12.328	0.123
19	0.472	18.286	0.027	0.012	19.877	0.027	0.000	14.628	0.082	12.772	0.071
20	0.552	34.077	0.014	0.067	58.052	0.014	0.000	14.283	0.142	12.471	0.123
21	0.683	20.118	0.026	0.019	27.691	0.026	0.000	14.527	0.091	12.683	0.079
22	0.768	24.886	0.022	0.035	42.038	0.022	0.000	14.408	0.103	12.580	0.090
23	0.929	18.851	0.029	0.014	21.876	0.029	0.000	14.705	0.081	12.839	0.070
24	1.000	26.885	0.019	0.042	46.028	0.019	0.000	14.495	0.115	12.656	0.100

UAF039-46 BASALT FROM PM Rd. SWNVF

Weighted average of J from standards = 0.000486 +/- 0.000008

Grain #	Cumulative 39Ar	40Ar/39Ar measured	37Ar/39Ar measured	36Ar/39Ar measured	% Atmospheric 40Ar	37Ca/39K	+/-	40*/39K	+/-	Age (Ma)	+/- (Ma)
23	0.144	13.755	0.011	0.000	0.788	0.011	0.000	13.618	0.066	11.893	0.058
24	0.443	14.004	0.009	0.001	1.479	0.009	0.000	13.769	0.074	12.024	0.064
25	0.623	14.222	0.009	0.002	4.272	0.009	0.000	13.587	0.065	11.866	0.057
26	0.655	14.127	0.011	0.002	4.305	0.011	0.000	13.491	0.067	11.783	0.058
27	0.753	13.761	0.009	0.001	1.248	0.009	0.000	13.561	0.064	11.843	0.056
28	0.781	17.726	0.448	0.014	23.253	0.448	0.002	13.586	0.078	11.865	0.068
29	0.866	14.047	0.009	0.001	1.392	0.009	0.000	13.823	0.067	12.071	0.058
30	0.965	13.834	0.010	0.000	1.052	0.010	0.000	13.660	0.070	11.929	0.061
31	0.965	-20142.136	-11.985	-0.652	0.952	-11.892	0.984	-	-	-	166.378
32	1.000	13.979	0.235	0.002	4.321	0.236	0.001	13.349	0.066	11.659	0.057

UAF039-49 3RM92-802-5 SWNVF

Weighted average of J from standards = 0.000486 +/- 0.000008

Grain #	Cumulative 39Ar	40Ar/39Ar measured	37Ar/39Ar measured	36Ar/39Ar measured	% Atmospheric 40Ar	37Ca/39K	+/-	40*/39K	+/-	Age (Ma)	+/- (Ma)
13	0.321	14.044	0.006	0.000	-0.650	0.006	0.000	14.106	0.067	12.318	0.058
14	0.560	14.195	0.070	0.001	1.520	0.070	0.000	13.952	0.067	12.183	0.059
15	0.770	14.031	0.188	0.001	1.704	0.188	0.001	13.766	0.067	12.021	0.058
16	1.000	14.383	0.044	0.003	6.646	0.044	0.000	13.401	0.068	11.704	0.059

UAF039-44 AFB-3-19 SWNVF

Weighted average of J from standards = 0.000486 +/- 0.000008

Grain #	Cumulative 39Ar	40Ar/39Ar measured	37Ar/39Ar measured	36Ar/39Ar measured	% Atmospheric 40Ar	37Ca/39K	+/-	40*/39K	+/-	Age (Ma)	+/- (Ma)
30	0.115	17.078	0.009	0.011	19.564	0.009	0.000	13.714	0.095	11.977	0.082
31	0.254	15.320	0.011	0.005	9.319	0.011	0.000	13.867	0.070	12.109	0.061
32	0.420	14.532	0.013	0.003	5.330	0.013	0.000	13.730	0.079	11.991	0.069
33	0.538	15.676	0.012	0.006	10.926	0.012	0.000	13.938	0.071	12.171	0.062
34	0.562	16.668	0.371	0.009	16.541	0.371	0.002	13.890	0.076	12.130	0.066
35	0.656	14.830	0.009	0.004	7.916	0.009	0.000	13.630	0.072	11.903	0.062
36	0.680	19.451	0.009	0.020	30.636	0.009	0.000	13.472	0.084	11.766	0.073
37	0.760	17.141	0.013	0.011	18.344	0.013	0.000	13.973	0.076	12.202	0.066
38	0.827	17.557	0.078	0.005	9.176	0.078	0.000	15.921	0.086	13.896	0.075
39	1.000	14.333	0.008	0.002	4.420	0.008	0.000	13.672	0.088	11.940	0.076

UAF039-8 AFB-14 BELOW SWNVF

Weighted average of J from standards = 0.000486 +/- 0.000008

Grain #	Cumulative 39Ar	40Ar/39Ar measured	37Ar/39Ar measured	36Ar/39Ar measured	% Atmospheric 40Ar	37Ca/39K	+/-	40*/39K	+/-	Age (Ma)	+/- (Ma)
1	0.706	14.162	0.009	0.002	4.164	0.009	0.000	13.545	0.065	11.829	0.057
2	1.710	16.641	0.009	0.011	19.255	0.009	0.000	13.413	0.075	11.715	0.065
3	0.758	-24.016	-0.014	-0.007	8.582	-0.014	0.000	-21.981	0.101	-19.364	0.089
4	0.917	34.178	0.826	0.075	64.774	0.827	0.004	12.036	0.149	10.515	0.130
5	1.000	51.059	0.034	0.143	82.579	0.034	0.001	8.890	0.227	7.773	0.198

UAF039-29 P6293-AD1 SWNVF

Weighted average of J from standards = 0.000486 +/- 0.000008

Grain #	Cumulative 39Ar	40Ar/39Ar measured	37Ar/39Ar measured	36Ar/39Ar measured	% Atmospheric 40Ar	37Ca/39K	+/-	40*/39K	+/-	Age (Ma)	+/- (Ma)
33	0.016	14.848	0.015	0.003	5.786	0.015	0.001	13.962	0.111	12.193	0.097
34	0.099	15.068	0.215	0.001	1.811	0.215	0.001	14.769	0.073	12.895	0.063
35	0.113	15.613	1.374	0.006	9.787	1.375	0.006	14.072	0.122	12.288	0.106
36	0.382	15.082	0.008	0.000	0.927	0.008	0.000	14.914	0.076	13.020	0.066
37	0.566	16.359	0.063	0.005	8.530	0.063	0.000	14.938	0.074	13.041	0.064
38	0.716	15.222	0.089	0.001	2.168	0.089	0.000	14.865	0.072	12.978	0.063
39	0.890	15.477	0.131	0.001	1.986	0.131	0.001	15.143	0.081	13.220	0.071
40	1.000	15.252	0.115	0.001	1.428	0.115	0.001	15.008	0.072	13.102	0.062

UAF039-31 P6293-AD3

Weighted average of J from standards = 0.000486 +/- 0.000008

Grain #	Cumulative 39Ar	40Ar/39Ar measured	37Ar/39Ar measured	36Ar/39Ar measured	% Atmospheric 40Ar	37Ca/39K	+/-	40*/39K	+/-	Age (Ma)	+/- (Ma)
26	0.179	19.137	0.010	0.013	20.785	0.010	0.000	15.137	0.093	13.214	0.081
27	0.295	20.383	0.050	0.022	31.892	0.050	0.001	13.863	0.102	12.106	0.089
28	0.590	15.152	0.065	0.001	1.345	0.065	0.000	14.920	0.076	13.026	0.066
29	1.000	17.036	0.024	0.007	12.981	0.024	0.000	14.800	0.077	12.922	0.067

UAF039-21 M-25 SWNVF

Weighted average of J from standards = 0.000486 +/- 0.000008

Grain #	Cumulative 39Ar	40Ar/39Ar measured	37Ar/39Ar measured	36Ar/39Ar measured	% Atmospheric 40Ar	37Ca/39K	+/-	40*/39K	+/-	Age (Ma)	+/- (Ma)
10	0.168	15.149	0.026	0.000	0.488	0.026	0.000	15.047	0.071	13.136	0.061
11	0.177	16.575	1.281	0.009	16.342	1.282	0.006	13.854	0.101	12.098	0.088
12	0.274	15.022	0.007	0.000	0.937	0.007	0.000	14.853	0.070	12.967	0.061
13	0.279	17.707	2.511	0.013	20.329	2.515	0.012	14.107	0.134	12.319	0.117
14	0.358	15.235	0.007	0.002	3.006	0.007	0.000	14.750	0.070	12.878	0.061
15	0.420	15.095	0.007	0.001	1.449	0.007	0.000	14.848	0.071	12.964	0.061
16	0.453	15.199	0.008	0.001	1.567	0.008	0.000	14.933	0.072	13.037	0.063
7	0.578	15.085	0.007	0.001	1.660	0.007	0.000	14.807	0.071	12.927	0.062
8	0.826	15.130	0.009	0.000	0.968	0.009	0.000	14.955	0.071	13.057	0.062
9	1.000	15.097	0.030	0.001	1.258	0.030	0.000	14.879	0.071	12.990	0.062

UAF039-23 M-24 SWNVF

Weighted average of J from standards = 0.000486 +/- 0.000008

Grain #	Cumulative 39Ar	40Ar/39Ar measured	37Ar/39Ar measured	36Ar/39Ar measured	% Atmospheric 40Ar	37Ca/39K	+/-	40*/39K	+/-	Age (Ma)	+/- (Ma)
23	0.121	15.449	0.022	0.001	2.708	0.022	0.000	15.003	0.074	13.098	0.065
24	0.339	15.467	0.011	0.000	0.505	0.011	0.000	15.360	0.079	13.409	0.069
25	0.526	15.614	0.012	0.001	2.048	0.012	0.000	15.266	0.072	13.327	0.063
26	0.696	15.454	0.015	0.001	1.447	0.015	0.000	15.202	0.073	13.271	0.064
27	0.841	15.662	0.013	0.001	1.294	0.013	0.000	15.431	0.079	13.470	0.069
28	0.944	15.515	0.035	0.001	2.386	0.035	0.000	15.117	0.072	13.197	0.063
29	1.000	15.759	0.264	0.001	1.724	0.264	0.001	15.462	0.075	13.497	0.065

UAF039-24 M-23 SWNVF

Weighted average of J from standards = 0.000486 +/- 0.000008

Grain #	Cumulative 39Ar	40Ar/39Ar measured	37Ar/39Ar measured	36Ar/39Ar measured	% Atmospheric 40Ar	37Ca/39K	+/-	40*/39K	+/-	Age (Ma)	+/- (Ma)
30	0.257	15.337	0.012	0.000	0.312	0.012	0.000	15.261	0.072	13.322	0.062
31	0.570	15.427	0.012	0.000	0.685	0.012	0.000	15.293	0.072	13.350	0.062
32	0.729	15.293	0.014	0.001	1.424	0.014	0.000	15.047	0.089	13.136	0.078
33	0.881	15.380	0.013	0.000	0.509	0.013	0.000	15.273	0.073	13.333	0.064
34	1.000	15.364	0.017	0.001	1.455	0.017	0.000	15.112	0.073	13.193	0.064

UAF039-5 M-22A SWNVF

Weighted average of J from standards = 0.000486 +/- 0.000008

Grain #	Cumulative 39Ar	40Ar/39Ar measured	37Ar/39Ar measured	36Ar/39Ar measured	% Atmospheric 40Ar	37Ca/39K	+/-	40*/39K	+/-	Age (Ma)	+/- (Ma)
1	0.132	15.308	0.015	0.000	0.341	0.015	0.000	15.227	0.071	13.293	0.062
2	0.259	15.495	0.086	0.000	0.833	0.086	0.000	15.339	0.072	13.390	0.063
3	0.327	15.399	0.074	0.001	1.791	0.074	0.000	15.096	0.077	13.179	0.067
4	0.340	22.654	0.692	0.018	23.712	0.692	0.003	17.268	0.138	15.067	0.120
4	0.353	20.321	0.692	0.018	26.438	0.692	0.003	14.934	0.131	13.038	0.114
5	0.412	15.578	0.076	0.001	1.656	0.076	0.000	15.292	0.077	13.350	0.067
6	0.477	15.506	0.055	0.001	1.871	0.055	0.000	15.189	0.074	13.259	0.065
41	0.632	15.476	0.044	0.001	1.052	0.044	0.000	15.285	0.073	13.343	0.064
42	0.840	15.340	0.013	0.000	0.451	0.013	0.000	15.242	0.072	13.306	0.062
43	1.000	15.839	0.027	0.001	0.950	0.027	0.000	15.661	0.074	13.670	0.064

UAF039-19 M-21 SWNVF

Weighted average of J from standards = 0.000486 +/- 0.000008

Grain #	Cumulative 39Ar	40Ar/39Ar measured	37Ar/39Ar measured	36Ar/39Ar measured	% Atmospheric 40Ar	37Ca/39K	+/-	40*/39K	+/-	Age (Ma)	+/- (Ma)
8	0.056	16.536	1.324	0.004	7.356	1.325	0.006	15.307	0.089	13.362	0.078
9	0.263	16.110	0.264	0.002	4.102	0.264	0.001	15.424	0.075	13.464	0.065
10	0.473	15.349	0.114	0.001	1.396	0.114	0.001	15.107	0.072	13.189	0.063
11	0.640	15.601	0.205	0.001	1.843	0.205	0.001	15.287	0.074	13.345	0.064
12	0.851	17.402	0.035	0.007	12.263	0.035	0.000	15.243	0.081	13.307	0.071
13	1.000	15.684	0.249	0.002	3.478	0.249	0.001	15.113	0.076	13.194	0.066

UAF039-22 M-22 SWNVF

Weighted average of J from standards = 0.000486 +/- 0.000008

Grain #	Cumulative 39Ar	40Ar/39Ar measured	37Ar/39Ar measured	36Ar/39Ar measured	% Atmospheric 40Ar	37Ca/39K	+/-	40*/39K	+/-	Age (Ma)	+/- (Ma)
40	0.112	15.678	0.027	0.001	2.180	0.027	0.000	15.308	0.075	13.364	0.066
35	0.268	16.183	0.036	0.006	11.287	0.036	0.000	14.331	0.074	12.514	0.064
36	0.432	15.989	0.015	0.002	3.650	0.015	0.000	15.378	0.074	13.424	0.064
37	0.563	15.588	0.020	0.001	1.013	0.020	0.000	15.402	0.077	13.445	0.067
38	0.755	15.704	0.020	0.001	2.567	0.020	0.000	15.273	0.075	13.333	0.066
39	1.000	16.912	0.032	0.006	9.792	0.032	0.000	15.230	0.078	13.296	0.068

039-18 M-19, M-21A

Weighted average of J from standards = 0.000486 +/- 0.000008

Grain #	Cumulative 39Ar	40Ar/39Ar measured	37Ar/39Ar measured	36Ar/39Ar measured	% Atmospheric 40Ar	37Ca/39K	+/-	40*/39K	+/-	Age (Ma)	+/- (Ma)
34	0.005	19.537	1.538	0.017	25.519	1.539	0.160	14.544	0.685	12.699	0.596
35	0.435	15.673	0.034	0.001	1.638	0.034	0.002	15.389	0.069	13.434	0.060
36	0.521	15.510	0.054	0.001	1.684	0.054	0.009	15.221	0.077	13.288	0.067
37	0.617	17.000	0.213	0.007	11.633	0.213	0.008	14.999	0.078	13.094	0.068
42	0.618	19.753	7.518	0.021	28.759	7.555	0.508	14.121	2.092	12.331	1.821
40	0.693	15.471	0.023	0.001	0.947	0.023	0.010	15.296	0.080	13.353	0.070
39	0.968	15.333	0.035	0.000	0.873	0.035	0.003	15.171	0.069	13.244	0.060
43	1.000	38.884	0.818	0.084	63.830	0.819	0.024	14.061	0.182	12.279	0.158

UAF039-17 M-19 SWNVF

Weighted average of J from standards = 0.000486 +/- 0.000008

Grain #	Cumulative 39Ar	40Ar/39Ar measured	37Ar/39Ar measured	36Ar/39Ar measured	% Atmospheric 40Ar	37Ca/39K	+/-	40*/39K	+/-	Age (Ma)	+/- (Ma)
41	0.180	16.368	0.016	0.003	5.558	0.016	0.000	15.431	0.075	13.470	0.066
42	0.397	17.490	0.009	0.007	12.387	0.009	0.000	15.299	0.076	13.355	0.066
43	0.468	16.312	0.152	0.003	4.786	0.152	0.001	15.505	0.076	13.535	0.066
1	0.483	16.368	1.688	0.005	8.382	1.690	0.008	14.986	0.089	13.083	0.077
2	0.550	15.943	0.078	0.002	4.351	0.078	0.000	15.222	0.075	13.289	0.065
3	0.600	15.955	0.120	0.002	4.379	0.120	0.001	15.231	0.075	13.296	0.065
4	0.799	9.597	0.078	0.001	2.691	0.078	0.000	9.312	0.039	8.141	0.034
5	0.900	15.628	0.164	0.001	2.284	0.164	0.001	15.244	0.072	13.308	0.063
6	0.970	16.575	0.185	0.004	7.439	0.185	0.001	15.317	0.076	13.371	0.066
7	1.000	16.620	0.631	0.007	12.332	0.631	0.003	14.552	0.082	12.705	0.071

UAF039-25 M-9 BASE

Weighted average of J from standards = 0.000486 +/- 0.000008

Grain #	Cumulative 39Ar	40Ar/39Ar measured	37Ar/39Ar measured	36Ar/39Ar measured	% Atmospheric 40Ar	37Ca/39K	+/-	40*/39K	+/-	Age (Ma)	+/- (Ma)
17	0.029	19.308	2.482	0.015	21.459	2.486	0.011	15.167	0.102	13.240	0.089
18	0.076	19.819	2.324	0.017	24.721	2.328	0.011	14.920	0.093	13.026	0.081
19	0.383	15.765	0.008	0.000	0.675	0.008	0.000	15.630	0.074	13.643	0.065
21	0.559	15.595	0.047	0.000	0.606	0.047	0.000	15.472	0.075	13.506	0.065
22	0.679	15.958	0.009	0.001	1.412	0.009	0.000	15.704	0.075	13.708	0.065
23	0.787	15.632	0.009	0.000	0.784	0.009	0.000	15.481	0.076	13.514	0.066
24	0.992	15.898	0.009	0.001	1.162	0.009	0.000	15.685	0.077	13.691	0.067
25	1.000	15.391	0.673	0.004	7.865	0.673	0.004	14.160	0.218	12.365	0.190

UAF039-20 M-10 FEET SWNVF

Weighted average of J from standards = 0.000486 +/- 0.000008

Grain #	Cumulative 39Ar	40Ar/39Ar measured	37Ar/39Ar measured	36Ar/39Ar measured	% Atmospheric 40Ar	37Ca/39K	+/-	40*/39K	+/-	Age (Ma)	+/- (Ma)
14	0.505	16.798	0.012	0.005	8.043	0.012	0.000	15.421	0.076	13.461	0.066
15	0.990	15.616	0.011	0.001	1.612	0.011	0.000	15.336	0.081	13.388	0.070
16	1.000	18.221	1.051	0.016	24.989	1.052	0.007	13.656	0.424	11.926	0.369

039-7 M-30 FEET SWNVF

Weighted average of J from standards = 0.000486 +/- 0.000008

Grain #	Cumulative 39Ar	40Ar/39Ar measured	37Ar/39Ar measured	36Ar/39Ar measured	% Atmospheric 40Ar	37Ca/39K	+/-	40*/39K	+/-	Age (Ma)	+/- (Ma)
21	0.132	41.759	0.139	0.000	0.278	0.139	0.002	41.618	0.202	36.102	0.174
22	0.277	15.750	0.054	0.001	2.748	0.054	0.001	15.290	0.070	13.348	0.061
23	0.474	15.867	0.013	0.000	0.649	0.013	0.001	15.735	0.087	13.735	0.076
24	0.536	15.784	0.010	0.000	0.496	0.010	0.003	15.678	0.073	13.685	0.063
23	0.574	15.823	0.127	0.002	2.982	0.127	0.005	15.324	0.072	13.378	0.063
31	0.581	19.084	1.436	0.008	12.513	1.438	0.028	16.687	0.139	14.562	0.121
30	0.781	15.678	0.021	0.001	2.635	0.021	0.001	15.237	0.077	13.302	0.067
29	0.793	15.513	0.049	0.001	1.174	0.049	0.017	15.303	0.100	13.359	0.087
28	0.822	18.218	0.236	0.011	17.287	0.236	0.007	15.047	0.080	13.137	0.070
27	0.824	1366.325	2.726	2.336	50.498	2.731	0.098	677.550	5.821	513.223	3.838
32	0.977	15.468	0.032	0.001	1.164	0.032	0.001	15.260	0.083	13.322	0.073
33	1.000	15.427	0.018	0.000	0.496	0.018	0.009	15.323	0.078	13.376	0.068

UAF039-39 AT19-36 SWNVF

Weighted average of J from standards = 0.000486 +/- 0.000008

Grain #	Cumulative 39Ar	40Ar/39Ar measured	37Ar/39Ar measured	36Ar/39Ar measured	% Atmospheric 40Ar	37Ca/39K	+/-	40*/39K	+/-	Age (Ma)	+/- (Ma)
36	0.128	13.685	0.015	0.000	1.039	0.015	0.000	13.515	0.065	11.803	0.057
38	0.269	13.606	0.021	0.001	1.453	0.021	0.000	13.380	0.069	11.686	0.060
39	0.402	13.448	0.013	0.000	0.576	0.013	0.000	13.342	0.068	11.652	0.059
40	0.498	13.540	0.014	0.000	0.696	0.014	0.000	13.417	0.065	11.718	0.056
41	0.629	13.637	0.025	0.001	2.073	0.025	0.000	13.327	0.063	11.639	0.055
42	0.819	13.942	0.017	0.002	3.278	0.017	0.000	13.457	0.065	11.753	0.057
43	1.000	14.348	0.012	0.003	6.991	0.012	0.000	13.318	0.066	11.632	0.058

UAF039-41 3EAT92-729-10 SWNVF SANIDINE

Weighted average of J from standards = 0.000496 +/- 0.000008

Grain #	Cumulative 39Ar	40Ar/39Ar measured	37Ar/39Ar measured	36Ar/39Ar measured	% Atmospheric 40Ar	37Ca/39K	+/-	40*/39K	+/-	Age (Ma)	+/- (Ma)
29	0.167	13.776	0.069	0.002	3.237	0.069	0.003	13.303	0.082	11.619	0.072
30	0.340	14.124	0.096	0.002	4.936	0.096	0.003	13.401	0.064	11.704	0.056
31	0.378	13.803	0.173	0.002	3.608	0.173	0.011	13.279	0.067	11.597	0.058
32	0.429	15.073	0.491	0.007	14.468	0.491	0.009	12.871	0.069	11.243	0.060
33	0.485	14.821	0.355	0.006	11.548	0.355	0.008	13.087	0.068	11.430	0.059
34	0.556	13.894	0.179	0.002	4.965	0.179	0.006	13.179	0.064	11.511	0.055
35	0.644	13.974	0.143	0.002	4.049	0.143	0.005	13.382	0.063	11.688	0.055
36	0.669	38.715	2.686	0.083	62.518	2.691	0.021	14.526	0.192	12.683	0.167
37	0.746	13.868	0.105	0.002	4.038	0.105	0.006	13.282	0.064	11.600	0.056
38	0.791	14.265	0.349	0.004	7.487	0.349	0.010	13.174	0.070	11.506	0.061
40	0.821	14.584	0.338	0.005	8.974	0.338	0.015	13.252	0.078	11.574	0.068
41	0.875	13.971	0.215	0.002	4.473	0.215	0.008	13.321	0.066	11.634	0.058
42	0.936	14.315	0.143	0.003	6.642	0.143	0.007	13.338	0.066	11.649	0.057
43	1.000	13.658	0.054	0.000	0.866	0.054	0.007	13.511	0.063	11.800	0.055

UAF039-43 AT92-730-31-32 SWNVF SANIDINE

Weighted average of J from standards = 0.000486 +/- 0.000008

Grain #	Cumulative 39Ar	40Ar/39Ar measured	37Ar/39Ar measured	36Ar/39Ar measured	% Atmospheric 40Ar	37Ca/39K	+/-	40*/39K	+/-	Age (Ma)	+/- (Ma)
1	0.154	13.758	0.018	0.000	0.787	0.018	0.001	13.621	0.071	11.896	0.062
2	0.192	13.823	0.020	0.000	0.676	0.020	0.004	13.701	0.063	11.965	0.055
3	0.199	21.376	2.599	0.029	39.311	2.603	0.024	12.978	0.099	11.335	0.087
4	0.297	14.042	0.060	0.001	2.655	0.060	0.001	13.642	0.063	11.914	0.055
5	0.404	14.747	0.025	0.004	7.093	0.025	0.001	13.675	0.068	11.942	0.059
6	0.498	14.047	0.057	0.001	2.062	0.057	0.002	13.730	0.062	11.990	0.054
7	0.582	13.861	0.065	0.001	1.599	0.065	0.002	13.612	0.062	11.887	0.054
8	0.643	14.389	0.033	0.002	4.751	0.033	0.002	13.678	0.063	11.945	0.055
9	0.742	13.964	0.031	0.000	0.771	0.031	0.001	13.828	0.063	12.076	0.055
10	0.821	14.096	0.040	0.001	2.036	0.040	0.002	13.782	0.062	12.035	0.054
11	0.881	13.754	0.038	0.000	0.945	0.038	0.002	13.596	0.061	11.874	0.053
13	0.886	16.186	2.283	0.012	21.403	2.286	0.032	12.718	0.106	11.109	0.092
12	0.955	14.341	0.118	0.002	4.604	0.118	0.002	13.654	0.064	11.924	0.056
14	0.958	14.825	2.007	0.005	9.243	2.010	0.040	13.446	0.122	11.743	0.106
15	1.000	13.789	0.045	0.001	1.174	0.045	0.003	13.599	0.062	11.877	0.054

UAF039-42 AT19-PINK SWNVF

Weighted average of J from standards = 0.000486 +/- 0.000008

Grain #	Cumulative 39Ar	40Ar/39Ar measured	37Ar/39Ar measured	36Ar/39Ar measured	% Atmospheric 40Ar	37Ca/39K	+/-	40*/39K	+/-	Age (Ma)	+/- (Ma)
26	0.108	315.921	0.034	1.053	98.536	0.034	0.000	4.625	1.440	4.048	1.259
26	0.216	315.917	0.034	1.053	98.536	0.034	0.000	4.625	1.440	4.048	1.259
28	0.270	137.049	0.044	0.435	93.826	0.044	0.000	8.460	0.627	7.397	0.547
28	0.324	137.138	0.044	0.435	93.832	0.044	0.000	8.457	0.628	7.395	0.548
29	0.324	-11.084	-1.622	0.179	-476.079	-1.620	0.098	-63.948	7.832	-56.920	7.082
30	0.459	18.091	0.031	0.017	27.048	0.031	0.000	13.177	0.092	11.509	0.080
31	0.465	35.399	0.055	0.081	67.998	0.055	0.001	11.320	0.163	9.891	0.142
32	0.678	14.425	0.055	0.004	7.489	0.055	0.000	13.319	0.066	11.632	0.058
33	0.787	30.786	0.046	0.060	57.190	0.046	0.000	13.168	0.139	11.501	0.121
34	0.879	24.870	0.052	0.040	47.111	0.052	0.000	13.138	0.105	11.475	0.092
35	1.000	14.266	0.020	0.003	6.982	0.020	0.000	13.243	0.068	11.567	0.059

UAF039-45 2AT92-728-1-5 SWNVF

Weighted average of J from standards = 0.000486 +/- 0.000008

Grain #	Cumulative 39Ar	40Ar/39Ar measured	37Ar/39Ar measured	36Ar/39Ar measured	% Atmospheric 40Ar	37Ca/39K	+/-	40*/39K	+/-	Age (Ma)	+/- (Ma)
25	0.107	14.058	0.021	0.002	3.711	0.021	0.000	13.509	0.069	11.798	0.060
26	0.195	14.033	0.022	0.002	3.774	0.022	0.000	13.476	0.065	11.769	0.057
27	0.335	13.763	0.021	0.001	1.466	0.021	0.000	13.533	0.065	11.819	0.057
28	0.426	14.434	0.022	0.003	6.218	0.022	0.000	13.510	0.066	11.798	0.057
29	0.558	14.195	0.020	0.003	5.326	0.020	0.000	13.411	0.066	11.713	0.057
30	0.653	13.816	0.032	0.001	2.683	0.032	0.000	13.418	0.065	11.719	0.056
31	0.761	13.904	0.032	0.001	2.137	0.032	0.000	13.579	0.064	11.859	0.056
32	0.782	13.785	0.021	0.001	1.888	0.021	0.000	13.497	0.067	11.788	0.058
33	0.859	13.676	0.021	0.001	1.983	0.021	0.000	13.377	0.065	11.683	0.056
34	1.000	13.704	0.020	0.001	1.098	0.020	0.000	13.526	0.067	11.813	0.058

UAF039-47 7-30-92 SWNVF SANIDINE

Weighted average of J from standards = 0.000486 +/- 0.000008

Grain #	Cumulative 39Ar	40Ar/39Ar measured	37Ar/39Ar measured	36Ar/39Ar measured	% Atmospheric 40Ar	37Ca/39K	+/-	40*/39K	+/-	Age (Ma)	+/- (Ma)
16	0.003	15.423	10.346	0.010	13.935	10.416	0.365	13.339	0.960	11.650	0.836
17	0.007	22.750	9.359	0.037	44.814	9.417	0.226	12.616	0.573	11.020	0.499
18	0.017	18.349	1.834	0.017	27.168	1.836	0.092	13.359	0.249	11.667	0.217
19	0.113	13.897	0.024	0.001	1.561	0.024	0.009	13.652	0.066	11.923	0.058
20	0.128	16.089	1.642	0.009	15.575	1.643	0.062	13.573	0.172	11.854	0.150
21	0.182	13.874	0.021	0.001	1.144	0.021	0.017	13.688	0.076	11.953	0.066
22	0.781	15.025	0.121	0.005	9.945	0.121	0.002	13.506	0.066	11.795	0.057
23	0.794	15.257	2.048	0.009	15.683	2.051	0.070	12.857	0.190	11.231	0.165
24	0.822	16.791	1.893	0.012	20.558	1.895	0.034	13.333	0.110	11.645	0.095
25	0.836	15.576	2.115	0.009	16.219	2.118	0.065	13.044	0.177	11.393	0.154
26	0.846	14.379	1.868	0.004	7.102	1.870	0.092	13.348	0.245	11.658	0.213
27	0.929	15.431	0.029	0.006	12.277	0.029	0.011	13.512	0.070	11.800	0.061
28	0.934	15.071	11.682	0.009	11.097	11.772	0.196	13.476	0.458	11.769	0.398
29	1.000	13.880	0.035	0.001	1.714	0.035	0.015	13.614	0.071	11.889	0.062

UAF039-48 2EAT92-729-9 SWNVF SANIDINE

Weighted average of J from standards = 0.000486 +/- 0.000008

Grain #	Cumulative 39Ar	40Ar/39Ar measured	37Ar/39Ar measured	36Ar/39Ar measured	% Atmospheric 40Ar	37Ca/39K	+/-	40*/39K	+/-	Age (Ma)	+/- (Ma)
30	0.108	15.038	0.032	0.005	9.509	0.032	0.002	13.583	0.065	11.862	0.056
31	0.169	14.092	0.029	0.002	4.091	0.029	0.004	13.489	0.069	11.780	0.060
32	0.184	24.368	1.006	0.035	41.899	1.007	0.019	14.151	0.102	12.356	0.089
33	0.196	13.997	0.058	0.001	2.534	0.058	0.022	13.615	0.082	11.890	0.072
34	0.248	14.042	0.037	0.002	3.163	0.037	0.005	13.571	0.063	11.852	0.055
35	0.345	14.008	0.048	0.002	3.747	0.048	0.003	13.456	0.062	11.752	0.054
36	0.449	18.418	0.122	0.016	25.658	0.122	0.003	13.672	0.075	11.940	0.066
37	0.639	14.995	0.130	0.004	8.002	0.130	0.002	13.769	0.067	12.025	0.058
38	0.747	16.155	0.170	0.008	14.599	0.170	0.003	13.773	0.070	12.028	0.061
39	0.802	18.579	0.731	0.019	29.360	0.731	0.006	13.110	0.087	11.451	0.076
40	0.849	14.511	0.178	0.004	7.270	0.178	0.006	13.431	0.066	11.730	0.057
41	0.874	17.551	0.939	0.016	26.534	0.940	0.012	12.880	0.083	11.251	0.073
42	0.926	14.768	0.110	0.003	6.540	0.110	0.005	13.776	0.066	12.030	0.057
43	1.000	14.940	0.089	0.005	8.911	0.089	0.004	13.583	0.065	11.862	0.057

039-4 AT92-729-84 SWNVF

Weighted average of J from standards = 0.000486 +/- 0.000008

Grain #	Cumulative 39Ar	40Ar/39Ar measured	37Ar/39Ar measured	36Ar/39Ar measured	% Atmospheric 40Ar	37Ca/39K	+/-	40*/39K	+/-	Age (Ma)	+/- (Ma)
1	0.1315	13.457	0.044	0.001	2.381	0.044	0.003	13.109	0.059	11.450	0.052
2	0.3209	14.323	0.073	0.003	6.713	0.073	0.002	13.335	0.062	11.647	0.054
3	0.4220	13.599	0.035	0.002	4.025	0.035	0.004	13.024	0.063	11.376	0.055
4	0.6630	13.786	0.052	0.002	4.185	0.052	0.002	13.182	0.064	11.513	0.056
5	0.7664	14.064	0.048	0.002	4.668	0.048	0.004	13.38	0.063	11.686	0.055
6	0.8157	13.701	0.074	0.002	4.496	0.074	0.008	13.058	0.068	11.406	0.059
7	0.8194	23.564	0.889	0.04	50.245	0.889	0.103	11.717	0.492	10.237	0.429
8	0.8950	14.206	0.05	0.003	7.204	0.05	0.005	13.157	0.063	11.491	0.055
9	0.9103	27.888	1.868	0.053	55.999	1.871	0.026	12.273	0.19	10.722	0.165
10	1.0000	13.571	0.043	0.001	2.381	0.043	0.004	13.22	0.062	11.546	0.054

039-6 AT92-728-13 SWNVF

Weighted average of J from standards = 0.000486 +/- 0.000008

Grain #	Cumulative 39Ar	40Ar/39Ar measured	37Ar/39Ar measured	36Ar/39Ar measured	% Atmospheric 40Ar	37Ca/39K	+/-	40*/39K	+/-	Age (Ma)	+/- (Ma)
11	0.112	15.410	0.411	0.009	16.199	0.412	0.007	12.893	0.073	11.262	0.063
12	0.296	15.588	0.164	0.007	13.408	0.165	0.004	13.474	0.068	11.768	0.059
18	0.597	14.300	0.096	0.003	6.074	0.096	0.002	13.405	0.063	11.708	0.055
17	0.652	13.674	0.092	0.001	2.568	0.092	0.013	13.295	0.084	11.612	0.073
16	0.780	13.609	0.061	0.001	2.037	0.061	0.006	13.304	0.064	11.620	0.056
14	0.895	14.613	0.095	0.005	9.192	0.095	0.006	13.244	0.067	11.567	0.059
13	0.921	14.054	0.123	0.003	5.472	0.123	0.028	13.259	0.145	11.580	0.126
19	0.972	14.293	0.097	0.004	7.722	0.097	0.014	13.163	0.088	11.497	0.077
20	1.000	15.238	0.175	0.008	14.602	0.175	0.026	12.989	0.134	11.346	0.117

039-28 AT19-288 SANIDINE SWNVF

Weighted average of J from standards = 0.000486 +/- 0.000008

Grain #	Cumulative 39Ar	40Ar/39Ar measured	37Ar/39Ar measured	36Ar/39Ar measured	% Atmospheric 40Ar	37Ca/39K	+/-	40*/39K	+/-	Age (Ma)	+/- (Ma)
1	0.161	41.294	0.042	0.096	69.036	0.042	0.001	12.778	0.181	11.161	0.158
2	0.235	353.245	0.112	1.153	96.476	0.113	0.002	12.449	1.545	10.875	1.345
3	0.347	20.218	0.070	0.024	35.010	0.070	0.001	13.121	0.081	11.460	0.070
4	0.400	34.176	0.130	0.072	62.581	0.130	0.002	12.779	0.135	11.162	0.118
5	0.510	16.161	0.397	0.009	16.323	0.397	0.002	13.503	0.077	11.793	0.067
6	0.660	79.409	0.237	0.221	82.147	0.237	0.001	14.174	0.376	12.376	0.327
7	0.775	39.863	0.047	0.092	68.083	0.047	0.001	12.714	0.161	11.106	0.140
8	0.816	286.979	0.047	0.947	97.525	0.047	0.003	7.102	1.261	6.212	1.101
9	0.945	19.812	0.070	0.023	33.916	0.070	0.001	13.074	0.078	11.419	0.068
10	0.982	13.576	0.064	0.000	1.012	0.064	0.004	13.411	0.063	11.712	0.055
11	1.000	13.368	0.047	0.000	0.931	0.047	0.007	13.215	0.065	11.542	0.057

UAF039-30 AT92-728-(-15) SWNVF

Weighted average of J from standards = 0.000486 +/- 0.000008

Grain #	Cumulative 39Ar	40Ar/39Ar measured	37Ar/39Ar measured	36Ar/39Ar measured	% Atmospheric 40Ar	37Ca/39K	+/-	40*/39K	+/-	Age (Ma)	+/- (Ma)
35	1.000	13.458	0.029	0.001	1.915	0.029	0.000	13.172	0.065	11.505	0.057

UAF039-32 AT92-803-0-2 SANIDINE SWNVF

Weighted average of J from standards = 0.000486 +/- 0.000008

Grain #	Cumulative 39Ar	40Ar/39Ar measured	37Ar/39Ar measured	36Ar/39Ar measured	% Atmospheric 40Ar	37Ca/39K	+/-	40*/39K	+/-	Age (Ma)	+/- (Ma)
12	0.006	15.796	0.253	0.010	18.494	0.253	0.053	12.853	0.204	11.227	0.178
18	0.187	13.509	0.026	0.001	1.238	0.026	0.002	13.314	0.069	11.628	0.060
17	0.279	13.755	0.034	0.001	2.425	0.034	0.004	13.393	0.062	11.697	0.054
13	0.341	13.667	0.011	0.001	1.715	0.011	0.005	13.404	0.062	11.707	0.054
14	0.477	15.928	0.020	0.008	15.423	0.020	0.002	13.447	0.068	11.744	0.059
15	0.517	13.592	0.021	0.001	1.267	0.021	0.008	13.392	0.067	11.696	0.058
16	0.584	14.035	0.051	0.002	4.840	0.051	0.005	13.329	0.064	11.641	0.055
19	0.716	19.947	0.087	0.022	32.484	0.087	0.003	13.449	0.080	11.746	0.069
20	0.804	13.576	0.033	0.001	1.194	0.033	0.004	13.385	0.062	11.690	0.054
21	0.850	13.828	0.089	0.002	3.598	0.089	0.007	13.304	0.064	11.620	0.056
22	1.000	13.522	0.052	0.001	1.997	0.052	0.002	13.224	0.066	11.550	0.057

BIBLIOGRAPHY

Allegre, C.J., and J.F. Minster, 1978, Quantitative models of trace element behavior in magmatic processes, Earth and Planetary Science Letters, v. 38, p. 1-25.

Andersen, D.J., Lindsley, D.H., and P.M. Davidson, 1993, QUILF: a Pascal program to assass equilibria among Fe-Mg-Mn-Ti oxides, pyroxenes, olivine, and quartz, Computers and Geosciences, v. 19, p. 1333-1350.

Bacon, C.R., and M.M. Hirschmann, 1988, Mg/Mn partitioning as a test for equilibrium between coexisting Fe-Ti oxides, American Mineralogist, v. 73, p. 57-61.

Blake, S. and Ivey, G.N., 1986a, Magma-mixing and the dynamics of withdrawal from stratified reservoirs, Journal of Volcanology and Geothermal Research, v. 27, p. 153-178.

Blake, S. and Ivey, G.N., 1986b, Density and viscosity gradients in zoned magma chambers, and their influence on withdrawal mechanics, Journal of Volcanology and Geothermal Research, v. 30 p. 201-230.

Boden, D.R., 1994, Mid-Tertiary magmatism of the Toquima caldera complex and vicinity, Nevada: development of explosive high-K, calc-alkaline magmas in the central Great Basin, USA, Contributions to Mineralogy and Petrology, v. 116, p. 247-276.

Broxton, D.E., Byers, Jr., F.M., and R.G. Warren, 1989, Petrography and phenocryst chemistry of volcanic units at Yucca Mountain, Nevada: a comparison of outcrop and drill hole samples.

Broxton, D.E., Warren, R.G., and F.M. Byers, Jr., 1989, Chemical and mineralogic trends within the Timber Mountain-Oasis Valley Caldera Complex, Nevada: evidence for multiple cycles of chemical evolution in a long-lived silicic magma system, Journal of Geophysical Research, v. 94, p. 5961-5985.

Byers, F.M., Jr., Carr., W.J., Orkild, P.P., Quinlivan, W.D., and Sargent, D.A., 1976a, Volcanic suites and related cauldrons of Timber Mountain-

Oasis Valley caldera complex, southern Nevada: U.S. Geological Survey Professional Paper 919, 70p.

Byers, F.M., Jr., Carr., W.J., Orkild, P.P., Quinlivan, W.D., and Sargent, D.A., 1976b, Geologic map of the Timber Mountain caldera area: U.S. Geological Survey Miscellaneous Investigation Series Map I-891, scale 1:48000.

Byers, F.M., Jr., Carr, W.J., and Orkild, P.P., 1989, Volcanic centers of southwestern Nevada: evolution of understanding, 1960-1988, Journal of Geophysical Research, v. 94, p. 5843-5960.

Calderone, G.M., Gronvold, K, and Oskarsson, N., 1990, The welded are-fall tuff layer at Krafla, northern Iceland; a composite eruption triggered by injection of basaltic magma, Journal of Volcanology and Geothermal Research, v. 44, p. 303-314.

Cambray, F.W., Vogel, T.A., and J.G. Mills, Jr., 1995, Origin of compositional heterogenieties in Tuffs of the Timber Mountain Group: the relationship between magma batches, and magma transfer and emplacement in an extensional environment, Journal of Geophysical Research, v.

Christensen, J.N., and D.J. DePaolo, 1993, Time scales of large volume silicic magma systems: Sr isotopic systematics of phenocrysts and glass from the Bishop Tuff, Long Valley, California, Contributions to Mineralogy and Petrology, v. 113, p. 100-114.

Civetta, L., Galati, R., and R. Santacroce, 1991, Magma mixing and convective compositional layering within the Vesuvius magma chamber, Bulletin of Volcanology, v. 53, p. 287-300.

Clemens, J.D., and C.K. Mawer, 1992, Granitic magma transport by fracture propagation, Tectonophysics, v. 207, p. 339-360.

Crisp, J., 1984, Rates of magma emplacement and volcanic output, Journal of Volcanology and Geothermal Research, v. 20, p. 177-211.

Daley, E.E., and D.J. DePaolo, 1992, Isotopic evidence for lithospheric thinning during extension: Southeastern Great Basin, Geology, v. 20, p. 104-108.

Davies, G.R., Halliday, A.N., Mahood, G.A., and C.M. Hall., 1994, Isotopic constraints of the production rates, cryatallisation histories and residence times of pre-caldera silicic magmas, Long Valley, California, Earth and Planetary Science Letters, v. 125, p. 17-37.

Davies, J., and C.J. Hawkesworth, 1994, Early calc-alkaline magmatism in the Mogollon-Datil Volcanic Field, New Mexico, USA, Journal of the Geological Society, London, v. 151, p. 825-843.

de Silva, and J.A. Wolff, 1995, Zoned magma chambers: the influence of magma chamber geometry on sidewall convective fractionation, Journal of Volcanology and Geothermal Reaearch, v. 65, p. 111-118.

Donnelly-Nolan, J.M., 1988, A magmatic model of Medicine Lake volcano, California, Journal of Geophysical Research, v. 93, p. 4412-4420.

Duffield, W.A., and E.A. du Bray, 1990, Temperature, size, and depth of the magma reservoir for the Taylor Creek Rhyolite, New Mexico, American Mineralogist, v. 75, p. 1059-1070.

Duffield, W.A., and J. Ruiz, 1992, Evidence for the reversal of gradients in the uppermost parts of silicic magma reservoirs, Geology, v. 20, p. 1115-1118.

Duffield, W.A., Ruiz, J., and J.D. Webster, 1995, Roof-rock contamination of magma along the top of the reservoir for the Bishop Tuff, Journal of Volcanology and Geothermal Research, v. 69, p. 187-195.

Eaton, G.P., 1984, The Miocene Great Basin of western North America as an extending back-arc region, in Carlson, R.L., and Kobayashi, K., eds., Geodynamics of back-arc regions, Tectonophysics, v. 102, p. 275-295.

Ewart, A., and W.L. Griffin, 1994, Application of proton-microprobe data to trace-element partitioning in volcanic rocks, Chemical Geology, v. 117, p. 251-284.

Farmer, G.L., Broxton, D.E., Warren, R.G., and W. Pickthorn, 1991, Nd, Sr, and O isotopic variations in metaluminous ash-flow tuffs and related volcnaic rocks at the Timber Mountain/Oasis Valley Caldera, Complex, SW Nevada: implications for the origin and evolution of large-volume silicic magma bodies, Contributions to Mineralogy and Petrology, v. 109, v. 53-68.

Ferguson, John F., Cogbill, Allen H., and Richard G. Warren, 1994, A geophysical-geological transect of the Silent Canyon caldera complex, Pahute Mesa, Nevada, Journal of Geophysical Research, vol. 99, 4323-4339.

Finn, C., and D.L. Williams, 1982, Gravity evidence for a shallow intrusion under Medicine Lake volcano, California, Geology, v. 10, p. 503-507.

Flood, T.P., 1987, Cyclic evolution of a magmatic system: The Paintbrush Tuff, SW Nevada Volcanic Field [Ph.D. Thesis], Michigan State University, East Lansing, Michigan, 147 p.

Flood, T.P., Vogel, T.A., and B.C. Schuraytz, 1989a, Chemical evolution of a magmatic system: the Paintbrush Tuff, Southwest Nevada Volcanic Field, Journal of Geophysical Research, v. 94, p. 5943-5860.

Flood, T.P., Schuraytz, B.C., and Vogel, T.A., 1989b, Magma mixing due to the disruption of a layered magma body, Journal of Volcanology and Geothermal Research, v. 36, p. 241-255.

Frizzel, Jr., V.A., and J. Shulters, 1990, Geologic map of the nevada test site, southern Nevada, USGS miscellaneous investigations series, Map I-2046.

Frost, B.R., and D.H. Lindsley, 1992, Equilibria among Fe-Ti oxides, pyroxenes, olivine, and quartz: Part II. Application, American Mineralogist, v. 77, p. 1004-1020.

Hertogen, J., and R. Gubels, 1976, Calculation of trace element fractionation during partial melting, Ceochemica et Cosmochemica Acta, v. 40, p.313-322.

Hildreth, W., 1979, The Bishop Tuff: Evidence for the origin of compositional zonation in silicic magma chambers, GSA Special Paper 180, p. 43-75.

Hildreth, W., and Michael, P.J., 1983, Comment and Relpy on 'Chemical differentiation of the Bishop Tuff and other High-silica magmas through crystallization processes', Geology v. 11, p. 622-623.

Hildreth, W., Halliday, A.N., and R.L. Christiansen, 1991, Isotopic and chemical evidence concerning the genesis and contamination of basaltic and rhyoligic magma beneath the Yellowstone Plateau Volcanic Field, Journal of Petrology, v. 32, p 63-138.

Hudson, M.R., Sawyer, D.A., and R.G. Warren, 1994, Paleomagnetism and rotation constraints for the middle Miocene southwestern Nevada volcanic field, Tectonics, v. 13, p. 258-277.

Huysken, K.T., Chemical variation of the tephra fall beneath the Rainier Mesa ash-flow sheet: implications for incremental growth of a large magma body, Masters Thesis, Michigan State University, East Lansing, MI, 85 p.

Huysken, Kristin T., Thomas A. Vogel, and Paul W. Layer, 1994, Incremental growth of a large volume, chemically zoned magma body: a study of the

tephra sequence beneath the Rainier Mesa ash-flow sheet of the Timber Mountain Tuff, 1994, Bulletin of Volcanology, v. 56, p. 377-385.

Imai, A., Listanco, E.L., and T. Fujii, 1993, Petrologic and surfer isotopic significance of highly oxidized and sulfer-rich magma of Mt. Pinatubo, Philippines, Geology, v. 21, p. 699-702.

Jackson, M.P.A., and B.C. Vendeville, 1994, Regional extension as a geologic trigger for diapirism, Geological Society of America Bulletin, v. 106, p. 57-73.

Johannes, W., and F. Holtz, 1991, Formation and ascent of granitic magmas, Geologische Rundschau, v. 80, p. 225-231.

Langmuir, C.H., 1989, Geochemical consequences of in situ crystallization, Nature, v. 340, p. 199-205.

Langmuir, C.H., Klein, E.M, and T. Plank, 1992, Petrological systematics of mid-ocean ridge basalts: constraints on melt generation beneath ocean ridges, American Geophysical Union Geophysical Monograph 71, 280 p.

Lu, F., 1991, The Bishop Tuff: Origins of the high-silica rhyolite and its thermal and compositional zonations, Ph.D. Thesis, Department of the Geophysical Sciences, The University of Chicago, Chicago, IL, 331 p.

Mahood, G., and Hildreth, W., 1983, Large partition coefficients for trace elements in high-silica rhyloites, Geochemica et Cosmochemica Acta, v. 47, p. 11-30.

Marsh, B.D., 1989, Magma Chambers, Annual Review in Earth Planet. Sci., v. 17, p. 439-474.

Mattson, S.R., Vogel, T.A., and J.T. Wilband, 1986, Petrochemistry of the silicic-mafic complexes at Vesturhorn and Austurhorn, Iceland: evidence for zoned/stratified magma, Journal of Volconology and Geothermal Research, v. 28, p. 197-223.

McDougall, Ian, and T. Mark Harrison, 1988 Geochronology and Thermochronology by the $^{40}Ar/^{39}Ar$ Method, Oxford University Press, New York, 212 pp.

McKenzie, D., and M.J. Bickle, 1987, The volume and composition of melt generated by extension of the lithosphere, Journal of Petrology, v. 29, p. 625-679.

Metz, J.M, and Mahood, G.A., 1991, Development of the Long Valley, Califonria, magma chamber recorded in precaldera rhyolite lavas of Glass Mountain, Contributions to Mineralogy and Petrology, v. 106, p. 379-397.

Michael, P.J., 1983, Chemical differentiation of the Bishop Tuff and other high-silica magmas through crystallization processes, Geology, v. 11, p. 31-34.

Michael, P.J., 1987, Partition coefficients for rare earth elements in mafic minerals of high silica rhyolites: The importance of accessory mineral inclusions, Geochemica et Cosmochimica Acta, v. 52, p. 275-282.

Mills, J.G., Jr., 1991, The Timber Mountain Tuff, southwestern Nevada volcanic field: geochemistry, mineralogy, and petrogenesis, Ph.D. Thesis, Michigan State University, East Lansing, MI, 332 p.

Mills, J.G., Jr., and Rose, T.P., 1991, Manganoan fayalite ($(Fe,Mn)_2 SiO_4$): A new occurrence in rhyolitic ash-flow tuff, southwestern Nevada, U.S.A., American Mineralogist, v. 76, p. 288-292.

Mills, J.G., Jr., Saltoun, B.W., and T.A. Vogel, *in review*, Magma batches in the Timber Mountain system, southwestern Nevada volcanic field, Navada, USA.

Minster, J.F., and Allegre, C.J., 1978, Systematic use of trace elements in igneous processes, Contributions to Mineralogy and Petrology, v. 68, p. 37-52.

Nash, W.P., and H.R. Crecraft, 1985, Partition coefficients for trace elements in silicic magmas, Geochimica et Cosmochimica Acta, v. 49, 2309-2322.

Noble, D.C., Sargent, K.A., Mehnert, H.H., Ekren, E.B., and Byers, Jr., R.M., 1968, Silent Canyon volcanic center, Nye County, Nevada, Studies of Geology and Hydrology, Nevada Test Site, Geological Society of America, Memoir 110, p. 65-75.

Orsi, G., Civetta, L., D'Antonio M., Di Girolamo, P., and Piochi, M., 1995, Step-filling and development of a zoned magma chamber: the Neapolitan Yellow Tuff case history, Journal of Volcanology and Geothermal Research, v.

Pankhurst, R.J., 1977, Open system crystal fractionation and incompatible element variation in basalts, Nature, v. 268, p. 36-38.

Papale, P., and D. Flavio, 19 , Modeling of the ascent of magma during the plinian eruption of Vesuvius in A.D. 79, Journal of Volcanology and Geothermal Research, v. 58, p. 101-132.

Paterson, S.R., and T.K. Fowler, Jr., 1993, Re-examining pluton emplacement processes, Journal of Structural Geology, v. 15, p. 191-206.

Paterson, S.R., and O.T. Tobisch, 1992, Rates of processes in magmatic arcs: implications for the timing and nature of pluton emplacemnet and wall rock deformation, Journal of Structural Geology, v.14, p. 291-300.

Paterson, Scott R., and Ron H. Vernon, 1995, Bursting the bubble of ballooning plutons: A return to nested diapirs emplaced by multiple processes, GSA Bulletin, v. 107, 1356-1380.

Rolandi, G., Maraffi, S., Petrosino, P., and L. Lirer, 1993, The Ottaviano eruption of Somma-Vesuvio (8000 y. B.P.): a magmatic alternating fall and flow-forming eruption, Journal of Volcanology and Geothermal Research, v. 58, p. 43-65.

Rolandi, G., Mastrolorenzo, G., Barrella, A.M., and A. Borrelli, 1993, The Avellino plinian eruption of Somma-Vesuvius (3760 y. B.P.); the progressive evolution from magmatic to hydromagmatic style, Journal of Volcanology and Geothermal Research, v. 58, p. 67-88.

Rollinson, H., 1993, Using geochemical data: evaluation, presentation, interpretation, Longman Scientific and Technical, Essex, 352 p.

Rose, T.P., 1988, A model for the origin of the chemically zoned Ammonia Tanks Member of the Timber Mountain Tuff due to crystal fractionation, Masters Thesis, Michigan State University, East Lansing, MI, 71 p.

Santacroce, R., Bertagnini, A., Civetta, L., Landi, P., and A. Sbrana, 1993, Eruptive dynamics and petrogenetic processes in a very shallow magma reservoir; the 1906 eruption of Vesuvius, Journal of Petrology, v. 34, p. 383-425.

Sarna, W.A.M., Meyer, C.E., Woodward, M.J., and P.J. Lamothe, 1981, Composition of air-fall ash erupted on May 18, May 25, June 12, July 22, and August 7, in Lipman, P.W., and D.R. Mullineaux, The 1980 eruptions of Mount St. Helens, Washington, U.S. Geological Survey Professional Paper 1275, p. 667-681.

Sarna, W.A.M., Waitt, Jr., R.B., Woodward, M.J., Shipley, S., Rivera, J.R., Dzurisin, D., Wood, S.H., Zielinski, R.A., Sawyer, M.G., and V.L. Hansen,

1981, Air-fall deposits, in U.S. Geological Survey Professional Paper 1275, p. 157-158.

Saltoun, B.W., 1996, The high silica Rainier Mesa magmas: implications on the origin of large volume, compositionally zoned magma systems, Masters Thesis, Michigan State University, East Lansing, MI.

Sawyer, D.A., Fleck, R.J., Lanphere, M.A., Warren, R.G., Broxton, D.E., and M.R. Hudson, 1994, Episodic caldera volcanism in the Miocene southwestern Nevada volcanic field: Revised stratigraphic framework, $^{40}Ar/^{39}Ar$ geochronology, and implications for magmatism and extension, Geological Society of America Bulletin, v. 106, p. 1304-1318.

Sawyer, D.A., and K.A. Sargent, 1989, Petrologic evolution of divergent peralkaline magmas from the Silent Canyon Caldera Complex, southwestern Nevada volcanic field, Journal of Geophysical Research, v. 94, p. 6021-6040.

Schuraytz, B.C., 1988, Geochemical gradients in the Topopah Spring Member of the Paintbrush Tuff: evidence for eruption across a magmatic interface, Ph.D. Thesis, Michigan State University, East Lansing, MI, 146 p.

Schuraytz, B.C., Vogel, T.A., and L.W. Younker, 1989, Evidence for dynamic withdrawal from a layered magma body: the Topopah Spring Tuff, southwestern Nevada, Journal of Geophysical Research, v. 94, p. 5925-5942.

Sisson, T.W., 1991, Pyroxene-high silica rhyolite trace element partition coefficients measured by ion microprobe, Geochimica et Cosmochimica Acta, v. 55, p. 1575-1585.

Sisson, T.W., 1994, Hornblende-melt trace-element partitioning measured by ion microprobe, Chemical Geology, v. 117, p. 331-344.

Sparks, R.S.J., 1989, In situ differentiation in magma, Nature, v. 340, p. 187.

Sparks, R.S.J., Bursik, M.I., Ablay, G.J., Thomas, R.M.E., and S.N. Carey, 1992, Sedimentation of tephra by volcanic plumes: Part 2. Controls on thickness and grain-size variation of tephra fall deposits, Bulletin of Volcanology, v. 54, p. 684-695.

Spera, F.J. and Crisp, J.A., 1981, Eruption volume, periodicity, and caldera area: relationships and inferences on development of compositional zonation in silicic magma chambers, Journal of Volcanology and Geothermal Research, v. 11, p. 169-187.

Trial, A.F. and Spera, F.J., 1990, Mechanisms for the generation of compositional heterogeneities in magma chambers, Bulletin of the Geological Society of America, v. 102, p. 353-367.

van den Bogaard, 1995, $^{40}Ar/^{39}Ar$ ages of sanidine phenocrysts from Laacher See Tephra (12,900 yr BP): Chronostratigraphic and petrological significance, Earth and Planetary Science Letters, v. 133, p. 163-174.

Verplanck, P.L., G.L. Farmer, M. McCurry, S. Mertzman, and L.W. Snee, 1995, Isotopic evidence on the origin of compositional layering in an epizonal magma body, Earth and Planetary Science Letters, v. 136, 31-41.

Vogel, T.A., and R. Aines, 1996, Melt inclusions from chemically zoned ash flow sheets from the Southwest Nevada Volcanic Field, Journal of Geophysical Research, v. 101, p. 5591-5610.

Vogel, T.A., and Byers, Jr., F.M., 1989, Introduction to the special section on the southwestern Nevada volcanic field, Journal of Geophysical Research, v. 94, p. 5907.

Vogel, T.A., Woodburne, T.B., Eichelberger, J.C., and P.W. Layer, 1994, Chemical evolution and periodic eruption of mafic lava flows in the west moat of Long Valley Caldera, California, Journal of Geophysical Research, v.

Warren, R.G., Byers, F.M., Jr., and Caporusio, F.A., 1984, Petrography and mineral chemistry of unity of the Topopah Spring, Calico Hills and Crater Flat tuffs, and older volcanic units, with emphasis on samples from drill hole USW G-1, Yucca Mountain, Nevada Test Site, Report Los Alamos National Laboratory, La-10003-MS, p. 1-78.

Warren, R.G., Byers, Jr., F.M., Broxton, D.E., Freeman, S.H., and R.C. Hagan, 1989, Phenocryst abundances and glass and phenocryst compositions as indicators of magmatic environments of large-volume ash flow sheets in southwestern Nevada, Journal of Gephysical Research, v. 94, p. 5987-6020.

Warren, R.G., and G.A. Valentine, 1990, Precursor eruptive activity of the large-volume Rainier Mesa Tuff, southwestern Nevada, U.S.A., New Mexico Bulletin of Mining Geology, v.131, p. 287.

Warren, R.G., McDowell, F.W, Byers, Jr., F.M., Broxton, D.E., Carr, W.J., and P.P. Orkild, 1988, Episodic leaks from Timber Mountain Caldera: new evidence from ryolite lavas of Fortymile Canyon, SW Nevada Volcanic Field.

Warshaw, C.M., and R.L. Smith, 1988, Pyroxenes and fayalites in the Bandelier Tuff, New Mexico: Temperatures and comparison with other rhyolites, American Mineralogist, v. 73, p. 1025-1037.

Weiss, S.I., and D.C. Noble, 1989, Stonewall Mountain volcanic center, southern Nevada: stratigraphic, structural, and facies relations of outflow sheets, near-vent tuffs, and intercaldera units, Journal of Geophysical Research, v. 94, p. 6059-6074.

Weiss, S.I., Noble, D.C., and E.H. McKee, 1989, Paleomagnetic and cooling constraints on the duration of the Pahute Mesa-Trail Ridge eruptive event and associated magmatic evolution, Black Mountain volcanic center, southwestern Nevada, Journal of Geophysical Research, v. 94, p. 6075-6084.

Whitney, J.A., Dorais, M.J., Stormer, Jr., J.C., Kline, S.W., and D.J. Matty, 1988, Magmatic conditions and development of chemical zonation in the Carpenter Ridge Tuff, Central San Juan volcanic field, Colorado, American Journal of Science, v. 288, p. 16-44.

Wolff, J.A., Worner, G. and Blake, S., 1990, Gradients in physical parameters in zoned felsic magma bodies: implications for evolution and eruptive withdrawal, Journal of Volcanology and Geothermal Research, v. 43, p. 37-55.